IJRTEI
International Journal of Research and Technology in Electrical Industry

Shahid Beheshti University

International Journal of
Research and Technology in Electrical Industry

IJRTEI

Volume 1, Issue 1, March 2022, Pages 1-113

ISSN: 2821-0190

Article titles

IJRTEI, Volume 1, Issue 1, March 2022, Pages 1-113

Journal Description

IJRTEI is an open access journal which is published at Shahid Beheshti University. IJRTEI is an international peer-reviewed journal that publishes original research papers and review articles covering broad ranges of topics in the field of the Electricity Industry. The focus of the journal is on high-quality academic (theoretical or empirical) and practical papers aimed at providing a suitable platform for information exchange and advancement of scientific level in the electricity Industry.

Publisher:
Shahid Beheshti University
ISSN: 2821-0190
Frequency: Semiannual
Language: English

Website: IJRTEI.sbu.ac.ir
E-Mail: IJRTEI@sbu.ac.ir
Phone: (+98)21-73932321
Fax: (+98)21-73932321

Contents

International Journal of Research and Technology in Electrical Industry

journal homepage: ijrtei.sbu.ac.ir

Shahid Beheshti University

Power Distribution Grid Reliability Assessment Considering Protection and Control Devices' Optimal Post-Fault Operation

Ali Jalilian [1,*], Milad Mohamadyari[2], Homayun Rahimi[1], Majid Karami[1]

[1] *Kermanshah Power Electrical Distribution Company (KPEDC), Kermanshah, Iran*
[2] *Electrical Engineering Department, Tehran University, Tehran, Iran*

ARTICLEINFO

Article history:
Received 23 November 2021
Received in revised form 05 February 2022
Accepted 24 February 2022

Keywords:
Reliability indices
Service restoration
Protection devices
Isolating switches
Distribution system

ABSTRACT

The reliability level of the distribution network is a judgment tool of the grid and protection design quality, the effectiveness of the fault management unit, and customers' satisfaction. In this paper, a new approach is presented to evaluate common reliability indices namely ENS, SAIDI, SAIFI, MAIFIe, etc., while reliability improvement via optimal post-fault restoration describes the coordinated operation of various protection and control devices in temporary and permanent fault event conditions. Customers' outage times are calculated considering different switching operation times to capture manual operation issues, e.g., traffic level, geographical issues, fuse replacements, etc. The optimal service restoration scheme being formulated in a mixed-integer linear programming (MILP) fashion is constrained to network technical limitations, e.g., line thermal capacity, load points voltage level, DG units' parameters, and island operation. The performance of the proposed framework is verified in IEEE 33-bus test system.

Nomenclature

Sets

B	set for network buses
L	set for lines
D_b	set for buses downstream of the bus b

Parameters

CDF_b	customer outage costs
F_ℓ	sending node of the line ℓ
T_ℓ	receiving node of the line ℓ
M	sufficiently big value
T_ℓ^{sw-c}	required time for switching operation. This parameter is zero for closed switches and non-switchable lines.
T_ℓ^{sw-o}	required time for switching operation. This parameter is zero for opened switches and non-switchable lines.
R_ℓ^{line}	resistance of the network lines
X_ℓ^{line}	reactance of the network lines
$\underline{V}$	minimum allowable voltage level
$\overline{V}$	maximum allowable voltage level
$\overline{S}_\ell^{Line}$	line power capacity
$\underline{P}_b^G$	min. active power generation capacity
$\overline{P}_b^G$	max. active power generation capacity
$\underline{Q}_b^G$	min. reactive power generation capacity
$\overline{Q}_b^G$	max. reactive power generation capacity

* Corresponding author
E-mail address: alijalilian918@yahoo.com
http://dx.doi.org/ 10.52547/ijrtei.1.1.1

λ_{Sc} annual rate for the fault scenario

N_b^c number of customers in each bus

N_{total}^c total number of customers

T^{p-min} minimum permanent fault duration

Variables

T_b^{out} bus outage duration

α_b^{ref} binary variable showing reference node

α_b^{Master} binary variable showing master DG node

α_b^{sub} binary value showing if a bus is a substation

β_ℓ^{Line} binary variable for line connection status

β_ℓ^{Nor} binary variable showing that the power flow direction of the line ℓ in new configuration is as normal, i.e., sending node is parent and receiving node is offspring.

β_ℓ^{Rev} binary variable showing reverse power flow direction

U_b square of the buses voltage level

P_ℓ^{Line} active power flow through each line

Q_ℓ^{Line} reactive power flow through each line

P_b^{load} load point active power demand

Q_b^{load} load point reactive power demand

P_b^G active power generation

Q_b^G reactive power generation

1. Introduction

Reliability assessment is an integral part of designing, planning, operation, and many other analyses of today's power systems, as it is able to quantify the quality of the energy which is being delivered to the costumers in terms of continuity or interruption. Monte Carlo Simulation (MCS) [1-4] is one of the most widely used method for evaluating the reliability of distribution systems. Studies like [5-7] propose an algorithmic way of estimating the reliability indices. In [7], the spanning tree search algorithm is used to generate optimal distribution system reconfiguration scheme for load restoration and finding minimum switching operations. However, this model has not considered network's technical limitations, and microgrids are modeled as separate modules with fixed load points and they don't contribute to island formation coordinated with switching actions. [6] proposes an optimal restoration sequence based on minimum costumers' interruption cost. A fault traversal algorithm has been used to trace the faulted area and the involved switches for fault-isolation and service restoration. This model also does not take into account network's technical constraints, and DGs' operation, and only circuit breaker and isolating switches are considered. In [5] a technique for reliability assessment of distribution systems, considering restoration sequence is presented. A parent-visit technique is used to determine the affected area after a failure, and a breadth-first search is used to divide the affected load points to different classes based on restoration times. The stated algorithmic models [5-7] lack a solid mathematical formulation to be modeled as a standard optimization problem. The numerous advantages, such as being globally optimum and easily solved by off-the-shelf software, of well-known optimization programming models like MILP, have captured the attention of many power system researchers for quite a long time [8, 9]. However, providing a standard mathematical model for reliability assessment of distribution systems seems to be overlooked until recently. Among the first attempts to address this issue is [10], where a multi-objective mixed-integer second-order conic programming model is introduced to simultaneously minimize power losses and improve network's reliability. [11] is another pioneer in establishing a non-simulation-based linear programming approach for reliability assessment of distribution networks. It develops a mathematical formulation for calculation of expected nodal repair-and-switching and switching-only rates and durations using a fictitious power flow optimization model. Some of the common reliability indices are then calculated. These analytical models aim to overcome the approximate techniques needed for solving reliability-constrained optimization models. These works rely on optimization-based methods for calculation of the shortest path between each load node and its connected substation. Later in [12], an algebraic approach was proposed to improve the time-consuming computational performance of the previous models, where a set of algebraic equations replaced the linear programming model used in [11, 12] to calculate reliability indices. However, these models lack several important features of a comprehensive reliability assessment framework.

An important issue in distribution feeders' restoration arises when facing complex structures. Some reliability assessment frameworks in literature consider only radially designed feeders [11]. In [13] mesh structured designs is considered but only when the maneuver points can connect the end buses of different feeders or laterals. thus, the presented model is not applicable to more complex structures in which maneuver points connect laterals from the same substation or two load points of a single lateral. An analytical reliability assessment model is proposed in [13] to compensate some of the weaknesses of [10-12]. Here, the authors highlight the importance of a model-based method capable of evaluating the reliability of meshed-constructed networks. This paper aims to enhance the reliability by performing post-fault network reconfiguration as it has been proven in many cases [10, 14-20]. Although [13] offers a considerable improvement compared to [10-12] in terms of reliability enhancement, taking into account network's technical constraints and model scalability, it is not already able to deal with and take advantage of many active distribution networks' strategies, such as complex feeder structure, DG and microgrid operation and different protection devices. Also, several assumptions are made in [14] that are not practical in real distribution systems, e.g., placing switches on both sides of each feeder branches, only one circuit breaker on each feeder, etc. In their most recently published work

[21], the authors try to cover some shortcomings of [13] by proposing another optimization model-based reliability assessment method that linearly characterize the placement of circuit breaker and switches and their actions. Despite being an obvious improvement over their previous model [13], the model in [21] has yet to be developed from different aspects to be applicable to real world distribution networks as a sound reliability assessment package.

Studies like [22] have attempted to face the reliability assessment problem from different angle and introduced a linear model for topology-variable-based distribution systems. This model focuses on providing a systematic way of calculating reliability indices, rather than reliability enhancement. It does not consider networks technical constraints, DGs and microgrids, and different protection devices. Like previous works, it does not take into account temporary faults.

Although temporary faults have a greater rate of occurrence, their impact in reliability indices calculation is forsaken in all the mentioned literature. A comprehensive assessment of the distribution reliability should consider temporary faults not only in temporary outage measures like Momentary Average Interruption Frequency Index (MAIFI) but also when they cause permanent outages. The latter condition happens when the protection does not have reclosing capability. In this paper, the MAIFIe index is preferred over MAIFI which is independent of how many reclosing cycles a temporary fault lasts. Furthermore, it better reflects the customers' experience in terms of power supply continuity.

As mentioned in earlier studies, e.g. [11, 22], and admitted by many others, a complete assessment of reliability of distribution network should consider: additional post-fault network reconfiguration to restore services for load nodes downstream of the fault, island operation capability, temporary faults, line overloading, etc. Thus, motivated by lack of a comprehensive reliability assessment framework for distribution systems, this paper proposes a novel analytical model-based reliability assessment method that covers several existing gaps.

The main contributions of this paper are as follows:

1) Proposing a novel reliability assessment framework using MILP. This model is able to not only evaluate network's reliability by various existing indices, but also adopts an active reliability assessment approach to minimize costumes' interruption duration, achieved by optimal fault-isolation, network reconfiguration and restoration that results in notable reliability enhancement compared to passive reliability calculations.

2) Compared to all previous works, this model is not limited to only radial or mesh-constructed networks, and can evaluate the reliability of any complex network design.

3) The proposed model takes into account one of the critical features of today's smart distribution grids, i.e. the integration of distributed generations and microgrids in the system, which has been overlooked in previous studies. Here, the model is capable of not only evaluating the reliability in the presence of grid-connected DGs and islanded-microgrid operations, but also harnessing this feature for further improvement of reliability indices.

4) This paper presents a model for a serious concern that has been addressed in pervious pioneer works, i.e. the impact of temporary faults on system's reliability. Besides the sustained faults and their impact on various common reliability indices, the proposed model evaluates the impact of temporary faults via some special quantitative reliability indices, such as MAIFIe.

5) The proposed model takes into account the network's technical constraints, such as power flow equations, nodal voltage magnitude, line's thermal capacity, and guarantees that these variables are within their specified limitations in each network configuration.

6) Unlike previous studies that only consider circuit breakers and typical sectionalizing switches, this model makes distinction between many protection devices, e.g. Circuit Breakers (CBs), Reclosers (Rs), Manual Switches (MSs), Remote Control Switch (RCSs), and Fuses (both fuse-saving and fuse-blowing settings), in terms of protection coordination and switching sequence.

Table I summarizes the proposed model's capabilities and features compared to some of the pioneer reliability assessment models in the literature.

Table I. Summarization of distribution network's reliability assessment model

Model	Assessment approach	Reliability enhancement	Post-fault restoration	DG and microgrid	Mesh-constructed grid	Complex feeder structure	Temporary faults	Diverse protection devices	Network Constraints
[6]	Algorithmic	✓	✓		✓				✓
[10]	Optimization-based	✓			✓				✓
[11]	Analytical								
[12]	Algebraic								
[13]	Analytical	✓	✓		✓				✓
[21]	Optimization-based	✓	✓		✓				✓
Proposed	Optimization-based	✓	✓	✓	✓	✓	✓	✓	✓

2. Proposed Framework

The proposed method for evaluating reliability indices can be described in three steps.

1- Gathering the required information - This information includes network parameters such as network structure, line parameters, control and protection devices locations, loading capacity, etc., information related to the load and

DG such as power consumption or generation, customer counts, etc., as well as reliability parameters.
2- Data processing – Network configuration and devices location is used to determine the set of downstream nodes for each protection device as well as the protection of any temporary or permanent fault in the network.
3- Calculation of reliability indices - In this step, different scenarios of fault events in the network are generated. In each scenario, customers' outage duration based on the optimal restoration is calculated. Then, according to the obtained outage times and scenario rate, different reliability indices are calculated.
Data flow among different steps in the proposed algorithm is illustrated in Fig. 1.

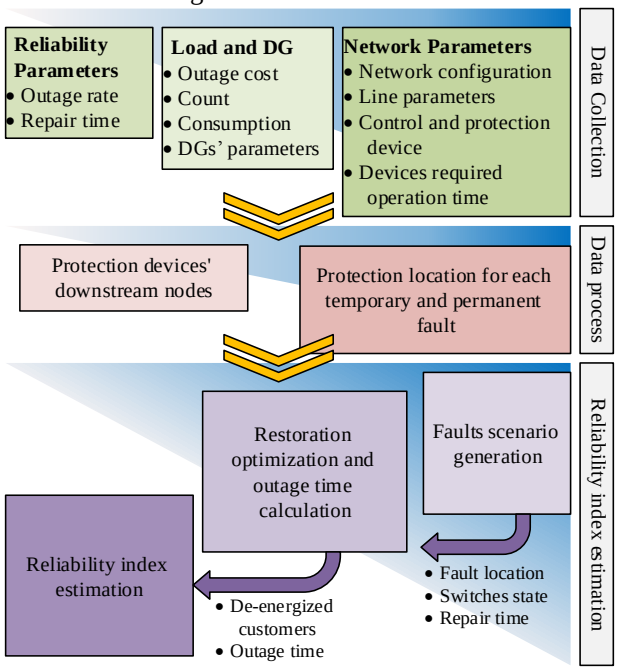

Fig. 1. Reliability estimation procedure data flow

3. Optimal Restoration

Restoration optimization in each fault scenario determines de-energized customers and their outage time.

3.1. Restoration Objective

The prime objective of restoration schemes in utilities may vary based on different policies toward critical loads, customers' vulnerability, reporting indices to higher authorities, or meeting a certain standard which in turn affects the post-fault correction actions and reliability indices. In this paper, the service restoration procedure aims to minimize the total customers' outage costs (1).

$$Min: \sum_{b\in \mathrm{B}} CDF_b\left(T_b^{out}\right) \tag{1}$$

Where, CDF_b determines customer outage costs as a function of outage duration. The description of customer costs could be linear or partially linear to hold MILP framework.

3.2. Restoration Constraints

The restoration optimization problem constraints include distribution network reconfiguration, outage times calculation, and network technical constraints.

3.2.1 Network Reconfiguration

Network graph connectivity and radiality entails each node to have exactly one parent as reference node to be supplied from, unless the node is a substation or hosts a master DG in island operation. In (2) and (3), this concept is mathematically stated.

$$\alpha_b^{ref} = \alpha_b^{sub} + \alpha_b^{Master}; \forall b \in \mathrm{B} \tag{2}$$

$$\sum_{\substack{l\in L \\ \mathrm{T}_\ell = b}} \beta_\ell^{Nor} + \sum_{\substack{l\in L \\ \mathrm{F}_\ell = b}} \beta_\ell^{Rev} = 1 - \alpha_b^{ref}; \forall b \in \mathrm{B} \tag{3}$$

If the line is connected, energization direction is determined (4).

$$\beta_\ell^{Nor} + \beta_\ell^{Rev} = \beta_\ell^{Line}; \forall \ell \in \mathrm{L} \tag{4}$$

3.2.2 Outage time

Due to the fact that each load point must somehow be connected to a reference bus, moving from reference nodes to end nodes through the path reconstructed in (2)-(4) and described by β_ℓ^{Nor} and β_ℓ^{Rev} variables, load points' outage time will increase.

$$T_b^{out} \geq T_{b'}^{out} - M \times \left(1 - \beta_\ell^{Nor}\right); \quad \forall b, b' \in \mathrm{B}, \ell \in \mathrm{L}, b = \mathrm{T}_\ell, b' = \mathrm{F}_\ell \tag{5}$$

$$T_b^{out} \geq T_{b'}^{out} - M \times \left(1 - \beta_\ell^{Rev}\right); \quad \forall b, b' \in \mathrm{B}, \ell \in \mathrm{L}, b' = \mathrm{T}_\ell, b = \mathrm{F}_\ell \tag{6}$$

Based on (5) and (6), outage time of each node is greater than its' parent.
If the reconfiguration process involves closing a switch, the downstream nodes should have outage time longer than the required switching time.

$$T_b^{out} \geq T_\ell^{sw-c} \times \beta_\ell^{Nor}; \forall b \in \mathrm{B}, \ell \in \mathrm{L}, b = \mathrm{T}_\ell \tag{7}$$

$$T_b^{out} \geq T_\ell^{sw-c} \times \beta_\ell^{Rev}; \forall b \in \mathrm{B}, \ell \in \mathrm{L}, b = \mathrm{F}_\ell \tag{8}$$

If a line is switched open during the network reconfiguration process, it means that the two sides of the switch could not be restored jointly. This may be due to a fault on either sides of the switch or for the matter that the restoration of both sides of the switch as a whole may result in a violation of system technical constraints such as the allowable line thermal or the voltage level limits. Accordingly, both sides of the switch cannot be energized before required switching time.

$$T_b^{out} \geq T_\ell^{sw-o} \times \left(1 - \beta_\ell^{Line}\right); \quad \forall b \in \mathrm{B}, \ell \in \mathrm{L}, b = \mathrm{T}_\ell \, or \, b = \mathrm{F}_\ell \tag{9}$$

If the line between two buses is switchable and this line is initially closed and remains closed until the end of the process, both sides buses will have equal outage time. This situation is similar to the line that is not switchable.
Since according to (5) and (6), the restoration time of an offspring is longer than its parent, (10) and (11) that assure longer outage time for parent node, guarantee the equal outage times for parent and offspring.

$$T_b^{out} \geq T_{b'}^{out} - M \times \left(1 - \beta_\ell^{Nor}\right); \quad \forall b, b' \in \mathrm{B}, \ell \in \mathrm{L}, b = \mathrm{F}_\ell, b' = \mathrm{T}_\ell, T_\ell^{sw-c} = 0 \tag{10}$$

$$T_b^{out} \geq T_{b'}^{out} - M \times \left(1 - \beta_\ell^{Rev}\right); \quad \forall b, b' \in \mathrm{B}, \ell \in \mathrm{L}, b = \mathrm{T}_\ell, b' = \mathrm{F}_\ell, T_\ell^{sw-c} = 0 \tag{11}$$

Outage time of a node in a fault condition must be longer than the fault required repair time.

$$T_b^{out} \geq T_b^{Repair}; \forall b \in \mathrm{B} \tag{12}$$

Although in (12) the fault repair time is only considered in the related node, previous constraints also propagate the fault effect through connected lines to other nodes. As the result, any node connected to a fault cannot be restored before the repair time.

3.2.3 Network Operation

Since load restoration process is associated with network reconfiguration, it is necessary to consider the permitted ranges for load points voltage level and lines power flows in the mathematical model. For this purpose, it is necessary to add power flow equations to the mathematical model of the problem.

The voltage drop constraint across each line is given in (13). According to this constraint, if the line is connected, the voltage drop is calculated between its two end buses [23].

$$\pm \left| U_b - U_{b'} - 2 \times \left(P_\ell^{Line} R_\ell^{line} + Q_\ell^{Line} X_\ell^{line} \right) \right| \leq \left(1 - \beta_\ell^{Line}\right) \times M \tag{13}$$

$$\forall b, b' \in \mathrm{B}, \ell \in \mathrm{L}, b = \mathrm{F}_\ell, b' = \mathrm{T}_\ell$$

In each network bus, the sum of input power is equal to output. (14) and (15) show the constraints on the real and reactive power balance at the buses of the network, respectively.

$$\sum_{b \in \mathrm{F}_\ell} P_\ell^{Line} + P_b^{load} = \sum_{b \in \mathrm{T}_\ell} P_\ell^{Line} + P_b^{G}; \forall b \in \mathrm{B} \tag{14}$$

$$\sum_{b \in \mathrm{F}_\ell} Q_\ell^{Line} + Q_b^{load} = \sum_{b \in \mathrm{T}_\ell} Q_\ell^{Line} + Q_b^{G}; \forall b \in \mathrm{B} \tag{15}$$

Voltage level is constrained in permitted range through (16).

$$\underline{V}^2 \leq U_b \leq \overline{V}^2; \forall b \in \mathrm{B} \tag{16}$$

Line thermal capacity limitation can be modelled as in (17).

$$\left(P_\ell^{Line}\right)^2 + \left(Q_\ell^{Line}\right)^2 \leq \left(\overline{S}_\ell^{Line}\right)^2; \forall \ell \in \mathrm{L} \tag{17}$$

However, this formulation which describe the feasible solution area as a circle, is non-linear. Therefore, an octagonal approximation is used here through (18)-(19) to preserve the model in MILP format [24].

$$\pm P_\ell^{Line} \pm Q_\ell^{Line} \leq 1.3066 \times \overline{S}_\ell^{Line}; \forall \ell \in \mathrm{L} \tag{18}$$

$$\pm P_\ell^{Line}, \pm Q_\ell^{Line} \leq 0.9239 \times \overline{S}_\ell^{Line}; \forall \ell \in \mathrm{L} \tag{19}$$

DGs' output power limitation is also considered in (20) and (21) .

$$\underline{P}_b^G \leq P_b^G \leq \overline{P}_b^G; \forall b \in \mathrm{B} \tag{20}$$

$$\underline{Q}_b^G \leq Q_b^G \leq \overline{Q}_b^G; \forall b \in \mathrm{B} \tag{21}$$

4. Reliability Index Calculation Algorithm

Having an optimization-based decision-making system introduced in previous section, the calculation of reliability indices consists of scenario generation for events, outage time calculation for load points and finally calculating each index through a weighted sum of load point outages. The process of calculating reliability indices is shown in Fig. 2.

Outage scenarios consist of permanent and temporary faults. For each fault scenario, repair time, upstream switch ($T_\ell^{sw-o} = 0$) with required closing operation time (T_ℓ^{sw-c}) at the beginning of the restoration process. If the protection type is a fuse, fuse replacement time is added to its close operation time. ENS and SAIDI indices calculation exclude momentary outages. So, T_b^{out} calculation for these faults is bypassed in Fig. 2.

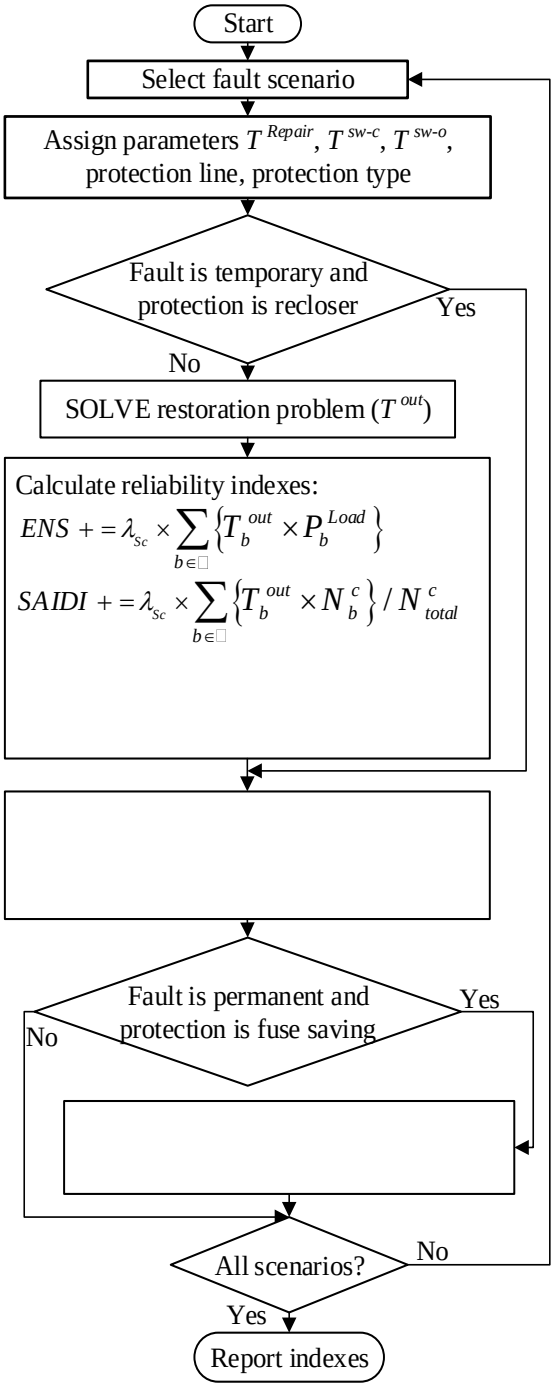

Fig. 2. Reliability estimation process

For permanent faults cleared by fuse-saving fuses, nodes which are downstream to the upstream recloser, but not downstream to the fuse-saving fuse would experience temporary outage.
Once SAIFI and SAIDI values are available, other indices such as CAIDI and ASAI can readily be calculated.

$$CAIDI = SAIDI / SAIFI \quad (22)$$

$$ASAI = 1 - SAIDI / 8760 \quad (23)$$

5. Numerical Analysis and Results

5.1. Network Information and Assumptions

The 33-bus IEEE network is intended for numerical studies in this section. As shown in Fig. 3, this network consists of 33 buses, 32 lines and 5 manoeuvre points. This network is connected to the upstream network through bus #1. Network loading information and line parameters are available in [25]. To the purpose of this paper's studies, the network is equipped with a circuit breaker in the substation, a recloser, two fuse-blowing fuses, two fuse-saving fuses, three manual and five remotely controllable sectionalizers.

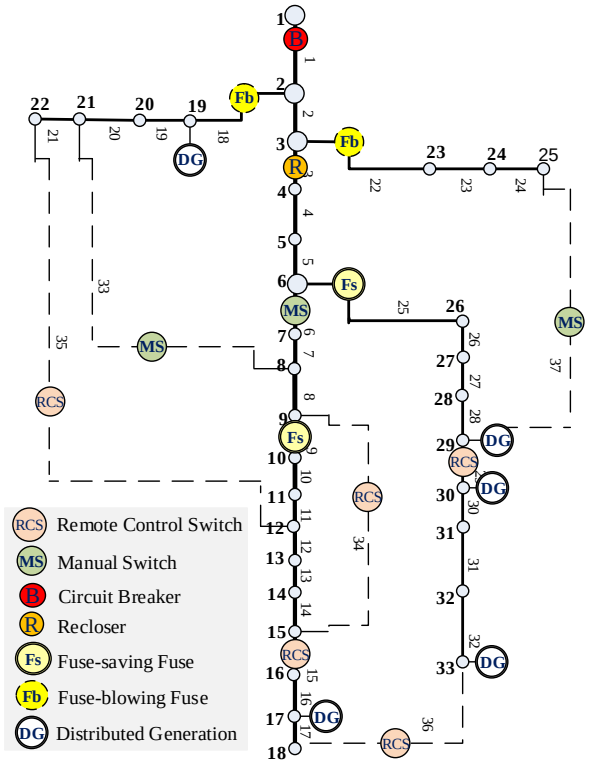

Fig. 3. Test feeder and switching devices

It is assumed that all switches involve in reconfiguration during load restoration process. The hypothetical times required for operation (opening or closing) of each switchable device or replacement of each fuse are given in Table II. One minute of operation time for remotely controllable switches is considered. It is also assumed that there are five distributed generation units in the network, information on which is given in Table III.
Network reliability information including the temporary and permanent fault rates, expected required repair times of the faults and the number of customers per bus are also hypothetically selected. Thus, the following parameters are selected as random numbers, annual rate of permanent faults per bus between 0.05 and 0.25, annual failure rate of temporary faults per bus between 0.05 to 0.6, the expected time needed to repair each fault between 70 to 150 minutes selected.

Table II. Equipment required operation time.

Equipment	Installed line	Operation time (min.)
CB	1	1
Recloser	3	1
FB fuse	18	20
FB fuse	22	23
FS fuse	9	45
FS fuse	25	37
MS	6	35
MS	33	32
MS	37	36
RCS	15، 29، 34، 35، 36	1

Table III. DG parameters.

No.	Installed bus	$\underline{P}^G, \bar{P}^G$ (kW)	$\underline{Q}^G, \bar{Q}^G$ (kVar)
1	17	25 , 250	-175 , 175
2	19	40 , 400	-280 , 280
3	29	50 , 500	-350 , 350
4	30	50 , 500	-350 , 350
5	33	20 , 200	-140 , 140

The number of customers per bus is calculated using nominal bus power and based on the assumption that customers demand an average of 5 kW in all buses.
Outages lasting more than 3 minutes are considered permanent interruptions. The permitted range of voltage levels of different buses is considered between 0.9 to 1.05.

5.2. Numerical Results

The proposed method has been implemented on the 33-bus network with the assumptions introduced. The relevant results are collected in Table IV.
In Table IV the share of both temporary and permanent faults in each calculated index is also presented. According to these results, ENS, SAIDI, and SAIFI are mainly caused by permanent faults due to necessary repair actions and less caused by temporary faults due to recloser function. Temporary faults lead into sustained outages only where the protection has no reclosing capability, i.e., fuse-blowing fuses and CBs, as a result, restoration is subject to manual switching actions. Another observation is that ENS and SAIDI's shares from temporary and permanent faults are equal. This result is due to the assumption of similarity of customers. Because, number of customers without power is linearly dependent to power not supplied.
Depending on only outage counts, the SAIFI value relatively has a greater share from temporary faults. Because this index does not consider de-energized power and outage time. As mentioned in algorithm explanation, a permanent fault cleared by fuse-saving fuse causes momentary interruptions for loads between the fuse and its upstream recloser. Except for this condition, results

regarding MAIFIe having greater value than SAIFI as well as the portion of MAIFIe caused by permanent faults show the prompt restoration which is the benefaction of the automation system, i.e., reclosing and remote switching. Expectedly, CAIDI values for temporary faults share are smaller due to restoration without repair actions. ASAI and SAIDI values being linearly dependent have similar shares from each kind of fault.

Table IV Results of reliability indices estimation

Reliability Index	Value	Temporary Fault	Permanent Fault
ENS	7236.322	6.51 (%)	93.49 (%)
SAIDI	1.94795	6.51 (%)	93.49 (%)
SAIFI	1.643	19.15 (%)	80.85 (%)
MAIFIe	4.574	83.40 (%)	16.60 (%)
CAIDI	1.1856	0.4029	1.3710
ASAI	0.9997776	0.999986	0.999792

ENS (kWh/y), SAIDI (hrs/customer/y), CAIDI (hrs/interruption), SAIFI (interruptions/customer/y), MAIFIe (interruptions/customer/y)

5.2.1 Load Points' Share in System Reliability Indices

Figure 4 shows the share of each load point in the unsupplied energy of the entire system. In this figure, as expected, load points with higher power consumption generally have a larger share of annual unsupplied energy. Because the load points that provide a large number of customers, will be de-energized all together in fault conditions.

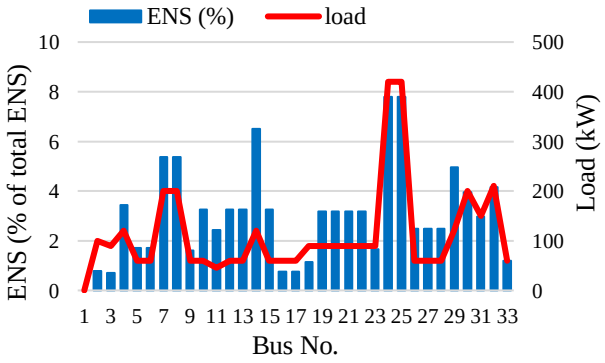

Fig. 4. Load points share in total ENS

In this regard, reliability considerations in the network planning stage can protect the distribution company from future power outage costs. Therefore, this figure can provide useful information about the weaknesses of the network in terms of unsupplied energy index. However, this figure does not provide useful information for evaluating system performance by comparing different load points. For example, looking at this figure, it cannot be concluded that the customers connected to bus #25 of the network are less satisfied with their power supply reliability than the customers connected to bus #26. To clarify this, consider Figure 5 showing the annual outage time of different load points in the network (known as the CID index). As can be seen in this figure, load point 25 experiences a shorter outage time per year than load point 26. Another noteworthy point in Figure 5 is that load points that cannot be separated by protective and control equipment have an equal outage time.

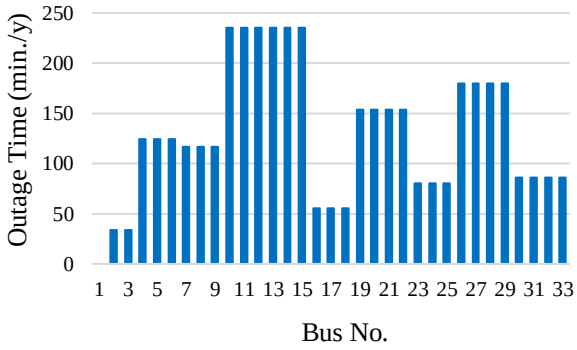

Fig. 5. Load points annual outage time

Since it is assumed that all network customers have the same power consumption, the number of customers at each load point is proportional to its power consumption, so the share of different network load points in the SAIDI index is exactly the same as energy not supplied.

In Figure 6, the share of each load point in the SAIFI and MAIFIe indices of the whole network is shown. In this figure, the effect of the number of customers on the two indices is evident. Since the temporary fault rate is higher than the permanent fault, the MAIFIe index always has larger values than the SAIFI index, except for the buses #19-#25.

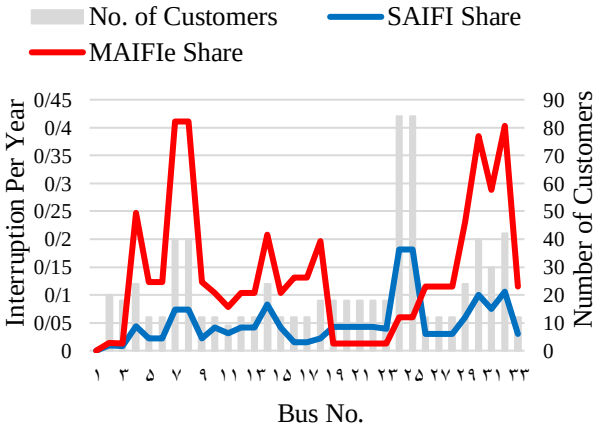

Fig. 6. Load points share in SAIFI and MAIFIe

In these buses, temporary fault due to fuse-blowing operation lead to permanent outage. Fuse-blowing fuses in these buses reduce the MAIFIe but increase the SAIFI.

5.2.2 The impacts of system's operational constraints on calculation of reliability indices

The load restoration process involves changing the normal configuration of the network and must be done in such a way that the network is in a safe operating condition. However, some authors have not considered the technical constraints of the system in their described load restoration process [11, 12, 22]. Figure 7 shows the error of indices estimation as the consequence of these constraints disregard.

The noticeable error occurred in the relaxed problem reveals that the restoration process in the absence of technical constraints suggests unacceptable configurations. This result is especially important where the estimated reliability measures are treated as a

touchstone for network planning programs such as switch placement. Because, bad planning suggestions like installing switches where some switching combinations would lead to operational constraint violation, degrade system's functionality and reliability.

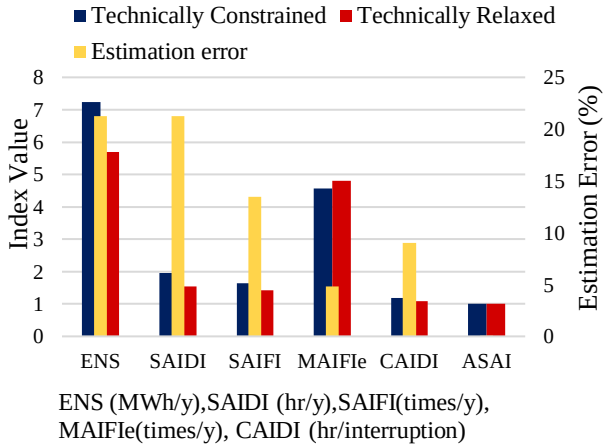

Fig. 7. Computational error in reliability indices in the absence of technical constraints

5.2.3 The Effect of DG Assisted Restoration on Outage Time

Load restoration through DGs' islanding operation is considered as an effective way to improve the reliability of local load points. In the 33-bus network described, the DG connected to bus #17 is very effective in accelerating the restoration of load points 16, 17 and 18. In order to evaluate the effect of the performance of this DG, the base problem investigated so far, has been compared with the case in which this DG is absent. Figure 8 compares annual outage time of different load points shown in Figure 5 with the new case. This figure introduces distributed generation resources as an efficient solution to reduce customers' outage times, especially for sensitive and crucial loads.

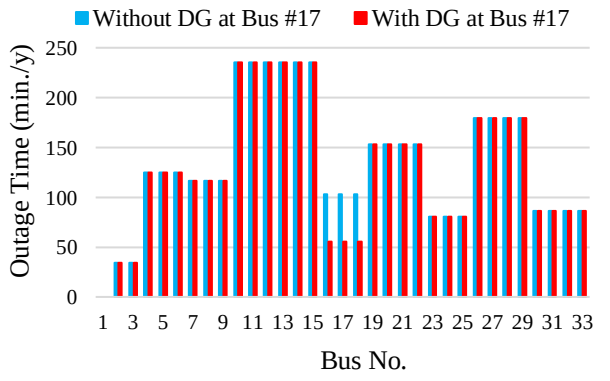

Fig. 8. DG effect on load points annual outage time

6. Conclusion

In this paper, a novel reliability assessment model was proposed to calculate common indices. As one of the main contributions, different protection and control devices function and post-fault optimal operation assessed. Applying the proposed model to 33-bus test network reveals the role of each device in system and load points reliability. Taking into account temporary and permanent faults, the model is able to calculate MAIFIe index. Results show that even for sustained interruption measures, temporary faults could have an undeniable share (6.5% in ENS and SAIDI and 19.15% in SAIFI). The optimal service restoration considers different switching operation times which could capture transportation system impacts and geographical issues. It also includes technical constraints to protect the evaluation framework from network unacceptable reconfigurations and erroneous results, especially when DGs contribute in island operation mode. Local restoration through island operation in the numerical example reduced annual outage time of three load points up to 46%.

7.

7. References

[1] R. N. Allan, "Reliability evaluation of power systems". Springer Science & Business Media, 2013.
[2] D. Elmakias, "New computational methods in power system reliability". Springer Science & Business Media, 2008.
[3] J. Faulin, A. A. Juan, S. Martorell, and J.-E. Ramírez-Márquez, "Simulation methods for reliability and availability of complex systems". Springer, 2010.
[4] W. Li, "Reliability assessment of electric power systems using Monte Carlo methods". Springer Science & Business Media, 2013.
[5] W. Li, P. Wang, Z. Li, and Y. Liu, "Reliability evaluation of complex radial distribution systems considering restoration sequence and network constraints," *IEEE Transactions on Power Delivery*, vol. 19, no. 2, pp. 753-758, 2004.
[6] P. Wang and W. Li, "Reliability evaluation of distribution systems considering optimal restoration sequence and variable restoration times," *IET Generation, Transmission & Distribution*, vol. 1, no. 4, pp. 688-695, 2007.
[7] Y. Xu, C.-C. Liu, and H. Gao, "Reliability analysis of distribution systems considering service restoration," in *2015 IEEE Power & Energy Society Innovative Smart Grid Technologies Conference (ISGT)*, 2015: IEEE, pp. 1-5.
[8] A. Jalilian, B. Taheri, and A. Safdarian, "Optimal Switch Placement in Power Distribution Systems with Complex Configurations," in *2019 Smart Grid Conference (SGC)*, 2019: IEEE, pp. 1-5.
[9] A. Jalilian, B. Taheri, and A. Safdarian, "Optimal Allocation of Human and Mobile Energy Resources in Fault Management of Power Distribution Systems", *Journal of Iranian Association of Electrical and Electronics Engineers*, vol. 19, no. 1, 2020.
[10] J. C. López, M. Lavorato, and M. J. Rider, "Optimal reconfiguration of electrical distribution systems considering reliability indices improvement," *International Journal of Electrical Power & Energy Systems*, vol. 78, pp. 837-845, 2016.
[11] G. Muñoz-Delgado, J. Contreras, and J. M. Arroyo, "Reliability assessment for distribution optimization models: A non-simulation-based linear programming approach," *IEEE Transactions on Smart Grid*, vol. 9, no. 4, pp. 3048-3059, 2016.
[12] A. Tabares, G. Munoz-Delgado, J. F. Franco, J. M. Arroyo, and J. Contreras, "An enhanced algebraic approach for the analytical reliability assessment of distribution systems," *IEEE Transactions on Power Systems*, vol. 34, no. 4, pp. 2870-2879, 2019.
[13] Z. Li, W. Wu, B. Zhang, and X. Tai, "Analytical reliability assessment method for complex distribution networks considering post-fault network reconfiguration," *IEEE Transactions on Power Systems*, vol. 35, no. 2, pp. 1457-1467, 2019.
[14] S. Elsaiah, M. Benidris, Y. Tian, and J. Mitra, "A comprehensive analysis of reliability-oriented optimal distribution system reconfiguration," in *2018 IEEE Industry Applications Society Annual Meeting (IAS)*, pp. 1-9.
[15] S. Heidari, M. Fotuhi-Firuzabad, and M. Lehtonen, "Planning to equip the power distribution networks with automation system,"

IEEE Transactions on Power Systems, vol. 32, no. 5, pp. 3451-3460, 2017.

[16] I. Hernando-Gil, I.-S. Ilie, and S. Z. Djokic, "Reliability planning of active distribution systems incorporating regulator requirements and network-reliability equivalents," *IET Generation, Transmission & Distribution*, vol. 10, no. 1, pp. 93-106, 2016.

[17] N. N. Mansor and V. Levi, "Integrated planning of distribution networks considering utility planning concepts," *IEEE Transactions on Power Systems*, vol. 32, no. 6, pp. 4656-4672, 2017.

[18] A. Nader, C. Ruben, S. C. Dhulipala, A. S. Bretas, and R. A. da Silva, "MILP model for reliability optimization in active distribution networks," in *2018 North American Power Symposium (NAPS)*, 2018: IEEE, pp. 1-6.

[19] Y. Tian, M. Benidris, S. Sulaeman, S. Elsaiah, and J. Mitra, "Optimal feeder reconfiguration and distributed generation placement for reliability improvement," in *2016 International Conference on Probabilistic Methods Applied to Power Systems (PMAPS)*, 2016: IEEE, pp. 1-7.

[20] M. Zare, R. Azizipanah-Abarghooee, R.-A. Hooshmand, and M. Malekpour, "Optimal reconfigurattion of distribution systems by considering switch and wind turbine placements to enhance reliability and efficiency," *IET Generation, Transmission & Distribution*, vol. 12, no. 6, pp. 1271-1284, 2018.

[21] Z. Li, W. Wu, X. Tai, and B. Zhang, "Optimization model-based reliability assessment for distribution networks considering detailed placement of circuit breakers and switches," *IEEE Transactions on Power Systems*, vol. 35, no. 5, pp. 3991-4004, 2020.

[22] M. Jooshaki *et al.*, "Linear formulations for topology-variable-based distribution system reliability assessment considering switching interruptions," *IEEE Transactions on Smart Grid*, vol. 11, no. 5, pp. 4032-4043, 2020.

[23] L. Gan and S. H. Low, "Convex relaxations and linear approximation for optimal power flow in multiphase radial networks," in *2014 Power Systems Computation Conference*, 2014: IEEE, pp. 1-9.

[24] H. Ahmadi and J. R. Martı, "Linear current flow equations with application to distribution systems reconfiguration," *IEEE Transactions on Power Systems*, vol. 30, no. 4, pp. 2073-2080, 2014.

[25] M. E. Baran and F. F. Wu, "Optimal capacitor placement on radial distribution systems," *IEEE Transactions on power Delivery*, vol. 4, no. 1, pp. 725-734, 1989.

International Journal of Research and Technology in Electrical Industry

journal homepage: ijrtei.sbu.ac.ir

Shahid Beheshti University

Overcurrent Relays Coordination Considering Transient Stability Study of Induction Generator Using a Method Based on Terminal Voltage

AmirHossein Taheri Jam [1,*], Reza Mohammadi chabanloo[1], Ehsan Bagherzadeh[1], Hossein Askarian Abyaneh[2], Mojtaba Nasiri[2]

[1] *Electrical Engineering Department, Shahid Beheshti University, Tehran, Iran*
[2] *Department of Electrical Engineering, Amirkabir University of Technology, Tehran, Iran*

ARTICLEINFO

Article history:
Received 27 November 2021
Received in revised form 16 February 2022
Accepted 24 February 2022

Keywords:
Induction generator
Transient stability
Grid fault
OCR coordination
Genetic algorithm

ABSTRACT

Nowadays, with increasing penetration of Induction Generators (IG) in the electricity grid, it is of great importance that IG be connected to the grid in the fault conditions. In this paper, a terminal voltage based method for transient stability study of IG is proposed. For this purpose, an improved analytical method is used to determine Critical Clearing Time (CCT) of IG in the state of grid fault, including near and non-near faults. For the faults occurring far from the terminal of generator, electromagnetic torque is not equal to zero during fault. Hence, equivalent circuit model of IG and network is used to calculate the CCT. A new formulation based on terminal voltage of IG is presented to consider the stability constraint on Over Current Relay (OCR) coordination, to prevent disconnecting of IG in grid fault condition. Simulations are carried out on two samples network, and the results demonstrate the efficiency of proposed method.

1. Introduction

In recent years, the use of new renewable energy has grown rapidly and among the renewable energy sources, wind power with Induction Generator (IG) is a more interesting choice to develop. Hence, the penetration level of IG in the grid has been increased. As a result, the transient stability of them is an important issue for continuous operation of grid [1]. In the previous works, transient stability analysis for fault near IG and its impact on IG characteristics have been studied [1-6]. Appropriate model for squirrel cage IGs (SCIG), including single-squirrel cage and double-squirrel cage IGs, is proposed for rotor speed stability studies [2]. The authors of [3] and [4] have studied equivalent model of a wind farm for transient stability studies using dynamic simulation. The effect of network parameters on transient stability of wind farm has been studied in [5]. Also, in [6], the transient analysis of IG at unbalanced fault has been performed and it has been compared with that of IG at balanced fault.

The authors of [7] have proposed a trial and error method using dynamic simulation to determine CCT, which involves several repetitive runs. CCT is the stability criteria in the generator transient stability. Hence, CCT estimation problem has been solved with dynamic simulation, which avoids repetitive runs [8-10]. Also,

* Corresponding author
E-mail address: amirhoseintaherijam@gmail.com
http://dx.doi.org/ 10.52547/ijrtei.1.1.10

methods for determining CCT with terminal voltage and rotor speed have been studied and have been compared with each other in [11].

The methods based on iterative analysis in the time domain have been proposed to determine CCT of IGs [12-14]. In [13], the transient stability of multi IG network has been studied for fault in different places of network. This method, which is based on step by step calculation, uses IG equivalent circuit and Norton equivalent model of network. In [14], Lyapunov function and controlling unstable equilibrium point (CUEP) have been obtained to calculate CCT using step by step time domain integration. An analytical method for transient stability of IG has been proposed only for fault in the terminal of IG in [15]. Also, the effect of IG parameters on transient stability has been investigated in the study.

Transient Stability if Dual Stator-Winding Induction Generator (DWIG) is studied in [28]. This paper improving transient stability by using slip frequency control containing braking resistors.

CCT calculation for doubly fed induction generator (DFIG) has been studied in [16]. In fault condition, crowbar protection acts to protect the rotor and convertor during the fault. When the crowbar protection is activated, DFIG action will be as same as IG with crowbar resistance connecting to the rotor side. So in this condition, DFIG can be analyzed by IG studies.

Also improving transient stability of DFIG is studied in [29], [30]. In [29] bridge fault current limiter used for reducing power transient stability of DFIG. In [30] investigate the influence of the closed-loop control system on transient stability

In [17] has been investigated CCT calculation for synchronous generator in presence multi induction generator. IGs were modeled as negative loads for CCT calculation of synchronous generator and stability of IGs were not considered.

Presence of renewable energy sources in distribution networks can associate problem for protection systems that overcurrent protection is one of them. In the result, some authors have been investigated overcurrent protection with renewable energy sources [18-20]. In [18], the authors solved over-current coordination problem by using fault current limiter (FCL) selection in presence of distributed generation (DG). Also in [19], has been improved coordination equivalents for distribution feeders with renewable generation.

In recent years, the modern grid code enforces the wind generators to remain connected to the grid in fault conditions [21]. This ability is known as low voltage ride through (LVRT). If the wind generator disconnects from the grid, it may be lost the active power generation after clearing the fault. In the previous works, setting of the generator bus relays has been determined considering CCT for faults at the generator terminal [22]. The contribution of IG to fault current and its impact on OCR coordination has been studied in [23]; however, the stability of IG has not been considered.

In this paper, an improved analytical method proposed for CCT calculation of IG in the state of grid fault. This method is based on the equivalent model of IG and network in three states: pre-fault, during fault and post-fault. After sensitivity analysis on the network parameters, a simplified method is derived for determining the CCT of IG per voltage sag in the terminal of IG. Two important application of this model in stability study of IG is presented; improving LVRT and considering stability constraint in OCR coordination. In fact, the contribution of this paper to earlier work includes three novelties as below:

- CCT calculation with considering non-zero electromagnetic torque of IG during grid fault
- Deriving a new formulation for CCT per voltage sag
- Considering the stability constraint of IG in OCR coordination algorithm using terminal voltage based method

The proposed method with related equations is fully described in the following.

2. Transient Stability of IG

In order to explain the transient stability of IG, a test network is considered as shown in Fig. 1(a). This test network consists of an IG with 2MVA capacity connected to a 2.4 kV, 50 Hz network [12].

It is supposed that a fault occurs in line 2. Fig. 1(b) shows torque-slip curve of IG in pre-fault and during fault states. As can be seen, during fault condition, electrical torque of IG reduces because of voltage sag, however, speed of mechanical torque variation is slower than electrical torque variation, so mechanical torque remains almost unchanged. For this reason, rotor speed increases, and the rotor slip starts to change from initial slip. Transient stability of IG depends on the clearing time of fault. IG will remain stable, if the fault is cleared before that rotor speed reaches to critical speed. As shown in Fig. 1(b), initial slip (s_i) and critical slip (s_c) can be obtained from intersection of electrical and mechanical curves.

Fig. 1(c) shows the torque-speed curves of IG when the fault is cleared by tripping the circuit breakers of line 2. In this state, network structure alters, hence, electromagnetic torque and critical slip (s_c) are changed.

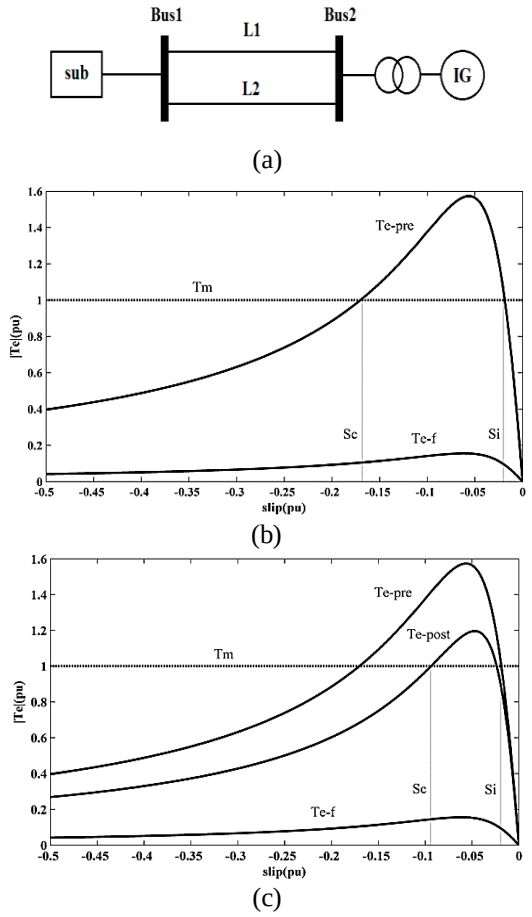

Fig. 1. Test network consists of IG. (a) Single line diagram of test network. (b) Torque-angle curve without changing in network structure in post-fault. (c) Torque-angle curve with tripping L2 in post-fault.

CCT calculation has been studied previously by assuming that fault occurs in the generator terminal [15]. In this condition, electromagnetic torque is equal to zero during fault and CCT is the linear function of slip. Relation between electrical torque and rotor slip can be given by:

$$\frac{ds}{dt} = -\frac{dw}{dt} = -\frac{1}{2H}(T_e - T_m) \quad (1)$$

Using (1) yields:

$$dt = \frac{2H}{T_m - T_e} ds \quad (2)$$

By integrating Eq. (2) from initial slip to critical slip, CCT is obtained as:

$$CCT = 2H \int_{s_i}^{s_c} \frac{ds}{T_m - T_e} \quad (3)$$

For fault in the terminal of the generator, T_e is equal to zero, and T_m is constant during fault. So, Eq. (3) is simplified as follows:

$$CCT = \frac{2H}{T_m}(s_c - s_i) \quad (4)$$

3. CCT Determining of IG For Non-near Fault

In non-near fault condition, the electromagnetic torque cannot be considered equal to zero, during fault, and Eq. (3) cannot be simplified as Eq. (4). In the other word, for CCT calculation using Eq. (3), the electromagnetic torque, during fault, should be obtained as a function of rotor slip. For this purpose, circuit modeling of IG is developed and used to calculate the electromagnetic torque.

3.1. Extended Circuit Model of IG

The model of IG is extended by considering network equivalent circuit and capacitor bank. As shown in Fig. 2(a), U_s and Z_s are the voltage and impedance equivalent of the network, respectively, and X_c is the reactance of the parallel capacitor bank. R_s+jX_s and $R_r/s+jX_r$ are the stator and rotor side impedance, respectively, and X_m is the magnetizing reactance of IG. $s = 1-\omega_r$ is the rotor slip, which ω_r is the rotor speed. Equivalent circuit is simplified as shown in Fig. 2(b). Where U_{th} and Z_{th} are thevenin equivalent values for voltage and impedance, respectively, which are seen from rotor side.

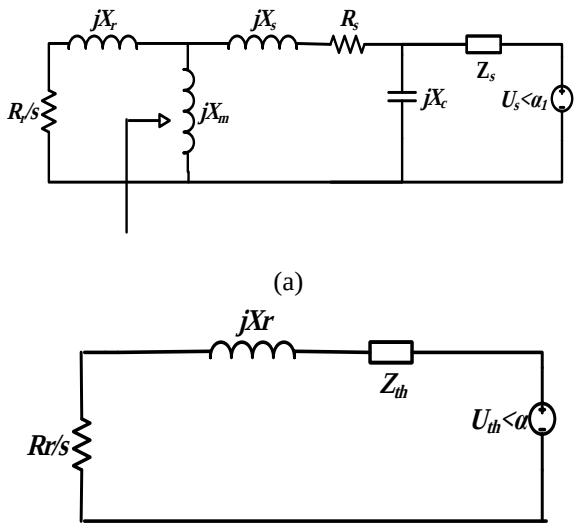

Fig. 2. Equivalent circuit of IG. (a) Complete equivalent circuit. (b) simplified equivalent circuit.

According to the simplified equivalent circuit of IG, rotor current I_r is calculated:

$$I_r = \frac{U_{th}}{\sqrt{\left(\frac{R_r}{s} + R_{th}\right)^2 + \left(X_r + X_{th}\right)^2}} \quad (5)$$

The electrical torque T_e can be determined as follows:

$$T_e = \frac{R_r}{s} I_r^2 \quad (6)$$

So, substituting Eq. (5) into Eq. (6), after some simplifications yields:

$$T_e = \frac{s}{as^2 + bs + c} \quad (7)$$

Where a, b and c are as below:

$$a=\frac{{R_{th}}^2+\left(X_r+X_{th}\right)^2}{R_r{U_{th}}^2},\quad b=\frac{2R_{th}}{{U_{th}}^2},\quad c=\frac{R_r}{{U_{th}}^2} \tag{8}$$

Electrical torque is obtained as a function of rotor slip in Eq. (7). This equation can be used to draw the torque-slip curve of IG as shown in Fig. 1 in three states: pre-fault, during fault and post-fault. Since, the parameters a, b and c are the functions of network thevenin voltage (U_s) and network thevenin impedance (Z_s), the torque-slip curve is different for three mentioned states.

CCT can be determined substituting Eq. (7) into Eq. (3) as below:

$$\begin{aligned} CCT &= \frac{2H}{T_m}\int_{s_i}^{s_c}\left(1+\frac{\frac{1}{T_m}s}{as^2+(b-\frac{1}{T_m})s+c}\right)ds \\ &= \frac{2H}{T_m}(s_c-s_i)+\frac{2H}{T_m}\int_{s_i}^{s_c}\left(\frac{\frac{1}{T_m}s}{as^2+(b-\frac{1}{T_m})s+c}\right)ds \end{aligned} \tag{9}$$

In Eq. (9), a, b and c are the parameters of torque-slip curve in the state of during fault, according to Eq. (7). Also, the parameters of torque-slip curve in pre-fault and post-fault states should be calculated to determine the initial slip (s_i) and critical slip (s_c), respectively.

3.2. Extended Circuit Model of IG

To calculate the CCT using Eq. (9), thevenin equivalent circuit of network, including thevenin voltage and thevenin impedance should be determined in three states: pre-fault, during fault and post-fault [23].

3.2.1 Thevenin Voltage

Thevenin voltage at the terminal of IG is equal to bus voltage without connecting of IG to the network. Bus voltage in pre-fault and post-fault states, can be determined using load flow calculations. In during fault condition, the bus voltage is determined using fault calculation analysis. When a fault occurs at bus f of a network with m buses, the voltage of all buses is obtained from fault analysis equation as follows [24]:

$$\begin{bmatrix}\Delta U_1\\ \vdots\\ \Delta U_n\\ \vdots\\ \Delta U_m\end{bmatrix}=\begin{bmatrix}Z_{11} & \cdots & Z_{1m}\\ Z_{21} & \cdots & Z_{2m}\\ \vdots & \ddots & \vdots\\ Z_{m1} & \cdots & Z_{mm}\end{bmatrix}\begin{bmatrix}0\\ \vdots\\ I_f\\ \vdots\\ 0\end{bmatrix} \tag{10}$$

Where ΔU_i is the voltage deviation between pre-fault and during fault conditions. Z is the impedance matrix of network, including Z_{11} to Z_{mm}, and also, I_f is the fault current which is calculated as below:

$$I_f=\frac{{U_f}^{(pre-f)}}{Z_{ff}} \tag{11}$$

Where ${U_f}^{(pre-f)}$ is the pre-fault voltage of bus f. Therefore, the voltage at the bus n which the IG is installed, in during fault, can be calculated substituting Eq. (11) into Eq. (10) as below:

$${U_n}^{(fault)}={U_n}^{(pre-f)}-Z_{nf}\left(\frac{{U_f}^{(pre-f)}}{Z_{ff}}\right) \tag{12}$$

3.2.1 Thevenin Impedance

Thevenin impedances at the bus n, in pre-fault and post-fault states are equal to the diagonal elements (Z_{nn}) of Z. Thevenin impedance in during fault is equal to Z'_{nn} in fault condition. Importing the fault in impedance matrix, Z changes to Z' which can be obtained easily by inverting the admittance matrix of network considering the fault.

$$Z'=(Y')^{-1} \tag{13}$$

3.3. Stability of IG per Terminal Voltage

3.3.1 CCT-VS Characteristic

As mentioned in the previous section, values of a, b and c are the functions of network thevenin voltage (U_S) and network thevenin impedance (Z_s) during fault. So the second part of Eq. (9) is a function of network parameters while, the first part is independent of them. Hence, Eq. (9) can be considered as below:

$$CCT=A+f(U_s,Z_s) \tag{14}$$

Where f (U_s, Z_s) and A are:

$$f(U_s,Z_s)=\frac{2H}{T_m}\int_{s_i}^{s_c}\left(\frac{\frac{1}{T_m}s}{a_2s^2+(b_2-\frac{1}{T_m}s)+c_2}\right)ds \tag{15}$$

$$A=\frac{2H}{T_m}(s_c-s_i) \tag{16}$$

Since, in the fault condition, thevenin impedance of network is very smaller than generator impedance, voltage drop caused by thevenin impedance can be neglected. To clarify this fact, in Fig. 3(a) the CCT values of IG is obtained using Eq. (9). It can be seen, assuming a constant U_S, the CCT value of IG is approximately constant to different thevenin impedances. The variation range of Z_s is between 0 and 0.02 ohm for fault in different points of simple network.

Since, the MVA capacity of IG should be in the allowable range for interconnecting to a network, the short circuit impedance in point of common coupling, which is equal to Z_s, is very smaller than generator impedance. On the other hand, the value of Z_s during fault is lower than it's value in pre-fault condition (0.02 ohm). Hence, neglecting of Z_s during fault condition is an acceptable approximation in all usual networks. So, Eq. (14) can be written as follows.

$$CCT=A+f(U_s) \tag{17}$$

The first part (A) is the CCT of IG when the fault is occurred in the terminal of IG and the terminal voltage become to zero, as studied in the previous works. It can

be seen from Eq. (16), the value of A depends on the installing point of IG in the network which determines S_c and S_i, and is independent of fault location.

Solving Eq. (17), considering test network parameters given in [11], the CCT formulation per terminal voltage can be determined as follows:

$$CCT = \left[\begin{array}{c} 2.13s + \dfrac{0.56 \times U_s^2 \times k_1(U_s) \times A\tan[\dfrac{k_1(U_s)}{k_2(U_s)}]}{k_2(U_s)} \\ -0.28 \times U_s^2 \times \log(s \times k_1(U_s) + s^2 + 0.006) \end{array} \right]_{s_i}^{s_c} \quad (18)$$

$$k_1(U_s) = 0.03 + 0.26 \times U_s^2 \quad (19)$$

$$k_2(U_s) = \sqrt{0.02 - 0.01 \times U_s^2 - 0.07 \times U_s^4} \quad (20)$$

Asymptote of CCT's curve determined by root of $K_2(U_S)$ function. According to the Eq. (17), CCT is obtained as a function of U_S and CCT-U_S curve that is shown in Fig. 3(b) for maximum and minimum of Zs. Note that U_S is terminal voltage of IG in the fault condition. The curve has asymptote between 0.71 and 0.73 for variation of Zs between maximum and minimum of it's rang. This voltage is a critical voltage for stability (CVS), and generator will remain stable if U_S is greater than CVS.

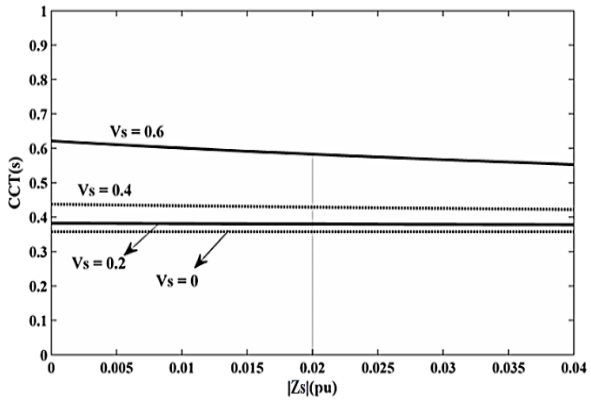

(a)

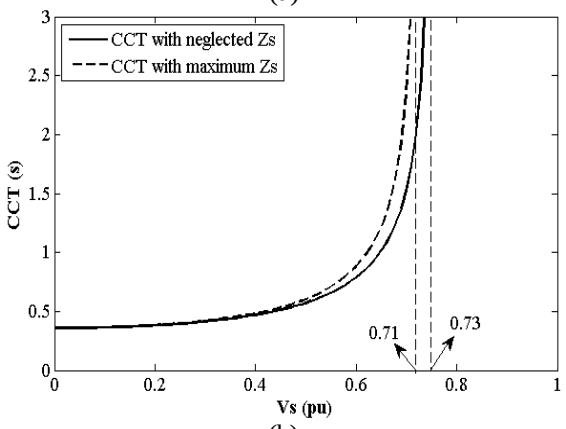

(b)

Fig. 3. (**a)** CCT versus thevenin impedance for different thevenin voltages. (b) CCT versus thevenin voltage for maximum and minimum thevenin impedance.

The curve of Fig. 3(b) can be determined for any IG, which depends on the installation point of IG in the network. So, CCT can be calculated for fault in different points of network and with different fault resistance only by determining voltage sag in the terminal of the generator.

3.3.2 OCR Coordination Considering CCT

With increasing the capacity of IGs in the network, it is important to stay them in the network for avoiding of inappropriate outages. Hence, the setting of relays in the distribution network can be modified to clear the grid fault before instability of IG. The proposed method using CCT-V_S curve can be applied to determine the CCT of IG for the fault in different point of the network. In order to achieve this goal, in this section, OCR coordination is studied by considering CCT.

Coordination of relays is carried out using GA which is a powerful artificial optimization technique [25-27]. In optimal coordination of OCR the decision variables which should be determined are Time Dial Setting (TDS) of relays. To achieve a better result in OCR coordination algorithm considering CCT of IG, the pickup current of relays (Ip) also are considered as decision variables. The performance of Ip in keeping the stability of IG is fully described in next section. The common objective function for optimal OCR coordination is as below:

$$Minimized: \quad OF = \sum_{i=1}^{N} (t_i) \quad (21)$$

$$Subject\ to: \quad t_i - t_j \geq CTI_1 \qquad \forall (i,j) \in \Omega \quad (22)$$

$$TDS_i^{min} \leq TDS_i \leq TDS_i^{max}, \quad \mathrm{Ip}^{min} \leq \mathrm{Ip} \leq \mathrm{Ip}^{max} \quad (23)$$

Where t_i is the operating time of i^{th} relay for the fault near to the relay and Ω is the set of main and backup relay pairs. ti and tj are the operating times of main and backup relays, respectively, for the fault near to the main relay. Furthermore, CTI_1 is the coordination time interval between main and backup relays which is assumed equal to 0.25.

The time interval between the relay operating time and the CCT of IG should be greater than CTI_2 to consider the delay of circuit breaker opening and safety margin. So, the second constraint is formulated as below:

$$CCT\left(fault(X,R)\right) - t_i\left(fault(X,R)\right) \geq CTI_2 \qquad fault(X,R) \in S_i \quad (24)$$

Where t_i and CCT, respectively, are the operating time of i^{th} relay and the CCT of IG, for the fault in the X percent of the protected line with the resistance R. S_i is the set of all three-phase faults occur along the protected line with different fault resistances. CTI_2 is assumed to be 0.2 sec. in this paper.

Since, the coordination algorithm using GA needs numerous iterations, calculation of Eq. (26) for all mentioned faults in each iteration will cause to large run time. In the other hand, many of the faults in a line with different resistances cause to similar voltage sag in the terminal of IG and lead to similar CCT. Therefore, Eq.

(24) is rewritten using CCT-Us curve. The relation between fault current (I_f) and terminal voltage of IG can be written from Eq. (10) as below:

$$U_k = VU_k(0) - Z_{k(n+1)} I_f \quad (25)$$

Where bus *k* is installing point of IG and n+1 is a new bus created to consider fault point on the line. The operating time of OC relay is a function of fault current and following popular time-current characteristic is considered:

$$t_i(I_f) = \left(\frac{A}{\left(\frac{I_f}{I_b}\right)^p - 1} + B\right) TDS \quad (26)$$

The parameters A, B and p are constants that vary with the type of used characteristic. Substituting Eq. (25) into Eq. (26) yields the operating time of relay as a function of IG terminal voltage (U_k).

$$t_i(V_k, Z_{k(n+1)}) = \left(\frac{A}{\left(\frac{V_k(0) - V_k}{Z_{k(n+1)}}\right)^k - 1} + B\right) TSM \quad (27)$$

If the protected line is assumed between bus n and m, considering the relation between impedance parameters $Z_{kn} \leq Z_{k(n+1)} \leq Z_{km}$, Eq. (27) can be considered with Z_{km}, instead of calculating all operating times of relay with changing the fault location on the line.

$$t_i(U_k) = \left(\frac{A}{\left(\frac{U_k(0) - U_k}{Z_{km}}\right)^k - 1} + B\right) TSM \quad (28)$$

CCT-Us curve can be compared easily with the operating time of relay using (28). So, Eq. (24) can be rewritten as Eq. (29):

$$CCT\ (U_k) - t_i(U_k) \geq CTI_2 \quad (29)$$

4. Simulation and Results

4.1. Simple Network

The first sample system to verify the method is a 10kv and 50Hz network with 1MVA capacity IG connected via a transformer, as shown in Fig. 4. The network parameters are given in Appendix.

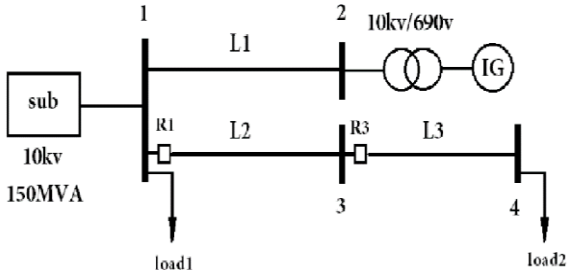

Fig. 4. Single line diagram of simple network.

4.1.1 Stability of IG for Grid Fault

The CCT of IG for fault over the line L2 (in Fig. 4) is given in Table I. In third column, CCT is calculated using a new analytical method by Eq. (9). As can be seen, the CCT value increases for faults occuring farther from the generator. To validate the result of new method, CCT determined by simulation in Simulink/MATLAB and the results are given in second column of Table I. It can be seen; the results of proposed analytical method have acceptable deviation (maximum 3.1%) compare to simulation method results.

The last column shows the voltage sag in the terminal of IG for faults occurring in line L2. According to section 2, part C, CCTs are determined from CCT-US curve by using voltage sag, and the results are given in the last column of Table II. As can be seen, maximum deviation compared to simulation method is 4.54 percent.

Table I. CCT result of new method for simple network during fault on line L2**.**

Fault distance from bus1 (pu)	Simulation method	New method (Eq. 9)			Simplified method using Voltage sag (Eq. 17)	
	CCT (ms)	CCT (ms)	Deviation (%)	Voltage of IG (pu)	CCT (ms)	Deviation (%)
0	360	357	0.83	0	357	0.83
0.1	375	367	2.13	0.09	362	3.46
0.2	385	376	2.34	0.16	373	3.11
0.3	400	390	2.50	0.23	391	2.25
0.4	420	407	3.10	0.28	409	2.61
0.5	439	426	2.96	0.33	430	2.05
0.6	460	447	2.83	0.37	455	1.08
0.7	485	470	3.09	0.41	486	0.20
0.8	505	495	1.98	0.44	511	1.18
0.9	530	521	1.70	0.47	548	3.39
1	550	539	2.00	0.50	575	4.54

4.1.2 OCR Coordination Considering CCT

After CCT calculation, the coordination of relays R1 and R3 are studied in Fig. 4 considering the stability of IG. According to coordination constraint in Eq. (22), the time interval between operating time of backup relay (R1) and main relay (R3) for the fault close to R3 should be equal to CTI_1=0.25. Since, the time setting and operation characteristic of relay R3 is assumed to be TDS_3=0.05 and extremely inverse, respectively, the operating time of relay R1 for the fault close to R3 is obtained 0.27 sec.

Then, time setting of R1 (TDS_1) can be calculated considering three standard characteristics, including normally, very and extremely inverse. Fig. 5(a) shows this three characteristics of relay R1 and the CCT curve versus the fault location in line L2 (without considering fault resistance).

IG will remain stable for fault in L2, if the operating time of R1 is smaller than CCT. In the other word, the stability constraint of Eq. (24) should be satisfied. According to the Fig. 5(a), the minimum time intervals between the curves of CCT and relay operating time by using NI, VI and EI characteristics are obtained 0.13, 0.23 and 0.28, respectively. Therefore, very and extremely inverse curves can be used for R1 to keep the stability of IG. But the NI curve does not satisfy the stability constraint even by changing the TDS of relay. If the TDS

of relay is reduced to satisfy the stability constraint, the operating time of relay R1 will decrease and the coordination of relay R1 and R3 will be disturbed. So, selecting the suitable characteristics of relays is required to achieve better results.

Since, the OCR characteristic selection has some limitations, the pickup current selection is the other solution which is used for this problem, as shown in Fig. 5(b). It can be seen, for fixed relay characteristic (assumed NI) the slope of relay curve increases by enhancement of pickup current. If I_p is selected lower than 600A, time interval between CCT and operating time of R1 will be lower than 0.2 sec. So, I_p should be selected higher than 600A to satisfy both of stability and coordination constraints. It is suggested that, in greater networks the optimization algorithm based on GA is used for determining TDS and I_p, simultaneously.

The curves of figures 5(a) and 5(b) are considered without fault resistance. To consider all faults with all resistances along the protected line, as described in section 4.3, the curves of operating time of relays and CCT of IG are obtained versus terminal voltage of IG. These curves are shown in Fig. 5(c). It can be seen that by selecting NI characteristic of relay, I_p=600A and TDS=0.1, the time interval between two curves is greater than CTI_2=0.2. This result also obtained from Fig. 5(b).

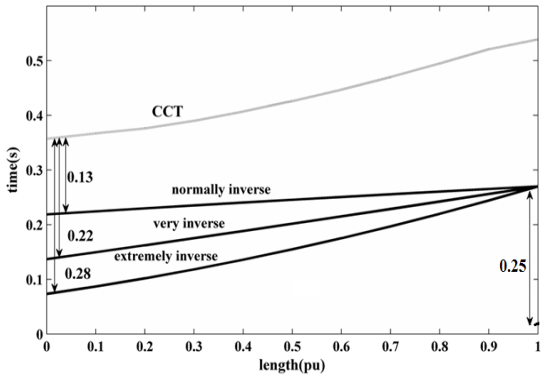

(a)

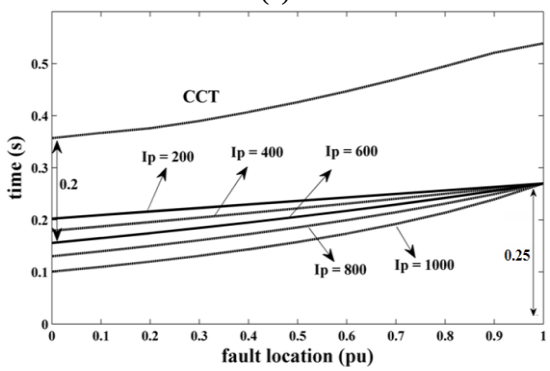

(b)

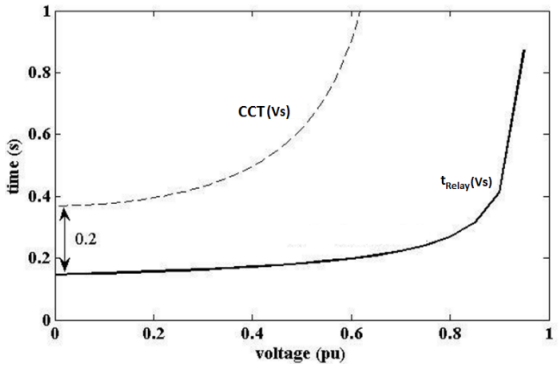

(c)

Fig. 5. Operating time of R1 and CCT for fault along line L2. (a) Considering various characteristic type of relay (without fault resistance). (b) Considering various relay pickup current (without fault resistance). (c) Operating time of R1 and CCT versus terminal voltage of IG (Us).

4.2. IEEE 30 Bus Network

The proposed method also has been applied to IEEE 30 bus network, which is a meshed sub-transmission/distribution system. The distribution section of the network that will be studied here is fed from three primary distribution substations 132/33 kV at buses 1, 6 and 13, as shown in Fig. 6. The information of network is given in [24]. Also, one IG has been installed at bus 10 that it's information is given in Appendix.

4.2.1 Stability of IG for Grid Fault

The CCTs are calculated for three-phase faults in different buses of network using the proposed method, as given in Table II. It can be seen; the stability of IG will be disturbed for fault in five buses of network. To validate the proposed method, CCTs also are obtained using simulation method in Simulink/MATLAB. The calculation result of CCT using two methods, is approximately similar with the maximum deviation of 3.05% percent, for five mentioned buses.

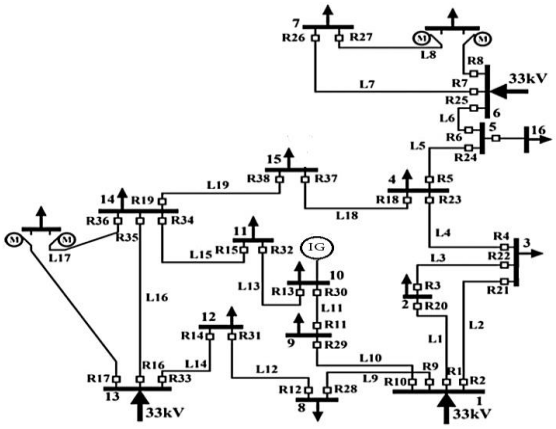

Fig. 6. Single line diagram of IEEE 30-bus distribution network.

Table II. CCTs for IEEE 30 bus system for fault in different buses.

Bus number	Simulation method CCT(ms)	Proposed method CCT(ms)	Deviation (%)
1	450	460	2.22
2	Stable	Stable	-
3	Stable	Stable	-
4	Stable	Stable	-
5	Stable	Stable	-
6	Stable	Stable	-
7	Stable	Stable	-
8	Stable	Stable	-
9	425	412	3.05
10	400	404	1.00
11	465	478	2.79
12	Stable	Stable	-
13	Stable	Stable	-
14	740	748	1.08
15	Stable	Stable	-

4.2.2 OCR Coordination Considering CCT

OCR coordination algorithm based on GA, as represented in section 3, is used to determine the OCR settings. Values of I_p and TDS is optimized in this algorithm. The range of TDS is considered between 0.05 and 2, and the range of I_p is assumed to be between 0.5 and 2.5 times of the nominal current. Also, characteristic of OCRs is assumed to be IEC extremely inverse curve. The proposed method is applied to network in two states; without considering CCT (stability constraint) and with considering CCT. In the state one, only coordination constraint according to Eq. (22), between all main and backup relays is considered to be satisfied. The result of TDS and I_p is given in Table III. In the state two, in addition to the coordination constraint, stability constraint according to Eq. (29) is satisfied.

Table III. OCR coordination result for TDS and Ip of relays**.**

Relay Num.	without considering CCT		With Considering CCT		Relay Num.	without considering CCT		With Considering CCT	
	TDS	Ip	TDS	Ip		TDS	Ip	TDS	Ip
1	0.45	437	0.19	747	**20**	0.51	103	0.19	191
2	0.14	403	0.24	347	**21**	0.25	100	0.31	100
3	0.51	281	0.22	494	**22**	0.26	380	0.33	399
4	0.21	423	0.73	249	**23**	0.46	219	1.56	142
5	0.13	474	0.86	201	**24**	0.35	188	0.35	227
6	0.07	395	0.93	117	**25**	0.09	615	0.08	721
7	0.12	322	0.81	103	**26**	0.17	100	0.07	100
8	0.16	170	0.39	110	**27**	0.05	329	0.05	100
9	0.42	486	1.97	241	**28**	0.31	176	0.10	362
10	0.38	429	1.06	294	**29**	0.35	154	0.75	101
11	0.92	197	0.97	221	**30**	0.27	312	1.02	143
12	0.40	280	1.30	182	**31**	0.11	441	0.10	512
13	0.47	231	1.80	123	**32**	0.18	378	0.20	371
14	0.29	185	1.30	104	**33**	0.13	663	1.69	200
15	0.56	118	0.05	441	**34**	0.58	306	0.26	476
16	0.25	400	0.82	254	**35**	0.43	185	0.36	235
17	0.08	182	0.35	100	**36**	0.10	100	0.05	157
18	0.06	100	0.05	100	**37**	0.16	322	0.14	398
19	0.05	100	0.05	100	**38**	0.14	326	0.15	371

Since, IG is unstable for fault in five buses of network (1, 9, 10, 11, and 14) according to Table II, the lines of network can be divided into three groups. First group consist of lines that are not connected to unstable buses. The voltage drop in the terminal of IG is greater than CVS for the fault in all over these lines. Hence, it is not required to consider these lines in the stability constraints. Second group includes four lines within unstable buses (i.e. L10, L11, L13 and L15), and third group contains six other lines, which are connected to unstable buses from one side (L1, L2, L9, L16, L17 and L19).

The faults on lines of groups 2 and 3 maybe cause to instability of IG. To prevent instability of IG, the setting of OCR relays on these lines are determined according to stability constraint. For example, relays R30 and R29 are located on lines L11 (group 2) and L10 (group 3), respectively. Fig. 7(a) shows the operating time of R30 for fault in L11 without considering CCT. According to Eq. (27), the relay curve is between upper relay curve (URC) and lower relay curve (LRC), depending on the fault location and resistance. The minimum margin between CCT and URC, without considering CCT constraint, is obtained 0,07. It can be seen from Fig.7(b), after applying the new method, the discrimination time between the CCT of IG and the operating time of OCR (URC) is greater than CTI_2=0.2 for the faults on different locations of the line.

It should be noted that, from Fig. 7(a), the voltage of IG (Us) for the faults without resistances is in the range of U1=0 to U2=0.11. The constraint between two curves is satisfied in this range. However, Us is in the range of 0 to CVS=0.72, with considering fault resistance, which the

margin is lower than CTI_2. Hence, the efficiency of new method which is based on IG terminal voltage, can be approved.

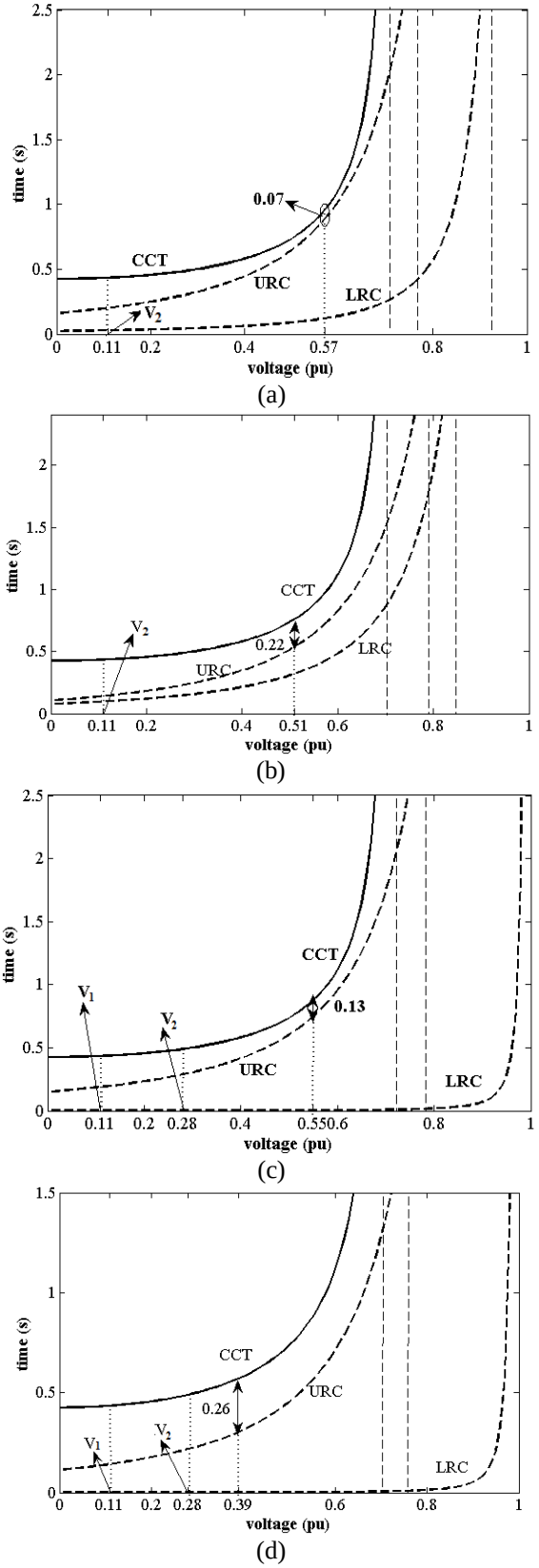

Fig. 5. Relay operating curves and CCT curves for fault throughout the lines. (a) Operation of R30 for fault in L11 without considering CCT. (b) Operation of R30 for fault in L11 with considering CCT. (c) Operation of R29 for fault in L10 without considering CCT. (d) Operation of R29 for fault in L10 with considering CCT.

5. Conclusion

In this paper, a terminal voltage based method is proposed for stability study of IG. To achieve this goal analytical method for CCT calculation is used for fault in all buses and lines of grid. The electrical torque of IG calculated as a function of rotor slip using the equivalent circuit of IG and network. Then, a new model is derived for representing the relation of CCT versus terminal voltage. the model is used to formulate OCR coordination algorithm considering stability constraints. By optimizing the pickup current of relays the appropriate curve of relay is selected proportional to CCT curve to satisfy the stability constraint. The proposed method is applied to two samples network and the results demonstrate the accuracy of new analytical method for CCT calculation. Also, the results show the efficiency of the new coordination algorithm in considering the stability of IG.

6. References

[1] O. Samuelsson, S. Lindahl, "On speed stability", *IEEE Transactions on Power Systems*, vol. 20, no. 2, pp. 1179-1180, 2005.

[2] J. Pedra, F. Corcoles, "On fixed-speed WT generator modeling for rotor speed stability studies", *IEEE Transactions on Power Systems*, vol.27, no. 1, pp. 397-406, 2012.

[3] DJ. Trudnowski, A. Gentile, "Fixed-speed wind-generator and wind-park modeling for transient stability studies", *IEEE Transactions on Power Systems*, vol. 19, no. 4, pp. 1911-1917, 2004.

[4] SK. Salman, ALJ. Teo, "Windmill modeling consideration and factors influencing the stability of a grid-connected wind power-based embedded generator", *IEEE Transactions on Power Systems*, vol. 18, no. 2, pp. 793-802, 2003.

[5] HR. Najafi, F. Robinson, F. Dastyar, AA. Samadi, "Transient stability evaluation of wind farms implemented with induction generators", In 43rd International Conference on Universities Power Engineering (UPEC), December 2008, Padua, Italy, pp. 1-5.

[6] R. Dashti, A. Vahedi, "Transient analysis of induction generator jointed to network at balanced and unbalanced short circuit faults", In 42nd International Conference on Universities Power Engineering (UPEC), September 2007, Brighton, UK, pp. 102-108.

[7] T. Senjyu, N. Sueyoshi, "Stability analysis of grid connected wind power generating system", In *Third International workshop on Transmission Networks for offshore wind farms, 2002.*

[8] SK. Salman, ALJ. Teo, "Investigation into the estimation of the critical clearing time of a grid connected wind power based embedded generator", In Transmission and Distribution Conference and Exhibition (TDC), October 2002, Yokohama, Japan, pp. 975-980.

[9] T. Senjyu, N. Sueyoshi, K. Uezato, K. Fujita, A. Funabashi, "Transient stability analysis of induction generator using torque-time characteristic", In Fifth International Conference on Power Electronics and Drive Systems (PEDS), November 2003, Singapore, pp. 760-765.

[10] P. Ledesma, J. Usaola, JL. Rodriguez, "Transient stability of a fixed speed wind farm", *Renewable Energy*, vol. 28, no. 9, pp. 1341-1355, 2003.

[11] YJ. Lin, "Comparison of speed and voltage based critical clearing time of squirrel cage induction generator", In 11th International Conference on Probabilistic Methods Applied to Power Systems (PMAPS), June 2010, Singapore, pp. 283-286.

[12] N. Amutha, BK. Kumar, "Effect of modeling of induction generator based wind generating systems on determining CCT", *IEEE Transactions on Power Systems*, vol. 28, no. 4, pp. 4456-4464, 2013.

[13] N. Zhou, P. Wang, Q. Wang, PC. Loh, "Transient stability study of distributed induction generators using an improved steady-state equivalent circuit method", *IEEE Transactions on Power Systems*, vol. 29, no. 2, pp. 608-616, 2014.

[14] H. Li, B. Zhao, C. Yang, HW. Chen, Z. Chen, "Analysis and estimation of transient stability for a grid-connected wind turbine with induction generator", *Renewable Energy*, vol. 36, no. 5, pp. 1469-1476, 2011.

[15] Ap. Grilo, A. Mota, L, Mota, W. Freitas, "An analytical method for analysis of large-disturbance stability of induction generators", *IEEE Transactions on power systems*, vol. 22, no. 4, pp. 1861-1869, 2007.

[16] AP. Grilo, MBC. Salles, FCL. Trindade, W. Freitas, "An analytical insight into large-disturbance stability of doubly fed induction generators", *Electric Power Systems Research*, vol. 122, pp. 29-32, 2015.

[17] PK. Naik, NKC. Nair, AK. Swain, "Impact of reduced inertia on transient stability of networks with asynchronous generation", *International Transactions on Electrical Energy Systems*, vol. 26, no. 1, pp. 175-191, 2016.

[18] MG. Maleki, RM. Chabanloo, H. Javadi, "Method to resolve false trip of non-directional overcurrent relays in radial networks equipped with distributed generators", *IET Generation, Transmission & Distribution*, vol. 13, no. 4, pp. 485-494, 2019.

[19] LH. Chen, "Overcurrent protection for distribution feeders with renewable generation", *International Journal of Electrical Power & Energy Systems*, vol. 84, pp. 202-213, 2017.

[20] D. Yoosefian, RM. Chabanloo, "Protection of distribution network considering fault ride through requirements of wind parks", *Electric Power Systems Research*, vol. 178, pp. 106019, 2020.

[21] M. Nasiri, J. Milimonfared, SH. Fathi, "A review of low-voltage ride-through enhancement methods for permanent magnet synchronous generator based wind turbines", *Renewable and Sustainable Energy Reviews*, vol. 47, pp. 399-415, 2015.

[22] R. Razzaghi, M. Davarpanah, M. Sanaye-Pasand, "A novel protective scheme to protect small-scale synchronous generators against transient instability", *IEEE Transactions on Industrial Electronics*, vol. 60, no. 4, pp. 1659-1667, 2013.

[23] H. Yazdanpanahi, W. XU, "Contribution of induction-machine distributed generators to fault current and assessing their impact on overcurrent protection", In *26th Annual IEEE Canadian Conference on Electrical and Computer Engineering (CCECE), May 2013*, Regina, SK, Canada, pp. 1-4, 2013.

[24] XF. Wang, Y. Song, M. Irving, "Modern power systems analysis", Springer Science & Business Media, 2010.

[25] R. Mohammadi, AH. Abyaneh, HM. Rudsari, HF. Fathi, H. Rastegar, "Overcurrent relays coordination considering the priority of constraints", *IEEE Transactions on Power Delivery*, vol. 26, no. 3, pp. 1927-1938, 2011.

[26] MR. Asadi, AH. Abyaneh, M. Mahmoodan, RA. Naghizadeh, A. Koochaki, "Optimal overcurrent relays coordination using genetic algorithm", in 11th International Conference on Optimization of Electrical and Electronic Equipment (OPTIM), May 2008, Brasov, Romania, pp. 197-202.

[27] SA. Hosseini, H. Askarian Abyaneh, SHH. Sadeghi, F. Razavi, "Merging the retrieval of the protection coordination of distribution networks equipped with DGs in the process of their siting and sizing", Journal of Emerging and Selected Topics in Power Electronic, vol. 8, no. 3, pp. 035502, 2016.

[28] N. Abdolghani, J. Milimonfared, MH. Zamani, "Improving Transient Stability of Dual Stator-Winding Induction Generator Based-Wind farms By Slip Frequency Control", *IEE Journal of Emerging and Selected Topics in Power Electronics*, vol. 9, no, 5, pp. 5354-5366, 2021.

[29] D. Baimel, N. Chowdhury, J. Belikov, "New type of bridge fault current limiter with reduced power losses for transient stability improvement if DFIG wind farm", *Journal of Electric Power System Research*, vol. 197, pp. 107293, 2021.

[30] HR. Shabani, M. Kalantar, A. Hajizadeh, "Investigation of the closed-loop control system on the DFIG dynamic models in transient stability studies", *International journal of Electrical Power and Energy Systems*, vol. 131, pp. 107084, 2021.

7. Appendix

The parameters of IGs in two case studies are listed in Table IV and also, transformer's parameters are listed in Table V. The line impedances in the simple network are:

$Z_{L1} = Z_{L2} = Z_{L3} = 0.12+j0.3\Omega$

The capacity of load1 and load2 are 2MW and 1MW, respectively.

Table IV. The parameters of IGs in the sample networks

parameters	Simple network	IEEE 30bus
capacity	2MVA	1MVA
voltage	690v	11kv
R_s	0.048 p.u	0.04 p.u
X_s	0.075 p.u	0.08 p.u
R_r	0.018 p.u	0.024 p.u
X_r	0.13 p.u	0.14 p.u
X_m	3.8 p.u	3.67 p.u
H	1.5s	1.06s
X_c	4 p.u	4 p.u

Table V. The parameters of transformers in the sample networks.

parameters	Simple network	IEEE 30bus
capacity	3MVA	1.25MVA
R_T	0.02 p.u	0.01 p.u
X_T	0.1 p.u	0.05 p.u

International Journal of Research and Technology in Electrical Industry

journal homepage: ijrtei.sbu.ac.ir

Shahid Beheshti University

Distribution System Restoration by Reconfiguration and MG Formation Considering Post-Restoration Failure Probability

Saeed Nikbakhsh Jahromi [1,*], Ehsan Hajipour[1], Mehdi Ehsan[1]

[1] *Center of Excellence in Power System Management & Control, Department of Electrical Engineering, Sharif University of Technology, Tehran, Iran*

ARTICLEINFO

Article history:
Received 08 December 2021
Received in revised form 12 March 2022
Accepted 13 March 2022

Keywords:
Resiliency
Reconfiguration
Microgrid
Restoration
Critical loads

ABSTRACT

Recent weather-related disasters experienced worldwide with considerable damages to the interconnected power infrastructure have highlighted the importance and urgency of enhancing the resiliency of the distribution grid. A Resilient distribution grid can withstand and recover from such rare events. Resiliency against extreme events is conceptualized in three distinct stages: prior, during, and after the event. Rapid recovery is a feature of after the event stage. In this paper, restoration strategies to restore maximum loads as quickly as possible are investigated. The proposed approach attempts to restore the critical loads by using tie-switches to reconfigure the network. In the case of isolated areas without the possibility of using upstream utility grid, sectionalizing the grid into several microgrids (MGs) is proposed to improve the system resiliency. The number of isolated MGs is an issue that is required to be correctly determined. So, a new approach is proposed to compromise between amount and reliability of supplied load to find the optimum number of MGs. The proposed method is simulated on the unbalanced IEEE-123 and 37-bus distribution grid with random locations for DERs.

1. Introduction

Catastrophic weather events have been experienced worldwide in recent years with massive damage to the power system infrastructure. These kinds of events have a low probability of occurring with high impacts. Therefore, power system resiliency is gaining progressive attention to mitigate the severe consequence of such extreme weather events. The severity of extreme events ranges from simultaneous/sequential multiple faults to the total loss of the upstream utility grid supplying the distribution system [1].

Sectionalizing a distribution system into several MGs is a comprehensive operation scheme to improve distribution system resilience. In [2], an optimization algorithm based on maximum load restoration and voltage stability in the isolated part of the network is presented to form MGs. However, practical usage of the tie-switches in the restoration process before establishing MGs is not well exploited. In [3], a mixed-integer linear programming method is proposed that dynamically forms MGs to achieve a resilient distribution system. In [4], an MG formation plan is proposed that adopts a three-phase network model to represent unbalanced distribution networks. The unbalanced operation constraint of synchronous Generators (SGs) is included in the formulation to prevent unbalanced operations that might

* Corresponding author
E-mail address: Saeed.nikbakhsh@ee.sharif.edu
http://dx.doi.org/ 10.52547/ijrtei.1.1.20

trip SGs. In addition, a linear approximation on the unbalanced operation constraint is also developed to handle more extensive networks.

The number of MGs in the isolated part of the network is an important issue. Reducing or increasing the number of MGs each has its advantages and disadvantages that have been discussed in various papers so far. In [5], it was presented that multiple sources in the network can be integrated by reducing the number of MGs (forming larger MGs), and more loads can be supplied. Also, the sources with limited power generation capability, like diesel generators, can be optimally allocated to critical loads. In [6], it was presented that different types of resources can be optimally coordinated by reducing the number of MGs. In [7], it was stated that reducing the number of MGs allows the uncertainty of renewable resources to be optimally managed. Based on IEEE standard 1547.4 [8], the operation and reliability of the distribution networks will increase if the grid could be split into multiple MGs (increase number of MGs) [7]. In [9], presented that the reliability of each MG is relevant to their included components. Therefore, increasing the number of MGs will result in fewer components in each MG and more reliability. In [10], presented that based on the amount of supplied load and MGs average repair time per year, the number of MGs should be detected by solving an optimization problem.

Reconfiguration of the distribution system before/after a natural disaster has been presented as one of the approaches to improving resiliency. Reconfiguration can be done with different purposes like bringing out the worn-out lines, connecting critical loads to resources, etc. In [11], an algorithm for system reconfiguration before a natural disaster is presented. This algorithm uses the fragility curve of different network lines, and the lines with a high probability of damage will replace with less probability of failure ones. In [12], reconfiguration of the system coordinated with MG formation after natural disasters is presented.

A comprehensive algorithm to increase the resiliency of the distribution system is an algorithm that considers:

- The potential of tie switches to connect loads to upstream network as much as possible. The reason is that there is an assurance of supplying loads when connected to the upstream network. And in this situation, the resiliency of the network will increase significantly.
- The algorithm should be suitable in unbalanced networks. Because of the limitations of unbalanced networks, the algorithms that are suitable for unbalanced networks can be applied to balanced ones, but the opposite is not possible.
- Specify the number of MGs before solving the optimization problem will take the answer away from the optimal global solution. So, in a suitable algorithm, the number of MGs is one of the problem variables.
- To consider the general case, a suitable algorithm should be useful for single or multiple faults. In other words, the network will separate into a connected and an isolated part in the general situation. So, a comprehensive algorithm should be organized for this situation.

This paper presents a comprehensive algorithm for restoring maximum possible loads after a natural disaster. In this algorithm, a configuration to connect all loads to the upstream network is presented. In addition, MGs should be formed in isolated areas in case of unavailability of a configuration to connect all network parts to the upstream network. So, there is the need for an index to determine the optimum number of MGs based on the amount of supplied loads and reliability of MGs. In general, the contributions of this paper include:

- Maximum possible load restoration is obtained by fully exploiting the potential of tie-switches before attempting to form isolated MGs.
- A strategy to obtain the maximum possible formable MGs in an unbalanced, isolated network is presented.
- A new index based on a compromise between the reliability of the formed MGs and the amount restored loads is proposed.

The proposed method is simulated on the IEEE-37 bus and IEEE-123 bus distribution networks with random locations for DERs and critical loads. These sample grids are unbalanced, so a three-phase power flow should be used to find the voltages and line flows. However, in some papers, the IEEE-123 sample network is treated as a balanced three-phase system with different simulation results.

This paper is organized as follows: section 2 describes the approach overview; section 3 provides restoration strategy, section 4 provides the numerical results and section 5 includes the paper and present the future research work.

2. Approach Overview

When a natural disaster occurs, some equipment will be damaged, and a part of the network will become isolated from the upstream network. In the first step of the proposed strategy, a reconfiguration will be performed to connect the isolated area to the upstream network if possible. The objective function for the reconfiguration is presented in section 3.1. But in some cases, with changing the configuration of the network, it is not possible to connect all the isolated areas to the upstream network. So, in this situation, forming MGs is recommended. Forming MGs can be performed with different objective functions. For example, the most popular objective function is maximizing the amount of restored critical loads. But because of probable secondary faults, this objective function will not be the best choice. So, in the next part of the proposed method, an objective function is proposed that is shown in section 3.2.2. Because the proposed objective function consists of different parts with a diverse range of change, in this section normalization approach of the proposed objective function is also presented. After proposing the objective function, it should be used with operational constraints to obtain feasible answers. The proposed objective function with operational constraints presented in section 3.2.3, should be performed for every possible number of MGs obtained with the method shown in section 3.2.1 to find optimum number and configuration of MGs among all possible configurations.

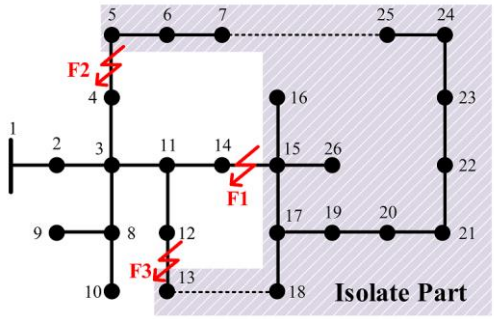

Fig. 1. An example of a network with different faults

3. Restoration Strategy

Distribution systems are loop/mesh designed but radially operated using tie-switches. In this paper, load restoration is done first by applying tie-switches. Whenever a fault occurs, automatic switches are used to isolate the fault. Next, the restoration process is triggered by using tie-switches. If multiple simultaneous/sequential faults occur, a large part of the network may be de-energized. Here, an isolated part would be established that could not be supplied by the upstream utility network. For example, consider Fig. 1 with the fault F1 on section 14-15. A de-energized part is established upon isolating the fault. Restoration of the isolated parts is possible either by closing tie-switch 7-25 or 13-18 depending on the optimization problem results, which will be presented in the preceding sections. Here, no load shedding is required. Two simultaneous faults, F1 and F2, on sections 4-5 and 14-15 are cleared by opening the relevant switches. Here, the concurrent closing of the tie-switches 7- 25 and 13-18 could only restore the isolated area, so it is not required to shed any load and the network is restored by using the tie-switches. For three simultaneous faults, i.e., F1, F2, and F3, the faulty sections 4-5, 12-13, and 14-15 are removed by opening the relevant switches. However, closing any of the tie-switches 7-25/13-18 could not restore the isolated area, so it is required to form autonomous MGs using the available resources in the isolated area.

3.1. Utility-grid Connected Network/Sub-network

In some cases, there is more than one configuration to connect the isolated part to the upstream network. In this situation, because of the assurance of supplying all loads, the optimum solution is a configuration with less switching and power loss as below:

$$Minimize \left(\left(\frac{N_{sw}}{N_m} \right) \times \left(\frac{P_{loss}}{P_{total}} \right) \right) \quad (1)$$

In some cases, no configuration can connect all the isolated parts to the upstream network because of the severity of the disaster or network topology. In this situation, the amount of restored loads is more important than the number of switching and power loss. Therefore, the optimum solution is the configuration that restores more amount of load as below:

$$Maximize \left(\frac{P_{res}}{P_{total}} \right) \quad (2)$$

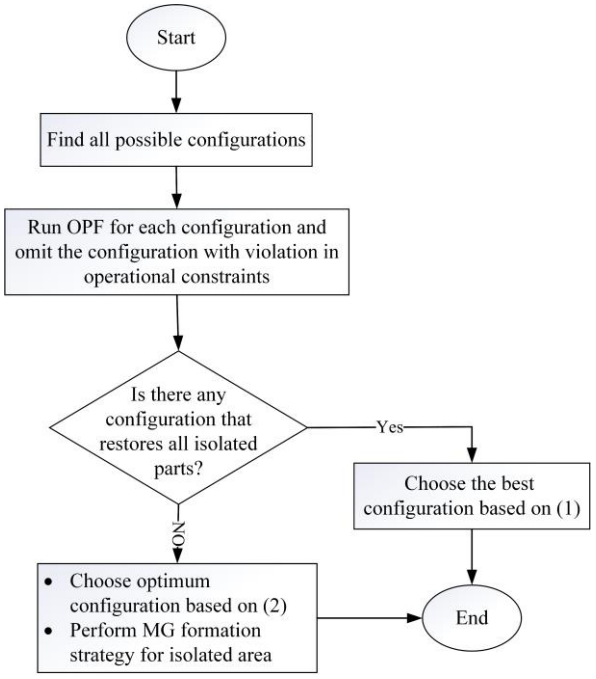

Fig. 2. Flow chart of the proposed method

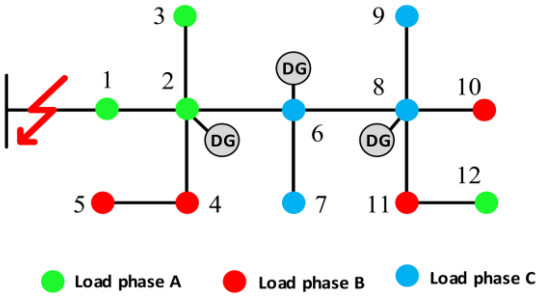

Fig. 3. Sample unbalanced network

After identifying the objective functions, the algorithm to find different configurations should be identified. In [13-14] spanning-tree search algorithm is presented to find all possible configurations in different situations. Therefore, when the network divides into connected and isolated parts, spanning tree algorithm can be used to identify the optimum configuration. The flowchart of the proposed strategy is presented in Fig. 2.

3.2. MG Formation Strategy

The MG formation strategy presented in this paper has three general sections. The first section is an algorithm to obtain the maximum number of formable MGs in the isolated part. The second section presents the objective function to determine the optimum number of MGs among all possible configurations (obtained in the first section). Finally, the third section presents mathematical formulation and constraints for MG formation.

3.2.1. Maximum formable MGs

MG formation methods are well documented in the literature. For example, in [2-3], the objective function maximizes the restored loads based on their priority in the isolated area. The assumption is the availability of one DG per MG that means the number of MGs is equal to the number of DGs. However, it is not always possible to

	1	2	3	4	5	6	7	8	9	10	11	12	*A*	*B*	*C*	*DG*
1	0	1	0	0	0	0	0	0	0	0	0	0	1	0	0	0
2	1	0	1	1	0	1	0	0	0	0	0	0	1	0	0	1
3	0	1	0	0	0	0	0	0	0	0	0	0	1	0	0	0
4	0	1	0	0	1	0	0	0	0	0	0	0	0	1	0	0
5	0	0	0	1	0	0	0	0	0	0	0	0	0	1	0	0
6	0	1	0	0	0	0	1	1	0	0	0	0	0	0	1	1
7	0	0	0	0	0	1	0	0	0	0	0	0	0	0	1	0
8	0	0	0	0	0	1	0	0	1	1	1	0	0	0	1	1
9	0	0	0	0	0	0	0	1	0	0	0	0	0	0	1	0
10	0	0	0	0	0	0	0	1	0	0	0	0	0	1	0	0
11	0	0	0	0	0	0	0	1	0	0	0	0	0	1	0	0
12	0	0	0	0	0	0	0	0	0	0	1	0	1	0	0	0

(3)

fulfill this task due to the constraint of the specified threshold for phase imbalance of the synchronous generators. This constraint asserts that the output powers of different phases of a synchronous generator should not violate a defined threshold. For example, the single-phase loads in the vicinity of the DG at bus 2 in the network presented Fig. 3 are mainly connected to phase A and B, and there is no load at phase C. Since the output power of phase C of DG_2 is zero, the output power of the other phases should remain near zero. It means that in such a condition, it is not possible to use this DG to establish a MG, so the MG needs to be formed with two DGs (DGs at bus 2 and 6) within one MG.

In balanced networks, the maximum number of MGs equals the number of synchronous generators. However, in unbalanced networks based on the network condition, the number of MGs does not follow a particular rule. For this reason, an algorithm will be presented to obtain the maximum number of MGs in the isolated part.

A feasible AC MG consists of three-phase loads with at least one synchronous generator. So, to determine the maximum number of formable MGs, the isolated part of the network should separate into the least sections with three-phase loads and synchronous generator(s). So, in the proposed algorithm, the network will simplify to three-phase nodes consisting of the synchronous generator(s). Finally, these nodes represent the maximum number of formable MGs. An essential point about the maximum formable MGs algorithm is that there is no guarantee about the feasibility of all numbers of MGs obtained in this algorithm. In other words, this algorithm will guarantee that more MGs than obtained MGs are undoubtedly impossible, but fewer MGs may be possible to be formed. So, the optimization algorithm and constraints will determine their feasibility.

In the proposed algorithm to obtain the maximum number of MGs, nodes with degree one (nodes that connect to one other node) will omit, and their load and generator will transfer to the neighbor bus. For this purpose, a network connection matrix will be formed. This matrix has three parts; the first is the connection part, the second is the phase part, and the third is the DGs part. For example, the connection matrix for the network presented in Fig.3 is shown in (3). To better explain this matrix, the first row of this matrix can be made as below:

- Node 1 just is connected to node 2, so just the second array of the first part of the matrix is equal to 1.
- Node 1 consists of load at phase A, so the first array of the second part of the matrix will be equal to 1.
- This node does not consist of DG, so the third part of the matrix equals 0.

It is clear from (3) that buses 1, 3, 5, 7, 9, 10, and 12 have degree 1. The new connection matrix will be like (4) by eliminating these buses.

	2	4	6	8	11	*A*	*B*	*C*	*DG*
2	0	1	1	0	0	1	0	0	1
4	0	1	0	0	0	0	1	0	0
6	1	0	0	1	0	0	0	1	1
8	0	0	1	0	1	0	1	1	1
11	0	0	0	1	0	1	1	0	0

(4)

It is clear from (4) that in this stage, buses 4 and 11 have degree 1. The new connection matrix will be like (5) by eliminating these buses. In (5), bus 8 has a three-phase load and contains a DG. So, this bus will stand for an MG, which will be omitted from considering in the connection matrix.

	2	6	8	*A*	*B*	*C*	*DG*
2	0	1	0	1	1	0	1
6	1	0	1	0	0	1	1
8	0	1	0	1	1	1	1

(5)

In (5), buses 2 and 6 are connected. By eliminating one and transferring the loads and generator to another, the connection matrix will be like (6).

	6	8	*A*	*B*	*C*	*DG*
6	0	1	1	1	1	1
8	1	0	1	1	1	1

(6)

In (6), two buses contain a three-phase load with a generator. So, in the network presented in Fig. 3, the maximum formable MGs is equal to 2. The first MG contains buses 1 to 7, and the second MG has buses 8 to 12.

3.2.2. Index for the optimum number of MGs

As presented, the number of MGs in isolated parts is essential while forming MGs. Generally, the amount of supplied loads and reliability of MGs will be affected by changing the number of MGs. By decreasing the number of MGs (forming larger MGs) as resources are pooled in the network, it is possible to supply more loads. In this situation, there will be more elements in each MG. Because the reliability of MGs is related to the reliability of the elements within them, their reliability will decrease as the number of MGs decreases. Another parameter that affects the reliability of the MGs is how loads are

distributed between them. By specifying the number of MGs, they may be formed in different configurations for load distribution. For example, for the sample network presented in Fig. 4, if it is decided to form 3 MGs, it is possible to form them as MG1 to MG3 (shown in Fig. 4) with the minimum possible area (minimum area with three-phase load and at least one synchronous DG). In this situation, a part will be a floating part (yellow part in Fig. 4) in the network. Assuming that any of the MGs can supply the floating part, the whole or a part of this area can be connected to each MG. So, an index should be proposed to determine how loads of floating parts disperse between MGs.

Based on the above information, the objective function for determining the optimum number of MGs should have three parts; the first part represents the amount of supplied load, the second part represents the number of MGs, and the third part represents the dispersion of the loads between MGs. So, the objective function will be presented (7). The larger the index, the more resilient the network will be.

$$obj = P_{res} \times n_m \times \prod_{n'=1}^{n_m} \xi_{n'} \tag{7}$$

In this equation, the first and second terms are supplied load and number of MGs, respectively. In the third term ξ_n is the amount of supplied load in MG n. An essential point about the third term is that when a few variables with a constant summation are multiplied together, the result will be maximum when all the variables are equal. So, the third term has a maximum value when the load separates between MGs equally. However, it is almost impossible to separate the loads between MGs equally. So, it could be said that the closer loads of MGs, the higher the third term will be. Finally, to normalize this index, it can be rewritten as below:

$$obj = \frac{P_{res}}{P_{total}} \times \frac{n_m}{MG_{max}} \times \frac{\prod_{n'=1}^{n_m} \xi_{n'}}{\left(P_{res}/n_m\right)^{n_m}} \tag{8}$$

3.2.3. *Algorithm for MG formation*

At this stage, the algorithm for MG formation and decision making for number of MGs and supplied load is presented. In this algorithm, maximum number of formable MGs is determined by the algorithm presented in (3.2.1). Then run the optimization problem for MG formation (9) to (24) for all possible number of MGs (1 to MG_{max}). Then the resiliency index (8) will be calculated for all conditions and the configuration with maximum resiliency index will choose as the optimum solution.

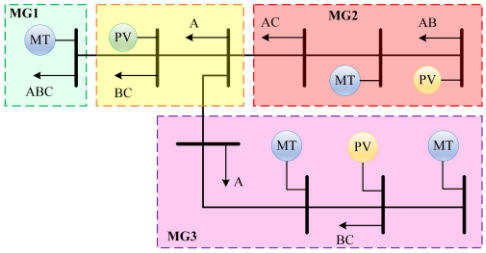

Fig. 4. Sample unbalance network

$$max\left(\sum_{n=1}^{n_m}\sum_{i=1}^{i_m}\sum_{t=1}^{t_{max}}\sum_{\delta} y_i^n \times \omega_i \times P_{i,t}^{D,\delta}\right) \tag{9}$$

$$1-\varepsilon \le \left|V_{i,t}^{\delta}\right| \le 1+\varepsilon \quad ,\forall i \in I, \delta \in P_0, \forall t \in T \tag{10}$$

$$\left(P_{ij,t}^{\delta}\right)^2 + \left(Q_{ij,t}^{\delta}\right)^2 \le \sigma_{ij}^n \left(S_{ij}^{max}\right)^2, \forall (i,j) \in L, \forall n \in N, \forall t \in T \tag{11}$$

$$\sum_{i=1}^{i_m} \sigma_{ik}^n P_{ik,t}^{\delta} + P_{i,t}^{G,\delta} - y_i^n P_{i,t}^{D,\delta} + s_i^{R,n} P_{i,t}^{R,\delta} - \sum_{j=1}^{i_m} \sigma_{kj}^n P_{kj,t}^{\delta} = 0, \forall k \in I, \forall n \in N, \forall t \in T, \forall \delta \in P_0 \tag{12}$$

$$\sum_{i=1}^{i_m} \sigma_{ik}^n Q_{ik,t}^{\delta} + Q_{i,t}^{G,\delta} - y_i^n Q_{i,t}^{D,\delta} + s_i^{R,n} Q_{i,t}^{R,\delta} - \sum_{j=1}^{i_m} \sigma_{kj}^n Q_{kj,t}^{\delta} = 0, \forall k \in I, \forall n \in N, \forall t \in T, \forall \delta \in P_0 \tag{13}$$

$$\beta_i^n V_i = \beta_j^n V_j - \sigma_{ij}^n \left(Z_{ij}^* S_{ij} + Z_{ij} S_{ij}^*\right), \forall (i,j) \in I, \forall n \in N \tag{14}$$

$$\sum_{\delta} \left(\left(P_{i,t}^{G,\delta}\right)^2 + \left(Q_{i,t}^{G,\delta}\right)^2\right) \le s_i^{G,n} S_i^{max}, \forall i \in I_g, \forall t \in T, \forall n \in N \tag{15}$$

$$\frac{\left|S_{i,t}^{G,a} + \alpha S_{i,t}^{G,b} + \alpha^2 S_{i,t}^{G,c}\right|}{\left|S_{i,t}^{G,a} + S_{i,t}^{G,b} + S_{i,t}^{G,c}\right|} \le T_{ub}, \forall i \in I_g, \forall t \in T \tag{16}$$

$$\sum_{n=1}^{n_m} \beta_i^n = 1, \qquad \forall i \in I \tag{17}$$

$$\beta_i^n \le \beta_u^n, \qquad \forall i \in I, \forall n \in N, u \in U_i \tag{18}$$

$$y_i^n \le \beta_i^n, \qquad \forall i \in I, \forall n \in N \tag{19}$$

$$\sigma_{ij}^n \le \beta_i^n \times \beta_j^n, \qquad \forall (i,j) \in L, \forall n \in N \tag{20}$$

$$\sum_{n=1}^{n_m} \sum_{(i,j)\in L} \sigma_{ij}^n = N_l - n_m + 1 \tag{21}$$

$$s_i^{G,n} = \beta_i^n \times sdg_i, \qquad \forall i \in I, \forall n \in N \tag{22}$$

$$s_i^{R,n} = \beta_i^n \times sr_i, \qquad \forall i \in I, \forall n \in N \tag{23}$$

$$\sum_{n=1}^{n_m} s_i^{G,n} \ge 1, \qquad \forall n \in N \tag{24}$$

Table I. Resources considered in 37-node test system

Bus #	Type	Phase (A, B, C)	Power (kVA)
703	DG	ABC	570
711	PV	C	10
712	PV	B	5
718	DG	ABC	600
722	DG	ABC	540
724	WT	B	15
725	PV	B	25
731	WT	B	20
736	WT	B	5
737	DG	ABC	250
741	DG	ABC	200
742	WT	B	50
775	DG	ABC	360

The objective is maximizing the restoration of critical loads subject to constraints (10) to (24). Constraint (10) applies the maximum voltage deviations; (11) sets the loadability of the lines; (12) and (13) set the balance of the input and output active and reactive powers of each bus, respectively; (14) is the formulation of voltage calculation; (15) sets the maximum output power of each DG; (16) sets the maximum tolerable unbalance condition for the synchronous generators; (17) indicates that a bus could only be in one microgrid; (18) asserts that a bus could only be in a MG only if its parent node is also present in that MG that parent nodes can be obtained using BFS search algorithm [15]; (19) indicate that each load could supply in a MG that its relevant bus belongs to; (20) explains that a line is within a MG, if both its end buses are within that MG, otherwise, that line does not belong to any MG; (21) shows the number of closed lines to form nm number of MGs; (22), (23) shows that a generator/renewable source belong to a MG if the buses that have these resources belong to that MG; (24) shows that there should be at least one generator in each MG.

4. Numerical Results

In order to show the effectiveness of the proposed method, it is simulated on two unbalance distribution networks; IEEE 37- node and 123-node test systems. In the simulations, unbalanced load flow performed with GrilLAB-D [16], and the optimization problem is performed with GAMS and BARON (basic open-source mixed-integer nonlinear programming) solver. It is supposed that the diesel generators are the only dispatchable generating sources. So, they are considered as PV buses.

4.1. IEEE 37-node Distribution Network

IEEE 37-bus distribution network that is considered in this simulation is presented in Fig. 5. Details about this system can be found in [17], and DGs' information is presented in Table I. Load ad DGs variation during a day is presented in Fig. 6. This network does not have any tie switches, so MGs should be formed by isolating a part of the system. The importance of different loads was randomly introduced in the range (1-10).

It is assumed that the fault occurrence on line 799-701 between 10 and 12 AM will isolate all parts of this network from the upstream network. With the maximum formable algorithm, it is obtained that up to 4 MGs can be formed. The minimum buses to form MGs, floating part (FP), and master DG (MDG) in each MG are presented in Table II.

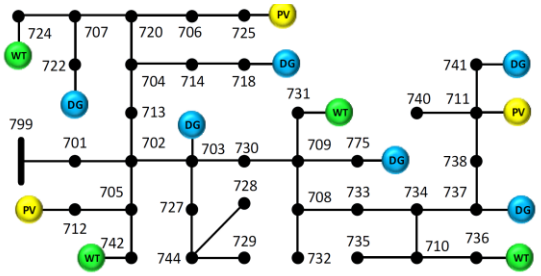

Fig. 5. IEEE 37-node test system

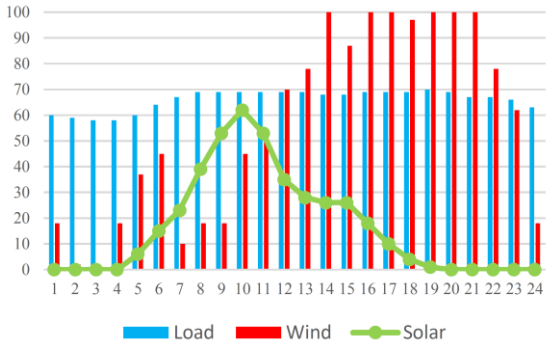

Fig. 6. Variation of load and renewable sources during a day

Table II. Minimum bused to form MGs in 37-node distribution network

MG	Nodes	MDG
1	704-714-718-720-706-725-707-722-724	718
2	703-727-744-728-729	703
3	708-709-731-732-775-733	775
4	734-710-735-736-737-738-711-740-741	737
FP	701-702-713-705-712-742-730	-

Table III. Results for MG formation in 37-node test system

n_m	$P_{res}^{p.u.}$	Reliability	Resiliency	Time (s)
1	0.8624	0.2500	0.2156	5.06
2	0.7936	0.4111	0.3262	9.50
3	0.7879	0.2909	0.2292	24.56
4	0.6007	0.6278	0.3771	58.23

It is assumed that the fault occurrence on line 799-701 between 10 and 12 AM will isolate all parts of this network from the upstream network. With the maximum formable algorithm, it is obtained that up to 4 MGs can be formed. The minimum buses to form MGs, floating part (FP), and master DG (MDG) in each MG are presented in Table II.

As mentioned, up to 4 MGs can be formed in the isolated area (MG_{max} = 4). So, all possible cases are forming 1 to 4 MGs that is presented in this section and the results are presented in Table III.

4.1.1. Forming one MG in the isolated area

In this case, the entire isolated network will be divided into a single MG. It is expected that in this situation the highest amount of load supplies. The results of solving the optimization problem for MG formation show that 1462.11 kW of the loads will be supplied. The total amount of loads in the isolated part is 1695.33 kW, so the supplied load index (the first part of (8)) is equal to 0.8624, and the reliability index (the second and third part of (8)) is equal to 0.25. So, the resiliency index (8) is equal to 0.2156.

4.1.2. Forming two MGs in the isolated area

In this case, the isolated part will be divided into two MGs. The optimization problem results for MG formation show that 1345.5 kW of the loads will be supplied. The optimum configuration for MGs is presented in Fig. 7(a). In this situation, supplied load in MG1 and MG2 equals 956.34 kW and 389.16 kW, respectively. As a result, the supplied load index is equal to 0.7936, the reliability index is equal to 0.4111, and as a result, the resiliency index is equal to 0.3262.

4.1.3. Forming three MGs in the isolated area

In this case, the isolated part of the network will be divided into three MGs. Results of the optimization problem show that 1335.84 kW of loads will be supplied. The optimum MGs configuration is presented in Fig. 7(b). In this situation, supplied load in MG1 to MG3 is equal to 956.34 kW, 175.95 kW, and 203.55 kW, respectively. So, the supplied load index is equal to 0.7879, the reliability index is equal to 0.2909, and as a result, the resiliency index is equal to 0.2292. The essential point, in this case, is that the number of MGs has increased compared to the previous case (forming one MG), but the reliability index has decreased. On this subject, it can be stated that the reliability index consists of two parts; the number of MGs and scattering over loads. In this case, the number of MGs increased, but there is a large discord between supplied loads in different MGs (956.34, 175.95, 203.55 kW).

4.1.4. Forming four MGs in the isolated area

In this case, the isolated part of the network is divided into four MGs. Results of the optimization problem show that 1018.44 kW of the loads will be supplied. The optimum configuration for MGs is presented in Fig. 7(c). In this situation, supplied loads in MG1 to MG4 are equal to 494.04 kW, 173.88 kW, 175.95 kW, and 174.57 kW, respectively. So, the supplied load index is equal to 0.6007, the reliability index is equal to 0.6278, and the resiliency index is equal to 0.3771.

As shown in Table III, forming 1 MG in the isolated area will result in the highest amount of supplied load and the least reliability. Moreover, forming 4 MGs will result in the least supplied load and the most reliability. Eventually, forming 4 MGs has the most resiliency index and is the optimum configuration for MG formation.

4.2. IEEE 123-bus distribution system

The modified IEEE 123-bus distribution network is used for simulations in this part. Details about this test system can be found in [17]. There are six tie-switches: 60-160, 97-197, 13-152 and 18-135 that are normally closed and 54-94, and 151-300 that are normally open. This system is a three-phase unbalanced one with single-phase loads and DGs. 123-node distribution network and considered sources are presented in Fig. 8. Simulations are done in three scenarios; in the first scenario, a single fault; in the second scenario, multiple minor faults and multiple major faults are determined in the third scenario.

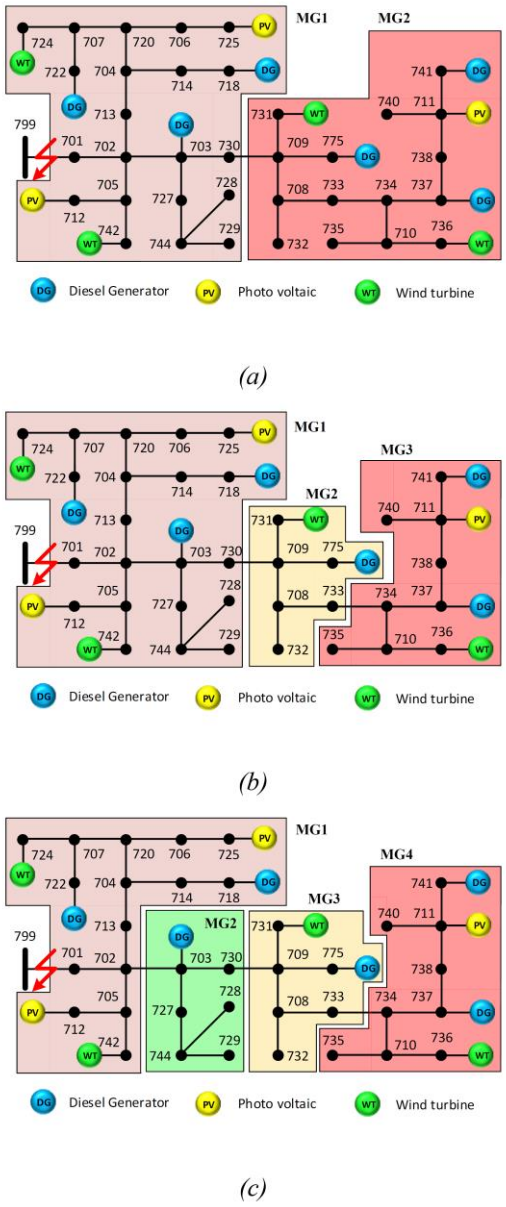

Fig. 7. Forming different number of MGs in isolated part; (a) Forming two MGs, (b) Forming three MGs, (c) Forming four MGs

4.2.1. Single fault

A single fault is assumed on line 60-160 (F1 in Fig. 8). The fault is cleared by opening the tie-switch 60-160. The methodology proposed in [2] is only based on forming MGs. In [2], for this particular scenario, seven MGs are formed after clearing the fault. Moreover, it is required to shed 20 kW load. However, in the proposed method, by using tie switches, isolated parts can be connected to the upstream network and there is no requirement of load shedding. As presented in Table IV,

there are five different configurations connect the isolated part to the upstream network. So, the optimum configuration should be chosen based on the objective function (1). The objective functions for different configurations are presented in Fig. 9. As it is evident in this figure, the second configuration is the optimum one.

4.2.2. Multiple minor faults

Two faults on line 18-135 and 60-160 (F1 and F2 in Fig. 8) are assumed the same as in [2]. The faults are cleared by opening the tie-switches 18-135 and 60-160. In [2], restoration is performed by forming nine MGs; meanwhile, 40 kW load is also shed due to the supply deficiency. In the proposed algorithm, by changing the configuration of the network, it is possible to connect all parts of the network to the upstream network. So, it is possible to restore all amount of loads without load shedding. In this situation, only one configuration can connect all the isolated areas to the upstream network. In this configuration, the tie-switches 54-94 and 151-300 should be closed.

4.2.3. Multiple major faults

This scenario assumes that three faults occur on lines 97-197, 18-135, and 60-160 (F1, F2, and F3 in Fig. 8). A large part would be isolated. In this situation, a configuration connects a part of the isolated area to the upstream network. As a result, a part of the system will remain isolated. According to the maximum formable MG algorithm that is presented in (3.2.1), 3 MGs can be formed in the isolated area. In this situation, supplied load, reliability, and resiliency index should be calculated for forming 1MG to 3MGs.

By forming one MG in the isolated area, 835 kW of the loads will be supplied. Due to the 1075 kW load in the isolated area entirely, the supplied load index is equal to 0.7767. The reliability index is equal to 0.3334, and finally, the resiliency index is equal to 0.2589. By forming two MGs in the isolated area, 815 kW of loads will be supplied and as a result, supplied load index is equal to 0.7581. In this situation, 280 kW of the loads will be restored in one MG, and 535 kW will be restored in the other one. So, the reliability index is equal to 0.6014, and the resiliency index is equal to 0.4559. By forming three MGs in the isolated area, 755 kW of the loads will be supplied, so the supplied load index equals 0.7023. In this situation 80 kW of the loads will be supplied in one MG, 335 kW of the loads will be supplied in another MG, and 340 kW of the loads will be supplied in the last MG. So, the reliability index is equal to 0.5717 and as a result, the resiliency index is equal to 0.4015. Finally, the whole calculated indexes are presented in Fig. 10. As it is clear from this figure, by forming one MG, the maximum amount of loads will be supplied and forming two MGs will result in the maximum amount for reliability index. Totally, forming two MGs is the optimum configuration in this situation that is presented in Fig. 11(b).

5. Conclusion

A Resilient distribution grid has the ability to withstand and recover from low-probability high-impact events. Resiliency against these events is conceptualized in three distinct stages: prior, during and after the event. Rapid recovery is a feature of after an event stage. In this paper, restoration strategies to restore maximum loads as quickly as possible are investigated. The proposed approach attempts to restore the critical loads by using tie-switches to reconfigure the network. In case of isolated areas without the possibility of using upstream utility grid, sectionalizing the grid into several microgrids (MGs) is proposed to improve the system resiliency. The number of isolated MGs is an issue that is required to be properly determined. So, a new approach is proposed to compromise between amount and reliability of supplied load to find the optimum number of MGs in order to optimally allocate the resources to critical loads. The proposed method is simulated on the unbalanced IEEE-123 and 37-bus distribution grid with random locations for DERs. The results show more critical supplied load using reconfiguration and optimal configuration for MGs based on the proposed objective function.

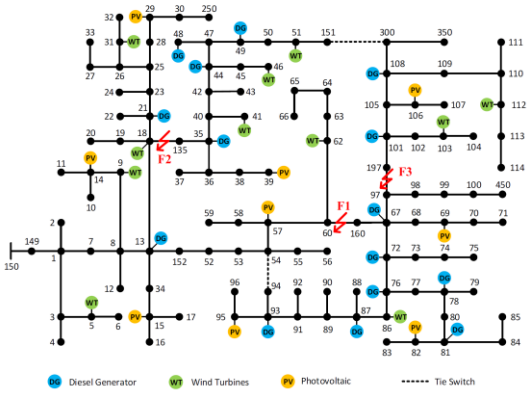

Fig.8. IEEE 123-bus distribution network

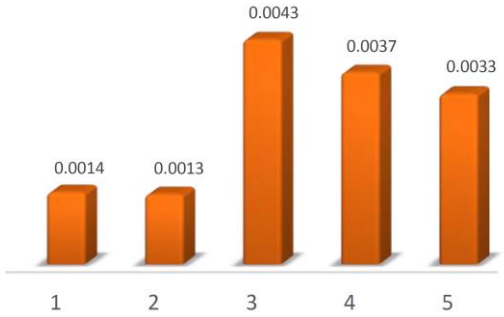

Fig. 9. Objective function for different configuration of first scenario of 123-node distribution network

Table IV. Different configurations for the first scenario in IEEE 123-node distribution network

Config.	Line with switch					switching	Loss (kW)
	54-94	151-300	13-152	18-135	97-197		
1	1	0	1	1	1	1	24.05
2	0	1	1	1	1	1	23.83
3	1	1	1	1	0	3	25.51
4	1	1	1	0	1	3	21.78
5	1	1	0	1	1	3	19.36

6. Acknowledgement

The authors thank Dr. Mojtaba Khedrzadeh for his excellent helps in writing this article during his lifetime.

7. References

[1] I. M. Diahovchenko, G. Kandaperumal, A. K. Srivastava, Z. I. Maslova, and S. M. Lebedka, "Resiliency driven strategies for power distribution system development," Electr. Power Syst. Res., vol. 197, p. 107327, 2021.

[2] Z. Wang and J. Wang, "Self-Healing Resilient Distribution Systems Based on Sectionalization into Microgrids," IEEE Trans. Power Syst., vol. 30, no. 6, pp. 3139–3149, 2015.

[3] C. Chen, J. Wang, F. Qiu, and D. Zhao, "Resilient distribution system by microgrids formation after natural disasters" IEEE Trans. on Smart Grid, vol. 7, no. 2, pp. 958 - 966, 2016.

[4] Z. Wang, J. Wang, and C. Chen, "A three-phase microgrid restoration model considering unbalanced operation of distributed generation," IEEE Trans. on Smart Grid, vol. 9, no. 4, pp. 3594-3604, 2018.

[5] Y. Wang, Y. Xu, J. He, C. C. Liu, K. P. Schneider, M. Hong, and D. T. Ton "Coordinating multiple sources for service restoration to enhance resilience of distribution systems," IEEE Trans. Smart Grid, vol. 10, no. 5, pp. 5781–5793, 2019.

[6] K. P. Schneider, F. K. Francis, M. A. Elizondo, C. C. Liu, Y. Xu, S. Backhaus, and D. Ton "Enabling resiliency operations across multiple microgrids with grid friendly appliance controllers," IEEE Trans. Smart Grid, vol. 9, no. 5, pp. 4755–4764, 2018.

[7] G. Liu, M. R. Starke, B. Ollis, and Y. Xue, "Networked Microgrids Scoping Study", 2016.

[8] IEEE Guide for Design, Operation, and Integration of Distributed Resource Island Systems with Electric Power Systems, IEEE Standard 1547.4, 2011, pp. 1 54.

[9] F. Shahnia, S. Bourbour, and A. Ghosh, "Coupling Neighboring Microgrids for Overload Management Based on Dynamic Multicriteria Decision-Making," IEEE Trans. Smart Grid, vol. 8, no. 2, pp. 969–983, 2017.

[10] S. A. Arefifar, Y. A. R. I. Mohamed, and T. H. M. El-Fouly, "Optimum microgrid design for enhancing reliability and supply-security," IEEE Trans. Smart Grid, vol. 4, no. 3, pp. 1567–1575, 2013.

[11] M. H. Amirioun, F. Aminifar and H. Lesani, "Resilience-Oriented Proactive Management of Microgrids Against Windstorms," IEEE Transactions on Power Systems, vol. 33, no. 4, pp. 4275-4284, July 2018.

[12] T. Ding, Y. Lin, Z. Bie, and C. Chen, "A resilient microgrid formation strategy for load restoration considering master-slave distributed generators and topology reconfiguration," Appl. Energy, vol. 199, pp. 205–216, 2017.

[13] M. Khederzadeh and S. Zandi, "Enhancement of Distribution System Restoration Capability in Single/Multiple Faults by Using Microgrids as a Resiliency Resource," IEEE Syst. J., vol. 13, no. 2, pp. 1796–1803, 2019.

[14] W. Mayeda and S. Seshu, "Generation of Trees without Duplications," in IEEE Transactions on Circuit Theory, vol. 12, no. 2, pp. 181-185, 1965.

[15] S. S. Ray, "Graph Theory with Algorithms and its Applications in applied science and technology", Springer, 2013.

[16] U.S. Department of Energy at Pacific Northwest National Laboratory, GridLAB-D, Power Distribution Simulation Software, 2015. [Online]. Available: http://www.gridlabd.org/.

[17] W. H. Kersting,, "Radial distribution test feeders", IEEE Trans. Power Syst., vol. 6, no. 3, pp. 975–985, 1991.

Nomenclature

$\boldsymbol{i, j, k}$	Bus index
δ	Phase index
n	Microgrid index
t	Time index
u	Parent node index
I	Set of buses
L	Set of lines
N	Set of microgrids
I_g	Set of buses with generating sources
U_i	Set of parent nodes for bus i
P_0	Set of phases (A, B, C)
S_{ij}^{max}	Maximum power flow through line ij
MG_{max}	Maximum number of formable MGs
$S_i^{G,max}$	Maximum power of generator at bus i
N_m	Number of switches in the network
n_m	Number of MGs that intended to be formed
P_{loss}	Total power loss
P_{total}	Total active load of the network
T_{UB}	Maximum tolerable unbalance of synchronous generators
ω_i	Importance coefficient of the load at bus i
n_m	Number of microgrids
$P_i^{D,\delta}/Q_i^{D,\delta}$	Active/reactive load at bus I ans phase $\boldsymbol{\delta}$
sdg_i	Binary parameter indicating whether a generator is connected to bus I or not
sr_i	Binary parameter indicating whether a renewable source is connected to bus I or not
$v_{i,t}^{\delta}$	Bus voltage at bus i at time t in phase $\boldsymbol{\delta}$
$P_{ij,t}^{\delta}/Q_{ij,t}^{\delta}$	Active /reactive power flow of line ij at time t in phase $\boldsymbol{\delta}$
$P_{i,t}^{G,\delta}/Q_{i,t}^{G,\delta}$	Active/reactive power generation by generator at bus I at time t in phase $\boldsymbol{\delta}$
$P_{i,t}^{R,\delta}/Q_{i,t}^{R,\delta}$	Active/reactive power generation by renewable sources at bus I at time t in phase $\boldsymbol{\delta}$
$P_{non-res}$	Total power not restored at the isolated part
N_{sw}	Number of switching
ξ_n	Total active power restored at microgrid n
P_{res}	Total active power restored
σ_{ij}^n	Binary variable indicating line ij belong to microgrid n
y_i^n	Binary variable indicating whether load i is picked up by microgrid n
$s_i^{G,n}$	Binary variable indicating whether DG i is belong by microgrid n
$s_i^{R,n}$	Binary variable indicating whether renewable source i is belong by microgrid n
β_i^n	Binary variable indicating whether bus i belong to microgrid n

International Journal of Research and Technology in Electrical Industry

journal homepage: ijrtei.sbu.ac.ir

Shahid Beheshti University

Development a New Flexibility Index Suitable for Power System Operational Planning

Homayoun Berahmandpour [1,*], Shahram Montaser Kouhsari[2], Hassan Rastegar[2]

[1] *Head of Bulk Power Transmission Technology Center, Niroo Research Institute, Tehran, Iran*
[2] *Electrical Engineering Department, Amirkabir university, Tehran, Iran*

ARTICLEINFO

Article history:
Received 28 December 2021
Received in revised form 19 February 2022
Accepted 24 February 2022

Keywords:
Power system flexibility
Flexibility index
Operational planning
Renewable resource integration

ABSTRACT

Power system flexibility is an important characteristic in both power system planning and operation, which should be evaluated and maintained in the desired value. On the other hand, more renewable energy integration leads to increasing uncertainty and variability in the power system. Therefore, the power system should have the sufficient ability to overcome the adverse effects of uncertainty and variability named as flexibility, which should be improved with suitable tools such as adequate reserve, fast ramp-up/down generation sources and suitable energy storage capacity. Power system flexibility evaluation is the main task that needs suitable indices to indicate the level of system flexibility correctly. In the current paper, a well-known system flexibility index named normalized flexibility index, which is used for power system planning horizon is modified to use for the operational planning time zone. In this concept, the flexibility index is separated into two components, each of them indicating the ability of the power system to withstand upward/downward net-load uncertainty and variability. In the further, this is shown these two components are the same as the upward/downward system reserve and can be converted to economic value simply. So, this concept facilitates the economic trade-off between operation cost and system flexibility, improving cost to achieve the best level of system flexibility.

1. Introduction

As the world shift to more renewable energy, especially variable ones such as wind and solar, a paradigm shift in the power sector has gradually taken place to meet the transition. In particular, is the growing trend of more focus on the so-called "Power System Flexibility" in the academic and industrial sectors in this field.

Power system flexibility is an important criterion that shows the capability of the power system to withstand uncertainty and variability arising from different resources such as electrical load behaviour, Variable Renewable Energy (VRE) output power, power market player actions and so on. One of the comprehensive definitions of this important power system specification can be found in [1].

The term flexibility describes the ability of a power system to cope with variability and uncertainty in both generation and demand, while maintaining a satisfactory level of reliability at a reasonable cost, over different time horizons.

Four main concepts of flexibility are underlined in this definition. The main concept is “uncertainty and variability” which establishes the main framework for power system flexibility studies and should be modelled

* Corresponding author
E-mail address: hberahmandpour@aut.ac.ir
http://dx.doi.org/ 10.52547/ijrtei.1.1.29

for each source of uncertainty correctly (such as load or renewable resource output). Also, uncertainty and variability are extended to both the generation and demand sides. Where the important key item "reliability at a reasonable cost" shows the need for the economic trade-off between reliability and operation costs to find the best level of flexibility in each power system and each operation situation (as generation point or network configuration). Finally, the last item shows the wide time range for flexibility study from real-time operation up to long term extension planning time horizons. Fig. 1 shows the main features of the flexibility study in the different time horizons.

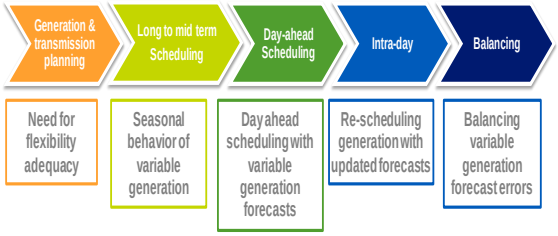

Fig. 1. Flexibility challenges in different time zones

According to the International Energy Agency, the flexibility of a power system refers to "the extent to which a power system can modify electricity production or consumption in response to variability, expected or otherwise" [2]. Another source described it as "the modification of generation injection and/or consumption patterns in reaction to an external signal (price signal or activation) in order to provide a service within the energy system" [3]. But the first definition seems to be more comprehensive and perfect.

The main challenge with insufficient power system flexibility in the operation time horizon is generation/load unbalance defect. It can appear as an unpermitted frequency deviation, unwanted load shedding and renewable curtailment, all of which expose extra costs to the power system planning and operation. On the other hand, increasing flexibility puts extra costs on the power system. So, balancing these two main costs leads to the economic level of power system flexibility. Fig. 2 shows the main tools for power system flexibility improvement concerning their costs. In this way, power system flexibility evaluation is one of the main tasks in the power system flexibility study. Where the power system flexibility level can be determined by a suitable and meaningful measure named as flexibility index.

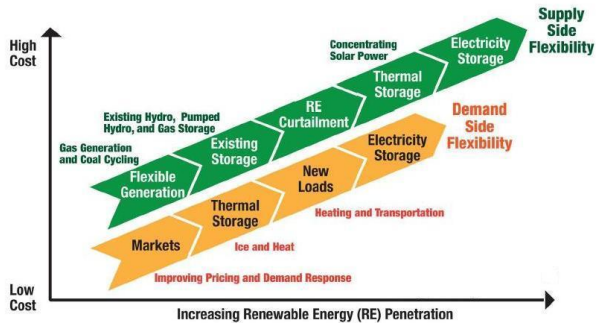

Fig. 2 Differenet tools for flexibility improvement

The current paper is complementary to the concept described in [4] to introduce the new concept as up/down components of the flexibility index. In this way and in the second part, a short review of the main approach for the flexibility evaluation is described. Part 3 presents the concept of operational planning flexibility which is the main approach of the current paper. One of the well-known flexibility indices for power system planning time horizon as "Normalized Flexibility Index (NFI)" is determined and discussed in part 4. The main contribution of this paper is to modify this index to use for operational planning time horizon, where it leads to a new flexibility index for power system flexibility evaluation and as said before, to separate the proposed index to up/down components each of them to evaluate the up/down system flexibility. The physical concept for the new index is explained in part 6. Where this is an important contribution that leads to the economic value of the flexibility index. Simulation and result analysis are presented in part 7 and finally, part 8 includes the conclusion.

2. Flexibility evaluation

Increasing the penetration of variable renewable generation in power systems worldwide is one of the main reasons for uncertainty and variability rapid growth in power systems and therefore to more pay attention to power system flexibility. It forces sufficient flexibility to overcome the uncertainty and variability that arise from these types of generation. Traditional capacity adequacy planning techniques have been supplemented with integration studies, which have been carried out in power systems with high targets for renewable generation. These have highlighted the increased variability that a system may experience in the future. As the system generation planning techniques evolve with the challenge of integrating variable generation, the flexibility of a system to manage periods of high variability needs to be assessed [5].

The first requirement for power system flexibility evaluation is to develop a suitable measure/index to quantify system flexibility level. The flexibility index should determine the ability of the power system to overcome both uncertainty and variability specifications in both generation and demand sides. The level of flexibility of two systems or two operating points of one system can be compared with this index and the improvement of the flexibility level by corrective and improvement actions can be obtained by increasing this index in the next step.

Generally, the accessible generation capacity and ramp rate capability of the system generation are two main characteristics of flexibility on the generation side. Therefore, generation units providing dynamic reserve by fast ramp rate characteristics are the essential tools to provide flexibility on the generation side. On the other hand, the energy stored in energy storage systems or accessible energy due to limited energy sources such as hydroelectric power plants or pumped-storage systems can help to improve system flexibility.

To have a clear overview of power system flexibility and also to compare the different power systems flexibility levels or one power system flexibility level in different situations, it needs to evaluate power system

flexibility by suitable flexibility index. This index should indicate the level of power system flexibility properly and also it should be converted to an economic value to facilitate the cost/benefit analysis of the power system flexibility in different levels. The insufficient ramping resource expectation (IRRE) metric is a well-known index proposed to measure power system flexibility mainly for use in long-term planning and is derived from traditional generation adequacy metrics [5]. Compared to existing generation adequacy metrics, flexibility assessment is more data-intensive. A flexibility metric can identify the time intervals over which a system is most likely to face a shortage of flexible resources, and can measure the relative impact of changing operational policies and the addition of flexible resources. The flexibility of the desired system with increasing penetrations of variable generation is assessed and the results highlight the time horizons of increased and decreased risk associated with the integration of the variable generation systems [6].

A large number of metrics and indicators are currently used in power systems to measure the power system different abilities such as reliability, security, transient stability and so on. Power system flexibility indices are also the measures for the ability of the power system against uncertainty and variability. The indicators such as Loss Of Load Expectation (LOLE) and Expected Energy Not Served (EENS) are used for power system flexibility evaluation in a planning context to determine the adequacy of future systems [7]. These metrics are very similar to the power system reliability indices and are categorized as probabilistic indices. On the other hand, some of the indices categorized as deterministic are calculated by the system parameters in each situation of the power system. Four main parameters of system generation are used to form these types of indices as system storage energy (ε), system power capacity (π), system ramp rate capability (ρ) and ramp duration time (δ) [6]. In a dominant approach for deterministic indices, the area bounded by the permitted values of these parameters forms the locus of system generation points which can be found to respond to net load uncertainty and variability. Fig. 3 shows the concept of the flexibility index based on the permitted area for system generation points bounded by the four mentioned parameters [7].

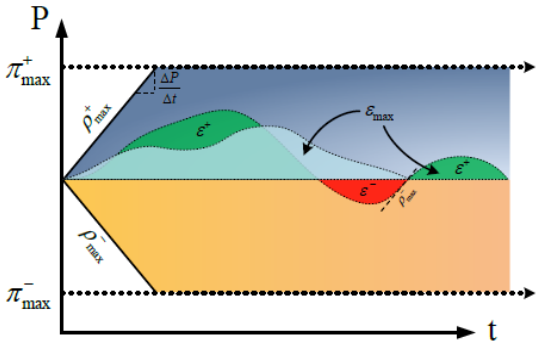

Fig.3. Permitted area concept for flexibility index

Fig. 4 shows an approach on the probabilistic index as Lack Of Ramp Probability (LORP) [8].

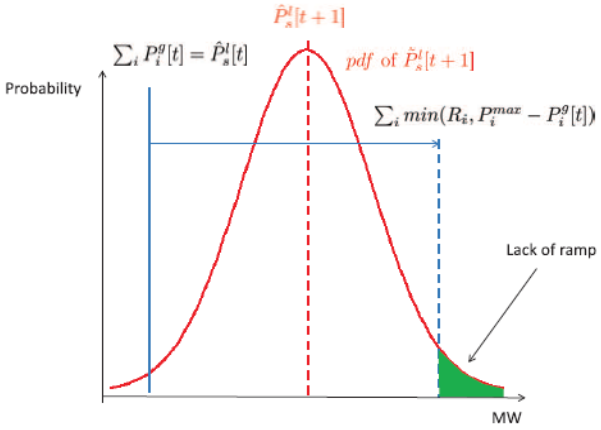

Fig. 4. LORP flexibility index

Here the probabilistic behaviour of the load power at the time (t+1), is shown by the normal probability distribution function. LORP shows the probability of the load power at the time (t+1) cannot be covered by the generation system capability because of the defect in the generation ramp rate. The green area in Fig. 4 shows this probability and correspondingly this index.

System Capability Ramp (SCR) [9], is another probabilistic index. This index is introduced as:

$$\mathrm{SCR}_{t+\Delta t} = \sum_{i=1}^{n} (A_{i,t}\, O_{i,t}) \min(P_{i,t}^{max} - P_{i,t}, Ramp_i \Delta t) \qquad (1)$$

Where A and O are the availability and situation of the unit i in time t respectively. P and Ramp are also the generation and ramp rate of this unit in time t. The main probabilistic nature of this approach is the unit availability which should be calculated by the conventional methods such as Markov chain-based capacity state model [9].

Ramping capability Shortage Expectation (RSE) [10] is another probabilistic index. In this approach, the risk of the ramping capability shortage is quantified where RSE is defined as the sum of the probabilities that the ramping capability requirement will be not satisfied. Clearly by decreasing RSE system generation flexibility will be increased. (Unlike SCR)

Finally, Ramping capability Shortage Probability (RSP) [11] is another well-known flexibility index used to evaluate system flexibility level. The RSP at time t is defined as the sum of the probabilities that net load variation during an interval between t−Δt and t could not be covered by the ramping capability of the system.

Now by the short review about the different approaches on the generation system flexibility indices, the operational planning flexibility concept which is the main concept of the current paper, is described.

3. Operational planning flexibility

Operational flexibility is an important property of electric power systems and is essential for mitigating generation/load unbalance comes from uncertainty and variability in short/mid-term power system operation. The availability of sufficient operational flexibility is a necessary prerequisite for effective power system operation, especially with grid integration of large shares

of fluctuating power resources mainly variable renewable energy sources [12].

Operational planning includes the time horizon in about a few minutes to one day or one week ahead (Fig. 5).

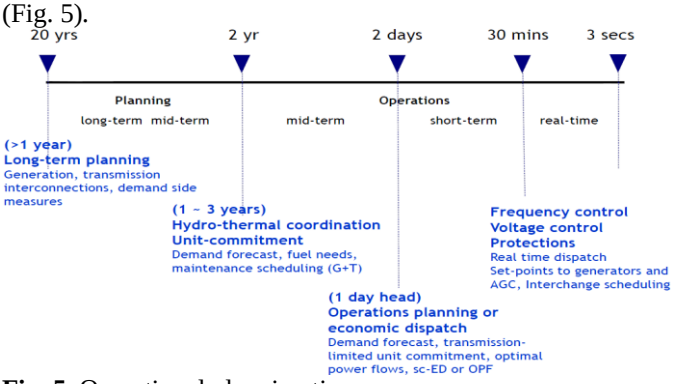

Fig. 5. Operational planning time zone

Economic Dispatch (ED) and Unit Commitment (UC) are two main tasks in this time horizon. In a shorter time scale (maybe a few minutes to 1 hour), economic dispatch is the main task for power system operational planning where the time horizon is less than generation unit start-up and shut-down times. The main focus of the current paper is in this time horizon to introduce the suitable index for power system flexibility evaluation.

Dependency to operation point is the main requirement for power system flexibility indices in the operational flexibility evaluation with respect to the planning evaluation horizon. This approach can be seen in the LORP index in Fig.4. Where the ability of the generation system to respond to net load uncertainty directly depends on the current system generation point.

In the next part the well-known flexibility index, which is mainly used for power system planning horizon is described and then this approach is modified for operational planning horizon by considering the current system generation point as the main requirement of the flexibility index in this time horizon.

4. Normalized Flexibility Index (NFI)

NFI is a well-known flexibility index mainly used for the evaluation of power system flexibility in planning time horizons [13]. This index is defined for one generation unit as:

$$flex(i) = \frac{0.5\left(P_{max}(i) - P_{min}(\mathrm{i})\right) + 0.5Ramp(i)\Delta t}{P_{max}(i)} \qquad (2)$$

P_{min}, P_{max} are the minimum and maximum bounds of the unit generation and Ramp in the mean of up/down generation ramp rate. Δt is the desired time interval for system generation response to the uncertainty and variability caused by the different factors. The high value of the unit flexibility index shows more capability to withstand uncertainty and variability in both the generation and demand sides. In the current paper, (2) is rewritten as (3) to define two items of the flexibility index.

$$flex(i) = \frac{0.5\left(P_{max}(i) - P_{min}(\mathrm{i})\right)}{P_{max}(i)} + \frac{0.5Ramp(i)\Delta t}{P_{max}(i)} \qquad (3)$$

The first item shows the capacity of the unit generation, the main capability to overcome generation/load uncertainty. This is the same parameter (π) mentioned in part 2. On the other hand, the second item shows the capability of the generation unit to withstand generation/load variability. Here the two parameters as (ρ) and (δ) are considered to form the second item. So, three parameters (π), (ρ) and (δ) are used to form this index.

The generation system flexibility index can be determined by combining all the generation unit indices. In this way all of these indices are combined by their generation capacities as the weighting factors [13]:

$$FLEX = \frac{\sum_{i=1}^{n} flex(i)P_{max}(i)}{\sum_{i=1}^{n} P_{max}(i)} \qquad (4)$$

So, the generation units with the higher generation capacity have more effect on the system flexibility index. As said before, this index is used for flexibility evaluation in the planning time horizon. But there are serious criticisms of using this approach for operation flexibility evaluation, mainly because of no appearance of the current operation point of the generation units in (2). The main challenges to using (2) and (4) for operational planning purposes can be summarized as below:

1-As can be seen, the flexibility index is independent of the current generation unit/generation system operation point. So, the current generation point has no effect on the flexibility index.

2-The ramp rate capability may be limited because of the up/down unit generation constraints. When the current generation point (P_g) is near the maximum or minimum boundaries, it may limit the ramp rate capability. As is shown in Fig. 6, if Rampup $\Delta t>(P_{max}-P_g)$ or Rampdn $\Delta t>(P_g-P_{min})$, $P_{max}-P_g$ or P_g-P_{min} should be considered as the boundaries of the generation ramp capability (dotted red/green lines respectively).

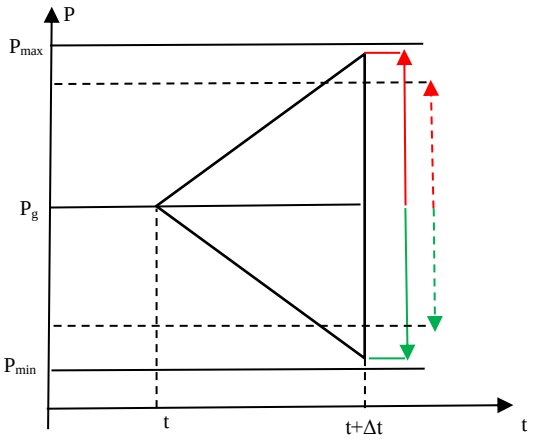

Fig. 6. Proposed flexibility index concept

3- The weighting factors of the two items in (3) are equal which has no acceptable reason.

Now in the next part, the contribution of this paper to extend NFI definition for use in power system operational planning is described. The main modification is to involve the current generation point to show the effect of the unit generation situation in the flexibility index.

5. NFI improvement for operational planning

As said before, the main approach in NFI modification is to consider the generation operation point in the flexibility index. This concept yields to combining the two items in the flexibility formulation described by (3). By considering $P_g(i)$ as the operation point of the generator (i) at the time (t), the generation point is bounded by $P_g(i)$+RampupΔt and $P_g(i)$-RampdnΔt in the time (t+Δt) which are shown by solid red/green lines in Fig. 6. But if $P_g(i)$+RampupΔt is more than $P_{max}(i)$, the upbound is limited to $P_{max}(i)$. Also, if $P_g(i)$-RampupΔt is less than $P_{min}(i)$, the downbound is limited to $P_{min}(i)$. In this case, the up/down bounds of the generator operation points are shown as the dotted red/green lines in Fig. 6.

By this approach, the modification of (3) to deal with the current generation point is shown by (5).

$$flex(i) = \min(Rampup(i)\Delta t, \left(P_{max}(i) - P_g(i)\right) + \min(Rampdn(i)\Delta t, (P_g(i) - P_{min}(i)) \quad (5)$$

Here the two up/down bounds of the generator operation point in time (t+Δt)) are considered as the first and the second items. So, the two characteristics as system generation capacity (π) and system ramp up/down (ρ) are combined together, eliminating the weighting factors in (3). Also, the up capacity/ramp and down capacity/ramp are separated to show the ability of the generation unit in each of the two directions. As can be seen, dividing by the generation capacity ($P_{max}(i)$) is ignored in the new formulation. The reason will be illustrated later. Now the two items of (5) can be separated and called up/down flexibility components of the flexibility index.

$$Up\_Comp(i) = \min(Rampup(i)\Delta t, \left(P_{max}(i) - P_g(i)\right) \quad (6)$$

$$Dn\_Comp(i) = \min(Rampdn(i)\Delta t, (P_g(i) - P_{min}(i)) \quad (7)$$

The up/down components are very meaningful and useful concepts that show the ability of the generation unit to cope with the net load uncertainty and variability in up and down directions respectively.

In the next step, the combination of the generator flexibility indices is described to calculate the system generation flexibility index. As can be seen in (3) and (4), $P_{max}(i)$ is in the denominator. On the other hand, in (4) flex(i) is multiplied by $P_{max}(i)$ again. Clearly, we can eliminate $P_{max}(i)$ both in (3) and (4). So, no need to divide (5), (6) and (7) by $P_{max}(i)$ and also again multiply by $P_{max}(i)$. In this way the combination of generator flexibility index can be simply derived as:

$$FLEX = \frac{\sum_{i=1}^{n} flex(i)}{\sum_{i=1}^{n} P_{max}(i)} \quad (8)$$

As the denominator of (4) is fixed for the system generation, it can be ignored in the system flexibility index calculation and the final generation flexibility index is written as:

$$FLEX = \sum_{i=1}^{n} flex(i) \quad (9)$$

Clearly, the up/down components of the system flexibility can be found in a combination of up/down components of the generation unit indices respectively.

$$FLEX\_UP = \sum_{i=1}^{n} Up\_Comp(i) \quad (10)$$

$$FLEX\_DN = \sum_{i=1}^{n} Dn\_Comp(i) \quad (11)$$

Where FLEX_UP and FLEX_DN are the up/down components of the system flexibility index.

6. Physical concept of the proposed index

Here the physical concept of (6), (10) and also (7), (11) is described. If we start from (10), it can be converted to:

$$\text{FLEX\_UP} = \sum_{i=1}^{n} \min(Rampup(i)\Delta t, \left(P_{max}(i) - P_g(i)\right) \quad (12)$$

$$\text{FLEX\_UP} = \sum_{i=1}^{n} \min\left(Rampup(i)\Delta t + P_g(i), P_{max}(i)\right) - \sum_{i=1}^{n} P_g(i) \quad (13)$$

$$\text{FLEX\_UP} = \sum_{i=1}^{n} Up\_limit(i) - \sum_{i=1}^{n} P_g(i) \quad (14)$$

Up_limit(i) is the maximum admissible operation point for generator (i) at the time (t+Δt) (the solid/dotted red line in Fig. 6).

$$\text{FLEX\_UP} = \sum_{i=1}^{n} [Up\_limit(i) - P_g(i)] \quad (15)$$

So, the difference between Up_limit(i) and $P_g(i)$ can be considered as the upward generation reserve at the time (t+Δt).

$$\text{FLEX\_UP} = \sum_{i=1}^{n} Up\_Reserve(i) = UP\_RESERVE \quad (16)$$

If we follow the same procedure for (11), the downward reserve can be defined and (17) and (18) are modified for flexibility down component correspondingly.

$$\text{FLEX\_DN} = \sum_{i=1}^{n} [P_g(i) - Dn\_limit(i)] \quad (17)$$

$$\text{FLEX\_DN} = \sum_{i=1}^{n} Dn\_Reserve(i) = DN\_RESERVE \quad (18)$$

So, the up component of the system flexibility index can stand for the upward reserve of the generation system where the down component shows the downward reserve. It establishes a suitable relation between the flexibility index especially its two components and the accessible system reserve mainly upward/downward reserve.

7. Simulation

In this part 30 bus IEEE test system is used for simulation. This test system has six generation units. The generation data and daily load curve data are presented in Tables I & II in the appendix. The network loss coefficients are mentioned in the appendix too.

By the assumption all the units are in operation in the daily time interval, the unit commitment (economic load dispatch) solution for 24 hours is done. Fig. 7. shows the variation of total generation and the system generation maximum and minimum boundaries.

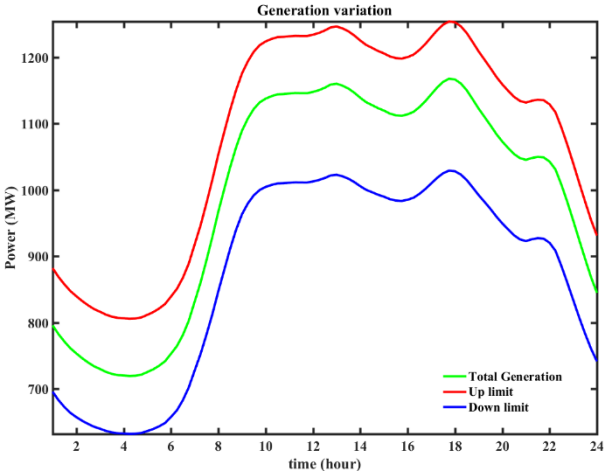

Fig.7. System generation, up/down constraints

When the total generation approaches the upper system generation limit, the system up reserve goes smaller. On the other hand, when the total generation approaches the downer system generation limit, less system down reserve is expected.

Fig. 8 shows the variation of the up/down components of the system flexibility index and also up/down system generation reserve. As can be seen, the up component of the flexibility index is the same as the generation up reserve. On the other hand, the down component of the flexibility index is the same as the system generation downward reserve. This is another reason for not dividing (5), (6) and (7) by $P_{max}(i)$ and also it needs to eliminate $\Sigma P_{max}(i)$ in (9), (10) and (11).

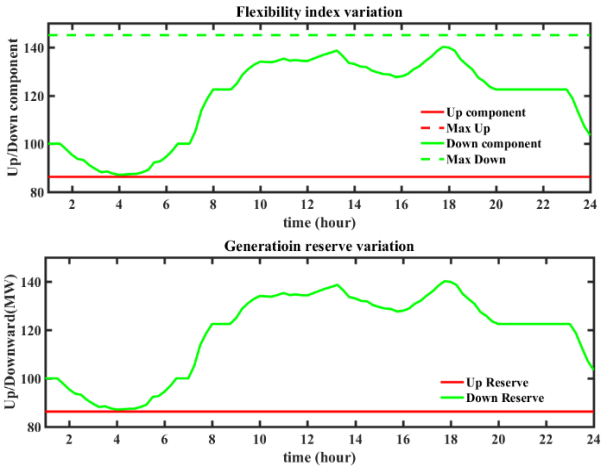

Fig.8. Up/down flexibility and system reserve

It is important the up component of the flexibility index lies on its maximum value with no change. This shows the maximum ability of the system generation exists to cope with the net load uncertainty and variability in the upward direction. But the down component varies in the daily time interval.

To show the variation of the flexibility index up component, the daily load curve is increased by 1.3125. Where the peak load is more than system generation capacity. So, it is expected load shedding in the peak load duration. Fig. 9. and Fig. 10. are similar to Fig. 7. and Fig. 8 correspondingly.

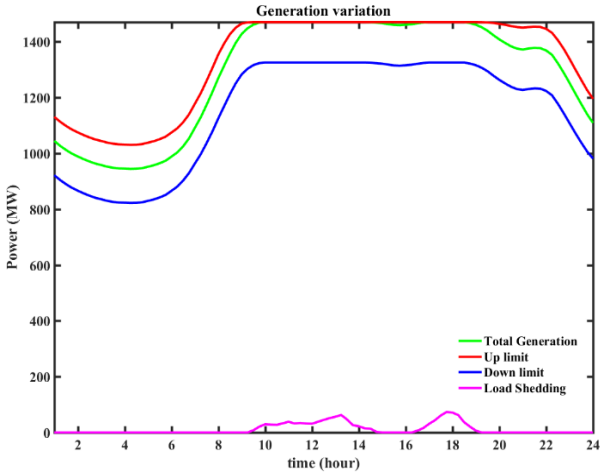

Fig. 9. System generation, up/down reserve and load shedding

As can be seen, the load shedding is forced into the system where the load plus system loss is more than system capacity. In contrast to the previous case, the downer component of the flexibility index lies in its maximum value in the large part of the load curve. But the up component goes down because of the considerable decrease in upward reserve and it lies zero when load shedding is forced into the system.

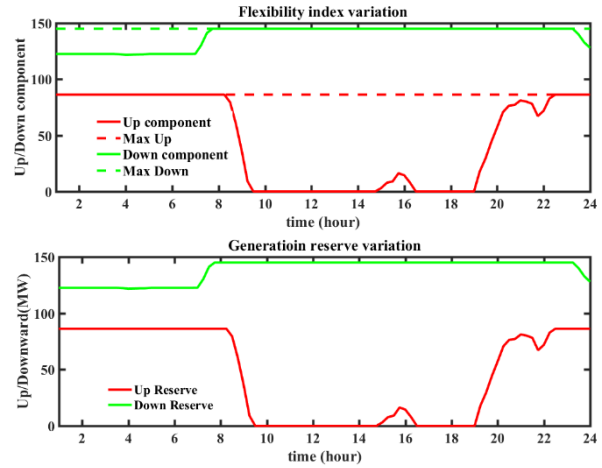

Fig. 10. Up/down flexibility and system reserve

8. Conclusion

Renewable energy integration is a main challenge for the power system flexibility, especially in the operational planning time zone. The current paper proposes an extension of the Normalized Flexibility Index (NFI) by considering the operation point of the generation unit/generation system as the main requirement of the flexibility index for use in the operation planning time zone. The proposed index has a direct relation to system generation reserve and can be converted to an economic value easily. This economic value can be combined with other system operation costs to find the optimal operation point considering the best level of the power system flexibility. It will be used to find the best penetration factor of the renewable energy sources or the best amount of the energy storage capacity in the power system

integrated by the renewable sources such as large scale wind and solar farms.

9. References

[1] "Flexibility in the Power System – Danish and European experiences", Danish Energy Agency, 2015
[2] "Harnessing Variable Renewables", Tech. rep., International Energy Agency (IEA), Paris, 2011
[3] "Flexibility and Aggregation Requirements for their Interaction in the Market", Euroelectric, aisbl, Brussels, 2014
[4] H. Berahmandpour, Sh. Montasar Kouhsari, H. Rastegar, "A New Power System Operational Planning Flexibility Index Development", 33th Power system Conference (PSC), Tehran, Iran, 2018 (in Persian)
[5] E. Lannoye, D. Flynn and M. O'Malley, "Evaluation of Power System Flexibility" IEEE Transactions on Power Systems, vol. 27, no. 2, pp. 922-931, May 2012
[6] E. Lannoye, D. Flynn and M. O'Malley, "Power System Flexibility Assessment — State of the Art" 2012 IEEE Power and Energy Society General Meeting, pp. 1-6, 2012
[7] A. Ulbig, "Operational Flexibility in Electric Power Systems," A thesis submitted to the degree of Doctor of Science of ETH Zurich, 2014.
[8] A. A. Thatte, L. Xie, "A Metric and Market Construct of Inter-temporal Flexibility in Time-coupled Economic Dispatch", IEEE Trans. Power Syst. 31 (5), pp. 3437–3446, 2015.
[9] C. G Min and M. K. Kim, "Flexibility-based Evaluation of Variable Generation Acceptability in Korean Power System", Energies, vol. 10, no. 6, 825, 2017.
[10] C. G. Min, J. K. Park, D. Hur, and M. K. Kim, "A Risk Evaluation Method for Ramping Capability Shortage in Power Systems", Energy, vol. 113, pp. 1316–1324, 2016.
[11] C.-G. Min, "Analyzing the Impact of Variability and Uncertainty on Power System Flexibility", Appl. Sci. vol. 9, no. 3, pp. 1–13, 2019.
[12] A. Ulbig and G. Andersson, "On Operational Flexibility in Power Systems", 2012 IEEE Power and Energy Society General Meeting, pp. 1-8, 2012
[13] J. Ma, V. Silva, R. Belhomme, D. S. Kirschen and L. F. Ochoa, "Exploring the Use of Flexibility Indices in Low Carbon Power Systems", 2012 3rd IEEE PES Innovative Smart Grid Technologies Europe (ISGT Europe), pp. 1–5, 2012

10. Appendix

a):Test system data

Table I. Generation data

Unit No.	P_{min}(MW)	P_{max}(MW)	Rampup(MW/h)	Rampdn(MW/h)	a ($/MW^2)	b ($/MW)	c ($)
1	100	500	120	80	0.0070	7.0000	240
2	50	200	90	50	0.0095	10.0000	200
3	80	300	100	65	0.0090	8.5000	220
4	50	150	90	50	0.0090	11.0000	200
5	50	200	90	50	0.0080	10.5000	220
6	50	120	90	50	0.0075	12.0000	190

Table II. Daily load data (MW)

Time	**Load**	Time	**Load**	Time	**Load**	Time	**Load**	Time	**Load**	Time	**Load**	Time	**Load**	Time	**Load**
00.00	**839.2**	03.00	**722.4**	06.00	**756.4**	09.00	**1113.1**	12.00	**1149.0**	15.00	**1114.1**	18.00	**1167.3**	21.00	**1041.8**
00.15	**826.2**	03.15	**723.6**	06.15	**782.4**	09.15	**1126.1**	12.15	**1154.3**	15.15	**1113.1**	18.15	**1147.8**	21.15	**1046.4**
00.30	**806.7**	03.30	**720.2**	06.30	**796.1**	09.30	**1135.8**	12.30	**1159.1**	15.30	**1107.6**	18.30	**1135.8**	21.30	**1063.3**
00.45	**793.5**	03.45	**718.3**	06.45	**822.9**	09.45	**1142.5**	12.45	**1163.0**	15.45	**1109.0**	18.45	**1124.9**	21.45	**1057.0**
01.00	**780.7**	04.00	**718.8**	07.00	**854.7**	10.00	**1141.6**	13.00	**1167.8**	16.00	**1114.1**	19.00	**1106.4**	22.00	**1035.6**
01.15	**770.3**	04.15	**719.5**	07.15	**900.4**	10.15	**1141.1**	13.15	**1155.3**	16.15	**1124.9**	19.15	**1097.5**	22.15	**1010.5**
01.30	**759.8**	04.30	**719.8**	07.30	**926.4**	10.30	**1144.9**	13.30	**1139.9**	16.30	**1131.9**	19.30	**1084.9**	22.30	**986.7**
01.45	**750.6**	04.45	**722.4**	07.45	**964.5**	10.45	**1149.3**	13.45	**1137.0**	16.45	**1143.5**	19.45	**1072.7**	22.45	**948.4**
02.00	**743.9**	05.00	**726.3**	08.00	**999.9**	11.00	**1144.7**	14.00	**1131.4**	17.00	**1153.4**	20.00	**1058.9**	23.00	**927.2**
02.15	**741.9**	05.15	**738.3**	08.15	**1043.5**	11.15	**1145.9**	14.15	**1130.2**	17.15	**1166.4**	20.15	**1049.8**	23.15	**895.4**
02.30	**733.7**	05.30	**740.0**	08.30	**1070.0**	11.30	**1144.4**	14.30	**1121.8**	17.30	**1176.0**	20.30	**1048.6**	23.30	**865.3**
02.45	**727.7**	05.45	**747.0**	08.45	**1092.4**	11.45	**1144.0**	14.45	**1117.7**	17.45	**1174.3**	20.45	**1039.4**	23.45	**844.8**

b) Loss coefficient matrix

$Loss=P^tBP+B_0P+B_{00}$

b-1) B matrix

0.0017	0.0012	0.0007	-0.0001	-0.0005	-0.0002
0.0012	0.0014	0.0009	0.0001	-0.0006	-0.0001
0.0007	0.0009	0.0031	0.0000	-0.0010	-0.0006
-0.0001	0.0001	0.0000	0.0024	-0.0006	-0.0008
-0.0005	-0.0006	-0.0010	-0.0006	0.0129	-0.0002
-0.0002	-0.0001	-0.0006	-0.0008	-0.0002	0.0150

b-2) B_0 vector

-0.3908	-0.1297	0.7047	0.0591	0.2161	-0.6635

b-3) B_{00} constant

$B_{00}=0.056$

International Journal of Research and Technology in Electrical Industry

journal homepage: ijrtei.sbu.ac.ir

Shahid Beheshti University

Reliability Enhancement by Strategic Placement of Remotely-Controlled Automation Devices: A Case Study on Tabriz Distribution Network

Arya Abdolahi[1,*], Rahim Ajabi Farshbaf[1], Abolfazl Abbaspour[1], Mohammad Khodayari[1]

[1] *Tabriz Electrical Distribution Company, Tabriz, Iran*

ARTICLEINFO

Article history:
Received 27 November 2021
Received in revised form 08 March 2022
Accepted 19 March 2022

Keywords:
Distribution automation
Modified NSGA-II
Reliability
RCS placement
Distribution system operation

ABSTRACT

Achieving high distribution-reliability levels and concurrently minimizing operating costs are as the main issues in distribution system optimization. Determination of the optimal number and location of remote control switches (RCS) in the distribution system network is an essential issue from the reliability and economic points of view. To address these issues, this paper develops a novel multiobjective model from the distribution system viewpoint, wherein the primary objective, optimal RCS placement is implemented aiming at minimizing the operating costs, while in the second objective, the reliability index improvement is taken into account. So, a novel approach from a robust heuristic algorithm, modified non dominated sorting genetic algorithm (MNSGA-II), is developed and presented to solve this multiobjective mixed-integer non-linear programming problem. Simulation results received by the genetic algorithm have been compared with the other popular optimization algorithms, seperately. Results show that the proposed algorithm provides extensively the best performance, in terms of quality of the answer received and computational efficiency. The feasibility of the proposed algorithm was examined by application to two distribution feeders of the Tabriz city distribution network containing the fourth feeder of the TractorSazai substation.

Nomenclature

F_1	RCS placement cost function
DS_i	Decision variable related to the installation or non-installation of RCS devices at the candidate site
CS	Cost of a RCS
n	Number of candidate locations for RCS installation
DT_j	Decision variable related to the construction or non-construction of maneuver point at the candidate site j
CT_j	Cost of the maneuver point construction on the candidate site j
m	Number of candidate locations for maneuver point construction
MC	Cost of equipment maintenance and operation
P_w	Economic factor to convert current costs of the study horizon to the current costs
Infr	Annual inflation rate
Intr	Annual interest rate
ny	Study horizon by year
ENS_T	Total energy not supply
ENS_i	Energy not supply in the distribution post i

* Corresponding author
E-mail address: a.abdollahi@azaruniv.ac.ir
http://dx.doi.org/ 10.52547/ijrtei.1.1.36

IC_i	Average cost of blackout in the distribution post *i*
K_i	Demand importance factor of *i*th post
nLP	Number of distribution points on the feeder
$AIC_i(.)$	Blackout cost
P_i	The percentage of each load in distribution post *i*
λ_i	Failure rate in *i*th mode
r_i	Repair rate
P	Average consumption at the load point
η_c	Crossover index
η_m	Mutation index
V_i	Voltage of the *i*th load point
I_i	Current of the *i*th load point
f_{i-1}^{k}	*k*th objective of the (*i-1*)th individual
f_{i+1}^{k}	*k*th objective of the (*i+1*)th individual
r	Iteration number
$x_i^{(1,t+1)}$ $x_i^{(2,t+1)}$	Offspring solutions
$x_i^{(1,t)}$ $x_i^{(1,t)}$	Parent solutions
u_i	Random number between 0 and 1
δ_i	Polynomial probability distribution
υ_i	Variance of crowding distance

1. Introduction

The issues and challenges in the distribution network are currently one of the most pressing concerns in the energy area, attracting the attention of all operation professionals. High power losses, voltage drops, and power interruptions are these problems, for which the installation of distribution automation devices is a crucial solution, given the enormous amount of investment and the requirement for optimal operation in this type of network. The network's end-consumers desire to get high-quality power with no disruptions. As a result, the distribution network's functioning is guided by the following two key ideas. 1) Consistency in delivering customer service 2) Keeping a high level of service quality. Due to the expanse of Tabriz city distribution network, the requirement for appropriate installation and placement of distribution network automation equipment is becoming increasingly apparent. The goal of distribution system automation is to reduce the amount of total power loss, energy not supply (ENS), the staff salaries, and the time it needs to discover faults. Aside from the technical benefits, the automation of distribution networks has economic profitability that is dependent on the optimum selection of the function [1], [2].

A reactive tabu search optimization technique is used in [3] to find the best locations for automation devices. The proposed strategy is considered the cost of long-term interruptions, automation equipment's purchase, and maintenance in the objective function. The author in [4] is studied a novel objective containing the cost of long-term interruptions and automation of distribution systems. To solve the suggested mixed-integer non-linear programming problem, the author is proposed a modified particle swarm optimization technique. The heuristic combinatory search technique developed in [5] decomposes the overall automation issue involving numerous types of automation devices into a series of simple sub-problems involving a single type of device. It specifies a set of heuristic criteria for determining the position of single feeding devices. The expense of long-term interruption and the cost of automation equipment is taken into account. In [6], from the metaheuristic algorithms, a genetic algorithm is selected in this paper to solve the optimal sectionalizing switches and reclosers placement problem. The dependability indices are optimized using this method, which takes into consideration the cost of automation equipment.

A long-term switch placement problem is presented in [7], considering load forecasting. The problem modeled as mixed-integer linear programming (MILP) formulation to include long-term load forecasting results obtained using the historical load data. A two-stage optimization algorithm is proposed in [8] to find the optimal number and place of automatic switches in the presented distribution network. In the first stage, the greedy optimization algorithm is applied to solve the restoration problem in the presence of contingencies. In the second stage, a cost function containing the ECOST and annual automatic switches cost is modeled and minimized due to the chosen locations of switches. An optimal distributed generation-based sectionalizing switches placement is investigated in [9] for distribution networks. The proposed problem is modeled as a mixed-integer non-linear programming (MINLP) problem and contains the cost of short-term outages and automation equipment. Optimal switch placement in the Ahvaz city distribution network is proposed in [10], in which the genetic algorithm is used to enhance the grid reliability. A model introduces in [11] to find the optimal number and location of automation devices. The presented model takes the benefit of MIP formulation making contributions to solving this extensive problem in an efficient run time and ensures the global optimum solution. The goal of this model is to minimize the total interruption and equipment costs.

Although valuable works have been done in the field of the optimal switch placement, but there are still many problems and deficiencies that need to be addressed properly. Briefly, the shortcomings of previous references are as follows:

a) The determination of the number and location of only one type of switch, mainly sectionalizes, is taken into account.

b) In the previously mentioned studies, switches are normally located in the predetermined positions in the feeders by default.

c) The calculation of operating cost function and the reliability service simultaneously in determining the best network automation solution is not addressed.

To address the shortcomings and drawbacks of previous literature, this paper attempts to provide the following contributions. The objective of this paper is to solve a multiobjective function in order to find compromised solutions both to enhance the reliability by optimal allocation of remote control switches (RCS) and minimize the total operating costs. In most of the prior works, where the optimal placement of switches has been considered, the number of RCS has been taken as fixed. In some literature where the number of RCS has been considered as a variable, multiobjective problem formulation has not been considered. In the present paper, both the number and location of RCS have been considered as variable, and a multiobjective function has been formulated. This paper develops a multiobjective model, wherein the primary objective, optimal

RCS is implemented to minimize the total operating costs, while in the second objective, the reliability improvement is taken into account. A novel modified non dominated sorting genetic algorithm (MNSGA-II) is presented in this paper to reach the optimum global solutions. The MNSGA-II achieves solutions to the RCS placement problem instead of a single solution. This makes the proposed solution more adaptable to different utilities' circumstances and eases the decision-making. The outcome of the proposed technique has been compared with well-established optimization techniques like particle swarm optimization (PSO), differential evolution (DE), ant colony optimization (ACO), and so on. The following is a quick summary of the paper's novelties and contribution:

❖ Applying a robust optimization algorithm like MNSGA-II to solve the proposed complicated MINLP multiobjective problem.

❖ Applying the large-scale and practical distribution test systems like the fourth feeder of the TractorSazi substation post.

❖ Developing a mathematical methodology based on MINLP to solve the suggested optimal RCS placement problem for efficient reliability enhancement in distribution grids considering the cost of power losses, construction of maneuvering points, installation of RCSs, and maintenance and operation.

The mathematical formulation of the suggested problem is described in Section 2. The backward-forward sweep-based method is explained in Section 3. Section 4 provides an overview of the MNSGA-II. Section 5 contains the simulation results and discussion. The conclusion is summarized in Section VI.

2. Problem formulation

The suggested method applies a multiobjective mathematical programming paradigm with two competing goals: 1) minimizing the cost of RCS deployment and 2) improving the service reliability (reducing the amount of ENS index). The primary objective is to keep the cost of sectionalizing RCSs as low as possible. To measure service reliability, the energy not supplied index is used.

2.1. First objective: RCS placement cost function

The following costs are involved in RCS placement and their locations design in distribution networks: i) Damages caused by not supplying energy to customers; ii) Costs related to the RCS construction, including price and installation cost; iii) Costs related to the RCS location, including RCS and line price, and iv) Cost of equipment maintenance and operation. In this case, the goal is to minimize the sum of these costs. Of course, it should be noted that some of these costs (items ii and iii) are in the form of initial investment, but items (i and iv) are in the form of current costs, and in combining these two categories into a single cost function, Using the parameters of engineering economics, all costs are converted into a template.

$$\text{Min } F_1 = \left\{ \begin{array}{l} \sum_{i=1}^{n} DS_i \times CS + \sum_{j=1}^{m} DT_j \times CT_j \\ + \sum_{t=1}^{ny} P_W^t \times MC + \sum_{l=1}^{L} P_{Loss}^t \times K_{Loss} \end{array} \right\} \quad (1)$$

$$P_W = \frac{1+\text{Infr}}{1+\text{Intr}} \quad (2)$$

2.2. Second objective: Energy not supply function

In this paper, reliability studies based on the analytical method are performed. The analytical method evaluates reliability based on failure mode and effect analysis. At first, the failure modes that affect each load point (distribution posts) are identified. Then, by evaluating their effect, the reliability index (ENS) is calculated in each load point. In this calculation, the impact of RCSs and their locations for fault separation, and the possibility of supplying load points through support communication lines are considered. The amount of ENS related to domestic and industrial consumers plays a crucial role in distribution system automation. Equation (6) shows the consequences of energy not supply function in distribution networks.

$$\text{Min } F_2 = \sum_{i=1}^{nLP} ENS_T = \sum_{i=1}^{nLP} IC_i \times ENS_i \times K_i \quad (3)$$

$$IC_i = \left\{ \begin{array}{l} AIC_i(\text{res}).P_i(\text{res}) + AIC_i(\text{com}).P_i(\text{com}) \\ + AIC_i(\text{ind}).P_i(\text{ind}) + AIC_i(\text{agr}).P_i(\text{agr}) \\ + AIC_i(\text{gen}).P_i(\text{gen}) \end{array} \right\} \quad (4)$$

$$\lambda_s = \sum_{i \in A} \lambda_i \qquad (\text{f / yr}) \quad (5)$$

$$U_s = \sum_{i \in A} \lambda_i r_i \qquad (\text{h / yr}) \quad (6)$$

$$r_s = \frac{U_s}{\lambda_s} \qquad (\text{h / f}) \quad (7)$$

$$ENS = PU_s \qquad (\text{kWh / yr}) \quad (8)$$

The average failure rate and average outage time are given in equations (8) and (9), respectively. Also, the annual average outage time and average ENS are presented as equations (10) and (11), respectively.

3. Backward-Forward sweep based algorithm

The backward sweep and the forward sweep are two phases of this procedure. Backward sweep calculates voltage and current from the farthest bus from the beginning bus, applying KVL and KCL rules. The downstream voltage starts from the beginning bus in the forward sweep. The bus-branch information is used as the algorithm's input data. The active and reactive power flows for sending and receiving buses, impedance, and susceptance of all branches are essential basic information. The significant steps of the suggested algorithm are listed as follows: [12], [13].

1) Assume rated voltages at end nodes only for first iteration and equals the value computed in the forward sweep in the subsequent iteration.

2) Start with the end node and compute the node currently. Apply the KCL to determine the current flowing from node *i*-1 towards node *i*.
3) Compute with this current the voltage at the *i*th node. Continue this step till the junction node is reached. At the junction node, the voltage computed is stored.
4) Start with another end node of the system and compute voltage and current as steps 2 and 3.
5) Compute with the most recent voltage at the junction node.
6) Similarly, compute till the reference node.
7) Compare the calculated magnitude of the rated voltage at the reference node with the specified source voltage.

$$I_i^t = \left(\frac{P_i + jQ_i}{V_i^{t-1}} \right)^* \tag{9}$$

$$I_{i-1,i}^t = I_i^t + \sum_k I_{i,k}^t \qquad k \geq i \tag{10}$$

$$V_i^t = V_{i-1}^{t-1} - \left(R_{i-1,i} + jX_{i-1,i} \right) I_{i-1,i}^t \tag{11}$$

Stop if the voltage difference is less than the specified criteria; otherwise, the forward sweep begins.

Forward Sweep:
1) Start with reference node at rated voltage.
2) Compute the node voltage in forward direction from the reference node to the end nodes.
3) Again start backward sweep with updated bus voltage calculated in forward sweep.

After calculating node voltages and line currents using a standard backward-forward sweep algorithm, the line losses are calculated.

4. Providing an Overview on MNSGA-II

Non-dominated sorting for fitness tasks is utilized by the MNSGA-II [14]. Both polynomial mutation and binary crossover produce different generations, and event choice is later employed to pick out the populace for the subsequent generation. Elitism resolves the trouble of dropping accurate answers for the duration of the optimization cycle because of chance impacts. One manner of coping with this issue is to join the old populace and the generation. The MNSGA-II with dynamic crowding distance (DCD) is utilized to tackle the suggested issue [15].

4.1. Simulated binary crossover (SBC)

In common, SBC places the strain on producing generation close to the parents. This crossover ensures that the volume of the youngsters or generation is equal to the parents' volume, and additionally supports that close to determine people are monotonically much more likely to be selected as youngsters than children remote from the parents with inside the answer space [16]. The process for detecting the generation answers $x_i^{(1,t+1)}$ and $x_i^{(2,t+1)}$ from parent answers $x_i^{(1,t)}$ and $x_i^{(2,t)}$ is presented as follows. u_i is a random number that is define between 0 and 1. Afterward, by using probability distribution function, the β_{qi} is obtained as equation (12):

$$\beta_{qi} = \begin{cases} (2u_i)^{1/\eta_c+1} & ,\text{if } u_i \leq 0.5; \\ \left(\frac{1}{2(1-u_i)}\right)^{1/\eta_c+1} & ,\text{otherwise.} \end{cases} \tag{12}$$

In equation (12), an indicator η_c is a positive number. Since finding β_{qi} , the children's answers are computed as equations (13) and (14):

$$x_i^{(1,t+1)} = 0.5\left[(1+\beta_{qi}) x_i^{(1,t)} + (1-\beta_{qi}) x_i^{(2,t)} \right] \tag{13}$$

$$x_i^{(1,t+1)} = 0.5\left[(1-\beta_{qi}) x_i^{(1,t)} + (1+\beta_{qi}) x_i^{(2,t)} \right] \tag{14}$$

The actions developed for the production of children are shortly addressed as below [17]:

Step 1: select a random number $u_i \in [0,1]$

Step 2: compute β_{qi} applying equation (12).

Step 3: a set of mutated parents $x_i^{(1,t)}$ and $x_i^{(2,t)}$ is chosen randomly to generate children's answers $x_i^{(1,t+1)}$ and $x_i^{(2,t+1)}$ by applying equations. (13) and (14).

4.2. Polynomial mutation

The possibility of making an answer close to the parents is better than making one remote from it. The form of the probability distribution is immediately managed via an outside parameter and stays constant at some stage in the iterations. Like withinside the SBC operator, the probability distribution also can be a polynomial function, in place of a normal distribution:

$$y_i^{(1,t+1)} = x_i^{(1,t+1)} + \left(x_i^{(U)} - x_i^{(L)} \right) \delta_i \tag{15}$$

Parameter δ is computed from the polynomial probability distribution

$$P(\delta_i) = 0.5(\eta_m + 1)(1 - |\delta|)^{\eta_m} \tag{16}$$

$$\delta_i = \begin{cases} (2r_i)^{1/\eta_m - 1} - 1 & ,\ if\ \ r_i < 0.5 \\ 1 - \left[2(1-r_i) \right]^{1/\eta_m + 1} & ,\ if\ \ r_i \geq 0.5 \end{cases} \tag{17}$$

For handling the bounded decision variables, the mutation operator is modified for two regions: $[x_i^{(L)}, x_i]$ and $[x_i, x_i^{(U)}]$.

4.3. Dynamic crowding distance (DCD)

In multiobjective evolutionary algorithms, the horizontal diversity of Pareto front is essential. The horizontal diversity is often realized by removing excess individuals in the non-dominated set (NDS) when the number of non-dominated

solutions exceeds population size. NSGA-II uses crowding distance (CD) measure as given in Eq. (18) to remove excess individuals. The individuals having lower values of CD are preferred to individuals with higher values of CD in the removal process.

$$CD_i = \frac{1}{r}\sum_{k=1}^{r}\left| f_{i+1}^{k} - f_{i-1}^{k} \right| \quad (18)$$

The main shortcoming of CD is the lack of uniform variety in the occupied non-dominated answers. To overcome this issue, the dynamic crowding distance (DCD) approach is newly proposed in [18]. In this method, one individual with the minimum DCD amount is deleted every time, and DCD is re-computed for the remaining individuals. The individual's DCD are computed as equation (19):

$$DCD_i = \frac{CD}{\log(1/\upsilon_i)} \quad (19)$$

where CDi is computed by equation (18) and V_i is based on equation (20),

$$\upsilon_i = \frac{1}{r}\sum_{k=1}^{r}\left(\left| f_{i+1}^{k} - f_{i-1}^{k} \right| - CD_i\right)^2 \quad (20)$$

v_i is the variation of CDs of individuals which are neighbors of the *i*th individual. V_i can provide data about the different variations of CD in various goals. Assume the population size is *N*, the non-dominated set at *t*th generation is *Q(t)*, and its size is *M*. If $M > N$, DCD-based strategy is utilized to delete $M-N$ individuals from the non-dominated set. The following steps can be adopted for the implementation of the MNSGA-II algorithm.

Step 1: Determine the variables for the suggested multi-objective problem.
Step 2: choose the amount of the parameters such as crossover, mutation, and population and generation number.
Step 3: produce the initial population.
Step 4: Assess the objective function for the primary population.
Step 5: Fix the generation number.
Step 6: Perform SBC crossover and polynomial mutation for the set of individuals.
Step 7: Perform non-dominated sorting.
Step 8: Calculate DCD.
Step 9: Perform selection based on tournament selection
Thereby a higher fitness is assigned to individuals located on a sparsely populated part of the front.
Step 10: Increment the generation count and repeat the steps from 6 to 9 until the count reaches the maximum number of generations.
To explain the summary of the proposed model and optimization algorithm, a flowchart is desired as figure 1.

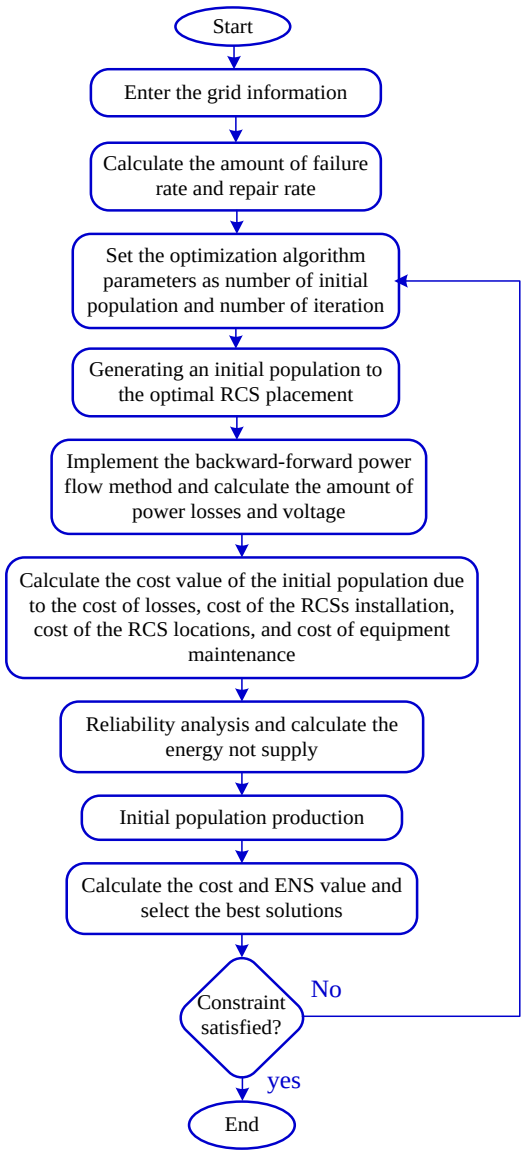

Fig. 1. The flowchart of the proposed method.

5. Simulation results and discussion

5.1. Case study

The suggested algorithm is used in a more complicated and effective system to investigate the model's applicability in actual conditions. The 4th feeder of TractorSazi substation from Tabriz city distribution network is shown in Fig. 2. It consists of 122 load points and there are 121 possible RCS locations in this system. The total load demand of this practical test system is 6.183 MW and 3.1 MVAR, respectively. The system is operated with the nominal bus voltage of 20 kV and 100 MVA base. The line and trans capacity data are given in Table IV. Also, the total length of the ground and overhead lines is 3.23 and 19.70 km, respectively. Moreover the consumption load data are presented in Fig. 3.

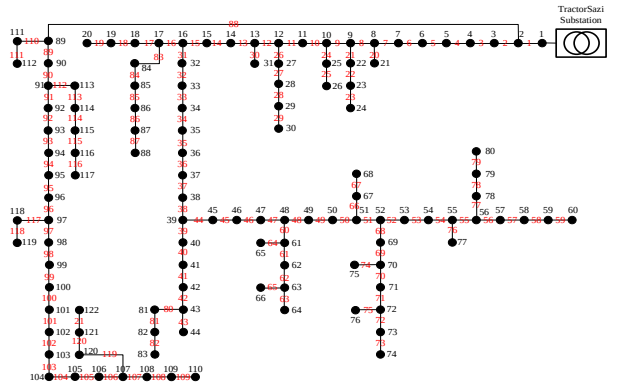

(a)

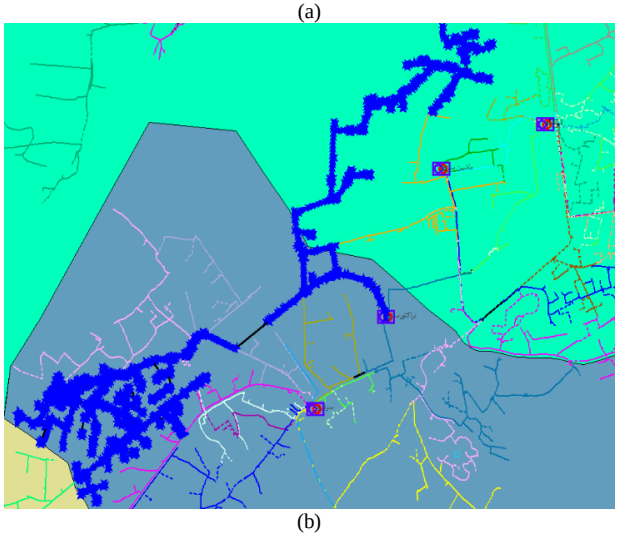

(b)

Fig. 2. 4th feeder of TractorSazi substation

There are some assumptions and modifications are applied to the fourth feeder of TractorSazi substation post.

1) The failure rate of all RCSs is assumed to be zero.
2) The proposed system is supplied only from the TractorSazi substation post.
3) The proposed feeder consists of both overhead and underground types.
4) From the viewpoint of providing the minimum level of protection in distribution systems, it is assumed that the main breaker feeder is installed before using the optimization method to optimally locate the RCSs.
5) Optimization algorithm is constrained to the limitation of (21) and (22)

$$V_i^{\min} < V_i < V_i^{\max} \quad (21)$$

$$I_i^{\min} < I_i < I_i^{\max} \quad (22)$$

The voltage limit $V^{\min}$ and $V^{\max}$ are assumed between 0.95 and 1.05 pu, respectively [19].

6) In this paper, the cost of each RCSs is supposed to be $ 4,700. The annual maintenance cost is 2% of the annual investment cost [20].
7) Average durations and number are presented in Table I [21].

Table I. Medium duration and number of proposed feeder

Failure	Average time (m)	Number
Unfavourable weather conditions	14	5
Bird encounter	45	12
Transient	5	6
Connecting in the cable of medium voltage	5	1
Replacement of defective bushings	72	1
Failure in cut-outs	55	5
Dealing with annoying trees	32	1
Problems in transformers	106	1
Problems in the insulator (plate, needle)	90	3
Failure in internal Pothead of Medium voltage	30	1
The network conductors collide with each other or with the body	41	2
Failure in Breakers	198	2
Unknown failure	20	12

8) The optimal RCS placement problem has been modeled and solved from the distribution system commission viewpoint.
9) The configuration of the proposed distribution network is assumed as a radial network, which is operating radially and not a closed-loop grid. So that, the RCSs are placed in such a way that the network does not lose its radial structure. Also, the protection relays are designed for the radial distribution network. If the RCSs places in such a way that the distribution network operates as a closed loop grid, the forecasted protection relays are acted and the feeder will be interrupted.
10) Since the proposed network type is considered as a distribution network, the R/X ratio is high and it can not use Newton-Raphson and Gauss-Seidel power flow methods. Therefore, in this paper, the sweet backward-forward power flow method is used.
11) The proposed model is a non-convex model and for this reason a meta-heuristic algorithm is used to solve this problem.

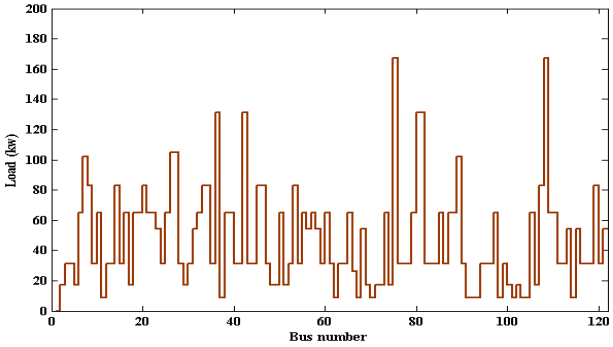

Fig. 3. Load curve of the suggested network

This article summarizes the steps, data collection, and implementation of simulation as follows:

Step 1: Obtaining the static data of the fourth feeder of TractorSazi substation from GIS containing the structure, load points, load data, and transformer types.
Step 2: Obtaining peak load information from the Tazarv software.
Step 3: Collect data related to medium voltage outages from the dispatching control center and events record software.
Step 4: Transfer network structure and data from GIS to MATLAB environment.
Step 5: Calculates the current flow of lines and voltage drop to implement the backward-forward power flow method.

Step 6: Find the best optimum global solutions using MNSGA-II.
Step 7: Print the results of minimum ENS and operating costs.

5.2. Simulation and numerical results

The results related to the first objective function are given in Table III. Because the suggested test system is a practical and large-scale system, it is obvious that the optimal positions for placing the RCSs are the critical points and main feeders. The outcomes achieved by using the suggested method show that the optimal positions for placing the RCSs are the critical points and main feeders containing the 3, 39, 44, and 88, proving the excellent performance of the MNSGA-II for this practical network. Figure 4 shows the ENS of the each section. The ENS of each section is calculated by using the objective function (6) and the MNSGA-II is used to minimizing the total amount of ENS in order to enhance the reliability service goals in the proposed distribution test system.

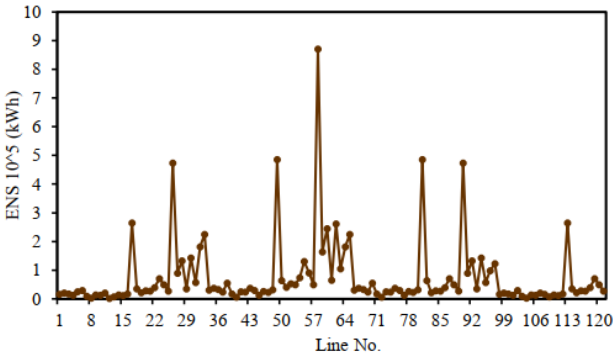

Fig. 4. Energy not supply

Figure 5 shows the voltage profile after and before applying the proposed method. As can be seen from this figure, after using proposed model the voltage magnitude of each node is significantly smooth in compare to the initial case. Figure 6 depicts the active power losses of the. It is clear that, employing the proposed multi-objective approach can be remarkably reduce the amount of power losses related to each line. Finally, these results deducted that optimal placement of remotely controlled automation devices have good impact on the system technical specification like voltage profile and total active power losses.

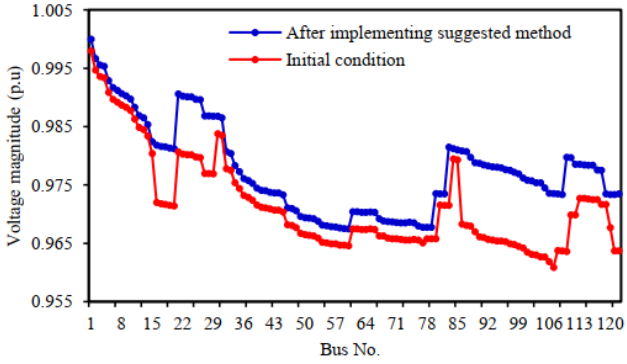

Fig. 5. Voltage profile after and before implementation of proposed model.

Table II shows the comparison of the real and optimal placement of RCSs in the proposed distribution system. This table declares that using a good performance with high convergence rate meta-heuristic algorithm like MNSGA-II has remarkably impact on the obtained results.

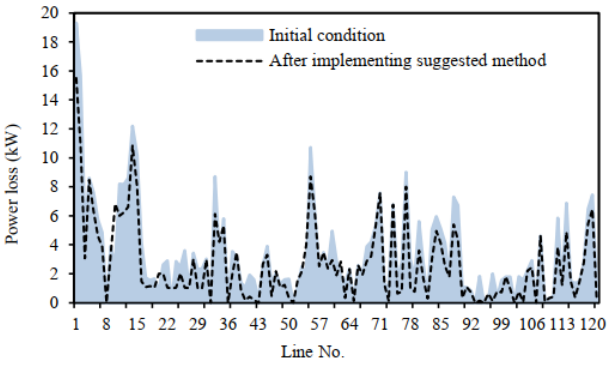

Fig. 6. Active power losses of the network.

So that, the minimum cost of switching equipment in optimal placement condition is reduced near to %79 of it's real and experimental placement condition. Also, the number of RCSs are decrease from 5 to 4 RCSs, which the proposed algorithm find the critical points of system according to the first objective function to locating these RCSs. Finally, the total ENS of the all section is reduced near to %23, which prove using MNSGA-II algorithm improve the reliability service of the distribution system. Table III presents the best results for the optimal switch placement obtained applying various methods. The best results related to optimal placement of automation devices with various methods are presented in Table III, and compared with each other by considering different elements. Regarding to this table, it is obvious that the proposed method had has more impact on the operating cost reduction and reliability service (energy not supply) improvement compared to other conventional methods.

Figure 7 displays the optimal Pareto curve obtained from MNSGA-II. All dominated members are eliminated, and non dominated members remain. The optimal solution is the blue square around it. This point is the best and optimum global solution, which is the minimum amount of operating cost and average ENS of all sections have been achieved.

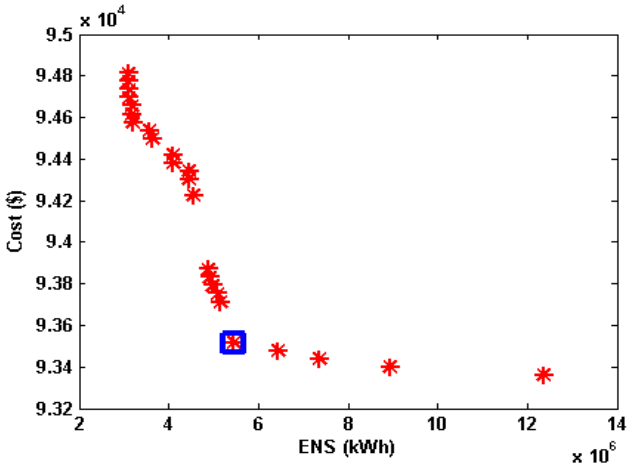

Fig. 7. Pareto curve of the proposed algorithm

This paper introduces a model for the optimal placement of the active distribution network. This model has been solved by the MNSGA-II algorithm to reach the optimum global solutions. Fig. 8 shows the convergence characteristic of the

RCS cost function. Due to Fig. 8, the first objective function (optimal placement of RCS) has been run in 100 iterations, and the amount of the objective function at every iteration has been depicted. The best optimum solution is obtained at iteration 46. Moreover, in this figure, the GA efficiency in comparison with other popular meta heuristic algorithms like PSO, GWO, DE, ABS, and ACO has been shown. It is clear the convergence rate and speed of the proposed algorithm are higher than other optimization algorithms. Fig. 9 shows the convergence curve of the second objective function (ENS function). Due to Fig. 9, the second objective function has been run in 100 iterations, and best optimum solution is obtained at iteration 49.

Table II. Comparison of the real and optimal placement of RCSs in the proposed distribution network

Item	Real and experimental placement condition (current condition)	Optimal placement condition using MNSGA-II
Minimum cost of switching equipment	116896.1938 ($/yr)	93516.9551 ($/yr)
Number of RCSs	5	4
RCS placement	S9, S22, S50, S88, S97	S3, S39, S44, S88
Total ENS	7055804.3384 (kWh)	5454100.5079 (kWh)

Table III. Best results for the optimal switch placement obtained applying various methods

Ref.	Proposed method	Test case	Type of automation device	Optimal device No.	ENS reduction (%)	Total cost ($)
[22]	Mixed integer linear programming	38 bus DN	Sectionalizing switch, fault passage indicator and Recloser	23	---	% 19.8
[23]	Fuzzy multiobjective model	23 bus DN	Sectionalizing switch	12	% 18.57	% 7.2
[24]	Multiobjective optimization based	IEEE 123 bus DN	Manual switch	28	% 4.91	---
[25]	Multiobjective optimization based	118 bus DN	Remote control switch	16	% 8.08	% 16.93
[7]	Mixed integer linear programming	38 bus DN	Remote control switch	30	---	% 8.50
[8]	Two-level optimization	1069 bus DN	Upgraded automatic switch	5	% 13.86	% 16.08
This paper	**Suggested method**	**122 bus DN**	**Remote control switch**	**4**	**% 22.70**	**% 21**

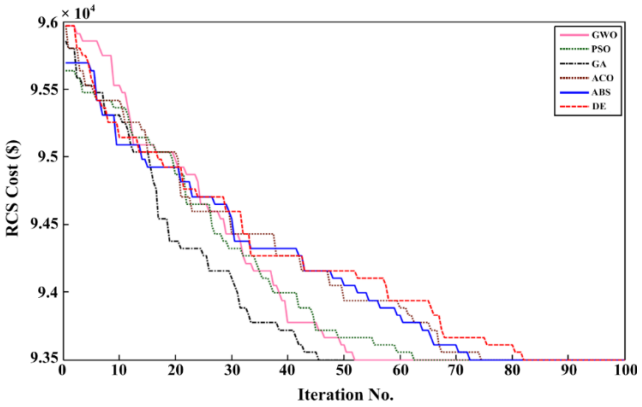

Fig. 8. Convergence curves of first objective function minimization.

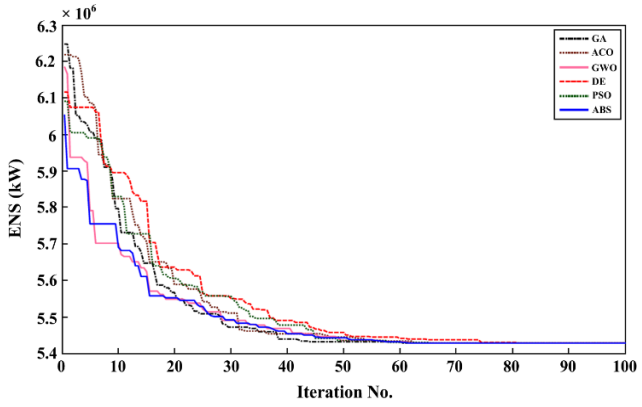

Fig. 9. Convergence curves of second objective function minimization.

6. Conclusion

This paper presents a new multiobjective model that includes two compromising goals: the cost of minimizing RCS placement and improving reliable service. The results showed that system reliability and total operating costs were significantly improved and reduced by optimizing RCS placement. The proposed approach is applied to a real distribution network, and the effectiveness of the MNSGA-II-based method for solving this MINLP problem is demonstrated through the obtained results. This work minimizes the RCS equipment cost to %79 of its real and experimental condition. Moreover, the amount of energy not supplied from reliability indices reduced to % 77.3 of its initial condition. Also, some system technical features such as voltage profile and total active power loss have been improved. Based on results, the following issues are achieved.

i. Optimal placement of RCS could minimize the operation costs of system and improve the reliability service.
ii. Multiobjective modelling was proposed to solve two compromising objectives simultaneously.
iii. Technical characteristics of the system such as voltage profile and power losses are improved.

7. References

[1] C. Smallwood and J. Wennermark, "Benefits of distribution automation," *IEEE Industry Applications Magazine*, vol. 1, no. 16, pp. 65-73, 2010.

[2] M. Murty and M. Rao, "Recent Trends in Automation of Distribution Systems: A Review," *IUP Journal of Electrical & Electronics Engineering*, vol. 14, no. 3, 2021.
[3] Bagheri, M. Bagheri, and A. Lorestani, "Optimal reconfiguration and DG integration in distribution networks considering switching actions costs using tabu search algorithm," *Journal of Ambient Intelligence and Humanized Computing*, vol. 12, no. 7, pp. 7837-7856, 2021.
[4] A. Shahbazian, A. Fereidunian, and S. D. Manshadi, "Optimal switch placement in distribution systems: A high-accuracy MILP formulation," *IEEE Transactions on Smart Grid*, vol. 11, no. 6, pp. 5009-5018, 2020.
[5] M. Elkadeem, M. Alaam, and A. M. Azmy, "Optimal automation level for reliability improvement and self-healing MV distribution networks," in *2016 Eighteenth International Middle East Power Systems Conference (MEPCON)*, 2016, pp. 206-213: IEEE.
[6] A. V. Pombo, J. Murta-Pina, and V. F. Pires, "A multiobjective placement of switching devices in distribution networks incorporating distributed energy resources," *Electric Power Systems Research*, vol. 130, pp. 34-45, 2016.
[7] J. Forcan and M. Forcan, "Optimal placement of remote-controlled switches in distribution networks considering load forecasting," *Sustainable Energy, Grids and Networks*, p. 100600, 2022.
[8] M. Isapour Chehardeh and C. J. Hatziadoniu, "Optimal placement of remote-controlled switches in distribution networks in the presence of distributed generators," *Energies*, vol. 12, no. 6, p. 1025, 2019.
[9] A. Heidari et al., "Reliability optimization of automated distribution networks with probability customer interruption cost model in the presence of DG units," *IEEE Transactions on Smart Grid*, vol. 8, no. 1, pp. 305-315, 2016.
[10] H. Karimi, T. Niknam, J. Aghaei, M. GhasemiGarpachi, and M. Dehghani, "Switches optimal placement of automated distribution networks with probability customer interruption cost model: A case study," *International Journal of Electrical Power & Energy Systems*, vol. 127, p. 106708, 2021.
[11] M. Farajollahi, M. Fotuhi-Firuzabad, and A. Safdarian, "Simultaneous placement of fault indicator and sectionalizing switch in distribution networks," *IEEE Transactions on Smart Grid*, vol. 10, no. 2, pp. 2278-2287, 2018.
[12] F. Jabari, F. Sohrabi, P. Pourghasem, and B. Mohammadi-Ivatloo, "Backward-forward sweep based power flow algorithm in distribution systems," in *Optimization of power system problems*: Springer, 2020, pp. 365-382.
[13] M. Amini, A. Jalilian, and M. R. P. Behbahani, "Fast network reconfiguration in harmonic polluted distribution network based on developed backward/forward sweep harmonic load flow," *Electric Power Systems Research*, vol. 168, pp. 295-304, 2019.
[14] F. Shabani-Naeeni and R. G. Yaghin, "Integrating data visibility decision in a multi-objective procurement transport planning under risk: A modified NSGA-II," *Applied Soft Computing*, vol. 107, p. 107406, 2021.
[15] J. Liu, W. Li, M. Liu, K. He, Y. Wang, and P. Fang, "Multi-Objective Aerodynamic Design Optimisation Method of Fuel Cell Centrifugal Impeller Using Modified NSGA-II Algorithm," *Applied Sciences*, vol. 11, no. 16, p. 7659, 2021.
[16] L. Pan, W. Xu, L. Li, C. He, and R. Cheng, "Adaptive simulated binary crossover for rotated multi-objective optimization," *Swarm and Evolutionary Computation*, vol. 60, p. 100759, 2021.
[17] K. Deb, "Multi-objective optimisation using evolutionary algorithms: an introduction," in *Multi-objective evolutionary optimisation for product design and manufacturing*: Springer, 2011, pp. 3-34.
[18] B. Luo, J. Zheng, J. Xie, and J. Wu, "Dynamic crowding distance? A new diversity maintenance strategy for MOEAs," *in 2008 Fourth International Conference on Natural Computation*, 2008, vol. 1, pp. 580-585: IEEE.
[19] A. Abdolahi, J. Salehi, F. S. Gazijahani, and A. Safari, "Assessing the potential of merchant energy storage to maximize social welfare of renewable-based distribution networks considering risk analysis," *Electric Power Systems Research*, vol. 188, p. 106522, 2020.
[20] A. Moradi and M. Fotuhi-Firuzabad, "Optimal switch placement in distribution systems using trinary particle swarm optimization algorithm," *IEEE Transactions on power delivery*, vol. 23, no. 1, pp. 271-279, 2007.
[21] A. Abdolahi, N. Taghizadegan, M. R. Banaei, and J. Salehi, "A reliability-based optimal μ-PMU placement scheme for efficient observability enhancement of smart distribution grids under various contingencies," *IET Science, Measurement & Technology*, vol. 15, no. 8, pp. 663-680, 2021.
[22] Ž. Popović, B. Brbaklić, and S. Knežević, "A mixed integer linear programming based approach for optimal placement of different types of automation devices in distribution networks," *Electric Power Systems Research*, vol. 148, pp. 136-146, 2017.
[23] H. Falaghi, M.-R. Haghifam, and C. Singh, "Ant colony optimization-based method for placement of sectionalizing switches in distribution networks using a fuzzy multiobjective approach," *IEEE Transactions on Power Delivery*, vol. 24, no. 1, pp. 268-276, 2008.
[24] J. R. Bezerra, G. C. Barroso, R. P. S. Leão, and R. F. Sampaio, "Multiobjective optimization algorithm for switch placement in radial power distribution networks," *IEEE Transactions on Power Delivery*, vol. 30, no. 2, pp. 545-552, 2014.
[25] S. Ray, A. Bhattacharya, and S. Bhattacharjee, "Optimal placement of switches in a radial distribution network for reliability improvement," *International Journal of Electrical Power & Energy Systems*, vol. 76, pp. 53-68, 2016.

8. Appendix

Table IV. The bus and line data of the proposed distribution network

Bus No.	Transformer capacity	Bus No.	Transformer capacity	Line No.	Impedance (Z)		Line No.	Impedance (Z)	
					Resistance (R)	Reactance (X)		Resistance (R)	Reactance (X)
1	200	62	25	1	0.0303	0.0999	62	0.04	0.1356
2	50	63	100	2	0.0129	0.0424	63	0.038	0.127
3	100	64	200	3	0.00176	0.00798	64	0.0601	0.189
4	100	65	200	4	0.0241	0.108	65	0.0191	0.0625
5	50	66	75	5	0.0119	0.054	66	0.0715	0.323
6	200	67	25	6	0.00459	0.0208	67	0.0715	0.323
7	315	68	160	7	0.00244	0.0305	68	0.0684	0.186
8	250	69	50	8	0	0.0267	69	0.0179	0.0505
9	100	70	25	9	0.00258	0.0322	70	0.0267	0.0752
10	200	71	50	10	0.0209	0.0688	71	0.0486	0.137
11	25	72	50	11	0.0203	0.0682	72	0.0203	0.0588
12	100	73	200	12	0.00595	0.0196	73	0.0405	0.1635
13	100	74	50	13	0.0187	0.0616	74	0.0263	0.122
14	250	75	100	14	0.0484	0.16	75	0.073	0.289
15	100	76	100	15	0.00862	0.034	76	0.0869	0.291
16	200	77	100	16	0.02225	0.0731	77	0.0169	0.0707
17	50	78	100	17	0.0215	0.0707	78	0.00275	0.00955
18	200	79	200	18	0.0744	0.2444	79	0.00488	0.0151
19	200	80	400	19	0.0595	0.195	80	0.0343	0.0966
20	250	81	400	20	0.0212	0.0834	81	0.0474	0.134
21	200	82	100	21	0.0132	0.0437	82	0.0343	0.0966
22	200	83	100	22	0.0454	0.1801	83	0.0255	0.0719
23	160	84	100	23	0.0123	0.0505	84	0.0503	0.2293
24	100	85	200	24	0.01119	0.0493	85	0.0825	0.251
25	200	86	100	25	0.0252	0.117	86	0.0803	0.239
26	315	87	200	26	0.012	0.0394	87	0.04739	0.2158
27	315	88	200	27	0.0183	0.0849	88	0.0317	0.145
28	100	89	315	28	0.0209	0.097	89	0.0328	0.15
29	50	90	100	29	0.0342	0.159	90	0.00264	0.0135
30	100	91	25	30	0.0135	0.0492	91	0.0123	0.0561
31	160	92	10	31	0.0156	0.08	92	0.00824	0.0376
32	200	93	25	32	0	0.0382	93	0	0.0386
33	250	94	100	33	0.0318	0.163	94	0.00172	0.02
34	250	95	100	34	0.01913	0.0855	95	0	0.0268
35	100	96	100	35	0.0237	0.0943	96	0.00901	0.0986
36	400	97	160	36	0	0.0388	97	0.00269	0.0302
37	25	98	25	37	0.00431	0.0504	98	0.018	0.0919
38	160	99	100	38	0.00799	0.086	99	0.018	0.0919
39	200	100	50	39	0.0474	0.1563	100	0.0482	0.218
40	100	101	25	40	0.0108	0.0331	101	0.0258	0.117
41	100	102	50	41	0.0317	0.1153	102	0	0.037
42	400	103	25	42	0.0298	0.0985	103	0.0224	0.1015
43	100	104	25	43	0.0229	0.0755	104	0.00138	0.016
44	100	105	200	44	0.038	0.1244	105	0.0844	0.2778
45	250	106	50	45	0.0752	0.247	106	0.0985	0.324
46	250	107	250	46	0.00224	0.0102	107	0	0.037
47	100	108	500	47	0.011	0.0497	108	0.03	0.127
48	50	109	200	48	0.0415	0.142	109	0.00221	0.4115
49	50	110	200	49	0.00871	0.0268	110	0.00882	0.0355
50	200	111	100	50	0.00256	0.0094	111	0.0488	0.196
51	50	112	100	51	0	0.0375	112	0.0446	0.18
52	100	113	160	52	0.0321	0.106	113	0.00866	0.0454
53	250	114	25	53	0.0593	0.168	114	0.0401	0.1323
54	100	115	160	54	0.00464	0.054	115	0.0428	0.141
55	200	116	100	55	0.0184	0.0605	116	0.0405	0.122
56	160	117	100	56	0.0145	0.0487	117	0.0123	0.0406
57	200	118	100	57	0.0555	0.183	118	0.0444	0.148
58	160	119	250	58	0.041	0.135	119	0.0309	0.101
59	100	120	100	59	0.0608	0.2454	120	0.0601	0.1999
60	200	121	160	60	0.0413	0.1681	121	0.00376	0.0124
61	100	122	160	61	0.0224	0.0901			

International Journal of Research and Technology in Electrical Industry

journal homepage: ijrtei.sbu.ac.ir

Shahid Beheshti University

Multi-objective Dynamic Environmental Economic Dispatch Problem Considering Plug in Electric Vehicles by Using the Improved Exchange Market Algorithm

Hossein Nourianfar[1], Hamdi Abdi[1,*]

[1] *Electrical Engineering Department, Engineering Faculty, Razi University, Kermanshah, Iran*

ARTICLEINFO

Article history:
Received 15 January 2022
Received in revised form 28 March 2022
Accepted 04 April 2022

Keywords:
Exchange market algorithm (EMA)
Valve-point loading effect
Multi-objective optimization
Dynamic environmental economic dispatch problem
Plug-in electric vehicles

ABSTRACT

Global Warming and progression of modern power networks have profoundly changed traditional power grids in terms of fossil fuel consumption and emission of toxic gases. Therefore, auxiliary power plants and ancillary services have been introduced as an effective alternative, to overcome these new challenges in power systems. In this work, the dynamic environmental economic dispatch (DEED) problem, is investigated by considering the plug-in electric vehicles (PEVs), minimizing the fuel cost and greenhouse gas emissions from fossil fuel units. In the mentioned problem, to make it more practical, various operational constraints, including valve-point loading effect (VPLE), ramp rate limits (RRLs) and generation capacity limits are considered. This paper proposes a new multi-objective exchange market algorithm (EMA) based on the non-dominated sorting theory to find the Pareto front. In addition, the impacts of PEVs, as an uncertainty source, on the mentioned problem are analysed in four different charging scenarios. The efficiency of the proposed method has been detailed on three experimental systems and the obtained results are compared with other algorithms in this field. The results show that the maximum percentage reduction in costs for test cases 1 to 3, are about 2.13, 2.69, and 39.48, respectively, and about 45.96, 48.20 and 44.07, for emission, respectively. The comparative analysis verify the proposed method efficiency, and accuracy in solving the suggested problem.

Nomenclature

List of symbols

$FC_i(P_i)$	Fuel cost function of the ith thermal unit
A_i ،B_i *and* C_i	Coefficients of thermal unit cost function i.
D and θ	Coefficients of VPLE
P_i	Generated power by thermal unit i
$E_i(P_i)$	Emission function of the ith thermal unit
α, β, γ, $\zeta$and λ	Emission coefficients of thermal unit
$P_{i,t}^{min}$ and $P_{i,t}^{max}$	Minimum and maximum power generated by unit i at time t
$P_{D,t}$ and $P_{L,t}$	Demand load and the power loses at time t.
$l_{ev,t}$	Charging load of PEVs, at time t
P_i^0	previous output power of the i^{th} unit
DR_i and UR_i	Down and up ramp rate limits of the i^{th} unit
$IND_{1,i}^{group1}$ and $IND_{2,i}^{group1}$	Individuals in the first category
R	A random number in the range of 0 and 1

* Corresponding author
E-mail address: hamdiabdi@razi.ac.ir
http://dx.doi.org/ 10.52547/ijrtei.1.1.46

δ_k	Value of the change in the share of the *k* member in the third group
W_k	Feedback coefficient of the *k* member in the third group
$Rank_k$	Rank of the *k* member in the third group
N_{POP}	Number of total population
Δn_{t1}^i and Δn_{t2}^i	Amount of change in the variables of the members of the second and third groups
Ψ_t^i	Exchange market information
ω_1	Risk factor for each member of group 2
μ	Risk increase coefficient that makes the last individuals of the ranking take more risks
$g_1^k and\ g_2^k$	common market risk for the second and third groups
$iter_{max}$	Maximum iteration
$g_{min}\ and\ g_{max}$	Minimum and maximum common market risk
$f_i(x)$ and $f_i(y)$	Output of the ith objective function for solutions *x* and *y*
CD_i	Crowding distance of the ith solution
φ	Penalty coefficient

Abbreviations

DEED	Dynamic Environmental Economic Dispatch
PEVs	Plug-in Electric Vehicles
VPLE	Valve-Point Loading Effect
RRLs	Ramp Rate Limits
ELD	Economic Load Dispatch
EED	Economic Emission Dispatch
AI	Artificial Intelligence
DE	Differential Evolution
MCSA	Modified Crow Search Algorithm
Dy-NSBBO	Dynamic Non-dominated Sorting Biogeography-Based Optimization
NSGA-II	Non-dominated Sorting Genetic Algorithm
KKO	Kho-Kho Optimization
WOA	Whale Optimization Algorithm
COA	Coyote Optimization Algorithm
MSFLA	Modified Shuffle Frog Leaping Algorithm
ICA	Imperialist Competitive Algorithm
EPRI	Electric Power Research Institute
PDF	Probability Distribution Function

1. Introduction

Power generation units play a significant role in the power system, to provide a reliable and safe electricity to consumers, in an economical and controllable manner. With the development of technology and industrialization, the need for electrical power is increasing gradually. On the other hand, meeting the increased power demand entails significant costs. Accordingly, reducing the power generation costs is remarkably involved in promoting the economic development of countries [1].

Supplying reliable energy at the minimum cost can be a very challenging subject that is highly dependent on grid operation and control strategies. So far, different operation concepts are considered to minimize the total cost of power generation units. In this regard, Economic load dispatch (ELD) is the most basic problem, as the cornerstone of operation studies, to provide the quality power to the customers, economically and safely. The ELD problem is defined as determining the optimal generations of power plants satisfying a set of different constraints, while minimizing total operating costs [2].

Mathematical methods cannot be used properly to address these problems due to the need for differentiable or continuous objective functions. Hence, various artificial intelligence (AI)-based optimization methods that randomly seek the optimal solutions are used effectively to solve the EED problem. As a result, these methods can be a suitable candidate. Some of these optimization techniques include Kho-Kho Optimization algorithm (KKO) [3], Whale Optimization Algorithm (WOA) [4], Coyote Optimization Algorithm (COA) [5], Modified Shuffle Frog Leaping Algorithm (MSFLA) [6], Modified Crow Search Algorithm (MCSA) [7], and Imperialist Competitive Algorithm (ICA) [8].

Integrating the environmental issues caused by produced emission gases from fossil fuel-based generators to the ELD problem, results in extending a single-objective problem to a multi-objective economic emission dispatch (EED) problem [9]. The EED problem is mentioned as a type of multi-objective problems with conflicting objectives. In other words, reducing the value of one-goal leads to increasing the value of another. Therefore, the appropriate solution must be obtained through an acceptable trade-off between different objectives.

This new problem is more complex than the earlier one, which needs applying some new techniques to solve it. The purpose of this new problem is to minimize the fuel cost and emissions simultaneously, which has made it as one of the most important research topics, and directions in modern power system operation studies. Solving this complex problem considering practical system-operating constraints such as valve-point loading effect (VPLE), due to its very nonlinear and non-convex nature, is a very challenging problem that cannot be solved by using traditional and classical methods [10].

As the literature confirms, there are many researches focussed on this issue, some of them are addressed in following.

One of the effective techniques to solve this problem is converting this two-objective problem to a single objective framework by using the classical optimization techniques. In this method the emission rate is considered as an operational constraint [11]. Depending on the problem model and solving strategy, this method has some complexities in finding a compromise solution among the fuel cost and emissions.

Another method is addressed in [12], which applied the goal-based programming to solve the EED problem. However, this method needs more run-time to be converged.

The classical optimization techniques are applied to solve the EED problem based on coordination equations that are not suitable for discontinuous cost functions. Therefore, in classical optimization methods, the cost curve must be estimated in proportion to the necessity of the problem.

A popular strategy is to convert the multi-objective EED problem into a single-objective problem using the price penalty factor and then extract the Pareto Front by varying the values of weighted coefficients for cost and emission. The weighted coefficients method suffers from

two main drawbacks [13]. First, the uniform distribution of weighted coefficients does not always result in a uniform distribution of solutions. Second, the solutions existing on the non-convex portions of the Pareto front cannot be found using this method.

In [14], the authors investigated various optimization problems in the field of operation of power systems, such as ELD, ELD in multi-area, ELD in the presence of combined heat and power (CHP) units, on the small- scale and large-scale cases and taking into account the effect of renewable energy resources. In this work, a modified version of the EMA is employed to solve the mentioned problems. In [15], the multi-objective EED problem is addressed using the combination emission with cost by the price penalty factor. In that research, a hybridization of adaptive inertia weight particle swarm optimization (PSO) and EMA, integrated with an effective constraint handling method is used for problem optimization. In [16], the bi-objective EED problem is solved by employing an improved bare-bone multi-objective PSO algorithm. In this algorithm, to extract the Pareto front and maintain the distribution diversity of Pareto-optimal solutions, the slope method and crowding distance are integrated in the algorithm. In addition, two operators' p_{best} and g_{best} are improved to enhance the performance of the algorithm. In [17], to deal with conflicting objectives in the EED problem, the concept of non-dominated sorting is embedded in the squirrel search algorithm. In this work, the crowding distance mechanism along with an external depository is utilized to distribute the solutions well in the target space.

On the other hand, the use of plug-in electric vehicles (PEVs) in recent years has received much attention due to their significant impacts on reducing emission and being a good option for storing electrical energy. Hence, many large automobile companies have turned to the production of these cars [18]. Increasing the number of EVs has caused the charging and discharging programs of these cars to be done in accordance with the load curve of the network. Therefore, it is always tried to direct the car charging mainly to non-peak times, and a portion of the stored energy in batteries of these cars is sold to the grid during peak hours.

In [19], the economic unit commitment examines power systems integrated with renewable energy resources and PEVs, considering only the unit costs and regardless of emissions. In [20], an energy storage model with network vehicles is proposed for ELD in the smart grid. In this work, weighting coefficients are used to convert the two objectives optimization problem, including emission and cost objectives, into a single objective function. In [21], in addition to PEVs, the effect of wind turbines on the DEED problem is analysed. The solution approach used in this work is the multi-objective virus colony search, and the non-dominated sorting procedure is employed to extract the Pareto front.

With the integration of PEVs in the power grid, the mentioned problem changes from optimal static power dispatch to dynamic ones. As a result, the complexity of the problem will be increased in the dynamic condition than in the static condition.

So far, several methods have been proposed for solving the mentioned problem in dynamic condition, which, in general terms, they can be grouped into two major categories. The first category includes different classical methods based on mathematical equation used to solve the DEED problem, such as linear, quadratic programming and gradient methods [22, 23]. Most mathematical methods are based on iteration. Although these methods offer somewhat accurate solutions to the problem, they are faced with several limitations in real-world problems, including the fact that the fuel cost curve of the units must be continuous.

In addition, although this is not the case with dynamic programming methods and there is no limit to the continuity of the fuel cost curve, it will take a lot of time and memory to solve the problem if the number of units increases.

Nevertheless, in intelligent algorithms, not only are they applicable to any problem without if the number of units any limitations, but also the time and dimensions required to solve the problem increase linearly with the number of units, making them a more suitable option for solving practical problems of ELD [21].

Among the algorithms used in recent researches to solve the DEED problem are the combination of multi-objective crisscross optimization and differential evolution (DE) [24] constriction factor-based particle swarm optimization [25] and the self-adaptive parameter operator multi-objective differential evolution integrated with local search operator based on non-dominant sorting [26].

In this paper, an improved EMA is used to solve the dynamic environmental economic dispatch (DEED) problem considering PEVs. This meta-heuristic algorithm has two operators that generate intelligent random numbers and two operators that strongly and efficiently absorb random numbers towards optimal numbers, simultaneously.

The main contributions of this paper are: improving the EMA, integrating the fast non-dominated sorting approach in the suggested method to find the pareto front of the problem, applying the addressed technique to the mentioned problem with modelling the PEVs, and evaluating the performance and effectiveness of the proposed method, by comparing the results obtained with the results of recent methods.

The rest of the paper is organized as follow. The formula for the DEED problem and the mathematical model of PEV charging are shown in section 2. Section 3 addresses the suggested technique in detail. The simulation results on different case studies are described in section 4. Finally, main conclusions and some suggestions for future works are stated in section 5.

2. Problem Formulation

In this section, the formulation of the EED problem is detailed.

2.1. Fuel Cost Function

The fuel cost function of thermal generation units is assumed to be a quadratic equation as [8]:

$$FC_i(P_i) = A_i + B_i P_i + C_i {P_i}^2 \quad (1)$$

A_i ($/h) ،$B_i$ ($/MW/h) and C_i ($/MW^2/h) are the coefficients of thermal power plant cost function *i*.

2.2. The VPLE

The fuel cost function considering the VPLE is modeled by adding a sine term to the objective function of Eq. (1) as [10]:

$$FC_i(P_i) = A_i + B_iP_i + C_iP_i^2 + |D * sin\ \{\theta(P_{min} - P)\}| \quad (2)$$

Where *D* ($/h), and θ (rad/MW) are the coefficients of VPLE, and P_{min} is the minimum generated power by thermal unit *i*.

2.3. Emission Function

The emission produced by each generation unit can be expressed in terms of generator output power as follow [9]:

$$E_i(P_i) = \alpha + \beta P_i + \gamma {P_i}^2 + \zeta\ exp(\lambda P_i) \quad \left(\frac{Kg}{h}\right) \quad (3)$$

In which, $\alpha, \beta, \gamma, \zeta$ and λ are the emission coefficients.

2.4. The DEED Formulation

The DEED problem formulation is similar to the static ELD, except that in the dynamic condition, the problem is investigated within 24 hours, and constraints such as the ramp rate limits (RRLs) are added to the problem. The DEED problem can be expressed as:

$$min\left\{\sum_{t=1}^{24}\sum_{i=1}^{N_P} E(P_i), \sum_{t=1}^{24}\sum_{i=1}^{N_P} FC(P_i)\right\} \quad (4)$$

2.5. The Effect of PEVs

Despite the advantages of EVs over conventional vehicles, one of the biggest challenges in using these vehicles is that if they are connected to the power grid suddenly during peak consumption, there is a possibility of network disruption and equipment damage. This is mainly due to the coincidence of the time of return of car owners to the place of residence at the end of office hours with the peak consumption to the place of residence time [21].

Severe fluctuations and sometimes sudden ascent in the load curve typically occur due to power consumption for home chargers and superchargers [21]. To prevent such disturbances in the power system, it is necessary to exercise appropriate control and coordination between car charging and the grid. Generally, four different strategies to charge the PEVs are addressed. These techniques are including EPRI forecasted load profile according to the PEVs driver behavior, stochastic charging, peak and off-peak charging.

According to EPRI, more than 60% of the power is consumed in seven hours, from 10 pm to 4 am. The Peak and Off-Peak profiles indicate the worst and best situations of vehicles charge, respectively. Finally, the stochastic profile based on the uncertainty of the charge of EVs is a daily casual charge distribution. In this scenario the probability distribution function (PDF) is considered with a normal distribution by mean value of 0.05. Table I shows the PDF for charging EVs based on different scenarios.

2.6. Maximum and Minimum Generation Capacity Limits

Each generation units must be operated within a certain range, due to some technical and economic reasons. The upper limit of this range is the nominal value of the generator and the lower one is the value that is necessary for the boiler stable operation.

$$P_{i,t}^{min} \le P_{i,t} \le P_{i,t}^{max} \quad (5)$$

$P_{i,t}^{min}$ and $P_{i,t}^{max}$ show the minimum and maximum generated powers by unit *i* at time *t*.

2.7. Power Balance

The sum of total power demand and power losses must be equal to the total power generated, as:

$$\sum_{i=1}^{N_P} P_{i,t} = P_{D,t} + P_{L,t} + l_{ev,t} \quad (6)$$

$P_{D,t}$ is the demand load, and $P_{L,t}$ is the electrical power losses at time *t*. $l_{ev,t}$ represents the charging load of PEVs, at time *t*. The power losses is determined by using the B-matrix coefficient method.

Table I. Charging scenarios of electric vehicles.

Charging Scenario		Time			
		01:00-06:00	07:00-12:00	13:00-18:00	19:00-24:00
Probability Distribution	EPRI	0.100	0.010	0.021	0.016
		0.100	0.003	0.021	0.036
		0.095	0.003	0.021	0.054
		0.070	0.013	0.001	0.095
		0.050	0.021	0.005	0.100
		0.030	0.021	0.005	0.100
	Off-Peak	0.185	0	0	0
		0.185	0	0	0
		0.090	0	0	0
		0.090	0	0	0
		0.040	0	0	0.185
		0.040	0	0	0.185
	Peak	0	0	0.185	0.040
		0	0	0.185	0.040
		0	0	0.185	0
		0	0	0.185	0
		0	0	0.090	0
		0	0	0.090	0
	Stochastic	0.057	0.087	0.038	0.028
		0.049	0.048	0.02	0.022
		0.048	0.011	0.021	0.055
		0.024	0.032	0.061	0.025
		0.026	0.021	0.032	0.035
		0.097	0.057	0.022	0.082

2.8. Ramp Rate Limits

The RRLs are the dynamic constraints, in terms of mechanical constraints and in the form of increasing or decreasing rates the output power. By considering this subject, the static EED problem is converted into a

dynamic EED problem that prevents possible damage to the rotor. These RRLs are expressed as:

$$Max\left(P_i^{min}, P_i^0 - DR_i\right) \le P_i \le Min(P_i^{max}, P_i^0 + UR_i) \quad (7)$$

In which, P_i^0 (MW) is the previous output power of the i^{th} unit, and DR_i (MW/h), and UR_i (MW/h) are the down and up ramp rate limits of the i^{th} unit, respectively.

3. Proposed Approach

The approach used in this work, consists of three general components:

I. Employing the improved EMA
II. Non-dominated sorting procedure and crowding distance calculations
III. Constraint handling

The main component of this approach is to use the improved EMA to optimize the intended problem. How this algorithm works is described in detail in Section 3.2. Nevertheless, since this algorithm is designed to address single-objective optimization problems, a mechanism is needed to find the Pareto front. For this purpose, non-dominated sorting and crowding distance are embedded in the algorithm.

3.1. Improved EMA

In this algorithm, there are two different market modes in each iteration, and after each mode, the viability is examined and individuals are sorted based on the value of their assets [28]. At the end of each market situation, the primary, middle, and final members of the population are known as members of groups one, two, and three. How to trade stocks in different market conditions and in different groups is as follows:

- **Normal Mode**

After producing the initial population and calculating the value of individuals' stocks, in normal mode, individuals are divided into three categories based on the amount of assets and the value of their stocks.

Then the first category, which includes individuals with the highest stock value, makes no effort to change their stock because of their position. [27].

However, individuals who are in the second category, change their shares according to the experience of the first category to reach the position of individuals in the first category and increase the value of their shares. The method of changing the shares of these individuals is as [28]:

$$IND_j^{group2} = R \times IND_{1,i}^{group1} + (1-R) \times IND_{2,i}^{group1} \quad (8)$$

$IND_{1,i}^{group1}$ and $IND_{2,i}^{group1}$ are the individuals in the first category. R is a random number in the range of (0,1).

In the third category, individuals change their stocks at greater risk than those in the second category because of the much lower stock value than those in the first category, as: [28]:

$$\delta_k = 2 \times W_k \times \left(IND_{1,i}^{group1} - IND_k^{group3}\right) \quad (9)$$

$$IND_k^{group3,new} = IND_k^{group3} + \delta_k \quad (10)$$

$$W_k = 2 \times {(Rank_k - N_{POP}/2)}/{N_{POP}} \quad (11)$$

δ_k is the value of the change in the share of the k member in the third group.

- **Oscillation Mode**

Similar to normal mode, the individuals are divided into 3 groups and the members of first group try to maintain their rank and remained unchanged. However, in the second group, the total shares of individuals is fixed and only the amount of some shares of each type increases and the amount of others decreases, so the total amount of shares of each individual remains unchanged. Initially, the number of shares of each individual increases according to [28]:

$$\Delta n_{t1}^i = n_{t1}^i - \Psi_t^i + (2 \times R \times \mu \times \omega_1) \quad (12)$$

$$\mu = t_{POP}/N_{POP} \quad (13)$$

$$n_{t1}^i = \sum_{y=1}^{n} |S_{ty}| \quad (14)$$

$$\omega_1 = n_{t1}^i \times g_1^k \quad (15)$$

$$g_1^k = g_{1,max} - \frac{g_{1,max} - g_{1,min}}{iter_{max}} \times k \quad (16)$$

$$\Psi_t^i = \phi^i + \theta_t^i(x) \quad (17)$$

Δn_{t1}^i is the amount of change in the variables of the members of the second group and Ψ_t^i is the exchange market information. R is a random number, ω_1 is the risk factor for each member of group 2. μ is the risk increase coefficient that makes the last individuals of the ranking take more risks. $g_1^k$is a common market risk and decreases with increasing the iteration.

In the second part of this section, it is necessary for each individual to sell some of his stocks of any kind at random in the same amount as he bought additional stocks, so that the total stocks of each individual remain unchanged. In this part, it is necessary for each individual to reduce his stocks by a total of Δn_{t2}^i. In this case, the value of each individual is equal to:

$$\Delta n_{t2}^i = n_{t2}^i - \Psi_t^i \quad (18)$$

Δn_{t2}^i is the amount of stock that each individual must sell.

In this section, unlike group two, the total number of stock of individuals changes with trading and each member buys or sells some shares. The shareholders of the third group change some of their stock according to the following relation [28]:

$$\Delta n_{t3} = (4 \times r_s \times \mu \times \omega_2) \quad (19)$$

$$r_s = (0.5 - rand) \quad (20)$$

$$\omega_2 = nt_1 \times g_2 \quad (21)$$

$$g_2^k = g_{2,max} - \frac{g_{2,max} - g_{2,min}}{iter_{max}} \times k \qquad (22)$$

Δn_{t3} is the amount of change in the variables of the members of the third group. *rand* is a random number, ω_2 is the risk factor for each member of group 2. μ is the risk increase coefficient that makes the last members in the ranking take more risks. Finally, g_2^k is the usual market risk for the third group in the oscillation mode and decreases with increasing iteration. The flowchart of the proposed approach is drawn in Figure 1.

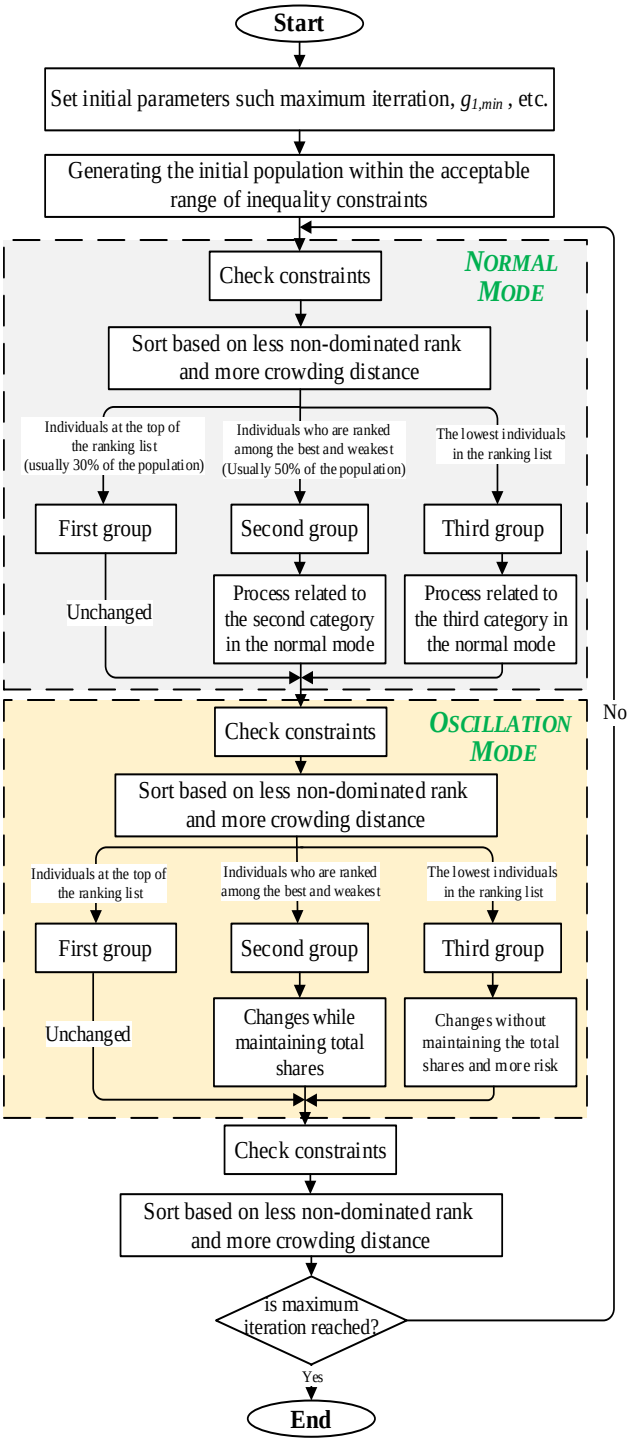

Fig. 1. The flowchart of the proposed approach

3.2. Non-Dominated Sorting Procedure and Crowding Distance Calculations

In the multi-objective EED problem, the aim is to reduce both costs and emissions. Therefore, solutions cannot be sorted on the basis of less cost alone. In these cases, the concept of dominance is used. One solution dominates another, if the following equations are met simultaneously [29].

$$f_i(x) \le f_i(y) \qquad \forall i = 1, 2, \dots, n \qquad (23)$$

$$f_i(x) < f_i(y) \qquad \exists i = 1, 2, \dots, n \qquad (24)$$

Where, $f_i(x)$ and $f_i(y)$ are the output of the i^{th} objective function for solutions *x* and *y*, respectively. In addition, n represents the number of objectives. In the non-dominated sorting procedure, the solutions that are not dominated by any other solution form the first front. Regardless of the available solutions in the first front, the same procedure is repeated, and the non-dominated solutions form the second front, and so on. In addition, to maintain diversity, in each front, the crowding distance of the solutions is calculated according to the following equation [10].

$$CD_i = \frac{1}{n}\sum_{o=1}^{n} |f_{i+1}^o - f_{i-1}^o| \qquad (25)$$

Where CD_i is the crowding distance of the i^{th} solution in that front, n is the number of objectives, and f_{i+1}^o and f_{i-1}^o represent the output of the o^{th} objective function for solutions *i*+1 and *i*-1, respectively.

First, the solutions are ranked based on the front which they are on it (solutions on the first front are better than solutions on the second front, and so on). Then, solutions on the same front are ranked based on the greater crowding distance. Table II shows a comparison between the features of the proposed modeling and solution approach.

Table II. Comparison between the features of the DEED problem and the proposed method.

Proposed method	DEED problem
Individual	Solution
Shares	Power output of units
Total shares	Total power
Information of exchange market	Problem data (e.g. power balance)
Buying/selling shares	Increasing/decreasing power outputs of units
Number of shareholders	Population (the number of solutions)
Sorting based on the value of Assets or stocks	Sorting based on front and crowding distance

3.3. Constraint Handling

Two steps are taken to satisfy inequality constraints such as generation capacity limits. In the first step, it tries to generate power within the acceptable range; in the second step, whenever it is violated, the power is corrected to the nearest margin of the feasible solution. Two actions are taken for equality constraints. In the first

one, the penalty function with a small value for the penalty coefficient is considered. The following equation shows the new fuel cost function by applying the penalty function.

$$FC_{new} = FC_{old} + \varphi \times \left|\sum_{i=1}^{N_P} P_i - P_D - P_L - l_{ev}\right| \quad (26)$$

Where, φ is the penalty coefficient, its value is considered small here, and FC_{old} is the fuel cost function before applying the penalty function. On the one hand, a small value cannot guarantee the exact fulfilment of the constraint; on the other hand, a large value for the penalty coefficient can lead to premature convergence. Hence, in the second action, to accurately satisfy the constraint, an intelligent search is performed during the algorithm optimization process according to Equations (12-17). In this way, it is tried that the total shares of individuals are always in such a way that the equality constraints are met.

4. Simulation

To confirm the effectiveness of the proposed algorithm in solving bi-objective DEED problems, three test systems including 6-unit static and dynamic systems, and 10-unit dynamic system with four electric vehicle-charging scenarios are used. The parameter settings of the proposed algorithm for solving each of the test systems are presented in Table III.

4.1. Test case I

In the first case, a simple test system without PEV is used to test the effectiveness of the proposed algorithm on a 6-unit test system. Load demand is set to PD=500 MW and other coefficients of generation units are selected based on [18].

The Pareto front obtained by the proposed method for this test system is shown in Figure. 2. As can be seen from this figure, the proposed method can obtain extreme solutions (minimum cost and minimum emission) well, and although the solutions do not have a uniform distribution, due to the low run-time and high accuracy of the outputs, the diversity of solutions is acceptable.

In addition, the best-compromised solution obtained by the proposed method is compared with the results of other methods in this field in Table IV.

As can be seen, the results of the proposed method are better than the other methods in terms of fuel cost and emission. In addition, the proposed method, unlike the other two methods, despite the losses, satisfies the power balance well.

Table III. Settings of algorithm parameters to solve different test cases.

Parameters	Test Case 1	Test Case 2	Test Case 3
Maximum Iteration	100	100	100
Population	50	50	100
g1 [max, min]	[0.005, 0.0005]	[0.01, 0.05]	[0.01, 0.05]
g2 [max, min]	[0.01, 0.001]	[0.02, 0.005]	[0.02, 0.005]

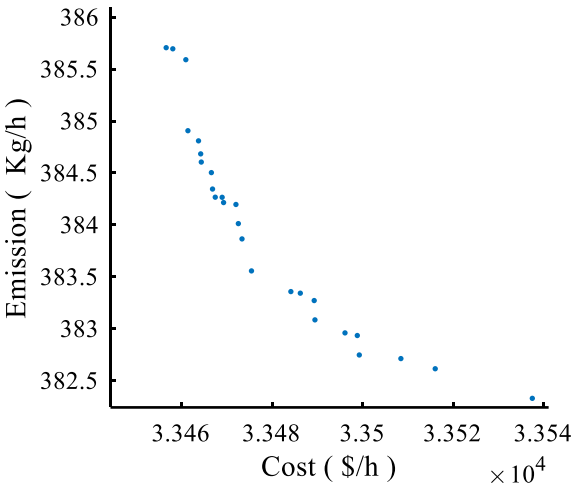

Fig. 2. Pareto front obtained by the proposed method for the test case 1.

Table IV. Comparison of results for test case 1.

Method	Dy-NSBBO [18]	Dy-NSGA-II [18]	Proposed method
P1	173.11	165.87	125.047
P2	149.52	158.13	130.376
P3	65.36	78.78	51.295
P4	47.41	55.44	60.097
P5	30.07	22.61	106.949
P6	34.51	19.23	81.591
Cost	34141.32	34214.25	33484.34
Emission	709.26	711.32	384.357

4.2. Test case 2

In this case, the same 6-unit test system with PEVs is employed to examine the proposed algorithm performance. The four PEV charging scenarios described in the previous section are applied. As the amount of charge changes over time, the problem will change to DEED.

In this case, it is assumed that there are some EVs, 18000 of low-hybrid vehicles equipped with 15 kWh batteries, 10000 of medium-sized hybrid vehicles with 25 kWh batteries, and 12000 of pure electric vehicles equipped with 40 kWh [21]. As a result, the total charge of PEVs for one day will be 1000MWh. This amount of charge is significant for the current network.

Figures 3 to 6 show the cost and emission for 4 different charging scenarios of EVs during 24 hours, respectively.

As can be seen from these figures, the best case is related to the Off-Peak scenario, in which the vehicles charging time is shifted to non-peak hours. Figure 3 shows that in the EPRI scenario, costs and emissions are almost the same at all day-hours, due to the almost uniform distribution of PEVs charges during the day, and figure 5 shows that costs and emissions peaked during peak hours. In the stochastic scenario, due to the fact that the amount of charge per hour is random, the cost and emission increase or decrease irregularly, at any day-hour.

The total cost and emission obtained by the proposed method for different scenarios is compared with the results of other methods in Table V.

Table V. Total cost and emission for the test case 2.

Method		EPRI	Off-Peak	Peak	Stochastic
Dy-NSBBO [18]	Total Cost	836509	835211	852666	849959
	Total Emission	18327	18250	18395	18338
Dy-NSGA-II [18]	Total Cost	852419	851100	869407	858470
	Total Emission	18542	18425	18772	18669
Proposed method	Total Cost	840130	845152	845983	844670
	Total Emission	13374.7	9768.6	9722.4	9940.3

Table V shows that for both peak and stochastic scenarios, the results of the proposed method are better than the results of the other two methods, in terms of both cost and emission. In other words, for these two scenarios, the results of the proposed method dominate the results of the other two methods. In addition, for the other two scenarios, the results of the proposed method dominate the results of the Dy-NSGA-II method.

It should be noted that in the case of the Dy-NSBBO method, for both EPRI and Off-Peak scenarios, we cannot speak with confidence about the superiority between the methods. Because the Dy-NSBBO costs less, while its emission is higher than the proposed method.

The total cost of the EPRI scenario is lower than the Off-Peak scenario. This is due to the fact that load demand used in the test system is considered the same at all hours. As a result, since the vehicles is charged more uniformly in the EPRI scenario, the total cost will be lower.

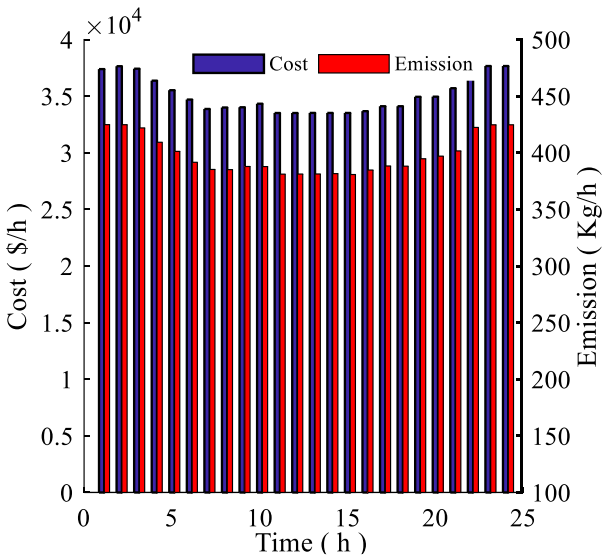

Fig. 3. The cost and emission for test case 2, in EPRI scenario.

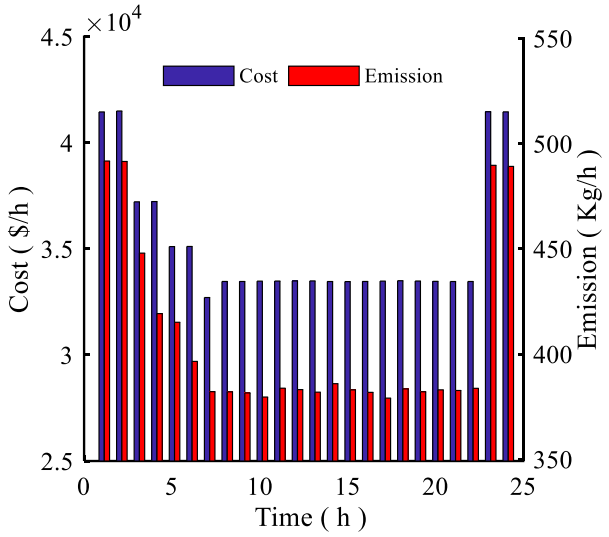

Fig. 4. The cost and emission of test case 2, in Off-Peak scenario.

4.3. Test Case 3

The third test system is a 10-unit system that takes into account the practical system constraints, including the VPLE, RRLs, losses and generation capacity limits, in the form of DEED over 24 hours. The demand load in this system is 900 MW and the system data are extracted from [18].

Since the complexity and scale of this test system is greater than the previous system, it is more appropriate to evaluate the performance of the proposed method.

The best compromising solutions for 24 hours in four different scenarios are given in Figures 7 to 10. Also, the total cost and emission of the proposed method compared to other methods are presented in Table VI.

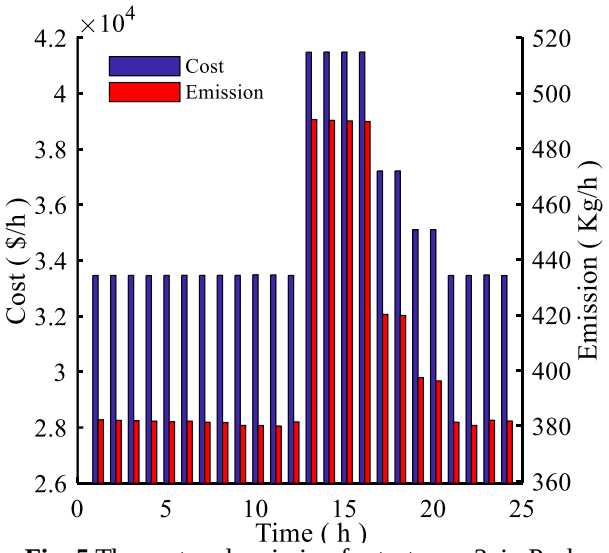

Fig. 5. The cost and emission for test case 2, in Peak scenario.

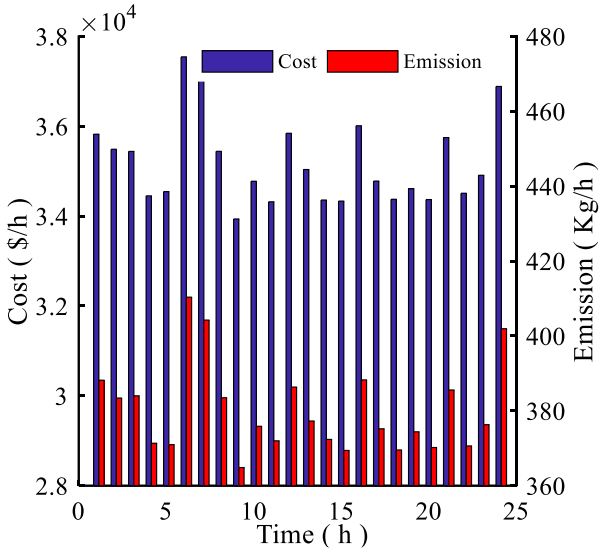

Fig. 6. The cost and emission for test case 2, in Stochastic scenario.

The proposed method for all scenarios is less costly and less emission than the other two methods. In other words, the results of the proposed method dominate the results of the other two methods for all four scenarios.

Furthermore, with the increasing problem scale, the superiority of the proposed method over the other two methods is more clearly demonstrated.

The percentage improvement in cost and emission for all three test cases and for different scenarios is shown in Table VII. As can be seen from this table, the costs and emissions obtained by the proposed method have been significantly improved, especially concerning emissions. The results in Table VII confirm the reduction up to 39% in costs and up to 48% in emissions.

Table VI. Total cost and emission for the test case 3.

method		EPRI	Off-Peak	Peak	Stochastic
Dy-NSBBO [18]	Total Cost	2061738	2061330	2067307	2062806
	Total Emission	153483	153321	154178	153778
Dy-NSGA-II [18]	Total Cost	2069298	2065476	2073424	2073017
	Total Emission	155443	154685	155932	155801
Proposed method	Total Cost	1448453	1456437	1456329	1449608
	Total Emission	92851	88506	87198	93063

Table VII. The percentage improvement in cost and emission for all 3 test cases.

Scenario		Method	Percentage improvement	
			Cost (%)	Emission (%)
Test case 1	-	Dy-NSBBO	1.92	45.80
		Dy-NSGA-II	2.13	45.96
Test case 2	EPRI	Dy-NSBBO	-0.43 [1]	27.02
		Dy-NSGA-II	1.44	27.86
	Off-Peak	Dy-NSBBO	-1.19	46.47
		Dy-NSGA-II	0.69	46.98
	Peak	Dy-NSBBO	0.78	47.14
		Dy-NSGA-II	2.69	48.20
	Stochastic	Dy-NSBBO	0.62	45.79
		Dy-NSGA-II	1.60	46.75
Test case 3	EPRI	Dy-NSBBO	29.74	39.50
		Dy-NSGA-II	30.00	40.26
	Off-Peak	Dy-NSBBO	29.34	42.27
		Dy-NSGA-II	39.48	42.78
	Peak	Dy-NSBBO	29.55	43.44
		Dy-NSGA-II	29.76	44.07
	Stochastic	Dy-NSBBO	29.72	39.48
		Dy-NSGA-II	30.07	40.26

[1] **A minus sign means higher cost of the proposed method**

5. Conclusion

Investigating different power system operation studies in modern power systems is an important task, which should be discussed, especially by considering some new concepts such as uncertainty, and environmental impacts. In this regard, in this paper, a new version of EMA, known as improved EMA is implemented to solve the DEED problem in the presence of PEVs, as an uncertainty sources in new power systems, with conflicting objectives

of fuel cost and emission. This optimization technique was applied to three test cases.

In the first test case, the Pareto front obtained by the proposed method had an acceptable diversity and spread, which shows the proper performance of applying the non-dominated sorting and crowding distance. In the second and third test cases, PEVs were also considered, which converted the static EED problem into a dynamic one. In these test cases, the results of the proposed method compared to state of the art methods, showed up to 48% reduction in emissions and up to 39% reduction in costs. From these results, it can be concluded that the proposed method can be a suitable candidate to solve the multi-objective DEED problems by considering the practical constraints. In addition, a comparison of four scenarios EPRI, Off-Peak, Peak, and Stochastic, showed that shifting the charging time of EVs to non-peak hours reduces costs and emissions.

Increasing the search ability of the algorithm by combining it with other optimization methods, and introducing some hybridizing optimization techniques, to apply it to multi-objective optimization problems of DEED with more practical constraints in a microgrid can be considered as future work in this field. Furthermore, considering a complete package of uncertainties in power systems, including the uncertainty of load, and renewable energy resources, can be mentioned as the most prominent topics for future researches.

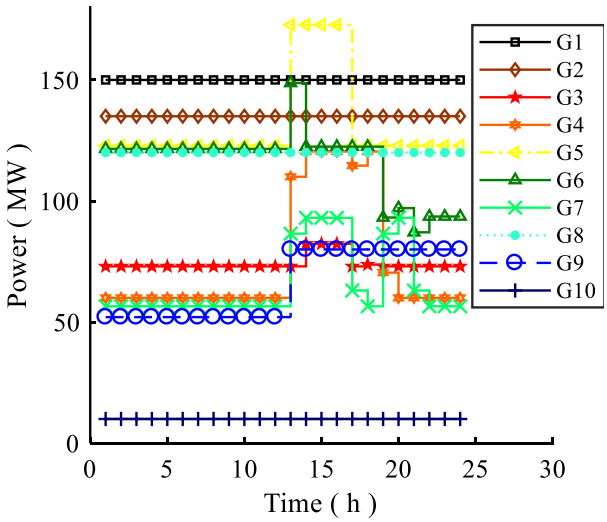

Fig. 7. Generated powers in test case 3 during 24 hours for Peak scenario.

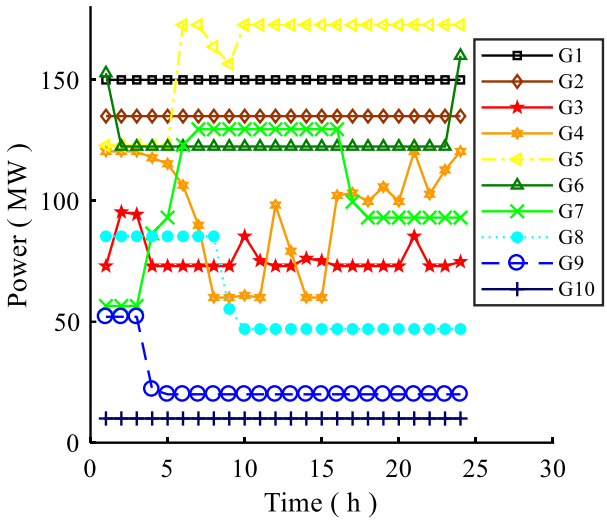

Fig. 2. Generated powers in test case 3 during 24 hours for Stochastic scenario.

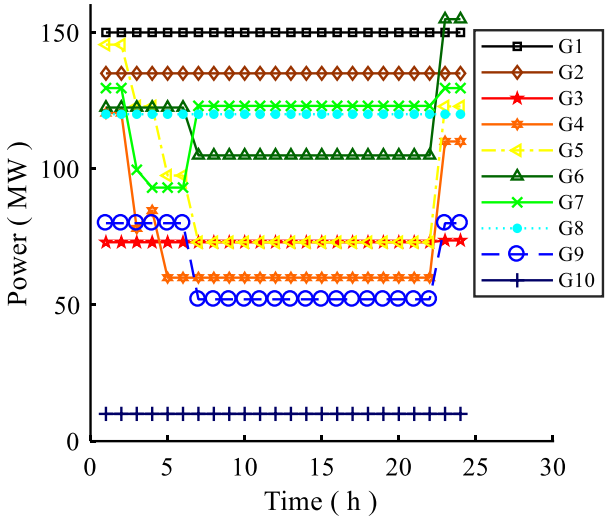

Fig. 9. Generated powers in test case 3 during 24 hours for Off-Peak scenario.

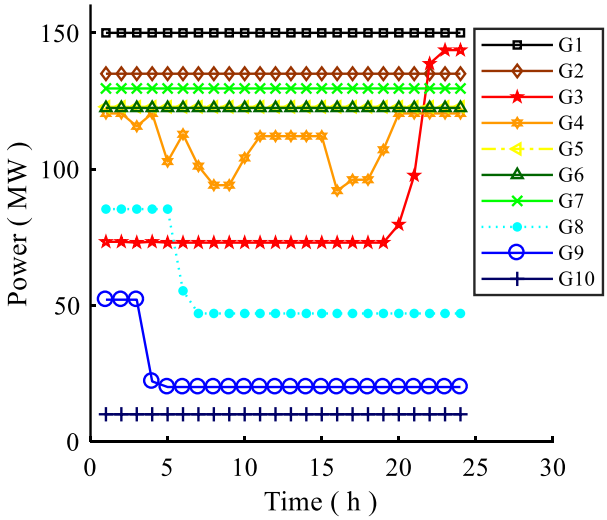

Fig. 10. Generated powers in test case 3 during 24 hours for EPRI scenario.

6. References

[1] Z. Lin, H. Chen,Q. Wu, W. Li, M. Li, T. Ji, "Mean-tracking model based stochastic economic dispatch for power systems with high penetration of wind power" , *Energy*, vol. 193, pp. 116826, 2020.

[2] T.C. Bora, V.C. Mariani, L. dos Santos Coelho, "Multi-objective optimization of the environmental-economic dispatch with reinforcement learning based on non-dominated sorting genetic algorithm", *Applied Thermal Engineering*, vol. 146, pp. 688-700, 2019.

[3] A. Srivastava, D.K. Das, "A new Kho-Kho optimization Algorithm: An application to solve combined emission economic dispatch and combined heat and power economic dispatch problem", *Engineering Applications of Artificial Intelligence*, vol. 94, pp. 103763, 2020.

[4] M. Nazari-Heris, M. Mehdinejad, B. Mohammadi-Ivatloo, G. Babamalek-Gharehpetian, "Combined heat and power economic dispatch problem solution by implementation of whale optimization method" *Neural Computing and Applications*", vol. 31, no. 2, pp. 421-436, 2019.

[5] U. Güvenç, E. Kaymaz, "Economic dispatch integrated wind power using coyote optimization algorithm", In 7th international Istanbul smart grids and cities congress and fair (ICSG), April 2019, Istanbul, Turkey, pp. 179-183. IEEE.

[6] E.E. Elattar, "Environmental economic dispatch with heat optimization in the presence of renewable energy based on modified shuffle frog leaping algorithm", *Energy*, vol. 171, pp. 256-269, 2019.

[7] F. Mohammadi, H. Abdi, "A modified crow search algorithm (MCSA) for solving economic load dispatch problem", *Applied Soft Computing*, vol. 71, pp. 51-65, 2018.

[8] H. Nourianfar, H. Abdi, "The application of Imperialist Competitive Algorithm to the combined heat and power economic dispatch problem", *Journal of Energy Management and Technology*, vol. 2, no. 4, pp. 59-69, 2018.

[9] N. Karthik, A.K. Parvathy, R. Arul, "Multi‐objective economic emission dispatch using interior search algorithm", *International Transactions on Electrical Energy Systems*, vol. 29, no. 1, pp. e2683, 2019.

[10] H. Nourianfar, H. Abdi, "Solving the multi-objective economic emission dispatch problems using Fast Non-Dominated Sorting TVAC-PSO combined with EMA", *Applied Soft Computing*, vol. 85, pp. 105770, 2019.

[11] J.F. Chen, S.D. Chen, "Multiobjective power dispatch with line flow constraints using the fast Newton-Raphson method", *IEEE Transactions on Energy conversion*, vol. 12, no. 1, pp. 86-93, 1997.

[12] J. Nanda, D.P. Kothari, K.S. Lingamurthy, "Economic-emission load dispatch through goal programming techniques", 1998.

[13] M.M. Deepika, A.K. Onkar, "Multicriteria optimization of variable thickness plates using adaptive weighted sum method", *Sādhanā*, vol. 46, no. 2, pp. 1-7, 2021.

[14] H. Nourianfar, H. Abdi, "Solving power systems optimization problems in the presence of renewable energy sources using modified exchange market algorithm", *Sustainable Energy, Grids and Networks*, vol. 26, pp. 100449, 2021.

[15] H. Nourianfar, H. Abdi, "Environmental/Economic Dispatch Using a New Hybridizing Algorithm Integrated with an Effective Constraint Handling Technique", *Sustainability*, vol. 14, no. 6, pp. 3173, 2022.

[16] G. Xiong, M. Shuai, X. Hu, "Combined heat and power economic emission dispatch using improved bare-bone multi-objective particle swarm optimization", *Energy*, pp. 123108, 2022.

[17] V.P. Sakthivel, M. Suman, P.D. Sathya, "Combined economic and emission power dispatch problems through multi-objective squirrel search algorithm", *Applied Soft Computing*, vol. 100, pp. 106950, 2021.

[18] H. Ma, Z. Yang, P. You, M. Fei, "Multi-objective biogeography-based optimization for dynamic economic emission load dispatch considering plug-in electric vehicles charging", *Energy*, vol. 135, pp. 101-111, 2017.

[19] Z. Yang, K. Li, Q. Niu, Y. Xue, "A comprehensive study of economic unit commitment of power systems integrating various renewable generations and plug-in electric vehicles", *Energy Conversion and Management*, vol. 132, pp. 460-481, 2017.

[20] U.K. Debnath, I. Ahmad, D. Habibi, A.Y. Saber, "Energy storage model with gridable vehicles for economic load dispatch in the smart grid", *International Journal of Electrical Power & Energy Systems*, vol. 64, pp. 1017-1024, 2015.

[21] Y. Zou, J. Zhao, D. Ding, F. Miao, B. Sobhani, "Solving dynamic economic and emission dispatch in power system integrated electric vehicle and wind turbine using multi-objective virus colony search algorithm", *Sustainable Cities and Society*, vol. 67, pp. 102722, 2021.

[22] G.C. Contaxis, C. Delkis, G. Korres, "Decoupled optimal load flow using linear or quadratic programming", *IEEE Transactions on Power systems*, vol. 1, no. 2, pp. 1-7, 1986.

[23] A.A. El-Keib, H. Ding, "Environmentally constrained economic dispatch using linear programming", *Electric power systems research*, vol. 29, no. 3, pp. 155-159, 1994.

[24] P. Mei, L. Wu, H. Zhang, Z. Liu, "A hybrid multi-objective crisscross optimization for dynamic economic/emission dispatch considering plug-in electric vehicles penetration", *Energies*, vol. 12, no. 20, pp. 3847, 2019.

[25] S. Behera, S. Behera, A.K. Barisal, "Dynamic Combined Economic Emission Dispatch integrating Plug-in Electric Vehicles and Renewable Energy Sources", *International Journal of Ambient Energy*, pp. 1-18, 2021.

[26] B. Qiao, J. Liu, "Multi-objective dynamic economic emission dispatch based on electric vehicles and wind power integrated system using differential evolution algorithm", *Renewable Energy*, vol. 154, pp. 316-336, 2020.

[27] N. Ghorbani, E. Babaei, "Exchange market algorithm for economic load dispatch", *International Journal of Electrical Power & Energy Systems*, vol. 75, pp. 19-27, 2016.

[28] N. Ghorbani, E. Babaei, "Exchange market algorithm", *Applied Soft Computing*, vol. 19, pp. 177-187, 2014.

[29] J. Sun, J. Deng, Y. Li, "Indicator & crowding distance-based evolutionary algorithm for combined heat and power economic emission dispatch", *Applied Soft Computing*, vol. 90, pp. 106158, 2020.

International Journal of Research and Technology in Electrical Industry

journal homepage: ijrtei.sbu.ac.ir

Shahid Beheshti University

A Comprehensive Study Approach for Evaluation of Resonance and Ferro-resonance in HV Substations

Mohamad Ali Amini[1], Mehdi SalayNaderi[2,*], Ali Asghar Farokhi rad[3], Gevork B. Gharehpetian[2]

[1] *Electrical Engineering Department, Iran University of Science and Technology, Tehran, Iran*
[2] *Electrical Engineering Department, Amirkabir University of Technology, Tehran, Iran*
[3] *Khuzestan Regional Electric Company (KREC), Khuzestan, Iran*

ARTICLEINFO

Article history:
Received 20 November 2021
Received in revised form 07 March 2022
Accepted 04 April 2022

Keywords:
Resonance
Ferroresonance
HV Substation
Power quality
Transient analysis

ABSTRACT

Resonance and ferroresonance in power systems are categorized as two destructive phenomena especially in HV networks which their occurrence are being initiated in consequence of a power system event. Hence, the study of resonance and ferroresonance requires an exhaustive evaluation of possible network events in different network configurations. In each event, the analysis of network voltages is conducted based on identified allowable limits by IEEE 519 standard as evaluation critera. In this paper, a novel comprehensive study approach is used for resonance and ferroresonance phenomena study in a real power system (KzREC). The utilized approach comprises different steps including substation equipment modeling, EMT simulation of the probable switching events, evaluation of correspondence results, and finally detecting the probable ferroresonance occurrence. Furthermore, voltage and current limits are implemented to define impedance criteria for performing resonance evaluation of network buses. In this paper, the detailed evaluation results of a 230 kV substation (Andimeshk) are presented as an example substation. By performing the proposed evaluations, the probable condition which may lead to resonance and ferroresonance occurrence are identified. The results are highly valuable for network operators in the prevention of unintended overvoltages occurrencesubstation.

1. Introduction

The ferroresonance term has first introduced at a conference in 1921 [1], refers to the phenomenon of voltage fluctuations in electrical circuits, which must include at least the following elements:

- A nonlinear inductor (ferromagnetic and saturable)
- A capacitor
- A voltage source (usually sinusoidal)
- Low loss (low ohmic resistance)

Power grids are comprised of a large number of saturable inductive equipments (such as power transformers, inductive voltage transformers (VTs) and shunt reactors). In addition, the presence of capacitive equipments (such as cable capacitances, transmission line

* Corresponding author
E-mail address: salaynaderi@aut.ac.ir
http://dx.doi.org/ 10.52547/ijrtei.1.1.57

capacitances, capacitive voltage transformers, parallel or series capacitor banks, grading capacitors of circuit breaker) is the other factor that can cause the occurrence of ferroresonance in the network. The main feature of the ferroresonance is that when it occurs, more than one parameter of the network are changed simultaneously and non-linearly [2]. Transient instabilities, lightning overvoltages, energization or de-energization of power transformers or loads, faults or faults clearing, and etc. may initiate the ferroresonance occurrence. Consequently, the operating points of the system can suddenly jump from a steady-state point (power frequency sinusoidal) to an operating point which the magnitude of voltage and current harmonics can seriously damage the equipment. Although history of the ferroresonance phenomenon in the power grid is very long, there is limited information about this complex phenomenon and it cannot be analyzed or predicted by linear computational methods [3, 4]. The lack of information and inaccurate identification of the phenomenon's behavior causes damages and malfunction of some equipment. Hence, the evaluation of ferroresonance in power networks requires the detailed modeling of network equipment. Then, according to standard criteria, the occurrence of ferroresonance is being evaluated.

On the other hand, resonance is an electromagnetic phenomenon of energy exchange between capacitive and inductive equipments of the network which store electric and magnetic fields, respectively. Various power system equipments, such as transformers and transmission lines that are modeled with capacitive and inductive elements, may cause resonance in electrical systems. If resonant frequencies of the system are initiated under certain conditions, for example by voltage or harmonic currents, significant current amplification or overvoltages can occur [5]. The resonance frequency is being determined by series and parallel configuration of capacitive and inductive elements in resonance circuit. If the harmonic frequencies of the currents are close to the system's parallel resonant frequencies, the voltage magnification in the system will be very high, especially in critical resonance situations. This can lead to malfunctions or, in the worst case, damage to electrical system equipments [6].

The study of resonance and ferroresonance in transmission substations requires a comprehensive study approach for the detection of their probable occurrence. Hence, in this paper, a novel and comprehensive study approach is proposed for the determination of the probable occurrence of the resonance and ferroresonance phenomena in power networks. The proposed approach comprises modeling of substation equipment, simulation of the probable switching events, evaluation of correspondence results, and finally detection of probable resonance and ferroresonance occurrence.

In this paper, Khuzestan regional electric transmission substations are evaluated in terms of possible resonance and ferroresonance conditions. Wherein, in the following, second section reviews the basic concepts of resonance and ferroresonance phenomena. Then, third section defines the utilized methodology for evaluations of resonance and ferroresonance phenomena in transmission substations. Afterward, in fourth section, the evaluation results are defined.

2. Basic concepts

Resonance and ferroresonance are electromagnetic transients which their occurrence affect the power quality indices of the network. In this paper, evaluation of their occurrence in HV substations of Khuzestan regional electric network is performed to identify the possible condition which their occurrence are probable. Hence, in order to present the evaluation method, in this section, the basic concepts of these two phenomena are briefly reviewed.

2.1. Ferroresonance in the electrical circuit

To explain the ferroresonance concept, a simple circuit comprising the critical elements for the ferroresonance study is presented in Fig. 1.

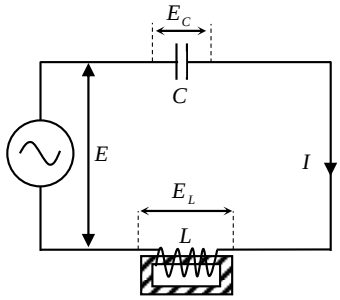

Fig. 1. Simple circuit for ferroresonance study

In an electrical circuit where an inductive element utilizes a ferromagnetic core, the relation between its voltage and current is non-linear. Fig. 2 shows the V-I characteristics of inductors and capacitors in the circuit.

As shown in Fig. 2, the inductor characteristic is non-linear and comprises linear and saturated regions. The non-linear characteristic shows that by increasing the inductor's voltage, the current would experience a large value. On the other hand, the V-I characteristic of a capacitor is linear. The equivalent impedance of series connection of non-linear inductor and linear capacitor results in a non-linear characteristic which is shown in the figure. By increasing the applied voltage from zero to a normal voltage (e), the operation point of M1 on the characteristic would determine the current value. In such conditions, the circuit current would be normal and the voltages across the elements would be lower than the applied voltage (e).

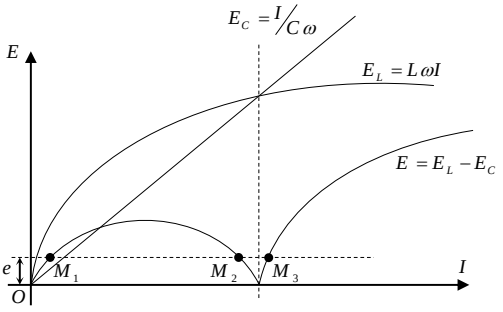

Fig. 2. V-I characteristics of inductor and capacitor in the circuit

As explained in the previous section, by the occurrence of an unwanted condition, such as network

faults, it is possible for the operation point to transfer from M1 to M2 or M3. In M2 or M3, the inductor is working in the saturated region and therefore the circuit current is high. Therefore, the network elements experience an overvoltage. A detail explanation of ferroresonance and the effect of element's values are presented in [7].

2.2. Resonance in the electrical circuit

The phenomenon of resonance exists in a large diversity of physical systems and arises when the system is affected by periodical excitation with a frequency similar to its natural frequency of oscillation. When a system is excited, it tends to oscillate at its natural frequency. If the excitation source has the same frequency as the system's natural frequency, the system's response to that excitation can be very large. In order to have resonance in a system, it is necessary to have two forms of energy storage, with energy being periodically transformed from one form to the other, and vice versa: in mechanical systems these are kinetic and potential energy, in electrical systems, these are electrical and magnetic energy. Thus, electrical circuits with magnetic and electric fields have the capability of resonating. Electrical resonance occurs when the magnetic and electric energy requirements are equal, just as a mechanical system resonates when kinetic and potential energy requirements are balanced. The phenomenon of resonance has very useful applications in some fields. For instance, in telecommunications, resonant circuits are used to select a group of frequencies from a broader group. Such application, as an example, can be part of a radio filter that selects one station for reception, rejecting all others, utilizing a variable capacitor.

A useful application of resonance in electrical power systems is the design of filters for the suppression of harmful harmonics. However, the phenomenon of resonance can also be very destructive in power systems. Special caution is required in the design and operation of the power network to avoid the occurrence of resonance at the power frequency (50/60 Hz). Such resonance occurrence would lead to uncontrolled system overvoltages that could stress and damage equipment.

Electrical resonance occurs in a circuit when the capacitive reactance (X_C) equals the inductive reactance (X_L) at the driving frequency. This frequency, also called natural frequency, is given by (1).

$$f_n = \frac{1}{2\pi\sqrt{L \cdot C}} \tag{1}$$

There are two types of resonance: series and parallel. A basic scheme of series resonance is in Fig. 3 (a) and parallel in Fig. 3 (b).

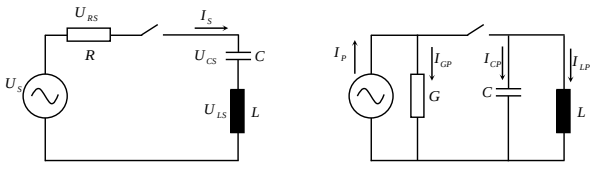

a) Series b) Parallel

Fig. 3. Basic scheme of series and parallel resonance

For every combination of L and C, there is only one frequency (in both series and parallel circuits) that causes XL to exactly match XC; this frequency is known as the natural or resonant frequency (1). When the resonant frequency is fed to a series or parallel circuit, XL becomes equal to XC, and the circuit is said to be resonant at that frequency.

In the case of series resonance, all circuit elements are in one branch with a common current (Fig. 3 (a)). The circuit impedance is given by (2). At low frequencies, the reactance of the capacitor dominates and the phase angle approaches 90°, with current leading voltage. As the frequency increases, the inductive reactance becomes significant and, at the resonant frequency (1), it grows to the point of canceling the reactance of the capacitor. At the resonant frequency, the inductor and capacitor series combination becomes invisible and R is the total impedance of the circuit. Voltages ULS and UCS reach high amplitudes but have opposing phase angles and cancel each other out. Note that series resonance must be excited by an alternating voltage source. At series resonance, the circuit current is limited only by the resistor R up to a value IS = US/R. At frequencies above resonance, the inductor dominates the circuit characteristics and the phase angle approaches 90° lagging.

$$Z_{series} = R + j\left(\omega L - \frac{1}{\omega C}\right) \tag{2}$$

In the case of parallel resonance, all circuit elements are in parallel and they have the same voltage (Fig. 3 (b)). The circuit admittance is given by (3). At low frequencies, the susceptance of the inductor is large and dominates the circuit admittance. As the frequency is increased, the inductive susceptance diminishes and the capacitive susceptance grows until they become equal at the resonant frequency (1). This resonance frequency is the same for parallel and series circuits. Thus, series and parallel resonance occur at the same frequency for the same combination of inductor and capacitor. At the resonant frequency, the inductor and capacitor parallel combination becomes invisible and G is the total admittance of the circuit. Currents I_{CP} and I_{LP} reach high amplitudes but have opposing phase angles and cancel each other out. Note that parallel resonance must be excited by an alternating current source. At parallel resonance, the circuit voltage is limited only by the conductance G. As the frequency increases above resonance, the capacitive susceptance dominates the circuit characteristics. Thus, the circuit admittance reaches its minimum at resonance and becomes very large at low and high frequencies. In other words, at low and high frequencies, the parallel circuit impedance is very small but it reaches a maximum at the frequency of resonance. This behavior is the opposite of the series circuit, where the impedance reaches its minimum at resonance.

$$Y_{parallel} = G + j\left(\omega C - \frac{1}{\omega L}\right) \tag{3}$$

3. Proposed approach for evaluation of resonance and ferroresonance in HV substations

3.1. Ferroresonance Study in HV Substation

Generally, the ferroresonance in HV substations occurred as a consequence of faults or fault clearing, circuit breaker operation and etc. Therefore, in order to evaluate the probable occurrence of ferroresonance in each substation, first, the critical substation components are modeled based on [7]. Ferroresonance is a local phenomenon and, as a general rule, large network models are not necessary. Only the main elements directly involved in the Ferro-resonant circuit (i.e. non-linear reactance, capacitances and voltage source) need to be represented in detail. Therefore both in ferroresonance and resonance studies, the feeding network can be represented as a Thevenin source equivalent calculated at power frequency. The critical components of each substation in ferroresonance studies are overhead lines, power and voltage transformers, shunt reactors and capacitor banks [7]. In this paper, in order to evaluate the probable situation of ferroresonance occurrence, all possible switching operation in each HV substation is considered. The voltages of substation buses are evaluated based on IEEE 519 standard to determine the occurrence of ferroresonance. In IEEE 519 standard (which is reviewed in appendix A), the allowable voltage distortion is defined based on each voltage level, allowable individual harmonic and Total Harmonic Distortion (THD) as presented in Table .

Table I. Allowable individual harmonic and total harmonic distortion based on IEEE 519 standard

Bus Voltage at PCC	Individual Harmonic (%)	Total Harmonic Distortion THD (%)
$V \leq 1.0kV$	5.0	8.0
$1.0kV < V \leq 69kV$	3.0	5.0
$69kV < V \leq 161kV$	1.5	2.5
$161kV < V$	1.0	1.5

As shown in the above table, for each voltage level, the allowable voltage distortion is determined by IEEE 519 standard to evaluate the occurrence of ferroresonance. In addition, in each voltage level, the RMS value of bus voltage is compared to allowable bus voltage [8-10]. In this paper, voltage distortion of substation buses are evaluated in three time intervals (TIs): before CB operation, after CB operation and after CB reclosing. The schematic time diagram of defined intervals is shown in Fig. 4.

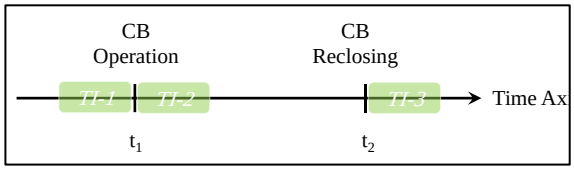

Fig. 4. Schematic time diagram of defined intervals

As shown in Fig. 4 three defined time intervals are evaluated in each CB operation. In addition, in each CB operation, three phases are evaluated to detect the probable occurrence of ferroresonance.

3.2. Resonance Study in HV Substation

The study of resonance in each HV substation is performed based on the proposed method in [8, 11]. In [8] a new method is proposed for the evaluation of impedance characteristic of network buses based on IEEE 519. According to IEEE 519, the allowable limit for current and voltages in each voltage level is defied. For further explanation, Fig. 5 shows the sample impedance characteristic in one of the network buses.

As shown in Fig. 5, the axis of harmonic order is divided into five zones based on the information provided in the standard in which the harmonic current limit is determined in each zone. By utilization of the allowable distortion of current and voltage, the acceptable value of impedance characteristic is determined as:

$$Z_{Zone_x}^{acceptable} = \frac{V^{h-allowed}(Table\ A.III)}{I^{h-allowed}(Table\ A.I - A.II)} \quad (4)$$

Where in zone x, according to table A.I-A.II of Appendix A, the acceptable impedance value ($Z_{Zone_x}^{acceptable}$) is calculated using the allowable voltage limit according to table A.III. The achieved impedance value is utilized for the evaluation of impedance characteristic of HV substation buses.

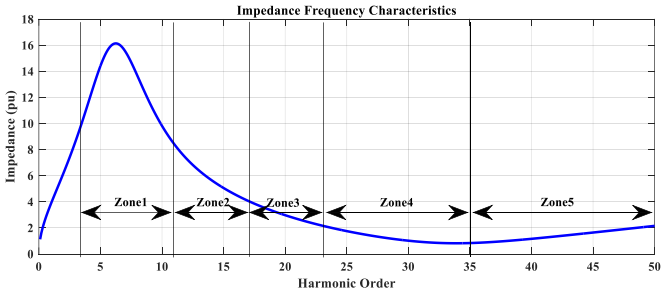

Fig. 5. Sample impedance characteristic in one of the network buses

3.3. Developed Infrastructure for Resonance and Ferroresonance Study

In order to provide an infrastructure for exhaustive study of resonance and ferroresonance evaluation, two well-known softwares are utilized: MATLAB and DIgSILENT Power Factory. DIgSILENT software is utilized in order to perform EMT studies of ferroresonance evaluation and impedance characteristic evaluation for resonance study. Then, the calculated results are transferred to the MATLAB software using a developed link to facilitate the evaluations studies with reference to the standard allowable limits. A schematic diagram of developed link is presented in Fig. 6.

Fig. 6. Developed Infrastructure for Resonance and Ferroresonance Study in Power Systems

As shown in the Fig. 6, two different softwares are utilized in this paper which constitute the study infrastructure for analysis of resonance and ferroresoancne in power systems. DIgSILENT software is implemented for performing power system related studies including EMT study for ferroresoancne analysis, load flow and short circuit studies for calculation of nominal and short circuit current magnitudes, and impedance frequency characteristic analysis for resonance evaluations. The calculation results are transferring to the MATLAB software for performing different analysis including FFT calculation, calculation of allowable voltage, current and impedance limits according to IEEE defined values, plotting comparative results and finally generating the final report.

4. Evaluation results

4.1. Current condition of the network

In order to evaluate the probable resonance and ferroresonance occurrence in each HV substation of the Khuzestan regional electricity network, the above-mentioned method is utilized. The Khuzestan regional electricity network comprises of 19 HV-400 kV and 37-230 kV substations. The defined evaluation process is performed on the HV substation one by one. In this paper, the detailed evaluation results of a 230 kV substation (Andimeshk) are presented. A single line diagram of the substation is shown in Fig. 7

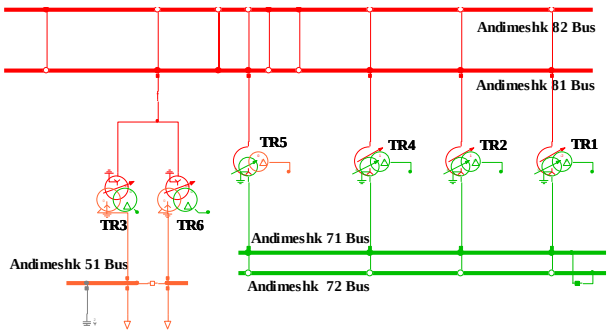

Fig. 7. Single line diagram of the Andimeshk 230 kV substation

As shown in Fig. 7, the substation contains three different voltage buses (230, 132 and 33 kV), 6 transformers and one capacitor bank. In order to perform an exhaustive study, all circuit breaker operations are considered and the resultant bus voltages are studied. Each circuit breaker is capable of single, two and three phase operations. Therefore, for each CB, seven operations are considered for three phases. In addition, in the ferroresonance study, for each CB, three time intervals are defined previously for evaluation. Therefore, for each CB, 3*7*3 different evaluation is performed for three parameters: Harmonic Distortion (HD), Total Harmonic Distortion (THD) and RMS value. For more explanation, the achieved results for one CB are presented here. Fig. 8 shows the maximum HD values in three phases for TI-1 in one circuit breaker (A7262 - Mentioned circuit breaker is one of 132 kV CBs - Andimeshk 71Bus.).

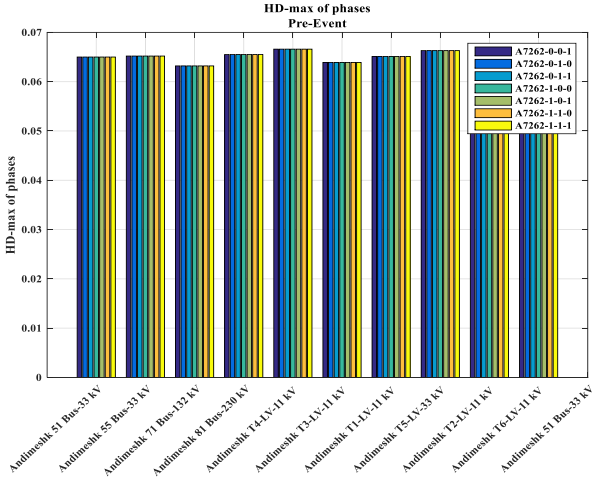

Fig. 8.: Maximum HD values in three phases for TI-1 in CB operation (A7262)

Fig. 8 shows the HD values in network buses for seven different operations of CB-A7262 in TI-1. As presented before in Table , the allowable limit for HD values in different voltage levels are satisfied. In addition, the THD values in TI-1 are presented in Fig. 9.

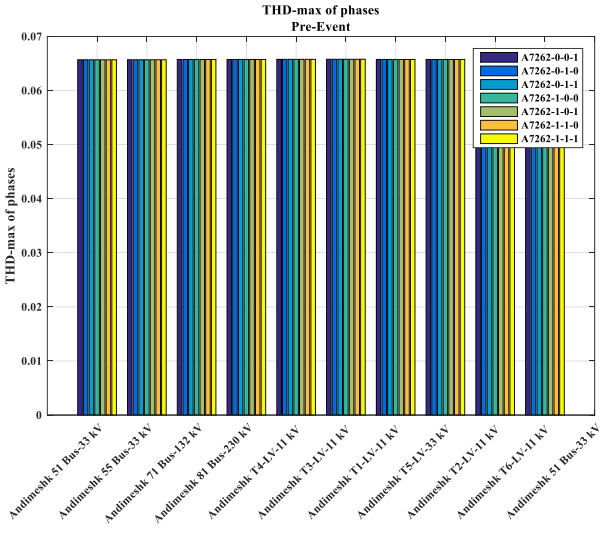

Fig. 9. Maximum THD values in three phases for TI-1 in CB operation (A7262)

Fig. 9 shows the THD values for different buses of Andimeshk 230 kV substation in TI-1. Comparing to Table , the THD values are within the allowable limit.

Fig. 10 shows the RMS values for different buses of Andimeshk 230 kV substation in TI-1.

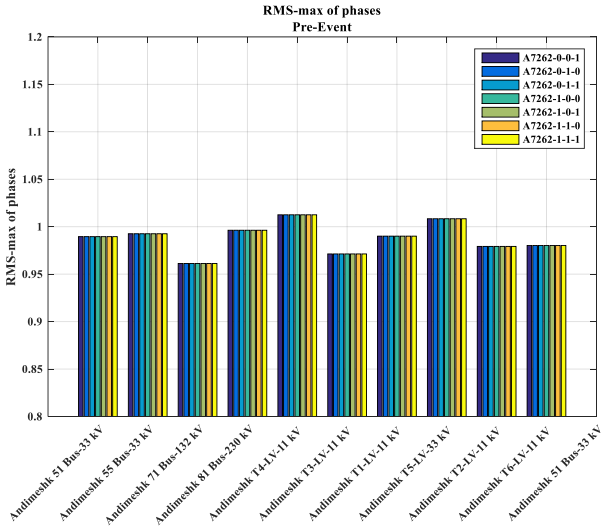

Fig. 10. Maximum RMS values in three phases for TI-1 in CB operation (A7262)

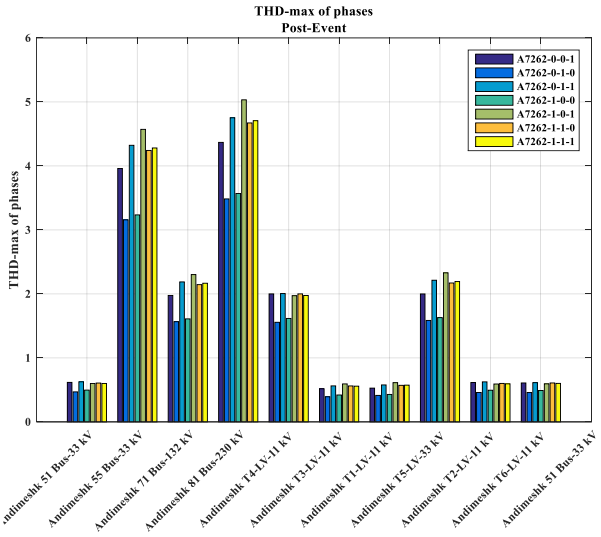

Fig 11. Maximum THD values in three phases for TI-2 in CB operation (A7262)

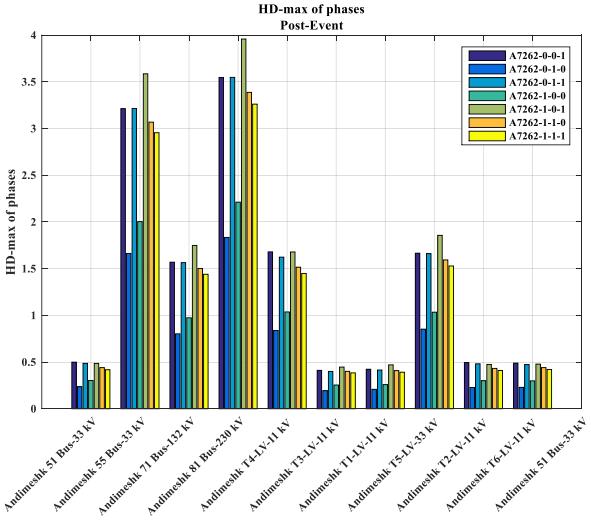

Fig. 12. Maximum HD values in three phases for TI-2 in CB operation (A7262)

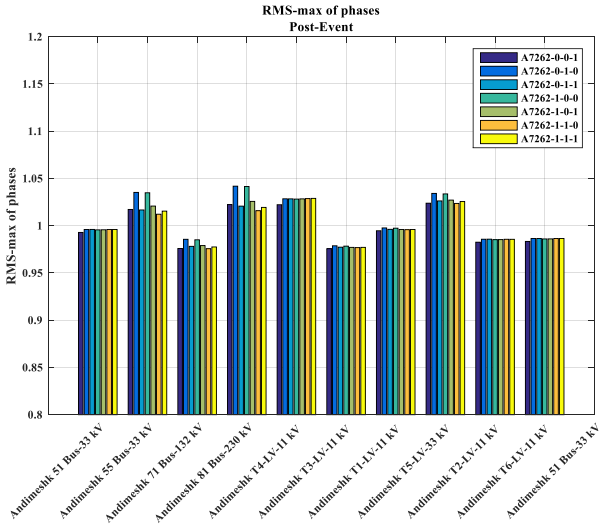

Fig. 13. Maximum RMS values in three phases for TI-2 in CB operation (A7262)

As shown in Fig. 10 the RMS values of bus voltages are in the allowable limit defined by IEEE standard.

In the following, Fig 11 to Fig. 13 shows the THD, HD and RMS values of bus voltages in TI-2 (i.e after CB operation).

As presented in the above figures, the THD and HD values in the 230 kV bus of the Andimeshk substation is out of the allowable limit. The resultant values indicate that the ferroresonance is occurs in some operations of A7262 CB and the 230 kV bus voltage is distorted. However, by consideration of the RMS value of the 230 kV bus in the mentioned CB operation, it is concluded that the ferroresonance severity is low and is neglectable since the resultant overvoltage in the 230 kV bus is not high enough to damage the equipment. The proposed approach is utilized in all HV substations of the Khuzestan regional electricity network.

On the other hand, the evaluation of the occurrence of resonance is performed by analysis of impedance characteristics of substation buses. The evaluation method is defined in the previous section. The impedance characteristics of bus 51 of Andimeshk substation in two operational conditions are shown in Fig. 14.

As shown in Fig. 14, the impedance characteristics of bus 51 while the capacitor bank is out of service are almost within the allowable limit. However, the impedance characteristic after the connection of the capacitor bank violates the allowable limit. This violation, increase the probability of resonance occurrence in harmonic order of 7-13. Flowing a harmonic current in the mentioned interval of harmonic order, would results in large harmonic voltage because of the occurrence of resonance. The mentioned evaluation is performed in all buses of network substations.

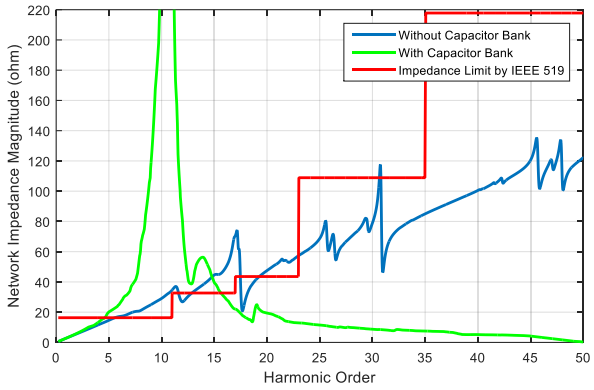

Fig. 14. Impedance characteristic of bus 33 kV of Andimeshk substation- with and without capacitor bank

4.2. Mitigation of Detected Resonance

In this section, the existing solutions to deal with the resonance phenomenon in the transmission network are categorized and presented. Strategies to deal with the resonance phenomenon are divided into active and inactive categories.

Passive solutions: refers to those methods of resonance mitigation which is performed in the design phase by modifying the power network, and therefore prevent the occurrence of resonance in the network.

Active solutions: refers to those methods of counteracting resonance that after identifying the phenomenon and subsequently, creating harmful overvoltages for the network and equipment, manual or automatic functions are activated and preventing from creating voltage or current stress on the equipment.

According to studies, in the 230 kV transmission substation of Andimeshk, if the 33 kV capacitive bank is connected to the 51 bus, there is a possibility of overvoltage due to resonance in the harmonic order of 10. It should be noted that due to the impedance characteristic of substation buses, power frequency resonance is not probable in this substation. Therefore, the possible occurrence of resonance at frequencies higher than the power frequency has been investigated. Since under normal conditions of the power network, there are no current flows in the network in harmonic orders other than the power frequency, so the occurrence of resonance overvoltage in these harmonic orders is not definite and is possible; Because only the presence of harmonic loads or saturation of magnetic cores in the network are the factors for the flow of harmonic currents in the network. Fig. 14 shows the impedance characteristic of bus 51 of this substation with and without capacitor bank. As shown in the figure, the value of the impedance characteristic of bus 51 in the condition of the capacitor bank in the harmonic order of about 10 is out of the allowable limit introduced by the standard. One of the effective ways to deal with overvoltages caused by the occurrence of resonance phenomenon is to modify the impedance characteristic so that in low harmonic orders where there is a possibility of harmonic currents, the impedance characteristic is a little less than the allowable limit.

For this purpose, a series reactor is integrated into the capacitive bank aimed at making a notch filter (single tune).

Fig. 15 shows the impedance characteristic of 33kV 51-bus of the substation.

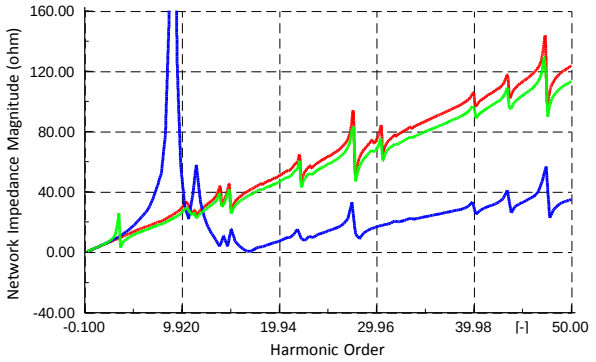

Fig. 15. Impedance characteristic of bus 33 kV of Andimeshk substation- Blue: With Capacitor bank, Red: Without Capacitor Bank, Green: With notch filter

As shown in the figure, the blue plot depicts the condition in which the capacitor bank is connected while the notch filter is not integrated. Besides, the red plot depicts the condition in which the capacitor bank is out of service and the red plot shows the impedance characteristic after the integration of the reactor to the capacitor bank. As it is concluded from the figure, the impedance characteristic is well improved and the resonance probability is resolved.

5. Conclusion

The occurrence of resonance and ferroresonance in power network result in overvoltages which are capable of damaging the network's equipment. In this research, efforts are made to identify the probable conditions for resonance and ferroresonance occurrence in Khuzestan regional electric network. Evaluation of ferroresonance is performed based on defined harmonic voltage distortion limits. IEEE 519 defines the harmonic distortion, total harmonic distortion and RMS values for different voltage levels in electrical networks. In addition, the defined allowable limits for current and voltage are utilized for defining an allowable limit for impedance characteristic in each voltage and current level. In general, the resonance and ferroresonance phenomena are initiated in consequence of network events such as intended or unintended CB operation. In order to perform an exhaustive research to identify the probable situation for the occurrence of resonance and ferroresonance, all CB operations including single phase, two phases and three phases in each substation are considered and evaluated. The resultant voltage waveforms in each substation's bus are evaluated in three time intervals including before CB operation, after CB operation and after CB reclosing. By performing the proposed evaluations, the probable condition which leads to the occurrence of resonance and ferroresonance are identified. The results are highly valuable for network operators for the prevention of unintended overvoltages.

6. References

[1] F. J. R. Margand, "Au sujet de l'existence de deux régimes en ferro-résonance," 1921.

[2] M. Yang, W. Sima, Q. Yang, J. Li, M. Zou, and Q. Duan, "Nonlinear characteristic quantity extraction of ferroresonance overvoltage time series," *IET Generation, Transmission & Distribution,* vol. 11, pp. 1427-1433, 2017.
[3] J. A. Corea-Araujo, F. González-Molina, J. A. Martínez, J. A. Barrado-Rodrigo, and L. J. I. T. o. P. D. Guasch-Pesquer, "Tools for characterization and assessment of ferroresonance using 3-D bifurcation diagrams," vol. 29, pp. 2543-2551, 2014.
[4] M. V. Escudero, I. Dudurych, and M. Redfem, "Understanding ferroresonance," in *39th International Universities Power Engineering Conference, 2004. UPEC 2004.*, 2004, pp. 1262-1266.
[5] C. Amornvipas and L. Hofmann, "Resonance analyses in transmission systems: Experience in Germany," in *IEEE PES General Meeting*, 2010, pp. 1-8.
[6] P. Mitra, A. De, A. J. I. J. o. E. P. Chakrabarti, and E. Systems, "Resonant behavior of EHV transformer windings under system originated oscillatory transient over voltages," vol. 33, pp. 1760-1766, 2011.
[7] Z. Emin, M. Martinez, M. Val Escudero, R. Adams, H. Bronzeado, B. Caillaut*, et al.*, "Resonance and Ferroresonance in Power Networks," *Electra - Cigrè,* vol. 272, pp. 81-85, 02/11 2014.
[8] M. Amini, A. Jalilian, and M. R. P. J. I. T. o. E. E. S. Behbahani, "A new method for evaluation of harmonic distortion in reconfiguration of distribution network," p. e12370, 2020.
[9] M. Amini, A. Jalilian, and M. R. P. J. E. P. S. R. Behbahani, "Fast network reconfiguration in harmonic polluted distribution network based on developed backward/forward sweep harmonic load flow," vol. 168, pp. 295-304, 2019.
[10] M. Amini and A. Jalilian, "Reduction of Short-Term Flicker Emission Using Genetic Algorithm-based Network Reconfiguration in Distribution Network," 2016.
[11] H. U. Patil, *Harmonic Resonance in Power Transmission Systems due to the Addition of Shunt Capacitors*: Arizona State University, 2015.
[12] T. M. Blooming and D. J. Carnovale, "Application of IEEE Std 519-1992 harmonic limits," in *Pulp and Paper Industry Technical Conference, 2006. Conference Record of Annual*, 2006, pp. 1-9.

7. Appendix a: defenition of IEEE std 519

The IEEE institute has introduced harmonic current and voltage limits to assess the harmonic status of power grids, including distribution and transmission networks[12]. The limits are defined based on Total Harmonic Distortion and Total Demand Distortion, according to (A.1) and (A.2), respectively.

$$THD_H = \frac{\sqrt{\sum_{i\geq 2} H_i^2}}{H_1} \qquad 1. \quad \text{(A.1)}$$

where H can be replaced by voltage and current.

$$TDD_I = \frac{\sqrt{\sum_{i\geq 2} I_i^2}}{I_{Max\,Demand}} \qquad 2. \quad \text{(A.2)}$$

IEEE Standard No. 519, which has been published to control harmonic distortions in power grids, determines the allowable harmonic distortion level at different harmonic orders according to Table A.I [12]. Table A.I represents the limits of harmonic voltages at a voltage level of 120 V to 69 kV and table A.II indicates the allowable range for a voltage level of 69 kV to 161 kV.

Table A.I. Current distortion limits for systems rated 120 V through 69 kV

I_{SC}/I_L	Maximum harmonic current distortion in presence of I_L					
	Individual harmonic order (odd harmonics)					
	$3\leq h<11$	$11\leq h<17$	$17\leq h<23$	$23\leq h<35$	$35\leq h<50$	TDD
<20	4	2	1.5	6	3	5
20<50	7	3.5	2.5	1	0.5	8
50<100	10	4.5	4	1.5	0.7	12
100<1000	12	5.5	5	2	1	15
> 1000	15	7	6	2.5	1.4	20

Table A.II. Current distortion limits for systems rated above 69 kV through 161 kV

I_{SC}/I_L	Maximum harmonic current distortion in presence of I_L					
	Individual harmonic order (odd harmonics)					
	$3\leq h<11$	$11\leq h<17$	$17\leq h<23$	$23\leq h<35$	$35\leq h<50$	TDD
<20	2	1	0.75	3	0.15	2.5
20<50	3.5	1.75	1.25	0.5	0.25	4
50<100	5	2.25	2	0.75	0.35	6
100<1000	6	2.75	2.5	1	0.5	7.5
> 1000	7.5	3.5	3	1.25	0.7	10

As shown in tables A.I and A.II, the allowable harmonic currents are divided into two general categories based on the voltage level. Also, at each voltage level, the harmonic current limits are also specified according to the short circuit level.

Furthermore, in this standard, according to the network voltage level, the THD limits and the individual harmonic distortion limit have been determined according to Table A.III.

Table A. III. Voltage Distortion Limit

Bus voltage V at PCC	**Individual Harmonic (%)**	**Total harmonic distortion THD (%)**
V≤***1kV***	5	8
1kV<*V*≤*69kV*	3	5
69kV<*V*≤*161kV*	1.5	2.5
161kV<*V*	1	1.5

3.

International Journal of Research and Technology in Electrical Industry

journal homepage: ijrtei.sbu.ac.ir

Shahid Beheshti University

A new approach to AC microgrids protection using a bi-level multi-agent system

Navid Ghaffarzadeh[1,*], Ali Bamshad[1]

[1] *Faculty of Technical and Engineering, Imam Khomeini International University, Qazvin, Iran*

ARTICLEINFO

Article history:
Received 17 January 2022
Received in revised form 28 March 2022
Accepted 04 April 2022

Keywords:
Microgrid protection
Bi-level MAS
Pilot impedance
Symlet DWT
Resilience
Uncertain parameters
DG

ABSTRACT

Nowadays, microgrids are expanding due to their numerous benefits. However, the control and protection of microgrids is a serious challenge. All the implemented plans for the protection of microgrids have drawbacks. This study presents a bi-level multi-agent system (MAS) approach to microgrids protection. The first level is responsible for microgrid lines protection. Firstly, it calculates the pilot impedance of each line. The pilot impedance is a limited number for internal faults of the line, but it is infinite for external faults of the line. so, the line's internal fault is detected by evaluation of pilot impedance with a predetermined value. The second level is responsible for Distributed Generation (DGs) protection. Firstly, it decomposes the DGs output signals by Discrete Wavelet Transform (DWT). Then, it multiplies the summations of the first and second level's details of each signal together as CC index. CC is zero in normal grid conditions and has a negative peak with a sharp negative rate in external faults, and will experience a positive peak with a sharp positive rate for internal faults and changes with a very slow rate in case of grid's natural transitions. So, the agent detects the fault by evaluating the CC. The simulation results in a 5-bus microgrid indicate the proposed scheme protects the microgrid with a reliability of 100% with considering all microgrid's uncertainties.

1. Introduction

A microgrid is defined in different ways from different perspectives. For example, the USA Energy Agency defines a microgrid as: "A microgrid consists of several loads and specific DG sources that can be controlled on their own. The microgrid can also be operated connected to the main grid or separately from it." Or from the perspective of the National Council for Electrical Systems, a microgrid is as: "A microgrid is a distribution network in which there are DG units and types of storage systems and loads, and can be operated separately or connected to the main distribution network [1]."

A concept that is common in all definitions is the presence of DGs in microgrids. In a way, a microgrid integrates DG resources with loads, which has various benefits, including:

- Improves power quality.
- Increases operating efficiency.
- Increases system reliability during power outages.
- Reduces project costs [2].

Literature review

However, in addition to the benefits of microgrids, and can meet the load's needs without emitting environmental pollution, there have also problems and complexities to

* Corresponding author
E-mail address: ghaffarzadeh@eng.ikiu.ac.ir
http://dx.doi.org/ 10.52547/ijrtei.1.1.66

control and protection [3]. Traditional distribution systems are often radial and fed from one side. However, microgrids contain DG units and can be fed from two sides, either connected to the main grid or separately from the network, which disrupts the protection coordination of the relays [4]. Some researchers proposed overcurrent relays for microgrids protection [5–7]. This approach is simple and economical but further studies should be performed on these plans to separate the short circuit fault from the transient states of the grid and also is influenced by microgrid topology it is more effective in islanded mode [1]. Some authors recommended directional overcurrent relays [8–10]. This approach has an additional complex coordination process and further studies should be performed on these plans to separate the short circuit fault from the transient states of the grid and is more expensive than overcurrent relaying [1].

Some other researchers recommended distance protection [11–13]. The main advantage of this plan is the lack of influence of source impedance. The drawbacks of this plan are the bidirectional power flow, power swing, and high impedance faults can disrupt the protection plan. Also, this plan is influenced by microgrid topology and is expensive [1]. Some other authors recommended implementing the differential protection plans [14,15]. This plan is sensitive and selective, fast and simple, and independent of power swing and fault resistance [1]. Any disturbance in telecommunication links or metering equipment, or delays in telecommunications links, can disrupt the whole plan. This plan is also too expensive [1].

Some researchers also implemented sequence or symmetrical components approaches [16-19]. The most important advantage of using this plan is that the relay settings change during different grid operation conditions and thus, the relay is prepared to detect any further fault [1]. One of the most important weaknesses of this plan is that it requires a lot of telecommunication links, and if any of them is disrupted, the whole plan will be useless. Also, this plan is influenced by microgrid topology and is too expensive [1].

Some other researchers proposed frequency and voltage-based approaches to protect the microgrids [20-23]. One of the important advantages of these plans is that the islanding detection is a low-cost prosecution and it does not have detrimental effect on the power quality. One of the biggest disadvantages of this plan is that there are many unrecognizable zones for the plan [1]. Other researchers proposed some methods based on traveling waves [24,25]. This plan has two main advantages [1]:

1) The first advantage is that the location of the fault can be correctly identified.

2) The second advantage of this plan is it detects the fault quickly.

Also, this plan has the following drawbacks [1]:

1) This plan requires a high sampling rate.

2) This plan needs a low-bandwidth communication channel to reach fast action.

Some other researchers proposed the multi-agent system (MAS) approach for protection [26-30]. It is a powerful tool that distributes the task of fault detection across multiple agent systems and in a way, decomposes the protection problem between multiple agent systems. Also, this approach has the following drawbacks [1][31]:

1) This plan has a peer-to-peer nature, so the security of the protection plan can be threatened.

2) Intelligent agent plan must be done properly to ensure the security and reliability of the plan.

3) These schemes often rely on a single CPU, which becomes useless if this CPU is disrupted.

4) These plans require telecommunication links, which increases the cost of the plan and the large burden of telecommunication links can disrupt the telecommunication operation, by grid & DG expansion.

1.2. Plan novelty

In this study, a bi-level multi-agent system (MAS) approach has been proposed to protect AC microgrids. the proposed Mas-based approach uses two vigorous techniques that make more powerful agent systems. The first agent detects and clears the faults in microgrid lines by a pilot impedance technique and the second agent detects and clears the internal faults of DGs by a Symlet discrete transform. In this way, the protection burden is decomposed between two agents and each agent has 100% reliability. The main advantages of the proposed plan can summarize as:

- The agents are very fast in fault detection.
- The plan is not dependent on a single CPU because each line has an independent agent.
- The agents need no telecommunication link together. So, the grid or DGs expansion will not influence the plan and there will be no disturbance on the communication link to disrupt the plan operation.
- The plan reliability and selectivity is 100%.
- Due to the lack of telecommunication links usage, which usually costs a lot, the plan will have a reasonable cost.

Various agent system-based schemes have been proposed to protect the distribution networks or microgrids so far. The main superiority of this study over other plans is the plan does not need coordination between protection installations or telecommunication links, while the previously proposed agent systems require coordination between protection installations or use telecommunication links. In some cases, such plans do not perform truly and the plan fails to operate. so the reliability is overshadowed or the cost of the plan increases too much [32-34].

2. Proposed approach

The implemented network in Fig. 4 has two parts. The first part is the network power lines and the second part is the DGs that are connected to the buses. Fig. 1 shows the proposed scheme for the protection of AC microgrid in Fig. 4. Each agent operates independently of the other. The first agent, determines the fault within each line correctly, using the pilot impedance technique. Firstly, the current and voltage samples of each terminal of the line are sent to the agent. It then calculates the impedance for both sides of the line by the pilot impedance equations. Finally, the agent realizes that a fault has occurred by evaluating this impedance.

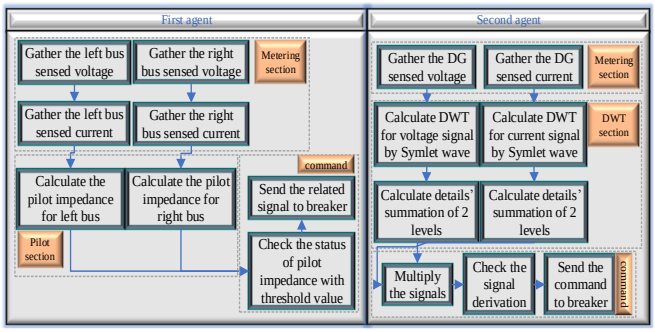

Fig. 1. Proposed agent system schematic

The second agent determines the fault within the DG units using Symlet DWT. First, the second agent receives the current and voltage output samples of each DG's output at its point of common connection (PCC) to the microgrid. It then decomposes the signals using a second level, eight order symlet DWT. Then, the mathematical summation of the first and second-level details of the signal is calculated at each moment. The obtained summations for the voltage signal and the current signal are multiplied by each other, and the agent detects the fault by evaluating the changes' rate of this product.

2.1. First agent

Fig. 2 is part of a microgrid, containing a line between two buses, in which a fault has occurred in this line:

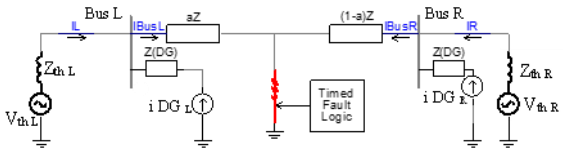

Fig. 2. a line of microgrid with internal fault

A KVL from the left side and right side to the fault point is written according to (1):

$$V_{th_L} - V_{th_L}.i_L - (\alpha Z)(i_L + i_{DG_L}) = V_{th_R} - V_{th_R}.i_R - (1-\alpha)Z\,(i_R + i_{DG_R}) \quad (1)$$

Where a is the length of faulted line in percent, $i_{DG\,L}$ and $i_{DG\,R}$ are the left side and right side DG contribution respectively and voltage and current passing through the buses can express as (2) to (5):

$$V_{th_L} - V_{th_L}.i_L = V_{Bus_L} \quad (2)$$

$$V_{th_R} - V_{th_R}.i_R = V_{Bus_R} \quad (3)$$

$$i_L + i_{DG_L} = i_{Bus_L} \quad (4)$$

$$i_R + i_{DG_R} = i_{Bus_R} \quad (5)$$

By interpreting (1) to (5) in (1):

$$V_{Bus_L} - (\alpha Z) i_{Bus_L} = V_{Bus_R} - (1-\alpha)Z\, i_{Bus_R} \quad (6)$$

$$V_{Bus_L} - V_{Bus_R} + Z\, i_{Bus_R} = (\alpha Z) i_{Bus_L} + (\alpha Z) i_{Bus_R} \quad (7)$$

By adding $\left(\frac{Z}{Z_{DG_L}} V_{Bus_L}\right)$ to both sides of (7):

$$V_{Bus_L} - V_{Bus_R} + Z\, i_{Bus_R} + \frac{Z}{Z_{DG_L}} V_{Bus_L} = (\alpha Z)(i_{Bus_L} + i_{Bus_R}) + \frac{Z}{Z_{DG_L}} V_{Bus_L} \quad (8)$$

By dividing both sides of (8) to $(i_{Bus_L} + i_{Bus_R})$:

$$\frac{V_{Bus_L} - V_{Bus_R} + Z\, i_{Bus_R} + \frac{Z}{Z_{DG_L}} V_{Bus_L}}{i_{Bus_L} + i_{Bus_R}} = \alpha Z + \frac{\frac{Z}{Z_{DG_L}} V_{Bus_L}}{i_{Bus_L} + i_{Bus_R}} \quad (9)$$

Where the left side of (9) is considered as the pilot impedance in point aspect of the left bus:

$$Z_{pilot_L} = \frac{V_{Bus_L} - V_{Bus_R} + Z\, i_{Bus_R} + \frac{Z}{Z_{DG_L}} V_{Bus_L}}{i_{Bus_L} + i_{Bus_R}} \quad (10)$$

Also (6) can be rewritten as:

$$V_{Bus_R} - V_{Bus_L} = Z\, i_{Bus_R} - (\alpha Z) i_{Bus_R} - (\alpha Z) i_{Bus_L} \quad (11)$$

By adding $\left(Z i_{Bus_L} + \frac{Z}{Z_{DG_R}} V_{Bus_R}\right)$ to both sides of (11):

$$V_{Bus_R} - V_{Bus_L} + Z\, i_{Bus_L} + \frac{Z}{Z_{DG_R}} V_{Bus_R} = (Z)(i_{Bus_L} + i_{Bus_R}) - (\alpha Z)(i_{Bus_L} + i_{Bus_R}) \frac{Z}{Z_{DG_R}} V_{Bus_R} \quad (12)$$

By dividing both sides of (12) to $(i_{Bus_L} + i_{Bus_R})$:

$$\frac{V_{Bus_R} - V_{Bus_L} + Z\, i_{Bus_L} + \frac{Z}{Z_{DG_R}} V_{Bus_R}}{i_{Bus_L} + i_{Bus_R}} = (1-\alpha)Z + \frac{\frac{Z}{Z_{DG_R}} V_{Bus_R}}{i_{Bus_L} + i_{Bus_R}} \quad (13)$$

Where the left side of (13) is considered as the pilot impedance in point aspect of the right bus:

$$Z_{pilot_R} = \frac{V_{Bus_R} - V_{Bus_L} + Z\, i_{Bus_L} + \frac{Z}{Z_{DG_R}} V_{Bus_R}}{i_{Bus_L} + i_{Bus_R}} \quad (14)$$

But for an external fault as depicted in Fig. 3:

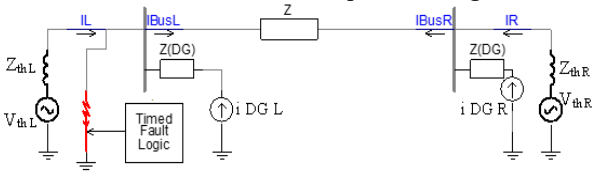

Fig. 3. a line of microgrid with external fault

(15) & (16) can be expressed as:

$$i_{Bus_L} = \frac{V_{Bus_L} - V_{Bus_R}}{Z} \quad (15)$$

$$i_{Bus_R} = \frac{V_{Bus_R} - V_{Bus_L}}{Z} \quad (16)$$

By implementation of (15) & (16) in pilot impedance of right bus and left bus, (17) is concluded for external faults:

$$Z_{pilot_R} = Z_{pilot_L} = \infty \quad (17)$$

Therefore, if the calculated pilot impedance is larger than the threshold value, it means that a fault has occurred outside the line and there is no need to operation of breakers of line, but if the output impedance has less than the threshold, This means that the fault occurred inside the protected line and the breakers at both ends of the line must operate and isolate the line. This is because a microgrid can be non-radial as shown in Fig. 4 and if the line is broken on one side, the fault is still fed on the other side. The threshold value of agent operation is also set at 3000.

This threshold has been set to distinguish some possible transient states, such as sudden changes in load, and output power of renewable units, with faults. Each change in load and renewables output is expressed with its normal probability function in this study.

2.2. Second agent

Initially, the current and voltage signals of each solar and wind unit, are sampled and sent to the second agent right at the PCC of units to the microgrid. Then each signal is decomposed as:

DG output current signal: $\rightarrow (g^1, h^1)$ (18)

DG output voltage signal: $\rightarrow (g^1, h^1)$ (19)

Where:

g^1 current signal: $\rightarrow (g^2, h^2)$ (20)

g^1 voltage signal: $\rightarrow (g^2, h^2)$ (21)

So:

current signal: $\rightarrow (g^2, h^2, h^1)$ (22)

voltage signal: $\rightarrow (g^2, h^2, h^1)$ (23)

where:

$$g^n = \left(g_1^n, g_2^n, g_3^n, g_4^n, g_5^n, g_6^n, g_7^n, g_8^n\right) \quad (24)$$

$$h^n = \left(h_1^n, h_2^n, h_3^n, h_4^n, h_5^n, h_6^n, h_7^n, h_8^n\right) \quad (25)$$

The current signal of each DG can be decomposed as (26):

$$current\ \ DWT = \sum_{k=1}^{N} h^1\ I\_DG(k) + \sum_{k=1}^{N} h^2\ I\_DG(k) \quad (26)$$

The voltage signal of each DG can be decomposed as (27):

$$voltage\ \ DWT = \sum_{k=1}^{N} h^1 V\_DG(k) + \sum_{k=1}^{N} h^2 V\_DG(k) \quad (27)$$

Where the N is the order of DWT that has been set on 8. Then the CC index is defined according to (28):

$$CC\ \ index = current\ \ DWT \times voltage\ \ DWT \quad (28)$$

Then the agent system calculates the rate of changes of the CC index. Two scenarios May happen:

A) If $\frac{d(CC)}{dt} > 0$, the fault is inside of DG.

B) If $\frac{d(CC)}{dt} < 0$, the fault is outside of DG.

This index will experience a sharp negative rate if the fault occurred outside of the DG unit. If this fault has occurred within the DG unit, this index will experience a sharp positive change. So, the derivation of the CC index is sent to the second agent's relay. The threshold margin value of this agent is considered to be 1300.

3. Results and discussion

In this section, the implemented network case study is interpreted at first, and then the proposed plan is implemented on the under-study network.

Implemented case study

To implement the proposed plan, a 5-bus microgrid is implemented according to Fig. 4:

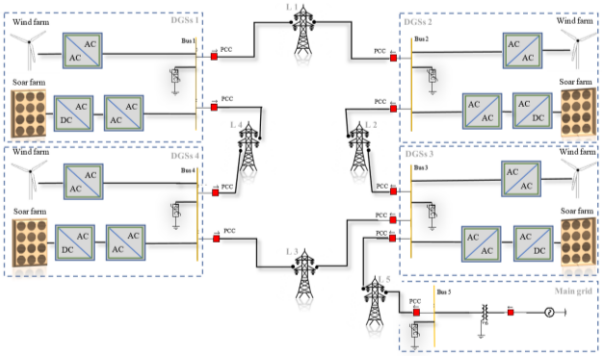

Fig. 4. understudy microgrid

circular grids have the following advantages over radial grids:

1) They have less blackout compared to the radial grid.

2) They don't need to use maneuver lines.

3) There is no worry about the insulation failure of the lines.

Also, the technical characteristics of photovoltaic panels can be expressed by Table. I:

Table I. photovoltaic panels feature

Solar panels characteristics	
Peak power (WP)	335
Open circuit voltage (V)	46.24
Short circuit current (A)	9.30
Voltage at Pmax (V)	38.12
Current at Pmax (A)	8.79
Efficiency (%)	17.19
Dimension (mm)	992*1964*35
Weight (Kg)	21.6 (+/-0.1)
Irradiation rate limit (in PSCAD)	1000 [1/s] / (W/m^2/sec)
Temperature rate limit (in PSCAD)	5 [1/s] / (C/sec)
Fire safety classification	Class C
Number of series modules per array	36
Number of parallel modules per array	24
Number of cells per panel	72

And the tie-line characteristics are depicted according to Table II:

Table II. lines characteristics

Tie line	R(ohm)	L (mH)
L_1	0.38 Ω	0.23 mH
L_2	0.45 Ω	0.16 mH
L_3	0.49 Ω	0.29 mH
L_4	0.71 Ω	0.32 mH
L_5	0.65 Ω	0.18 mH

Also, the technical characteristics of wind units are represented by Table III:

Table III. wind units feature

windfarm characteristics	
Rated power	2000kW
Cut-in wind speed	4m/s
Rated wind speed	13m/s
Cut-out wind speed	25m/s
Rotor diameter	90 m
Number of blades	3
Max rotor speed	14.9 U/min
Gearbox efficiency	97%
Governor proportional gain	6.2 [deg/p.u]
Governor integral gain	6.2
Governor deferential gain	0.05 [deg/p.u]
Governor gain multiplier	30 [deg/pu]
Tip speed	70 m/s

tower height	80*95*105 m

The following uncertainties are also considered for the network:

1) load uncertainty
2) Connection or disconnection from the main grid
3) Type of fault
4) fault impedance
5) fault location
6) Output of wind and solar units

These uncertainties are implemented according to the Table IV:

Table IV. uncertainty parameters of microgrid

parameter	Different status
Wind capacity	Wind speed=Norm (13,4)
PV capacity	Temp= Norm (40-10), Irrad= Norm (1200-200)
Fault location	Lines (#1-2-3-4-5), DGs (#6-7-8-9)
Fault type	1 ϕ (AG)- 2 ϕ (ABG)- 3 ϕ (ABCG)
Fault impedance	Bolt-10$_\Omega$-30$_\Omega$-60$_\Omega$
Connection to main grid	Connect (1), disconnect (0)
load	Norm (70,20Kw – 40,15Kvar)

Fault locations of #6-7-8-9 refer to fault inside of in DGs 1,2,3,4 respectively and fault location of #1-2-3-4-5 refers to a fault in lines of 1,2,3,4,5 respectively.

Uncertainties in the form of lists, such as fault location, fault type, fault impedance, and grid operation mode, do not require sampling and are defined as numbers (real or binary) for the Multiplerun module. Uncertainties, which are in the form of probability density function (PDF), are sampled using the CDF^{-1} method in Excel software in the first step. Then, the samples are entered into the Multiplerun module as the real numbers. Finally, all the uncertainties are implemented simultaneously in the Multiplerun block during simulation.

Simulation results

Uncertainties considered as normal PDFs, always change throughout the simulation independently. Other parameters such as fault location, fault impedance, type of fault, connection or disconnection of the microgrid from the main grid also created a total of 216 different states. Also, ten samplings were performed for PDFs using the library Monte Carlo method in each different 216 states. This means that ten sets of sampling are performed for each of these 216 cases. Eventually, 2160 different modes emerge. Table V depicts the implemented agent's operation on line 3, under all 2160 different modes:

Table V.a. L3 agent operation for fault in its zone

uncertainty	First agent relay command on L3	second agent relay command on DGs
R $_{load}$ ~ N(70, 20Kw|40,15Kvar) Wind speed ~N (13, 4) temp ~N (40, 10) Irrad ~N (1200,200) Fault type (1-2-3 phase) Fault impedance (0-10-30-60) Fault location (#3) PCC (0-1)	1	0

Table V.b. L3 agent operation for external faults 1 to 5

uncertainty	First agent relay command on L3	second agent relay command on DGs
R $_{load}$ ~ N(70, 20Kw|40,15Kvar) Wind speed ~N (13, 4) temp ~N (40, 10) Irrad ~N (1200,200) Fault type (1-2-3 phase) Fault impedance (0-10-30-60) Fault location (#1-2-4-5) PCC (0-1)	0	0

Table V. c. L3 agent operation for external faults 6 to 9

uncertainty	First agent relay command on L3	second agent relay command on DGs
R_{load} ~ N(70, 20Kw|40,15Kvar) Wind speed ~N (13, 4) temp ~N (40, 10) Irrad ~N (1200,200) Fault type (1-2-3 phase) Fault impedance (0-10-30-60) Fault location (#6-7-8-9) PCC (0-1)	0	1

Table VI depicts the implemented agent's operation on the DG 4, under all 2160 different modes. A fault has occurred in the wind generator.

Table VI. a. DG 4 agent action for external faults 1 to 5

uncertainty	First agent relay command on lines	second agent relay command on DGs' 4
R_{load} ~ N(70, 20Kw|40,15Kvar) Wind speed ~N (13, 4) temp ~N (40, 10) Irrad ~N (1200,200) Fault type (1-2-3 phase) Fault impedance (0-10-30-60) Fault location (#1-2-3-4-5) PCC (0-1)	0	0

Table VI. b. DG 4 agent action for external faults 6 to 8

uncertainty	First agent relay command on lines	second agent relay command on DGs' 4
R_{load} ~ N(70, 20Kw|40,15Kvar) Wind speed ~N (13, 4) temp ~N (40, 10) Irrad ~N (1200,200) Fault type (1-2-3 phase) Fault impedance (0-10-30-60) Fault location (#6-7-8) PCC (0-1)	0	0

Table VI. c. DG 4 agent action for internal fault

uncertainty	First agent relay command on lines	second agent relay command on DGs' 4
R_{load} ~ N(70, 20Kw|40,15Kvar) Wind speed ~N (13, 4) temp ~N (40, 10) Irrad ~N (1200,200) Fault type (1-2-3 phase) Fault impedance (0-10-30-60) Fault location (#9) PCC (0-1)	0	1

Also, Fig. 5 depicts the operation of 2 agents under different fault locations:

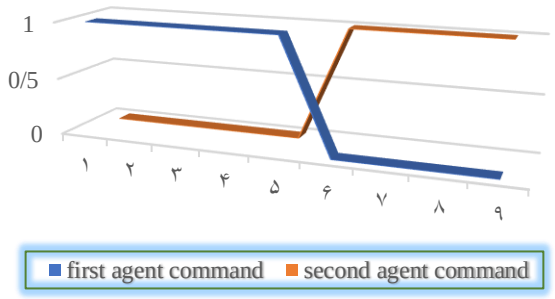

Fig. 5. agent's operation in different locations

Fig. 5 demonstrates the first agent system operates for faults in zones 1 to 5 where is its protection zone, and the relay output is equal to 1. On the other hand, the agent output is zero for faults in zones 6 to 9 where is not its zone and the agent does not act truly.

Also, the second agent system operates for faults in zones 6 to 9 where is its protection zone, and the relay output is equal to 1. On the other hand, the agent output is zero for faults in zones 1 to 5 where is not its zone and the agent does not act truly. This means the reliability and selectivity of the agents are 100%.

Figs. 6 & 7 depicts the first agent decision signal for the internal and external faults in line 1 for grid disconnected mode:

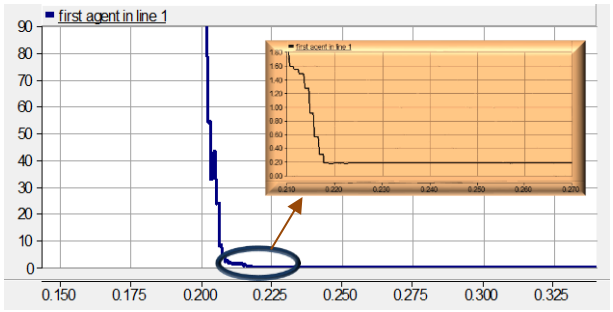

Fig. 6. 1st agent decision signal (2 ϕ ,30$_\Omega$ fault in L1)

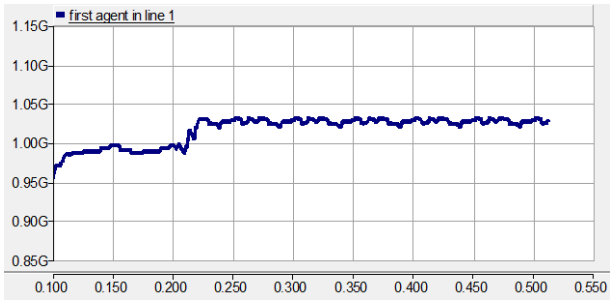

Fig. 7. 1st agent decision signal (2 ϕ ,30$_\Omega$ fault out of L1)

as it is visible in Figs 6 and 7, the almost constant and finite value of pilot impedance is related to an internal fault but a huge value for pilot impedance is related to an external fault for a line.

Also, Figs 8 to 11 depict the voltage and current waveforms for the internal 3 phase, bolt fault in 40% of the initial line 1 near to bus 1 in grid-connected mode:

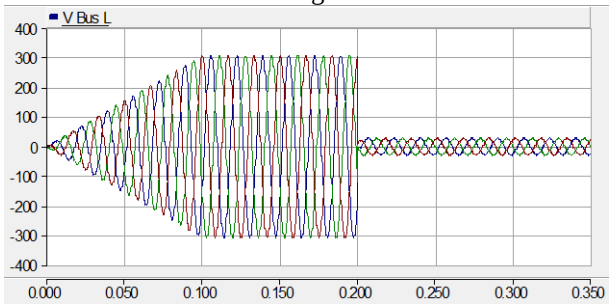

Fig. 8. voltage waveform in aspect of bus 1 (L1 fault)

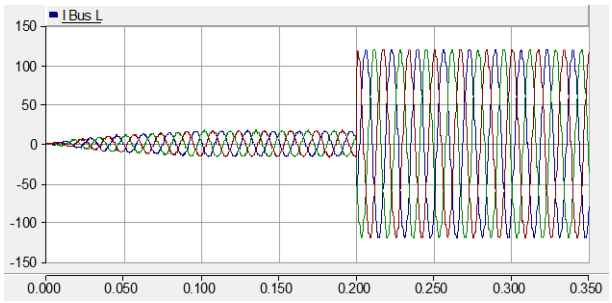

Fig. 9. current waveform in aspect of bus 1 (L1 fault)

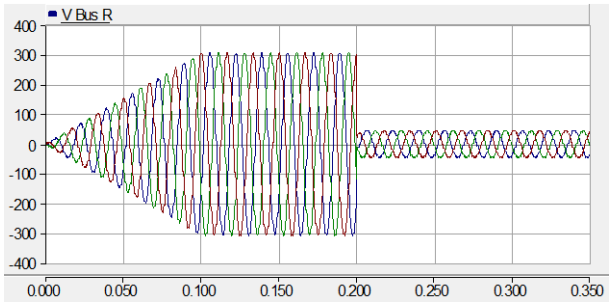

Fig. 10. voltage waveform in aspect of bus 2 (L1 fault)

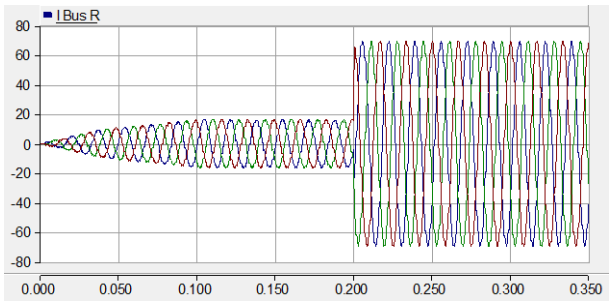

Fig. 11. current waveform in aspect of bus 2 (L1 fault)

Figs. 12 and 13 depict the second agent decision signal for the internal and external faults in DG 2 for grid disconnected mode:

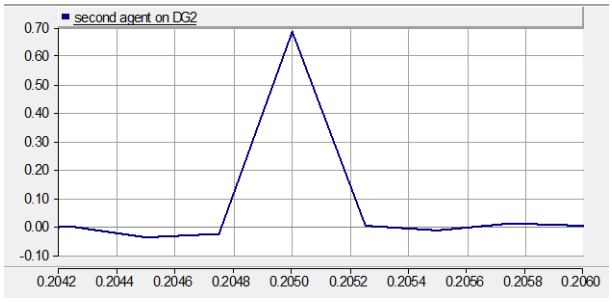

Fig. 12. 2nd agent decision signal (3 ϕ ,30$_\Omega$ fault in PV unit of DG2)

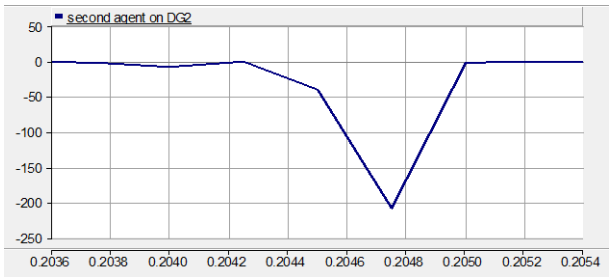

Fig. 13. 2nd agent decision signal (3ϕ ,30_{Ω} fault in L2)

as it is visible in Figs 12 & 13, the incremental ramp rate in the input signal of the second agent system meaning to an internal fault, and incremental ramp rate meaning to an external fault.

4. Conclusion

The presence of distributed generation sources in a microgrid changes its radial nature. This can cause conventional protection schemes to maloperation or be disrupted completely. Various approaches have been proposed to resolve this problem by researchers. But each plan has its drawbacks including the plan's cost, the poor performance of the plan in some conditions that threaten the reliability, complex online calculations, etc. In this study, a bi-level multi-agent system is presented for AC microgrid protection. The first level detects any faults on lines in less than one cycle using the pilot impedance technique and sends the trip command to the breaker. The second agent detects any faults within the distributed generations using a Discrete Wavelet Transform in maximum of 5 milliseconds and sends the trip command to the breaker. Therefore, the operational advantages of the plan can be summarized as:

1) High-performance speed in fault detection
2) Requires current and voltage samples only
3) Any disruption in an agent operation does not influence other agents and doesn't disrupt the other agents.

Also, the proposed plan has a reasonable cost to implement and has 100% reliability.

5. References

[1] B. Patnaik, M. Mishra, R. C. Bansal, and R. K. Jena, "AC microgrid protection – A review: Current and future prospective," *Appl. Energy*, vol. 271, no. May, pp. 115-210, 2020.

[2] A. Bamshad, O. Safarzadeh, "Effects of the move towards Gen IV reactors in capacity expansion planning by total generation cost and environmental impact optimization." *Nucl. Eng. Technol*, vol. 53, no. April, pp.1369–1377, 2021.

[3] P. T. Manditereza, R. C. Bansal, "Review of technical issues influencing the decoupling of DG converter design from the distribution system protection strategy," *IET Renew. Power Gener*, vol. 12, no. 10, pp. 1091–1100, 2018.

[4] D.A. Gadanayak, "Protection algorithms of microgrids with inverter interfaced distributed generation units—A review" *Electric Power Systems Research*, vol. 192, no. march, pp.106986, 2021.

[5] A.E.C. Momesso et al, "Adaptive directional overcurrent protection considering stability constraint," *Electric Power Systems Research*, vol. 181, no. 106190, pp. 0378-7796, 2020.

[6] M. Irfan, A. Wadood, T. Khurshaid, et al; "An Optimized Adaptive Protection Scheme for Numerical and Directional Overcurrent Relay Coordination Using Harris Hawk Optimization". *Energies*, vol. 14, no. 18, pp. 1996-1073, 2021.

[7] A. E. C. Momesso, W. Maycon, S. Bernardes, E. N. Asada, "Electrical Power and Energy Systems Fuzzy adaptive setting for time-current-voltage based overcurrent relays in distribution systems," *Electr. Power Energy Syst*, vol. 108, no. August 2018, pp. 135–144, 2019.

[8] M.A. Elsadd, T.A. Kawady, AM.I. Taalab, et al, "Adaptive optimum coordination of overcurrent relays for deregulated distribution system considering parallel feeders." *Electr Eng*, vol. 103, no. january 2021, pp. 1849–1867, 2021.

[9] J.A. O. Wilches; A.J. U. Farfan; E.A. Cano-Plata, "Modeling of a Communications-based Directional Overcurrent Protection Scheme for Microgrids," 2018 IEEE ANDESCON confrance, 22-24 Aug. 2018.

[10] M.H. Sadeghi, et al, "Optimal coordination of directional overcurrent relays in distribution systems with DGs and FCLs considering voltage sag energy index" *Electric Power Systems Research*, vol. 191, no. 106884, pp. 0378-7796, 2021.

[11] A. M. Tsimtsios, G. N. Korres, V. C. Nikolaidis, "A pilot-based distance protection scheme for meshed distribution systems with distributed generation," *Int. J. Electr. Power Energy Syst*, vol. 105, no. 8, pp. 454–469, 2019.

[12] Y. Yin, Y. Fu, Z. Zhang and A. Zamani, "Protection of Microgrid Interconnection Lines Using Distance Relay With Residual Voltage Compensations," *in IEEE Transactions on Power Delivery*, vol. 37, no. 1, pp. 486-495, Feb. 2022.

[13] B. K. Chaitanya, A. Yadav, and M. Pazoki, "An improved differential protection scheme for micro-grid using time-frequency transform," *Electr. Power Energy Syst*, vol. 111, no. September 2018, pp. 132–143, 2019.

[14] T. S. Aghdam, H. K. Karegar, H. H. Zeineldin, "Variable Tripping Time Differential Protection for Microgrids Considering DG Stability*," IEEE Trans. smart grid*, vol. 3053, no. c, pp. 2407 – 2415, 2018.

[15] V. C. Nikolaidis, G. Michaloudis, A. M. Tsimtsios, D. Tzelepis, C. D. Booth, "A Coordinated Multi-Element Current Differential Protection Scheme for Active Distribution Systems," *IEEE Transactions on Power Delivery*,vol. {}, no. {}, pp. {}, February 2022.

[16] Ansari, Salauddin, Gupta, O. Hari, "Differential positive sequence power angle-based microgrid feeder protection" *International Journal of Emerging Electric Power Systems*, vol. 22, no. 5, pp. 525-531, 2021.

[17] D. Library, "Sequence currents based adaptive protection approach for DNs with distributed energy resources," *IET Gener. Transm. Distrib*, Vol. 11, no. 1, pp. 154–165, 2017.

[18] N. K. Sharma, S. R. Samantaray, "PMU Assisted Integrated Impedance Angle-Based Microgrid Protection Scheme," *IEEE Transactions on Power Delivery*, vol. 35, no. 1, pp. 183-193, Feb. 2020.

[19] B. Wang, L. Jing, "A Protection Method for Inverter-based Microgrid Using Current-only Polarity Comparison," *Journal of Modern Power Systems and Clean Energy*, vol. 8, no. 3, pp. 446-453, May 2020.

[20] M. J. Daryani, A. E. Karkevandi, O. Usta, "Harmonics Content and Voltage Signal Based Hybrid Backup Scheme for Protection of Microgrid Under Different Contingencies," 2019 IEEE PES Innovative Smart Grid Technologies Europe (ISGT-Europe) confrance, pp. 1-5, 2019.

[21] R. R. Xwkdvdn, "Modeling of rate of change of under frequency relay for microgrid protection," 5 th Int. Electr. Eng. Congr. pattaya, pp. 6–9, 2017.

[22] M.A.U. Khan, Q. Hong, A. Dyśko, C. Booth, "An Active Protection Scheme for Islanded Microgrids", 15th International Conference on Developments in Power System Protection (DPSP 2020), 9-12 March 2020.

[23] S. Ranjbar, A.R. Farsa, S. Jamali " Voltage - based protection of microgrids using decision tree algorithms, " *Int Trans Electri Energy Syst*, vol. 30, no. November, pp. 1 – 15, April 2020.

[24] M. Asim, S. M. S. Hussain, I. Ali, T. Selim, "Electrical Power and Energy Systems Dynamic protection of power systems with high penetration of renewables : A review of the traveling wave based fault location techniques," *Electr. Power Energy Syst*, vol. 114, no. July 2019, pp. 0142-0615, 2020.

[25] R. Montoya, B.P. Poudel, A. Bidram, M.J. Reno, "DC microgrid fault detection using multiresolution analysis of traveling waves" *Electr. Power Energy Syst*, vol. 135, no. Febreary 2022, pp. 0142-0615, 2022.

[26] I. M. Faria, R. H. Furlan, P. E. T. Martins, T. S. Menezes, M. Oleskovicz, D. V. Coury, "The Proposition of a Multiagent System for Adaptive Protection of a Distribution System," 2018 Simposio Brasileiro de Sistemas Eletricos (SBSE) confrance, pp. 1–6, 12-16 May 2018.

[27] Y. Zheng, Y. Song, D. J. Hill, Y. Zhang, "Multi-Agent System Based Microgrid Energy Management via Asynchronous Consensus ADMM," *IEEE Trans. Energy Convers*, vol. 8969, no. c, pp. 1–3, 2018.

[28] A. Hussain, M. Aslam, S. Muhammad, "N-version programming-based protection scheme for microgrids : A multi-agent system based approach," *Sustain. Energy, Grids Networks*, vol. 6, no. June 2016, pp. 35–45, 2016.

[29] H. F. Habib, O. Mohammed, "Decentralized Multi-Agent System for Protection and the Power Restoration Process in Microgrids," Ninth Annu. IEEE Green Technol. Conf. Decentralized, pp. 359–365, 2017.

[30] S. Rahman et al, "Crop Field Boundary Delineation using Historical Crop Rotation Pattern," 8th Int. Conf. Agro-Geoinformatics, pp. 1–5, 2019.

[31] B. Fani et al, " A fault-clearing algorithm supporting the MAS-based protection schemes," *Int J Electr Power Energy Syst*, vol 103, no. June 2018, pp. 0142-0615, 2018.

[32] B. Fani, H. Bisheh, A. K. Horestani., "An offline penetration-free protection scheme for PV-dominated distribution systems," *Electr Power Syst Res*, vol. 157, no. April 2018, pp. 1-9, 2018.
[33] E. Abbaspour, B. Fani, E. H. Forushani., "A bi-level multi agent based protection scheme for distribution networks with distributed generation," *Int J Electr Power Energy Syst*, vol. 112, no. 11, pp. 209-220, 2019.
[34] B. Fani, M. Dadkhah, A. K. Horestani, "Adaptive protection coordination scheme against the staircase fault current waveforms in PV-dominated distribution systems*." IET Gener. Transm. Distrib*, Vol. 12 no. 9, pp. 2065-2071, 2018.

International Journal of Research and Technology in Electrical Industry

journal homepage: ijrtei.sbu.ac.ir

Shahid Beheshti University

Design and Implementation of a Modified Boost Topology with High Voltage Ratio and Efficiency Besides the Lower Semiconductors Stresses

Reza Sharifi Shahrivar[1], Hossein Gholizadeh[2,*], Alireza Siadatan[1], Ebrahim Afjei[2]

[1] *Electrical engineering faculty of Islamic Azad University , Tehran, Iran*
[2] *Department of Electrical Engineering, Shahid Beheshti University, Tehran, Iran*

ARTICLEINFO

Article history:
Received 07 November 2021
Received in revised form 25 April 2022
Accepted 08 May 2022

Keywords:
Boost converter,
Continuous input current,
DC-DC converter
High gain converters
Transformer-less converters

ABSTRACT

This paper has designed an upgraded form of the boost topology. The voltage ratio of the traditional step-up topology has been increased in quadratic form. Moreover, a low value of the duty cycle, number of components, and voltage/current stresses besides a high efficiency are bold features. The different parameters have been extracted for the ideal/non-ideal modes of the components and continuous/discontinuous current modes. In addition, the different features, such as the current/voltage stresses, have been compared. The efficiency of the designed topology has been extracted, and its various kind of power losses have been compared. The small-signal analysis has been done, and the bode diagram of the system has been extracted. Besides the increased voltage ratio of the designed topology compared to the traditional step-up converter, the continuity of the input current has remained a brilliant feature. Moreover, the semiconductors' stresses have been low-value compared to the recently proposed topologies. Moreover, higher efficiency besides higher voltage gain has been achieved. Finally, the experimental results have been compatible with the simulation and theoretical outcomes. The higher voltage gain of the proposed converter has been caused by the lower value of the duty cycle in comparison with the conventional boost converter, besides an acceptable efficiency and semiconductor stresses.

1. Introduction

With the pass of time, the new gates of science have been opened by the researchers to develop technology, simplify the industrial process, increase efficiency, reduce costs, and make human life more straightforward than in the past [1], [2], [6], [8]. Power electronics and the use of semiconductor devices are new fields that have been effective in power generation, transportation, a new generation of lamps, space satellites, distributed power generation, and daily life applications. DC-DC converters are another widely employed equipment in renewable energy applications, uninterruptible power supplies, electric cars, and new light bulbs [1],[2]. Generally, the DC-DC topologies are divided into two main groups: transformer-based and transformer-less DC-DC converters. Increasing the voltage ratio is quickly done by the isolated DC-DC topologies [2], [4], [5]. In other words, the voltage ratio can be changed by the winding ratio and duty cycle [2], [6]. It should be noted that the use of a high-frequency transformer is not without its drawbacks [4]- [8]. The saturation of the transformer core, EMI problems due to the leakage inductors, low efficiency, high voltage stress of switches, cost, and volume are some of the problems that have been caused by the transformer-based DC-DC topologies [4]- [8]. For this reason, the

* Corresponding author
E-mail address: ho.gholizadeh@mail.sbu.ac.ir
http://dx.doi.org/ 10.52547/ijrtei.1.1.75

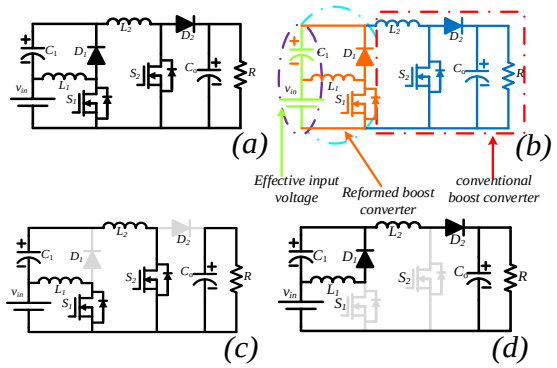

Fig. 1. **(a)** The proposed converter, **(b)** different parts of the proposed converter, **(c)** the equivalent circuit of the first mode, **(d)** the equivalent circuit of the second mode.

transformerless DC-DC topologies are used to solve the problems of DC-DC isolated converters. The simplest topology of non-isolated converters with the step-up behavior is the boost converter [4]-[8]. The topology of the mentioned converter comprises an inductor, a diode, a switch, and an output capacitor. The small components number of the mentioned converter is an advantage of the mentioned converter. It is worth noting that the boost converter has its limits. In other words, it is not possible to reach the desired high voltage gain by the mentioned converter. It is good to mention that the reverse recovery problems and the parasitic components of the devices are effective in the mentioned concept. As a result, modified and new structures must be used to achieve high voltage ratios [8].

In [9]-[17], new typologies of the DC-DC converters have been proposed. Quadratic buck-boost converters have been proposed in [9]- [13]. All the mentioned converters can operate as step-up/down and pass-through converters. The input current of [10], [13] are discontinuous. Therefore, the input filter capacitor will be increased and experience high current stresses. The number of storage components in [9], [11], [12] is high and can increase the dimension of the topology. Moreover, the voltage stress of semiconductor devices is high [12]. The voltage ratio of the proposed converters in [14], [15] is a multiplication of the voltage ratio of conventional boost and buck-boost topologies. The high number of storage components is a disadvantage in the mentioned converters. Moreover, the voltage stress of the
second diode is high in both converters. Furthermore, a duty cycle with a 50 percent value makes the output voltage twice the input voltage. In other words, they operate as the conventional boost converter. Another step-up converter has been proposed in [17]. While the duty cycle becomes 50 percent, the output voltage becomes three times more than the input voltage. However, the voltage/current stresses of semiconductor components are high, decreasing the efficiency even with the mentioned advantages.

In [9]- [17], new typologies of the DC-DC converters have been proposed. Quadratic buck-boost converters have been proposed in [9]- [13]. All the mentioned converters can operate as step-up/down and pass-through converters. The input current of [10], [13] are discontinuous. Therefore, the input filter capacitor will be increased and experience high current stresses. The number of storage components in [9], [11], [12] is high and can increase the dimension of the topology. Moreover, the voltage stress of semiconductor devices is high [12]. The voltage ratio of the proposed converters in [14], [15] is a multiplication of the voltage ratio of conventional boost and buck-boost topologies. The high number of storage components is a disadvantage in the mentioned converters. Moreover, the voltage stress of the second diode is high in both converters. Furthermore, a duty cycle with a 50 percent value makes the output voltage twice the input voltage. In other words, they operate as the conventional boost converter. Another step-up converter has been proposed in [17]. While the duty cycle becomes 50 percent, the output voltage becomes three times more than the input voltage. However, the voltage/current stresses of semiconductor components are high, decreasing the efficiency even with the mentioned advantages.

In this paper, it has been tried to achieve a high voltage gain by an upgraded form of the conventional boost topology. The voltage ratio of the designed topology is a quadratic form of the voltage ratio of the conventional boost topology. Moreover, a lower number of devices have achieved the mentioned voltage ratio. Furthermore, the continuity of the input current has been kept. Therefore, it is compatible with renewable energy resources. Moreover, it has been tried to have low and acceptable semiconductor voltage/current stresses besides its high voltage ratio. Therefore, the efficiency of the designed topology has an acceptable and high value. The bolded feature of this topology is its voltage-increasing technique. In other words, the summation of the input source voltage and the first stage capacitor helps the second part of the converter to have a higher voltage at the output terminal. Therefore, the voltage stress of the capacitor decreases, and it is not required to employ a capacitor with a high nominal voltage. It is worth noting that the mentioned concept has not been obeyed in the suggested converters of [9]- [17].

2. The introduced topology

The topology of the designed converter has been illustrated in Fig. 1(a). As can be understood from Fig. 1(b), the designed topology combines two conventional boost converters. As shown in Fig. 1(b), the first stage of the proposed converter has been designed to increase the input voltage of the second part. In other words, the first part has made an effective input voltage for the second stage. Moreover, the input voltage decreases the applied voltage of C1. In other words, the input voltage participates as the input of the second part and the first capacitor voltage. All the mentioned concepts and their creation procedure can be understood in Fig. 1(b). Both the switches in the proposed converter become turned ON and OFF synchronously. The conduction of diodes takes place during the switches are turned OFF. Consequently, two function modes can be considered for the proposed circuit. All the circuit components have been considered

ideal for simplifying the study of the suggested converter. Moreover, it has been accounted that the converter operates in the steady-state and the continuous current mode (CCM).

2.1. The first operation mode

During the first function mode, both the MOSFETs become ON. Consequently, both diodes become OFF. The appropriate circuit of this mode has been presented in Fig. 1(c). Both the inductors are magnetized by the capacitors and the input voltage, caused by their positive voltage. Moreover, the capacitors become discharged, caused by their negative current. The mentioned concepts have been expressed mathematically by (1):

$$\begin{cases} L_1 \dfrac{di_{L1}}{dt} = v_{in}, L_2 \dfrac{di_{L2}}{dt} = v_{in} + v_{c1} \\ C_1 \dfrac{dv_{C1}}{dt} = -i_{L2}, C_o \dfrac{dv_{Co}}{dt} = -I_o \end{cases} \quad (1)$$

2.2. The second operation mode

In this mode, both the MOSFETs are OFF. Therefore, both diodes become ON. The equivalent circuit of the forenamed mode has been presented in Fig. 1(d). The inductors become demagnetized due to their negative voltage in the mentioned model. Moreover, the positive current of capacitors causes their charging in the second mode. The expressing relations of the inductors voltage and capacitors current in the present mode are as (2):

$$\begin{cases} L_1 \dfrac{di_{L1}}{dt} = -v_{c1}, L_2 \dfrac{di_{L2}}{dt} = v_{in} + v_{c1} - v_{co} \\ C_1 \dfrac{dv_{C1}}{dt} = i_{L1} - i_{L2}, C_o \dfrac{dv_{Co}}{dt} = i_{L2} - I_o \end{cases} \quad (2)$$

2.3. The average of the capacitors voltage and inductors current

The voltage second balance refers to a zero average voltage of inductors. Therefore, by applying the mentioned concept to both relations of the inductors' voltage during both of the operation modes, the average value of the capacitors' voltage can be written as:

$$V_{C1} = \frac{D}{1-D} V_{in}, V_{Co} = \frac{1}{(1-D)^2} V_{in} \quad (3)$$

Employing the average voltage of the capacitors, the voltage gain of the mentioned converter has been written as (4):

$$\frac{V_{Co}}{V_{in}} = \frac{1}{(1-D)^2} \quad (4)$$

The Dual of the last concept can be applied to the capacitors. In other words, the current second balance refers to the zero average currents of capacitors. Consequently, applying this concept to the current relations of capacitors for both of the operation modes, the average current of the inductors can be formulated as (5):

$$I_{L1} = \frac{1}{(1-D)^2} I_o, I_{L2} = \frac{1}{1-D} I_o \quad (5)$$

2.4. Voltage/current stress of semiconductors

The average voltage which is applied to the semiconductor devices by the capacitors, and input voltage and their average current are as below:

$$V_{S1} = V_{D1} = \frac{V_{in}}{1-D}, V_{S2} = V_{D2} = \frac{V_{in}}{(1-D)^2} \quad (6)$$

$$I_{S1} = \frac{D}{(1-D)^2} I_o, I_{S2} = I_{D1} = \frac{D}{1-D} I_o, I_{D2} = I_o \quad (7)$$

2.5. Capacitors voltage ripple and inductors current ripple

The capacitors' voltage ripple refers to the subtraction of the maximum and the minimum value of the voltage waveform. It is worth noting that the value of the voltage ripple depends on the amount of the capacitors. The dual of the mentioned concept can be expressed for the inductors. The inductors' current ripple refers to the difference between the maximum and minimum amounts of the inductors' waveform. The capacitors' voltage gain and inductors' current ripple have been expressed as (8):

$$\begin{cases} \Delta V_{C1} = \dfrac{DI_o}{(1-D)C_1 f_s} \\ \Delta V_{Co} = \dfrac{DI_o}{C_o f_s} \end{cases} \quad \begin{cases} \Delta I_{L1} = \dfrac{DV_{in}}{L_1 f_s} \\ \Delta I_{L2} = \dfrac{DV_{in}}{(1-D)L_2 f_s} \end{cases} \quad (8)$$

3. Discontinuous conduction mode

The converter operating in CCM depends on the inductors' average current and inductors' current ripple. The inductors' average current decreases to less than half of the corresponding inductor's current ripple, concluding the discontinuous conduction mode (DCM). The inductors' average current depends on the average output current. (9) defines the border value of the output current for the constant input and output voltage.

$$\begin{cases} I_o = \dfrac{DV_{in}}{2L_2 f_s} \\ I_o = \dfrac{D(1-D)^2 V_o}{2L_2 f_s} \end{cases} \quad (9)$$

It is good to note that the calculated output current according to (9) defines the boundary value of the output current between CCM and DCM. If the output current were less than the calculated values by (9), the converter operates in DCM. Otherwise, the operation takes place in the CCM region.

The increase of the current ripple to more than the twice of the average current concludes the converter's operation in the DCM. Therefore, the minimum value of the inductors has been discussed as (10).

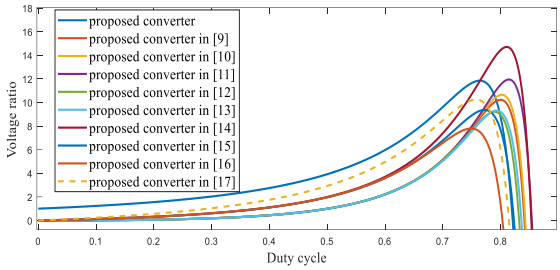

Fig. 2. The comparison of the non-ideal voltage gain of the proposed and recently suggested topologies.

$$\begin{cases} L_1 > \dfrac{D(1-D)^4 R}{2 f_s} \\ L_2 > \dfrac{D(1-D)^2 R}{2 f_s} \end{cases} \quad (10)$$

4. The improvements

4.1. Non-ideal voltage gains of the suggested converter and conventional converter as a point of view

Due to the non-ideal state of the circuit components, DC-DC converters cannot operate according to their ideal voltage ratio. The relation of the voltage ratio in non-ideal mode has been expressed to visualize the capability of the proposed converter compared with the conventional step-up topology as below:

$$\frac{V_O}{V_{in}} = \frac{1}{(1-D)^2} - \frac{r_L}{R} F_1(D) - \frac{r_{SD}}{R} F_2(D) - \frac{r_D}{R} F_3(D) \quad (11)$$

$$\begin{cases} F_1(D) = \dfrac{D^2 - 2D + 2}{(1-D)^6} \\ F_2(D) = \dfrac{D^3 - 2D^2 + 2D}{(1-D)^6} \\ F_3(D) = \dfrac{D^2 - 2D + 2}{(1-D)^5} \end{cases} \quad (12)$$

The corresponding plots of the mentioned relations have been plotted and illustrated in **Fig. 2**. With an approximation, all the mentioned coefficients r_L, r_S, and r_D have been assumed the same. It is good to note that the mentioned parasitic components belong to the equivalent series resistance of the inductors, switches, and diodes. As shown in Fig. 2, the maximum amount of the non-ideal voltage ratio is 12. Additionally, the maximum voltage gain of the boost converter has been extracted 12 according to the mentioned figure. However, the corresponding duty cycle to the maximum voltage gain of the boost converter is higher than the same one in the suggested topology. Consequently, the proposed converter provides a higher value of the voltage gain by a lower duty cycle value. It is worth noting that the higher value of the voltage gains in the boost converter by relative values of the duty cycle to unity makes its diode suffer from reverse recovery problems besides the dramatic voltage/current stresses. Moreover, The topology of the proposed converter has employed two traditional Boost topologies. The first one has been deformed to employ the input voltage directly in

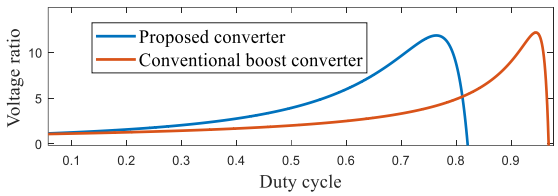

Fig. 3. The comparison of the non-ideal voltage gain of the proposed and recently suggested topologies.

increasing the voltage gain. In other words, the summation of the input voltage and the first capacitor act as a modified input source for the second part. Moreover, the voltage stress of the first capacitor is less than the corresponding capacitor in the cascaded boost topology.

4.2. Non-ideal voltage gains of the suggested converter and suggested converters in [9]-[17] as a point of view

To confirm the capability of the mentioned topology among mentioned converters of [9]- [17], the non-ideal the voltage gain of the presented converters has been compared and illustrated in Fig. 3. Except for the presented converter in [14], all cases have a lower value of maximum voltage gain than the proposed topology. The maximum amount of the voltage ratio of the mentioned topology of [14] has taken place in a duty

cycle, which causes poor efficiency. All the non-ideal voltage gain curves in Fig. 3 have been extracted with some assumptions such as:

- All the parasitic components that become apparent with the non-ideal voltage ratio of converters have been assumed to be the same.
- All the plots have been extracted for 80 W output power.

As can be understood from Fig. 3, the maximum voltage gain of the proposed converter in the same conditions for all has achieved an acceptable and high value. Moreover, as the duty cycle varies from 0 to the corresponding value of the duty cycle to its maximum point in the suggested converter, the voltage gain of this converter is higher than the others. All the plots have been extracted for 80 W output power.

4.3. The comparison of the different features and the parameters

The various features and parameters of the presented topology have been compared with the mentioned converters of [9]- [17] in Table I to confirm the advantages of the presented topology. In the proposed converter and the mentioned converters in [10], [13], [16], [17], there are two inductors and capacitors. The number of the mentioned components is 3 in the proposed converters of [9], [11], [12], [14], [15]. The number of the semiconductor devices is the same in the proposed and the mentioned converters of [9]- [17]. The input current continuity makes the DC-DC converters suitable for renewable applications by reducing the input filter capacitor value. As can be understood, the input current of the designed topology is continuous like the proposed

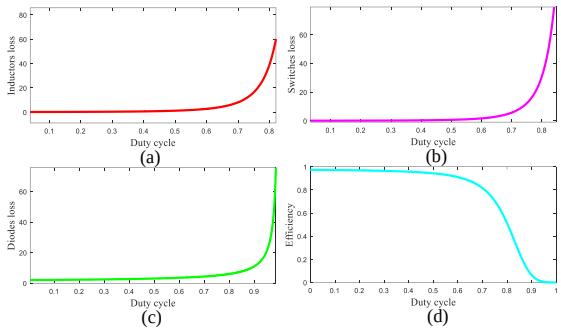

Fig.4. (a) Inductor loss, (b) switch loss, (c) diode loss, (d) efficiency.

converters of [9], [11], [12], [14]- [17]. The duty cycle value, which causes the voltage gain of 4, has been calculated for the proposed and mentioned converters of [9]- [17]. Compared with [9]- [17], the proposed converter needs a lower amount of the duty cycle. The semiconductors' normalized voltage/current stresses have been explained according to the corresponding duty cycle of each converter. As can be understood, the normalized value of the voltage stress of the first switch in the designed topology has the lowest value. By exception of the proposed converter of [15], the voltage stress of the second switch of the designed one is lower than the mentioned converters of [10]- [14],
[17]. The mentioned parameter has the same value in the proposed converters of [9], [16]. Moreover, the normalized value of the voltage stress of the first diode in the suggested topology has the lowest value among the mentioned converters of [9]- [17] as well as the second one has the lowest value among the mentioned converters of [9]- [14], [17]. It has to be announced that the voltage stress of the second diode in the presented topology is the same as the mentioned topologies of the rest. The current stress of both switches in the designed converter has achieved the lowest value among the mentioned converters of [9]- [17]. The current stress of the first diode in the designed topology has the same value as the mentioned converters of [9]- [13], a lower value than the mentioned converters of [15]- [17]. It has a higher value in comparison with [14]. The normalized current stress of the second diode has the same value in all the discussed and the proposed converter approximately. It is worth noting that the voltage of the output capacitor and input current are the base values to normalize the voltage and current stresses, respectively.

5. Efficiency

The power loss of the inductors, switches, and diodes has been considered to extract the mathematical relation of the efficiency. The power loss of the switches can be divided into conduction and switching loss. To simplify the extracted relation, the foko and hysteresis losses of the inductors and frequency loss of the diodes are neglected. All the mentioned types of the loss have been described below:

5.1. Inductors conduction loss

The conduction loss of the inductor is the production of the equivalent series resistance of the inductor with the quadratic form of its current RMS value.

$$P_L=\left\{I^2{}_{L1}r_{L1}+I^2{}_{L2}r_{L2}\right\}=\left\{\frac{1}{(1-D)^4}r_{L1}+\frac{1}{(1-D)^2}r_{L2}\right\}\frac{P_o}{R} \quad (13)$$

5.2. Conduction loss of switches

The switches' conduction loss is the production of the equivalent series resistance of the switch with the quadratic form of the RMS value of the current.

$$P_{SC}=\left\{I^2{}_{S1}r_{SD1}+I^2{}_{S2}r_{SD2}\right\}=\left\{\frac{D}{(1-D)^4}r_{SD1}+\frac{D}{(1-D)^2}r_{SD2}\right\}\frac{P_o}{R} \quad (14)$$

5.3. Switching loss of switches

The switches' switching loss is half of the production of the average voltage and current of switches with the frequency and the turn-OFF delay time.

$$P_{SS}=\frac{1}{2}f_s\left\{V_{S1}I_{S1}t_{OFF1}+V_{S2}I_{S2}t_{OFF2}\right\}=\frac{1}{2}f_sP_o\left(\frac{D}{1-D}\right)\left\{t_{OFF1}+t_{OFF2}\right\} \quad (15)$$

5.4. Conduction loss of diodes

The power loss of the diodes is the production of the average current of the diode with its threshold voltage.

$$P_D=V_{DF1}I_{D1}+V_{DF2}I_{D2}=\left\{V_{DF1}\left(\frac{1}{1-D}\right)+V_{DF2}\right\}I_o \quad (16)$$

After calculating the mentioned power losses, the efficiency is as below:

$$\eta=\frac{P_o}{P_o+P_{SC}+P_{SS}+P_D}\times 100\% \quad (17)$$

Fig. 4 presents the mentioned power losses and the efficiency for all duty cycle percentages. The corresponding output power of the plots in Fig. 4 is 80W. As can be understood from Fig. 4(d), the efficiency of the presented topology decreases from 98 % to 80 %. At the same time, the duty cycle varies from 0 to 75 %. In addition, the efficiency of the designed topology becomes 96 % when the duty cycle becomes 50 %. It is worth noting that the mentioned power losses vary from 0.01 W to lower than 10 W, as the duty cycle varies from 0 to 75 %.
Fig. 5 presents the efficiency of the topology for the various output powers and all values of the duty cycle. The efficiency is more than 94%, while the duty cycle varies from 0 to 50 %, and the output power varies from 20 W to 200 W, according to Fig. 5(a). In Fig. 5(b), the duty cycle varies from 50 % to 100 %. The efficiency is more than 80 percent for all the mentioned output power values, while the duty cycle is lower than 66 %. While the duty cycle varies to 75 %, only for the output power of 20W to 80 W, the efficiency is more than 80 %.

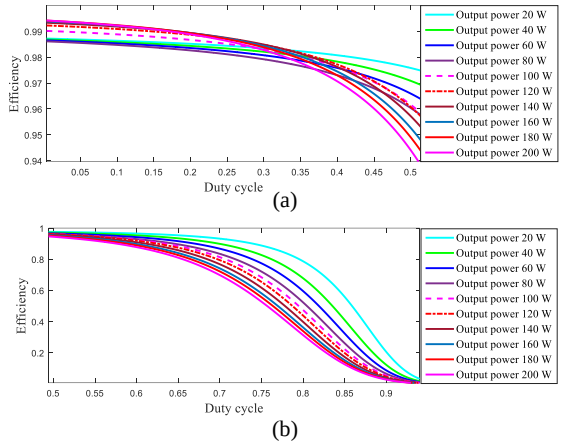

Fig. 5. The efficiency of the converter for the different output powers while the duty cycle varies from(a) 0 to 50 %, (b) 50 % to 100 %.

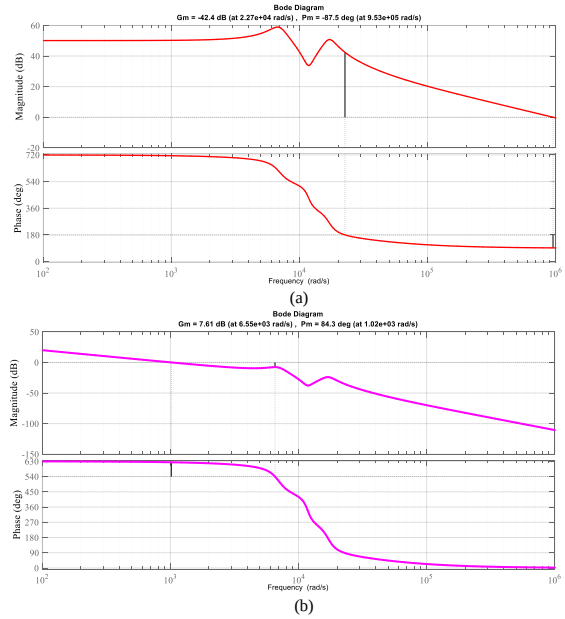

Fig. 6. The bode diagram of the proposed converter: (a) before compensating, (b) after compensating.

In Table 2, the mentioned power losses have been compared for the proposed converter and the mentioned converters of [9]- [17] for an amount of the duty cycle, causing the voltage gain of 4. The last column of Table 2 belongs to the calculated value of the duty cycle. The second column of Table 2 is for the inductor loss of the mentioned converters. It is good to note that the inductor loss of the proposed converter is lower than [9]- [16]. Moreover, the conduction loss of the switch in the presented topology has the lowest value compared to the mentioned converters of [9]- [17]. In addition, the switching loss of the proposed converter has achieved the lowest value compared with mentioned converters of [9]- [17]. Finally, the fifth column of the mentioned table compares the diode loss. The value of the diode loss for the proposed converter has the lowest value among the converters of [9]- [13], [15]- [17]. Consequently, the designed converter has a better efficiency among [9]-[17], while the duty cycle causes a voltage gain of 4.

6. Small signal analysis

To study the stability of the proposed converter, the state space variables of the proposed topology and their appropriate relations during both the function modes have been Witten as below:

$$\begin{cases} L_1 \dfrac{d\prec i_{L1}\succ}{dt} = d\prec v_{in}\succ -(1-d)\prec v_{C1}\succ \\ L_2 \dfrac{d\prec i_{L2}\succ}{dt} = \prec v_{in}+v_{C1}\succ -(1-d)\prec v_{Co}\succ \\ C_1 \dfrac{d\prec v_{C1}\succ}{dt} = -\prec i_{L2}\succ +(1-d)\prec i_{L1}\succ \\ C_o \dfrac{d\prec v_{Co}\succ}{dt} = -\prec \dfrac{v_{Co}}{R}\succ +(1-d)\prec i_{L2}\succ \end{cases} \quad (18)$$

All the space state variables can be assumed to be a DC and AC part summation. Moreover, the AC term of the mentioned variables is negligible in comparison with DC terms as below:

$$\begin{cases} \prec i_{L1}\succ = \prec I_{L1}\succ + \prec \hat{i}_{L1}\succ \\ \prec i_{L2}\succ = \prec I_{L2}\succ + \prec \hat{i}_{L2}\succ \\ \prec v_{C1}\succ = \prec V_{C1}\succ + \prec \hat{v}_{C1}\succ \\ \prec v_{Co}\succ = \prec V_{Co}\succ + \prec \hat{v}_{Co}\succ \\ d = D + \hat{d} \end{cases} \quad \begin{cases} \hat{i}_{L1} \ll I_{L1} \\ \hat{i}_{L2} \ll I_{L2} \\ \hat{v}_{C1} \ll V_{C1} \\ \hat{v}_{Co} \ll V_{Co} \\ \hat{d} \ll D \end{cases} \quad (19)$$

The space state equations can be formed as below:

$$\begin{cases} \dot{\hat{x}} = Ax + B\hat{d} \\ y = C\hat{d} \end{cases} \quad (20)$$

$$\begin{bmatrix} \dfrac{d\hat{i}_{L1}}{dt} \\ \dfrac{d\hat{i}_{L2}}{dt} \\ \dfrac{d\hat{v}_{C1}}{dt} \\ \dfrac{d\hat{v}_{Co}}{dt} \end{bmatrix} = \begin{bmatrix} 0 & 0 & \dfrac{D-1}{L_1} & 0 \\ 0 & 0 & \dfrac{1}{L_2} & \dfrac{D-1}{L_2} \\ \dfrac{1-D}{C_1} & \dfrac{-1}{C_1} & 0 & 0 \\ 0 & \dfrac{1-D}{C_o} & 0 & \dfrac{-1}{RC_o} \end{bmatrix} \begin{bmatrix} i_{L1} \\ i_{L2} \\ v_{C1} \\ v_{Co} \end{bmatrix} + \begin{bmatrix} \dfrac{V_{in}+V_{C1}}{L_1} \\ \dfrac{V_{Co}}{L_2} \\ \dfrac{-I_{L1}}{C_1} \\ \dfrac{-I_{L2}}{C_o} \end{bmatrix} \hat{d} \quad (21)$$

The bode diagram of the offered topology based on the described space state equations has been plotted and presented in Fig. 6(a) to find the stability requirements of the designed topology. According to the illustrated bode plot, the gain and phase margin of the proposed converter are as -42.4 dB at 22.7 kHz and -87.5 deg at 953krad/s. The positive value of the production of the gain and the phase margin is the stability requirement desired in this converter. Matlab software plotted the bode diagram and found the gain and phase margins. Negative values of the phase and gain margins refer to the non-minimum phase characteristics of the proposed deigned and the compensated bode diagram has been presented in Fig. 6 (b).

7. Simulation and experimental results

This section discusses all the simulations and the experimental outcomes. PLECS has got the mentioned results. The inductors' and capacitors' values are required

for the simulation. The percentage of the inductors' current ripple and capacitors' voltage ripple have to be valued to find the inductors and capacitors. Based on the power quality factors, the inductors' current ripple and capacitors' voltage ripple are 30 % and 5 %, respectively. The inductors' average current and capacitors' average voltage have to be found to use the mentioned percentages. The input voltage and output current have to be defined to find the mentioned average values from (3) and (5). The lab equipment limits and safety considerations lead to assuming the input voltage as 20 V and output current as 1 A. It is good to note that the switching frequency is considered 60 kHz due to the capability of the inductors' windings. According to the mentioned concepts the capacitors' average voltage and inductors' current are as (22).

Table I. The comparison of the different features.

	[9]	[10]	[11]	[12]	[13]	[14]	[15]	[16]	[17]	proposed
No. inductors	3	2	3	3	2	3	3	2	2	2
No. capacitors	3	2	3	3	2	3	3	2	2	2
No. switches	2	2	2	2	2	2	2	2	2	2
No. diodes	2	2	2	2	2	2	2	2	2	2
No.	10	8	10	10	8	10	10	8	8	8
Duty cycle	0.67	0.67	0.67	0.67	0.67	0.62	0.62	0.62	0.55	0.5
$\frac{V_{S1}}{V_O}$	$\frac{1-D}{D^2}=0.73$	$\frac{1-D}{D^2}=0.73$	$\frac{1-D}{D^2}=0.73$	$\frac{1}{D^2}=2.23$	$\frac{1-D}{D^2}=0.73$	$\frac{1-D}{D}=0.61$	$\frac{1-D}{D}=0.61$	$\frac{1-D}{D}=0.61$	$\frac{1-D}{D(2-D)}=0.62$	$1-D=0.5$
$\frac{V_{S2}}{V_O}$	1	$\frac{1}{D}=1.49$	$\frac{1}{D}=1.49$	$\frac{1}{D}=1.49$	$\frac{1}{D}=1.49$	$\frac{1}{D}=1.61$	$\frac{2D-1}{D}=0.38$	1	$\frac{1}{D(2-D)}=1.25$	1
$\frac{V_{D1}}{V_O}$	$\frac{1-D}{D^2}=0.73$	$\frac{1-D}{D^2}=0.73$	$\frac{1-D}{D^2}=0.73$	$\frac{1-D}{D^2}=0.73$	$\frac{1-D}{D^2}=0.73$	$\frac{1-D}{D}=0.61$	$\frac{1-D}{D}=0.61$	$\frac{1-D}{D}=0.61$	$\frac{1-D}{D(2-D)}=0.62$	$1-D=0.5$
$\frac{V_{D2}}{V_O}$	$\frac{1}{D}=1.49$	$\frac{1}{D}=1.49$	$\frac{1}{D}=1.49$	$\frac{1}{D}=1.49$	$\frac{1}{D}=1.49$	$\frac{1}{D}=1.61$	1	1	$\frac{1}{D(2-D)}=1.25$	1
$\frac{I_{S1}}{I_{in}}$	1	1	1	1	1	$D=0.62$	$2-D=1.38$	1	$\frac{1}{D(2-D)}=1.25$	$D=0.5$
$\frac{I_{S2}}{I_{in}}$	$\frac{1-D}{D}=0.5$	$\frac{1-D}{D}=0.5$	$\frac{1-D}{D}=0.5$	$\frac{2D-1}{D}=0.5$	$\frac{1-D}{D}=0.5$	$1-D=0.38$	$1-D=0.38$	$1-D=0.38$	$\frac{1-D}{(2-D)}=0.31$	$D(1-D)=0.25$
$\frac{I_{D1}}{I_{in}}$	$\frac{1-D}{D}=0.5$	$\frac{1-D}{D}=0.5$	$\frac{1-D}{D}=0.5$	$\frac{1-D}{D}=0.5$	$\frac{1-D}{D}=0.5$	$1-D=0.38$	$\frac{1-D}{D}=0.5$	$\frac{1-D}{D}=0.5$	$\frac{1-D}{D(2-D)}=0.62$	$1-D=0.5$
$\frac{I_{D2}}{I_{in}}$	$\left(\frac{1-D}{D}\right)^2=0.24$	$\left(\frac{1-D}{D}\right)^2=0.24$	$\left(\frac{1-D}{D}\right)^2=0.24$	$\left(\frac{1-D}{D}\right)^2=0.24$	$\left(\frac{1-D}{D}\right)^2=0.24$	$\frac{(1-D)^2}{D}=0.23$	$\frac{(1-D)^2}{D}=0.23$	$\frac{(1-D)^2}{D}=0.23$	$\frac{(1-D)^2}{D(2-D)}=0.24$	$(1-D)^2=0.25$
Continuity of I_{in}	Yes	No	Yes	Yes	No	Yes	Yes	Yes	Yes	Yes

Table II. The different losses comparison.

	P_L	P_{CS}		P_D	D
[9]	$\frac{D^4-2D^3+3D^2-2D+1}{(1-D)^4}\frac{P_o r_L}{R}=55\frac{P_o r_L}{R}$	$\frac{2D^3-2D^2+D}{(1-D)^4}\frac{P_o r_L}{R}=34\frac{P_o r_L}{R}$	$f_s P_o t_{OFF}\left(\frac{1+D}{1-D}\right)=5 f_s P_o t_{OFF}$	$V_{DF} I_O \frac{1}{1-D}=3V_{DF} I_O$	0.67
[10]	$\frac{5D^2-6D+2}{(1-D)^4}\frac{P_o r_L}{R}=20.4\frac{P_o r_L}{R}$	$\frac{2D^3-2D^2+D}{(1-D)^4}\frac{P_o r_L}{R}=34\frac{P_o r_L}{R}$	$f_s P_o t_{OFF}\left(\frac{1}{1-D}\right)=3 f_s P_o t_{OFF}$	$V_{DF} I_O \frac{1}{1-D}=3V_{DF} I_O$	0.67
[11]	$\frac{2D^4-6D^3+8D^2-4D+1}{(1-D)^4}\frac{P_o r_L}{R}=46.33\frac{P_o r_L}{R}$	$\frac{2D^3-2D^2+D}{(1-D)^4}\frac{P_o r_L}{R}=34\frac{P_o r_L}{R}$	$f_s P_o t_{OFF}\left(\frac{1}{1-D}\right)=3 f_s P_o t_{OFF}$	$V_{DF} I_O \frac{1}{1-D}=3V_{DF} I_O$	0.67
[12]	$\frac{3D^4-5D^3+7D^2-4D+1}{(1-D)^4}\frac{P_o r_L}{R}=92\frac{P_o r_L}{R}$	$\frac{5D^3-4D^2+D}{(1-D)^4}\frac{P_o r_L}{R}=34.4\frac{P_o r_L}{R}$	$f_s P_o t_{OFF}\left(\frac{D}{(1-D)^2}\right)=6.15 f_s P_o t_{OFF}$	$V_{DF} I_O \frac{1}{1-D}=3V_{DF} I_O$	0.67
[13]	$\frac{2D^2-2D+1}{(1-D)^4}\frac{P_o r_L}{R}=57\frac{P_o r_L}{R}$	$\frac{2D^3-2D^2+D}{(1-D)^4}\frac{P_o r_L}{R}=34\frac{P_o r_L}{R}$	$f_s P_o t_{OFF}\left(\frac{1}{1-D}\right)=3 f_s P_o t_{OFF}$	$V_{DF} I_O \frac{1}{1-D}=3V_{DF} I_O$	0.67
[14]	$\frac{2D^4-6D^3+8D^2-4D+1}{(1-D)^4}\frac{P_o r_L}{R}=23\frac{P_o r_L}{R}$	$\frac{2D^3-2D^2+D}{(1-D)^4}\frac{P_o r_L}{R}=16.4\frac{P_o r_L}{R}$	$f_s P_o t_{OFF}\left(\frac{1+D}{1-D}\right)=4.26 f_s P_o t_{OFF}$	$V_{DF} I_O \frac{1}{1-D}=2.63V_{DF} I_O$	0.62
[15]	$\frac{3D^2-4D+2}{(1-D)^4}\frac{P_o r_L}{R}=33.7\frac{P_o r_L}{R}$	$\frac{2D^3-6D^2+5D}{(1-D)^4}\frac{P_o r_L}{R}=63.5\frac{P_o r_L}{R}$	$f_s P_o t_{OFF}\left(\frac{1+D}{1-D}\right)=4.26 f_s P_o t_{OFF}$	$V_{DF} I_O \frac{1+D}{1-D}=4.26V_{DF} I_O$	0.62
[16]	$\frac{D^2-2D+2}{(1-D)^4}\frac{P_o r_L}{R}=57.22\frac{P_o r_L}{R}$	$\frac{D^3-2D^2+2D}{(1-D)^4}\frac{P_o r_L}{R}=35.5\frac{P_o r_L}{R}$	$f_s P_o t_{OFF}\left(\frac{1+D}{1-D}\right)=4.26 f_s P_o t_{OFF}$	$V_{DF} I_O \frac{2-D}{1-D}=3.63V_{DF} I_O$	0.62
[17]	$\frac{2D^2-2D+1}{(1-D)^4}\frac{P_o r_L}{R}=12.31\frac{P_o r_L}{R}$	$\frac{D^3-2D^2+2D}{(1-D)^4}\frac{P_o r_L}{R}=16.12\frac{P_o r_L}{R}$	$f_s P_o t_{OFF}\left(\frac{1}{(1-D)(2-D)}\right)=1.43 f_s P_o t_{OFF}$	$V_{DF} I_O \frac{1+D}{1-D}=3.4V_{DF} I_O$	0.55
proposed	$\frac{D^2-2D+2}{(1-D)^4}\frac{P_o r_L}{R}=20\frac{P_o r_L}{R}$	$\frac{D^3-2D^2+2D}{(1-D)^4}\frac{P_o r_L}{R}=10\frac{P_o r_L}{R}$	$f_s P_o t_{OFF}\left(\frac{D}{1-D}\right)=f_s P_o t_{OFF}$	$V_{DF} I_O \frac{2-D}{1-D}=3V_{DF} I_O$	0.5

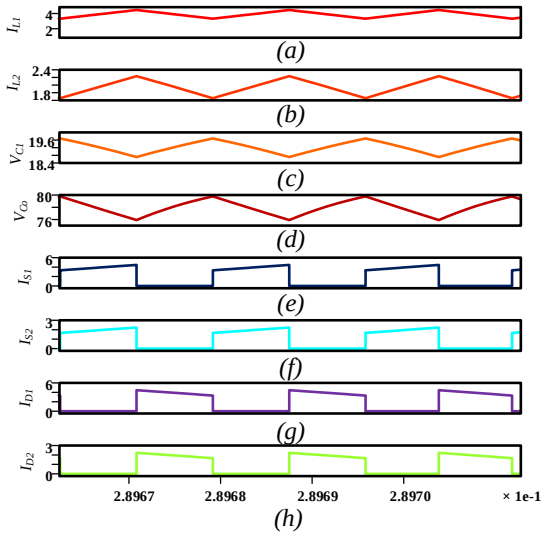

Fig. 7. Simulation results. (a) first inductor current, (b) the second inductor current, (c) the first capacitor voltage, (d) the output voltage.

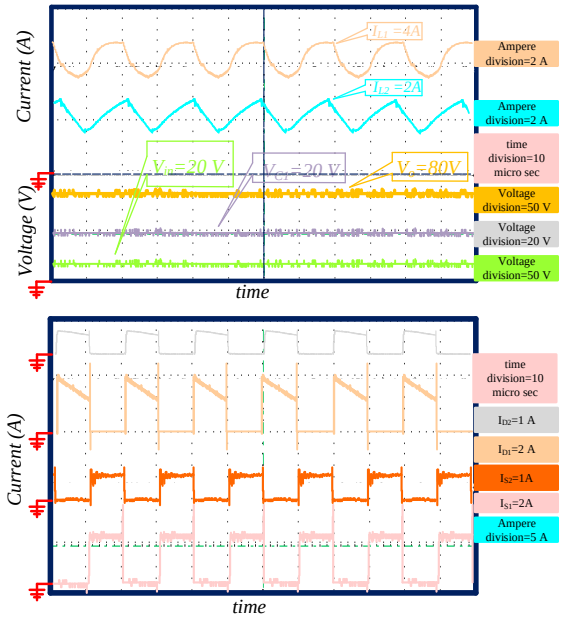

Fig. 8. Experimental results.

$$\begin{cases} V_{in}=20V \\ V_{c1}=20V \\ \mathrm{V_o}=80V \\ \Delta v_c=5\% \\ D=50\% \end{cases} \begin{cases} I_{L1}=4A \\ I_{L2}=2A \\ I_O=1A \\ \Delta i_L=30\% \\ \mathrm{f_s}=60\,\mathrm{kHz} \end{cases} \quad (22)$$

As can be understood, the output power has been assumed to be 80 W. By accounting for the assumed amount of the capacitor's voltage, the inductors' current, the capacitors' voltage ripple, the inductors' current ripple, and the value of the duty cycle and employing the theoretical relations of the inductors' current ripple and the capacitors' voltage ripple, the value of the inductors and the capacitors can be expressed.

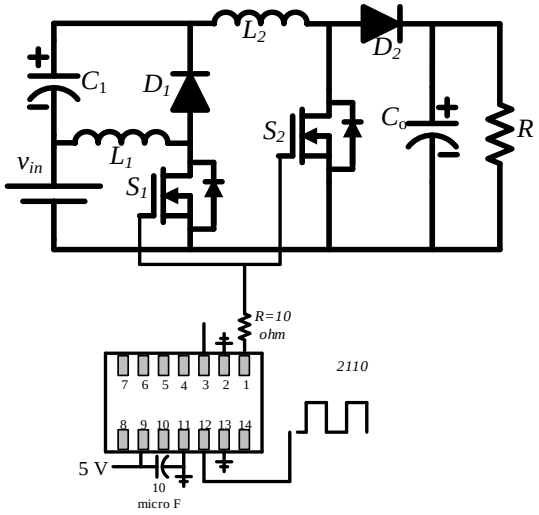

Fig.9. The explanation of the MOSFET driver

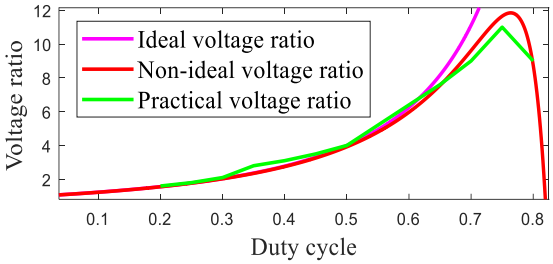

Fig. 10. The comparison of the ideal/non-ideal and practical voltage gains.

and the capacitors can be expressed. The mentioned values are as followed:

$$\begin{cases} L=140\mu H \\ L2=555\mu H \\ C_1=27\mu F \\ C_O=2.1\mu F \end{cases} \quad (23)$$

Fig. 7 refers to the simulation results. The inductors' average current and capacitors' average voltage are as (24), according to the simulation results:

$$\begin{cases} V_{c1}=19.6V \\ \mathrm{V_o}=78V \\ I_{L1}=4A \\ I_{L2}=2A \end{cases} \quad (24)$$

Comparing the extracted results and calculted results concludes their compatibilty. The negligible difference between the reported values stands from applying the parasitic components to the simulation setup. The experimental results of the designed topology have been extracted and illustrated in Fig. 8 to show the compatibility of the theoretical relations and simulation results with reality. It is good to note that IRF540 has been considered for the switches, FES8GT for the diodes, E-I type (45*35*15) inductor cores, and electrolyte and MKT capacitors in the prototype. It is worth noting that the mentioned assumptions in the simulation have been accounted in the experimental results.

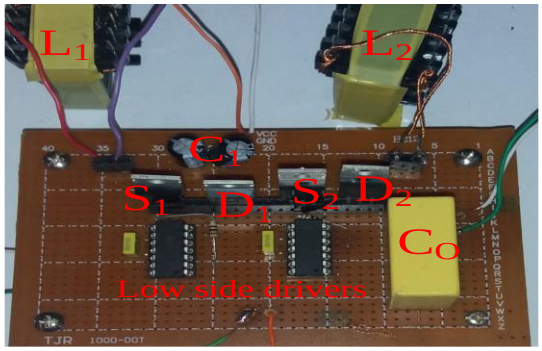

Fig. 11. The built-up circuit.

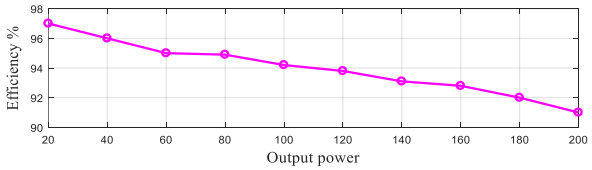

Fig. 12. The efficiency of the converter for the different output powers.

It is good to note that the calculated values in (23) are the minimum value of the components to satisfy the ripple considerations. Therefore, the capacitors have been considered as 100 and 10 micro F. Fig. 11 presents the prototype. It is good to note that IRF2110 is the MOSFET driver of the prototype, according to Fig. 9. Fig. 8 shows the voltage waveform of the input sources and capacitors. Moreover, the inductors' and semiconductors' current waveforms are the other extracted waveforms. The compatibility of the simulation results with the experimental outcomes proves the correctness of the extracted relations. Moreover, in Fig. 10, the practical voltage ratio has been extracted concerning the different amounts of the duty cycle. As can be understood, the non-ideal voltage ratio based on the extracted relation of the non-ideal voltage ratio is compatible with the practical voltage ratio based on the experimental outcomes. Moreover, the maximum value of the voltage ratio is 12 by 78 percent, according to the relation of the non-ideal voltage ratio. The practical results predicted the mentioned value of 11.8 by 75 percent as a value of the duty cycle. Fig. 12 illustrates the efficiency of the designed topology for the different output power values. The efficiency value based on the experimental results decreases from 97% to 91%, while the output power varies from 20W to 200W. Consequently, the expressed relations of the non-ideal voltage ratio are compatible with the experimental results. Therefore, the correctness of the theoretical relations is deduced.

8. Conclusion

This article proposed a modified form of the traditional step-up topology. The voltage gain was the quadratic form of the voltage gain of the traditional step-up topology. The continuity of the input current was kept, and the voltage/current stress of the semiconductor devices was low valued and suitable. The non-ideal mode of the designed topology was discussed, and the describing voltage gain of the mentioned model was extracted and compared with the practical voltage gain based on the experimental results. Moreover, the non-ideal voltage gain of the designed converter was compared with the non-ideal voltage gain of the high gain converters, and the capability of the designed converter was concluded. Moreover, the efficiency of the designed topology was discussed for 80 W of the output power. As the duty cycle becomes 50 %, the efficiency of the designed converter based on the experimental results was 95 %. The efficiency of the presented topology was discussed for different values of the output power for all amounts of the duty cycle. Furthermore, the various kinds of power loss were discussed for a duty cycle value, which concludes the voltage gain of 4 for the presented topology and other high gain converters, and the lower power loss of the designed converter was concluded. The small-signal analysis of the designed topology was discussed, and the bode diagram was extracted. The simulation outcomes based on PLECS software and the experimental results were extracted, compared, and their compatibility proved the correctness of all theoretical relations. These kinds of converters can be used HID lamps which require high voltage and low current. Moreover, such a DC-DC converter can be employed in electrical bicycles. Furthermore, the mentioned types of converters can be applied to micro inverters.

9. References

[1] Varesi, K, Hassanpour, N, Saeidabadi, S. Novel high step-up DC–DC converter with increased voltage gain per devices and continuous input current suitable for DC microgrid applications. Int J Circ Theor Appl. 2020; 48: 1820– 1837.

[2] H. Ardi, A. Ajami, F. Kardan and S. N. Avilagh, "Analysis and Implementation of a Nonisolated Bidirectional DC–DC Converter With High Voltage Gain," in IEEE Transactions on Industrial Electronics, vol. 63, no. 8, pp. 4878-4888, Aug. 2016.

[3] N. Tewari, V.T. Sreedevi, "A novel single switch dc-dc converter with high voltage gain capability for solar PV based power generation systems, " Solar Energy, 171: 466-477, 2018.

[4] R.R. Gopi, S. Sreejith, "Converter topologies in photovoltaic applications – A review, " Renewable and Sustainable Energy Reviews, 94, 1-14, 2018.

[5] A. Amir, A. Amir, H.S. Che, A. Elkhateb, N.A. Rahim, "Comparative analysis of high voltage gain DC-DC converter topologies for photovoltaic systems," Renewable Energy, 136: 1147-1163, 2019.

[6] M.H. Taghvaee, M.A.M. Radzi, S.M. Moosavain, H. Hizam, M.H. Marhaban, "A current and future study on non-isolated DC-DC converters for photovoltaic applications," Renewable and Sustainable Energy Reviews, 17: 216-227, 2013.

[7] B.S. Revathi, M. Prabhakar, "Non isolated high gain DC-DC converter topologies for PV applications - A comprehensive review, " Renewable and Sustainable Energy Reviews, 66: 920-933, 2016.

[8] J. Marjani, A. Imani, A. Hekmati and E. Afjei, "A new dual output DC-DC converter based on SEPIC and Cuk converters," in Anacapri International Symposium on Power Electronics, Electrical Drives, Automation and Motion (SPEEDAM): 946-950, 2016.

[9] H. Gholizadeh, M. Salehi, Z. Rafiee, E. Afjei and M. Hamzeh, "A Transformer Less Quadratic Buck-Boost Converter with Wide Range of Output Voltage and Low Switch Stresses," in Tehran 11th Power Electron., Drive Systems, and Tech. Conf. (PEDSTC): 1-6, 2020.

[10] S. Miao, F. Wang and X. Ma, "A New Transformer Less Buck–Boost Converter with Positive Output Voltage," IEEE Trans. on Ind. Electron., 63(5): 2965-2975, 2016.

[11] H. Gholizadeh, A. Sarikhani and M. Hamzeh, "A Transformer Less Quadratic Buck-Boost Converter Suitable for Renewable Applications," in Tehran 10th International Power Electronics, Drive Systems and Technologies Conf. (PEDSTC): 470-474, 2019.

[12] A. Sarikhani, B. Allahverdinejad, M. Hamzeh, E. Afjei, "A continuous input and output current quadratic buck-boost converter with positive output voltage for photovoltaic applications," Solar Energy: 19-27, 2019.
[13] Y. Babazadeh, E. Babaei and M. Sabahi, "A New Non-Isolated Buck-Boost Converter with High Voltage Gain and Positive Output Voltage for Renewable Energy Applications," in Shiraz 10th International Power Electron., Drive Systems and Tech. Conf. (PEDSTC): 201-206, 2019.
[14] H. Gholizadeh, S. Aboufazeli, Z. Rafiee, E. Afjei and M. Hamzeh, "A Non-Isolated High Gain DC-DC Converters with Positive Output Voltage and Reduced Current Stresses," in Tehran 2020 11th Power Electron., Drive Systems, and Tech. Conf. (PEDSTC): 1-6, 2020.
[15] N. Totonchi, H. Gholizadeh, E. Afjei and M. Hamzeh, "A Novel Transformer Less High Gain DC-DC Converter with Continuous Input Current and Suitable for Photo Voltaic Panels," in Iran 2020 11th Power Electronics, Drive Systems, and Technologies Conference (PEDSTC): 1-6, 2020.
[16] P. M. Garcia-Vite, J. E. Valdez-Resendiz, J. C. Mayo-Maldonado, J. C. Rosas-Caro, M. del Rosario Rivera-Espinosa and A. Valderrabano-Gonzalez, "Quadratic gain converter with output voltage ripple mitigation," in Cincinnati, OH IEEE Energy Conversion Congress and Exposition (ECCE): 2253-2259, 2017.
[17] S. Ding and F. Wang, "A New Negative Output Buck-Boost Converter with Wide Conversion Ratio," IEEE Trans. on Ind. Electron., 64(12): 9322-9333, 2017.

International Journal of Research and Technology in Electrical Industry

journal homepage: ijrtei.sbu.ac.ir

Shahid Beheshti University

Reliability Evaluation of Power System based on Demand Response Program in the Presence of the Electric Vehicles

Reza Asadi [1,*], Mansour Moradi[2], Mohammad Naseh Hasanzadeh[1]

[1] *Department of Electrical Engineering, Sanandaj Branch, Islamic Azad University, Sanandaj, Iran*
[2] *Department of Electrical Engineering, Technical and Vocational University (TVU), Kermanshah, Iran*

ARTICLEINFO

Article history:
Received 04 January 2022
Received in revised form 23 April 2022
Accepted 07 May 2022

Keywords:
Reliability
Demand Response (DR)
Electric Vehicles (EVs)
Well Bing Method
Composite System

ABSTRACT

The use of Demand-Side Management (DSM) to increase the reliability of composite power systems at hierarchical level II (HLII) with Electric Vehicles (EVs) is an important issue that has not been studied so far. Studies that have been conducted assumed that EVs are connected to the power system during the mid-peak load and peak load in two charge levels with uncertainty in influence and three load shifting levels (85%, 90%, and 95%). The reliability indices Loss of Load Expectation (LOLP), Expected Energy Not Supplied (EENS), Expected Health Duration (EHDUR), and Expected Margin Duration (EMDUR) are calculated. The present paper uses Monte Carlo Simulation (MCS) in modeling the uncertainty in the generation and transmission capacity of the power system and the influence of EVs. The modeling was performed on IEEE-RBTS standard system using the MATLAB software. The result indicates that more penetration of EVs will lead to higher load levels, and thereby LOLP and EENS indices will change much more, a trend that increases even more when EVs are charged during peak load. It is possible to increase EHDUR and EMDUR values by increasing load-shifting levels (95% to 90% and 85%).

Nomenclature

U	Random number in range (0, 1)
P_h	Probability of system health
P_m	Probability of system margin
P_r	Probability of system risk
Thi	Duration of the ith healthy states (hours)
Tmi	Duration for the ith marginal states (hours)
Tri	Duration for the ith risk states (hours)
T, Tx	Total simulation time (hours)
m	The length of the program period is based on the year
F(h)	Frequency of health (occurrences/year)
F(m)	Frequency of marginal (occurrences/year)
F(r)	Frequency of risk (occurrences/year)
n(h)	Total number of healthy states
n(m)	Total number of marginal states
n(r)	Total number of risk states
N	Total number of simulated (year)

Subscripts

A	Availability

Greek

λ	Expected failure rate
μ	Expected repair rate

Abbreviations

FOR	Forced Outage Rate
TTF	Time To Failure
TTR	Time To Repair

LOLP	Loss of Load Probability
EENS	Expected Energy Not Supplied (mwh/year)
EHDUR	Expected Health Duration (hours/occurrences)
EMDUR	Expected Margin Duration

1. Introduction

Global environmental concerns, the decline in fossil fuels, and the consequent rise in fuel prices have led to an ever-increasing demand for electric energy. At the same time, electric power generation and transportation sectors are some but directly linked with 21st-century issues like maximum oil production, climate change, and energy independence. Currently, the facilities to build up transportation and greater electric power generation use more than 60% of the world's primary energies [1]. As a result, there is a growing interest in technologies such as EVs that can replace combustion fuel cars. These technologies help reduce dependence on petroleum products and the emission of greenhouse gases [2]. Electric transportation is considered a good alternative as it can considerably reduce the need for petroleum products and facilitate the use of renewable energies [2]. In recent decades, electric transportation systems such as electric trains have developed significantly and can be considered the primary infrastructure in the field of transportation in the future.

With the growing popularity of EVs, there is a severe challenge to the stability of the power system, as large volumes of mobile consumers across the grid cause imbalances [3]. Increasing the availability of electric machines and lack of proper energy management can lead to instability of the power system [4]. In order to study the reliability and suitability of the grid, it is necessary to recognize the behavior of EVs owners and appropriate management methods for these vehicles. Many researchers and methods have tried to find ways to mitigate these undesirable.

1.1. Background of the Research

In general, various studies and methods have been proposed to reduce the adverse effects of EVs on different loads. For example:

To predict the expected daily power for the uncoordinated charging power demand of an EV, a stochastic process has been utilized in [5]. Different charging time distributions and departure time as another random variable are considered in the model presented to manage the autonomous Demand Response (DR) technique to control the EV charging demand. In

The effect of integration of EVs on DR programs considering classifications types of customers with an emphasis on invaluable services that EVs can provide in smart grid assets is scrutinized in [6].

An optimal power dispatch problem on a 24-hours basis for distribution systems incorporated with directly controlled shiftable loads and renewable energy resources has been introduced. The number of optimization variables has been reduced using the optimization approach presented in [7].

The economic impacts of the vehicle to grid regulation reserves considering the restrictions arising from unpredictable mobility by vehicle users is analyzed through an actual case study in which a dynamic approach reveals a significant improvement compared with static ones is presented in [8].

A stochastic scheduling approach is proposed for many EVs parked in an intelligent parking lot is introduced in [9]. A self-scheduling model for an intelligent parking lot equipped solar systems and distributed generation through which practical constraints, solar radiation uncertainty, spinning reserve requirements, and EVs owner satisfaction are considered.

To coordinate the charging and discharging of EVs considering the frequency deviation signal to deal with the uncertainty of renewable energy generations, a dynamic demand control has been proposed in [10] leads to distinguishing characteristics such as simplicity, efficiency, robustness, and readiness for practical applications.

In [11], DSM of Plug-in Hybrid EVs (PHEVs) will become necessary to reduce peak loads as the penetration of PHEVs becomes greater. Trying to flatten the power-demand curve at transformers will avoid overloading and defer investment.

To control the risk management and participation planning of EVs in the smart grid at high penetration level of renewable energy resources, a stochastic model is introduced from the Independent System Operator's perspective in a away that cover all uncertainties caused by renewables, load patterns, parking patterns, and transmission lines' reliability [12].

In [13] has developed a model to create coordination between various PHEVs charging and discharging to reduce the electricity consumption peak and valley. In addition, the PHEVs owners earn economic profit in the grid through the demand peak and valley reduction. A DR scenario is presented as a corrective action following a contingency to maintain the power system within its limits during the urgent condition.

To quantify the reliability performance under different scenarios considering the influence of information and communication technology as well as automatic control scenarios, Sequential MCS are employed [14].

1.2. Classification of Power Systems for Evaluating Reliability

Modern electric systems are characterized by a vast and complex set of units from generation to individual consumers. Therefore, digital software and hardware are not entirely sufficient for the job of accurate and inclusive reliability evaluation of the grids. The power system parts are classified into three categories of generation, transmission, and transmission, based on their performance and reliability. This classification can be integrated to form hierarchical levels for reliability analysis [15].

The first hierarchical level (HLI) involves the assessment of reliability at the level of generation units and the ability of these generation units to satisfy local loads.

Reliability evaluation of Hierarchical Level II (HLII), includes generation units as well as a transmission network. Reliability evaluation of composite power systems is, in

fact, the analysis of the capability to transmit electrical energy to consumers or main load points. Reliability evaluation of the third hierarchical level includes generation, transmission network, and distribution systems, and it considers the system's ability to provide energy for all consumers. Given the compartmentalization of the power system, reliability indices vary at different levels. Therefore, the present study focuses on the reliability indices of HLII.

DSM strategy can be considered a practical solution to increase the reliability of the power system in the presence of EVs [16]. Therefore, DSM can increase the reliability of the power system without expanding it, which helps improve the presence of EVs while maintaining reliability indices.

1.3. DSM plans

The DSM includes two mutually effective plans: Energy efficiency and DR [17]. Energy efficiency or management analyzes daily or seasonal energy consumption and reformats it into an optimal consumption scheme. DR refers to a set of practices that consumers follow in reforming consumption models, enhancing network reliability for greater productivity of facilities, boosting economics of investments, and removing energy limits. These practices help control costs, especially during peak load periods [17]. Various methods of remodeling load in DR are presented in Fig.1. [18].

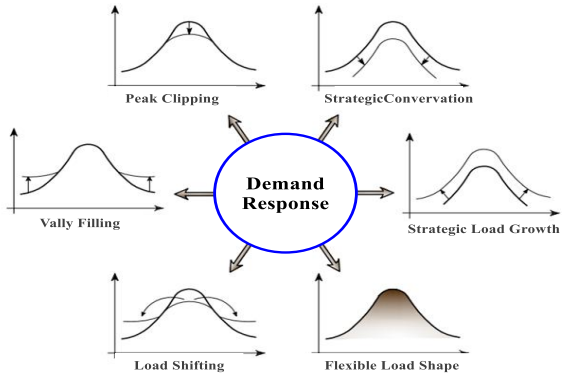

Fig.1. Different methods to change the load curve and shape in the DR program [18].

DR by load shifting technique is a widely used in DSM [19]. The extent DR using the load shifting technique influences reliability indices of the power system is excellent and depends on the shift amount from peak load during low load periods. Therefore, shifting load was performed at different levels, and resulting indices were used to analyze the model [20]. One of these indices is the application of the indices of system well-being criteria incorporating deterministic criteria in the probabilistic framework. These indices can integrate deterministic criteria in probability calculations to determine the system behavior [21]. Well-being analysis can also be considered in establishing the definite or probable criteria for determining the reserve required by power systems [21]. The present paper uses DR (concerning probable state programs for initiatives) at three levels to investigate the impact of the presence of EVs at three levels of 85%, 90%, and 95%, despite the uncertainty. The behavior of the power system in the selected model was evaluated using well-being analysis and indices as basic indices in assessing the reliability of the power system.

1.4. Innovation and Novelty

In general, during the reliability evolution of composite power system, it is necessary to understand calculated indices, which make the problem more complex [22] In this situation, system adequacy assessment is used to evaluate the considered indices. To gain the probability of lacking the system adequacy in the complex power system, each system's power flow analysis is performed considers the load model defined for that network. The load modeling can be done in three different ways: constant current, constant power, and constant impedance loads. load changes over time and each specific amount of load is valid just for an instant. Therefore, the AC power flow analysis is conducted for loads and generators for a short period. As a result, the main purpose of the AC power flow is to determine the steady state condition of bus voltages considering the constant power load model as the worst-case scenario considered in this paper.

Overall, in the present study, the applicability of DSM for enhancing the productivity of the facilities and enhancing the reliability of a hybrid power system, including generation, transmission lines, and loads in the presence of EVs, is evaluated using the MCS method and in correspondence to their uncertainty. It is assumed:

The probabilistic situations created by MCS for load, generation, and transmission lines for 1000 years of the study (due to the enormity of the calculations) are equal to 36 matrices representing 36 different modes of penetration of EVs. Each matrix includes the number of hours (8736000 rows) and 25 columns (the symbols of probabilistic loads, generation, transmission lines).

That EVs are connected to the power system during the critical and influential mid-peak load and peak load in two charging levels with uncertainty in influence and three load shifting levels (85%, 90%, and 95%).

Considering the voltage of busbars as a critical criterion to determine the level of a load shift. (A voltage range of 0.97-1.05V is chosen for the present study. In case voltages fall outside this range after the power flow, reactive power can be injected to put voltages within the predetermined limits. Thus, these cases in the evaluation of the variables can be considered as non-problematic situations.)

Employing well-being for the reliability evolution of the power system.

An AC power flow is selected to better evaluate the research variables, including LOLP, EENS, EHDUR, and EMDUR, so that the effects of the transmission lines on the precise evaluation of variables can be analyzed.

This is the case because when the loading level of power transmission lines is considered the loading criteria, the DC power flow is enough. But, while the busbar voltage value is also considered, the AC power flow should be used [23].

Because the AC power flow helps determine the effects of transmission lines on the provision of load and thus a better evaluation of the variables.

DR programs are generally divided into two types (i.e., price-based DR and incentive-based DR). In this paper, DR is considered motivational which is determined by companies and governments.

2. Proposed Methods

2.1. Simulation Flowchart

In this paper, MCS was applied to simulate different states of power system with uncertainty in generation capacity and in transmission and also well-being model was applied to evaluate different states of operation of the system in HLII level with penetration of EVs (shown in Fig.4. MCS is a probabilistic method with approximate results which vary a little in various runs [24]. Thus, these results can be minimized and negligible when the method is applied carefully. The present study, therefore, conducted 1000 samples (equal to 1000 years).

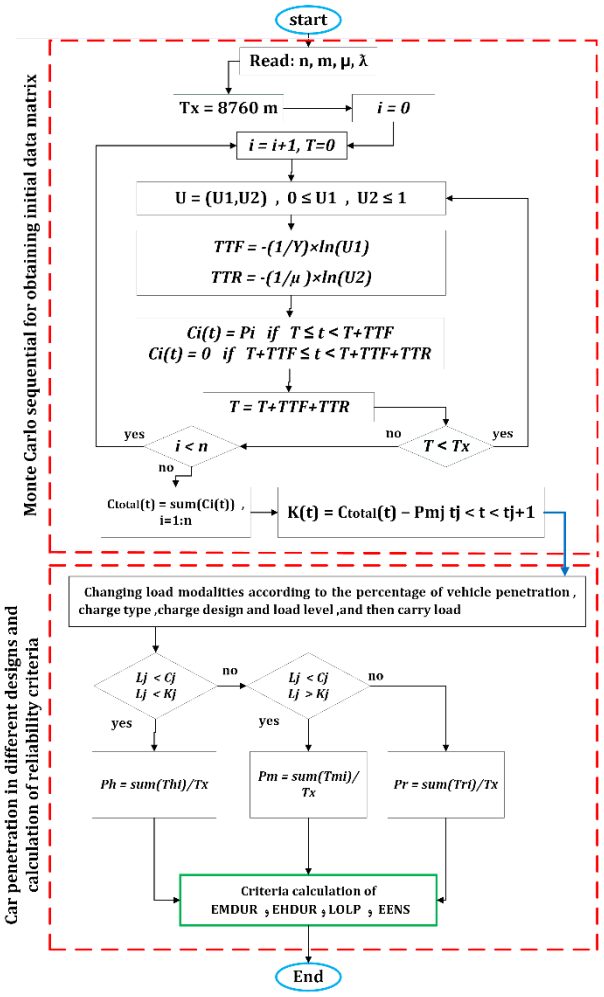

Fig. 2. Proposed simulation flowchart

3. Formulating the Problem

3.1. Well-being analysis Models

Health state refers to a condition when a power system can provide the required load and secure a desirable reserve. When the system fails to provide the necessary load, it is in a risk state. Any condition that falls between these two states is known as marginal: the system can only provide its required load [25], [26].

Since the actual load is continually fluctuating, the uncertainty in predicting short-term load and possible errors create particular problems. A sufficient reserve load must be thought out to adequately feed the required load [26]. MCS can track working/failed generation units and, thus, can be used to evaluate the operation of the power system. Accordingly, the reserve is calculated when the most significant unit is subtracted from the available capacity at any given reserve level. Then heath, risk, and marginal states are determined by assuming the following periods:

The risk is linked to those levels with loads more abundant than available capacity and is calculated by the following equation [26].

$$P_r = \frac{\sum Tri}{T} \quad (1)$$

Health defines the condition when the system provides its load and has a desirable reserve. In other words.

Capacity of the total load < (Available Capacity largest unit)

Equation 2 shows the probability of system health [26].

$$P_h = \frac{\sum Thi}{T} \quad (2)$$

A risk state refers to a state when the system can provide its load but cannot maintain a reserve load [18].

$$P_m = \frac{\sum Tmi}{T} \quad (3)$$

Where:

$$P_h + P_m + P_r = 1 \quad (4)$$

A better and more detailed description of these states is given in Fig.3.

3.2. Reliability

The primary task of a power system is to provide electric energy for consumers economically and reliably [27]. There are many parameters in a power system that affect reliability [28]: load demand, generation units' specifications, associated systems, consuming available resources, and load control and management. In HLII or composite system, the Loss of Load Expectation (LOLP) and Expected Energy Not Served (EENS) are essential factors which are calculated by (٥) and (٦). Other reliability indices are health and marginal duration, which are represented in (7) and (8), respectively [26].

3.3. Monte Carlo Simulation (MCS)

According to references [29], there are two ways to determine the reliability indices: deterministic or analytical method and probabilistic or accidental simulation. The analytical methods usually employ mathematical models that include simplification. Here, reliability indices are achieved through solving the mathematical problems directly. However, in simulation methods, these indices are determined along the actual process and according to system behavior.

MCS is a widely used method for determining reliability indices [27]. The term MCS is generally applied to any technique that estimates quantitative variables through simulation. Finally, it is fair to say that MCS can be used to simulate the power system and penetration of

EVs [30].

$$LOLP = \frac{\sum_{i=1}^{n(r)} t(r)_i}{N \times 8760} \quad (5)$$

$$EENS = \frac{\sum_{i=1}^{n(r)} e_i}{N \times 8760} \quad (6)$$

$$EHDUR = \frac{\sum_{i=1}^{n(H)} t(H)i}{n(H)} \quad (7)$$

$$EMDUR = \frac{\sum_{i=1}^{n(M)} t(M)i}{n(M)} \quad (8)$$

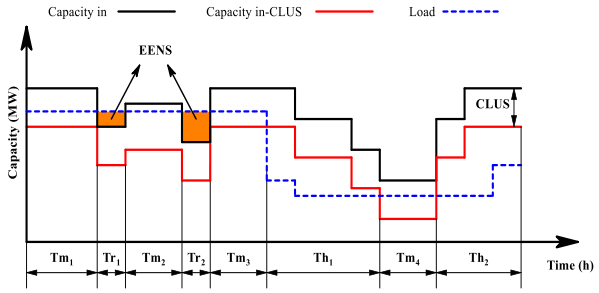

Fig.3. Three modes of health, margin, and risk in power systems according to load profile and generation capacity

3.4. States of Generating Units

The trial IEEE-RBTS system under study is characterized by 11 generating units with 240MW capacity. These units can be coupled in discreet and mutually incompatible pairs. Therefore, the case where working and failed units are displayed as available and unavailable in a bimodal demonstration (Forced Outage Rate). The probability of other occurrences demands the introduction of a highly complex arrangement in mode space. The probability of the bimodal availability and unavailability is computed by using the following equations in the analytical method [27], [32]:

$$A = \frac{\mu}{\mu + \lambda} \quad \text{Available Status} \quad (9)$$

$$FOR = \frac{\lambda}{\mu + \lambda} \quad \text{Unavailable Status} \quad (10)$$

In the present paper, the MCS of units in the bimodal unit is possible by using a random value between (0 - 1).

3.5. The Duration of States

The random value must be transferred to the time domain to determine the duration of the state. The bimodal generating units are described by the model presented in Fig.4.

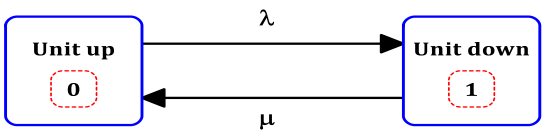

Fig.4. Dual-mode generation unit [14], and [19].

The random values for time to failure (TTF) and time to repair (TTR) for a bimodal model of the generating units (Fig.4.) are computed as follows [17], [32]:

$$TTF = -\frac{1}{\lambda} Ln\, U_1 \quad (11)$$

$$TTR = -\frac{1}{\mu} Ln\, U_2 \quad (12)$$

Where U1 and U2 represent two random values between 0 and 1.

The sequential sampling of the functioning, failure, and usage-repair can be realized by a chronological sampling of the values for TTF, TTR, and TTF.

4. Simulation results of the proposed method

One of the main parts of simulation is the matrix arrangement of the data about the system that are the input for MCS. The simulation is considered for 1000 years to get better accurate results. Therefore, the matrixes include 25 columns and 8736 rows, and therefore the entire matrix has 8736000 rows. Given the probability function of MCS about integrating loads, generation, and transmission lines, there are some states that have no generation or transmission lines. This means that some buses display drop or decrease in load (in this study, the min and max voltages are 0.97 and 1.05, respectively). To correct the voltage profile and identify buses, AC loads are distributed to any rows from the matrix and buses with a drop in voltage are corrected through adding reactive power to both buses no. 4 and 6 up to 10MVar in 0.01 steps. If after this addition, the voltage of buses remains still beyond the desirable range, the load is interrupted in steps of 0.1MW to correct the voltage profile. In case that voltage drop is still not corrected, it is considered a defective state and will be removed from the matrix and analytical calculations of the power system. In the power system under study, 165000 rows are removed from the matrix. As such, 25 columns and 8571000 rows are considered.

After removing defective states, 36 penetration states are applied to the matrix. As a result, 36 matrixes with 25 columns and 8571000 rows are under study. Distribution is conducted for each row of these 36 matrixes, and those EVs whose voltage profiles are not corrected at this point are removed from the matrix and then the reliability indices are computed.

4.1. The System under Study

This research studies a 6-bus IEEE-RBTS system for which a Single-Line Diagram (SLD) is used in this article [31]. This system consists of 6 buses, and buses no. 1 and 2 represent generation units. On the whole, there are 11 generating units. Transmission lines operate with 230KV the total capacity is 240MW, and the peak load is 185MW. The network also includes two distribution systems installed in buses no. 2 and 4. These systems are comprehensive and contain main reforms and factors [30]. This research studies a 6-bus IEEE-RBTS system for which a Single-Line Diagram is presented in Fig. 5.

4.2. Simulating Parameters

4.2.1. *Load Simulation*

There are two main ways to display variations in the load employed in MCS: temporal and non-temporal [24].

- The temporal method extends the load levels in the order or chronological format of their actual or possible occurrences. This can be annually or in

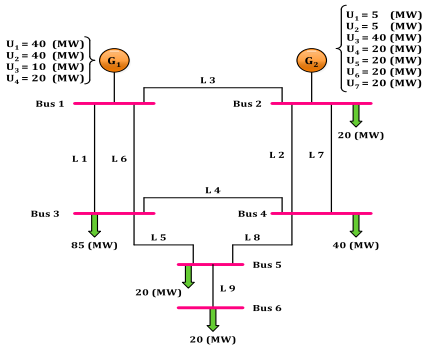

Fig.5. SLD of the IEEE-RBTS network.

other time frames. In the simulation, in 365 days, the maximum demands are specified, while it can also be displayed on an hourly basis, i.e., 8760 hours.

- The non-temporal method displays the load levels in decreasing order and form of cumulative values.

The present paper uses an hourly temporal method to display the variations.

4.2.2. Estimating the number of Consumers

The trial IEEE-RBTS system includes six buses with two distribution systems in buses no. 2 and 4. Buses 2 and 4 feed 1850 and 4700 household consumers, respectively [28]. Moreover, every consumer has an average share of 3.981KW (Table I). The total number of household consumers was computed by dividing the total household load by the mean share of each consumer.

The average consumption of household loads is equal to 62.9 MW, with the number of consumers equal to 15800 people; the same amount of EVs can be added to the power system.

4.2.3. The Penetration Schemes for EVs

Introducing EVs into the system means an extra load for the system. The load curve changes according to the number, speed, and charge time of these EVs. Load simulation shows days with the maximum load if a year is assumed to have 365 days. The present paper analyzes various scenarios and different states along with penetration percentage, time, charge amount and length of the plug-in are as follow:

4.2.3.1. Penetration percentage

Adding EVs happens at different levels. This research considers three levels (Table II): 10%, 20%, and 30% [31].

4.2.3.2. Speed and duration of the charge

Today, there are different models of EVs, and these models will develop in performance and range. According to references [32], this study considers three models of EVs (Table III). A single type of battery (24.1KW) is assumed here in this study, while the equation (16) is held to be true for all EVs and shows the average size battery [33].

$$\text{EVs' composition (\%)} \times \text{Battery Capacity (kWh)} = \quad (16)$$

$$(0.37 \times 35) + (0.1 \times 16) + (0.53 \times 18) = 24.1 \text{ (kwh)}$$

Table I. Residential Consumer Specifications for IEEE-RBTS Distribution Systems

Bus	Number of residential customers	Total residential load in the bus MW	Average load per consumer KW
2	1580	7.25	3.919
4	4700	19	4.043
Average			3.981

Table II. EV penetration percentage

State of	% Penetration	Number of EV
1	10	1580
2	20	3160
3	30	4740

Table III. Electrical vehicle info

EV's Parameter	EV type	Value
EVs' composition (%)	BEV	37
	City-BEV	10
	PHEV90	53
Battery Capacity (kWh)	BEV	35
	City-BEV	16
	PHEV90	18
Average battery capacity (kWh)		24.1

Two modes are considered for charging EVs (Table IV) that vary according to the hours of charge and the power received from the network [34].

Table IV. Battery charge time

Charge type	Charging time (hrs)	Consuming EV at the time of recharging (kW)
Slowly	6	3.7
Fast	2	11

Table V. Available states of 10% and 20% of EV penetration, with Taking load levels

State of	1 to 18						19 to 36					
Charging speed	Fast						Slowly					
Scheme type	1			2			1			2		
Load level %	85	90	95	85	90	95	85	90	95	85	90	95

4.2.3.3. Hours of connection to the network

Previous studies usually assume that EVs are charged during low load periods [34]. This study assumes that some EVs are also charged during mid-peak and peak load. For this purpose, two charge schemes are considered:

- ❖ Scheme 1: 70% of the vehicles are charged during low load periods and 30% during mid-peak hours.
- ❖ Scheme 2: 60% are charged during low load hours, 30% during mid-peak load, and 10% during peak load hours.

There are three penetration levels (10%, 20%, and 30%), two charge modes, two penetration schemes, and three load shifting levels. Therefore, 36 states are considered for EVs under this study (Table V).

4.3. Well-Being Model

According to section 3.3.5. EVs were added to the power system under study while applying DSM. As a result, the load curve changed, and consequently, the values

for the probability of health, risk, and marginal states underwent changes since the primary factor for evaluation of penetration of EVs, analysis of DSM, and comparison of different states is the analysis of the probability of risk mode in the system.

It is necessary to determine the reliability indices at default conditions to evaluate the penetration of EVs and evaluate the effect of DSM on the reliability of the power system in the presence of EVs. Therefore, a table shows the definite capacity of generating units before adding EVs. Then, the probability values in each health, risk and marginal states are computed according to the load curve. The probability values of each state at default phase are computed using values for Th, Tm, Tr as well as total time period of applying the management (Table VI).

Table VI. Results for the simulated power system at the base state.

PR	Pm	Ph
0.00229	0.01794	0.97852

As indicated in section 4.2.3, penetration schemes for EVs are as follow:

- Penetration percentage (10%, 20% and 30 %.)
- Speed and duration of the charge
- Hours of connection to the network (Scheme 1 and Scheme 2)
- DR, according to Fig. 6.
- A simulation of 36 different penetration states for EVs is presented in Table 7.

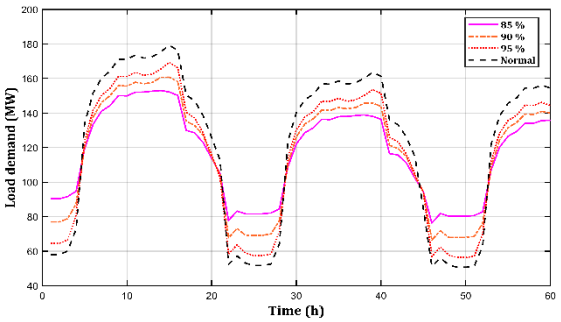

Fig.6. Small Portion of the DR curve in the load shifting approach for three levels, including 85%, 90%, and 95%.

As shown in Table VII, it is possible to conclude that the probability of a health state is 85% greater than the default conditions since in low load levels, fewer portions of peak load are in a risk state and vice versa. For instance, the probability of risk mode for penetration of EVs at three penetration levels and at three load shifting levels, and in 2 penetration schemes at a fast charge is given in Figs. 7 and 8.

As shown in Figs. 7 and 8, the probability of risk mode increases with the penetration of EVs and an increase in load shifting levels. According to Fig.8, the probability of risk mode in scheme 2 is higher than in scheme one since 10% of EVs are charged during peak load. Also, the probability of risk mode for the system has decreased by 85% of response in proportion to default conditions. This shows the importance of demand-side management.

Table VII. Simulation results for various DR considering EVs penetration

Penetration level			% 10		% 20		% 30	
			Slow	Fast	Slow	Slow	Slow	Slow
Ph	1	%85	0.97829	0.97827	0.97806	0.97790	0.97775	0.97755
		%90	0.97687	0.97687	0.97664	0.97647	0.97637	0.97612
		%95	0.97388	0.97405	0.97388	0.97373	0.97368	0.97337
	2	%85	0.97816	0.97817	0.97775	0.97776	0.97740	0.97741
		%90	0.97665	0.97666	0.97620	0.97621	0.97569	0.97571
		%95	0.97385	0.97385	0.97336	0.97336	0.97285	0.97289
Pm	1	%85	0.01965	0.01967	0.01986	0.02002	0.02015	0.02036
		%90	0.02021	0.02029	0.02036	0.02063	0.02055	0.02095
		%95	0.01944	0.01965	0.01958	0.01996	0.01971	0.02031
	2	%85	0.01977	0.01977	0.02015	0.02014	0.02048	0.02047
		%90	0.02023	0.02023	0.02039	0.02039	0.02057	0.02057
		%95	0.01937	0.01937	0.01938	0.01938	0.01957	0.01957
Pr	1	%85	0.00081	0.00081	0.00083	0.00082	0.00086	0.00084
		%90	0.00167	0.00163	0.00175	0.00165	0.00184	0.02095
		%95	0.00544	0.00505	0.00529	0.00506	0.00536	0.00507
	3	%85	0.00082	0.00082	0.00085	0.00085	0.00087	0.00087
		%90	0.00187	0.00187	0.00216	0.00215	0.00249	0.00247
		%95	0.00553	0.00553	0.00600	0.00600	0.00632	0.00629

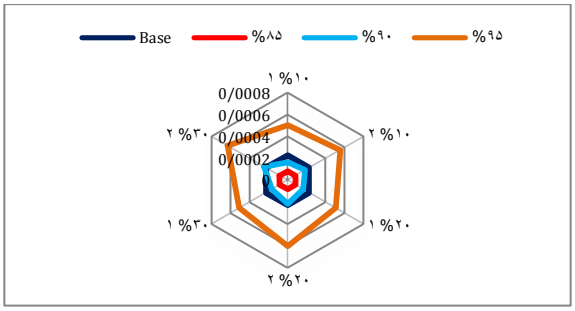

Fig.7. The probability of risk mode for EVs penetration scenarios with 10, 20, and 30% at three load movement levels, two penetration schemes, and EVs fast recharge.

4.4. EHDUR and EMDUR criteria

The duration of heath and marginal states is another reliability index useful for evaluating the reliability of generating the energy required by the consumers. The portion of time when the system remained in health and marginal states is computed using equations no. 7 and 8. The values for EHDUR and EMDUR are shown in Tables VIII and IX: they are based on simulation results for the default state and other states.

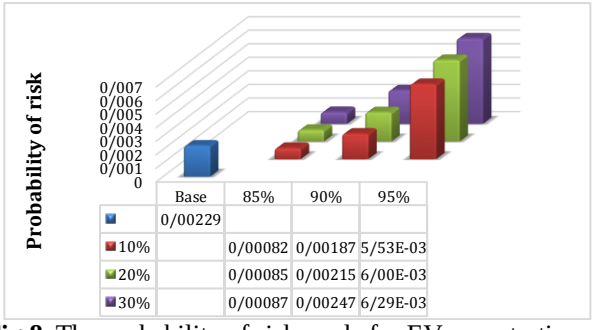

Fig.8. The probability of risk mode for EVs penetration scenarios with 10, 20, and 30% at three load movement levels, second scheme, and EVs fast recharge.

According to results presented in Tables VIII and IX, it can be said that more extensive penetration of EVs and the consequent elevation of load shifting levels (90% and 95% instead of 85%) lead to shorter duration of health and marginal states. It is possible to hold that duration of health and marginal states are in a reverse relationship with the penetration percentage of EVs and load shifting level. Duration of health and marginal states is maximum in case of 85% response. For instance, the duration of the health state in 85% and 90% response to load is better than the default state, which a fact that confirms the necessity of demand-side management. In scheme 2, health durations and marginal conditions have been reduced more than in scheme 1.

Table VIII. Durability index for modes of health and margin in the base state (in percentages)

EHDUR	EMDUR
0.0380	6.00782

Table IX. Frequency index in modes of health, margin, and risk for various load levels (in percentages).

Load	Penetration level		10%		20%		30%	
	Type of Scheme	Load	Slow	Fast	Slow	Fast	Slow	Fast
EHDUR	1	%85	496.51834	496.94421	495.36586	477.91435	493.49100	466.67067
		%90	451.08798	451.30899	450.17465	445.44184	448.41521	435.03752
		%95	376.85885	381.71031	368.45478	380.81724	365.35846	377.64950
	2	%85	495.53324	495.53550	494.35177	494.41310	492.37771	492.38036
		%90	441.97182	442.36246	434.60940	434.63420	426.53329	426.62569
		%95	376.83047	376.88077	369.44418	369.44431	366.40120	365.67198
EMDUR	1	%85	9.66733	9.69004	9.74640	9.50499	9.85555	9.45225
		%90	7.87525	7.91312	7.92634	7.96325	7.96451	7.93532
		%95	5.32436	5.52758	5.12961	5.61060	5.09155	5.68124
	2	%85	9.70058	9.69839	9.87512	9.87313	9.99659	9.99413
		%90	7.53177	7.55008	7.34443	7.34498	7.13702	7.13650
		%95	5.32461	5.32506	5.14466	5.14460	5.14753	365.67198

4.5. LOLP and EENS criteria

LOLP and EENS, other useful reliability indices, are computed by equations 5 and 6. The values for LOLP and EENS are shown in Tables X and XI: they are based on simulation results for the default state other states.
Furthermore, LOLP and EENS in the event of EV penetration for 10%, 20%, and 30% at three load shifting levels and according to 2 penetration schemes at fast charge mode are presented in figs. 9 and10.
According to results presented in Tables X and XI as well as figs. 9 and 10, it can be said that more extensive penetration of EVs and the consequent elevation of load levels lead to more significant variations in LOLP and EENS that can bring about a higher probability of risk state. Since 10% of the EVs are charged during peak load in scheme 2, the variations in LOLP and EENS are higher than in scheme 2.

Table X. The probability of loss of load index and expected unsupplied energy at various load levels (in percentages)

Penetration level			% 10		% 20		% 30	
			Slow	Fast	Slow	Fast	Slow	Fast
LOLP	1	%85	0.00081	0.00081	0.00083	0.00082	0.00086	0.00084
		%90	0.00167	0.00163	0.00175	0.00165	0.00184	0.00168
		%95	0.00544	0.00505	0.00529	0.00506	0.00536	0.00507
	2	%85	0.00082	0.00082	0.00085	0.00085	0.00087	0.00087
		%90	0.00187	0.00187	0.00216	0.00215	0.00249	0.00247
		%95	0.00553	0.00553	0.00600	0.00600	0.00632	0.00629
EENS	1	%85	158.34029	157.36419	162.41795	160.46481	167.03972	164.10974
		%90	205.94852	204.29843	209.08356	205.56381	213.09863	207.43705
		%95	396.71956	375.93725	390.37591	377.02637	398.96287	378.25962
	2	%85	160.88077	160.80423	167.35078	167.18895	174.18564	173.93146
		%90	213.26638	213.09636	224.88555	224.48871	238.21935	237.53162
		%95	404.96918	404.48007	437.82488	436.75410	472.96213	471.31908

Table XI. The probability of loss of load index and expected unsupplied energy for the base power system (in percentages)

LOLP	EENS
0.00023	310.31593

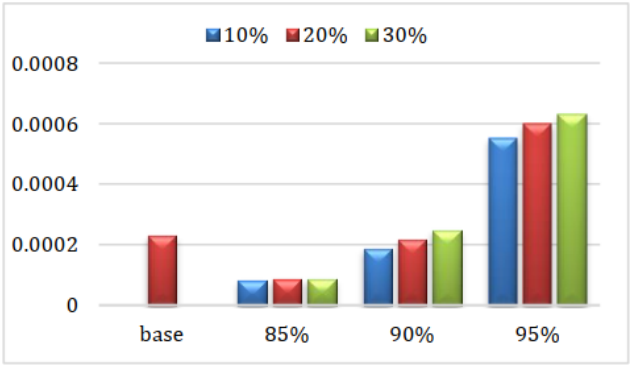

Fig.9. LOLP index for EVs penetration scenarios with 10, 20, and 30% at three load movement levels, second schemes, and EVs fast recharge.

5. Analysis of results

- Since the present study assumed the 10%, 20%, and 30% penetration levels for EVs at three load shifting levels (85%, 90%, and 95%), the following results can be expressed:
- EVs reduce the probability of a health state and increase the probability of marginal and risk states. With more significant penetration percentages or more EVs added to the system, the probability of risk mode increases while the reliability of the power system decreases. In other words, the following relationship holds in this study according to the assumed penetration levels:

The probability of risk mode at 30% penetration level > Probability of risk mode at 20% penetration level > Probability of risk mode at 10% penetration level

- According to the results, charging EVs during peak load reduces reliability much more than during mid-peak load and low load. This leads to an increased probability

of the risk state. Therefore, it is better to charge EVs during low and mid-peak loads.

- Reduction or addition of load during peak loads has the most significant impact on the risk probability. In other words, charging the EVs during peak load can negatively affect system reliability.

Probability of Risk in Scheme 2 > Probability of Risk in Scheme 1

When the number of EVs charged at different times is determined, the speed of charging can have a different impact on system risk. The results show that the probability of risk for the system in slow charging mode is higher than in fast charging mode.

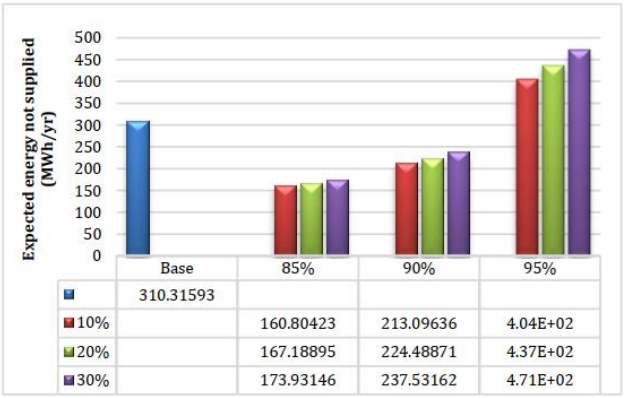

	Base	85%	90%	95%
	310.31593			
10%		160.80423	213.09636	4.04E+02
20%		167.18895	224.48871	4.37E+02
30%		173.93146	237.53162	4.71E+02

Fig.10. EENS index for EVs penetration scenarios with 10, 20, and 30% at three load movement levels, second scenario s, and EVs fast recharge.

6. Conclusion

This paper investigates the effects of EVs in power systems regarding penetration percentage, charging speed, time of charging speed, and various penetration schemes. The analyses show that adding EVs into HLII as new loads lead to an increase in the risk state in the power system. Therefore, demand-side management can be applied as an effective and inexpensive way to reduce the probability of risk mode without expanding facilities of the grid or transmission lines. The application of demand-side management with load shifting technique in HLII showed that this method could maintain the penetration level of EVs and enhance the reliability level of the power system.

References

[1] F. Rassaei, W. Soh and K. Chua, "Demand Response for Residential Electric Vehicles With Random Usage Patterns in Smart Grids", *IEEE Transactions on Sustainable Energy*, vol. 6, no. 4, pp. 1367-1376, 2015.

[2] E. Akhavan-Rezai, M. Shaaban, E. El-Saadany and F. Karray, "Online Intelligent Demand Management of Plug-In Electric Vehicles in Future Smart Parking Lots", *IEEE Systems Journal*, vol. 10, no. 2, pp. 483-494, 2016.

[3] R. Green, L. Wang and M. Alam, "The impact of plug-in hybrid electric vehicles on distribution networks: A review and outlook", *Renewable and Sustainable Energy Reviews*, vol. 15, no. 1, pp. 544-553, 2011.

[4] A. Kavousi-Fard, A. Abbasi, M. Rostami and A. Khosravi, "Optimal distribution feeder reconfiguration for increasing the penetration of plug-in electric vehicles and minimizing network costs", *Energy*, vol. 93, pp. 1693-1703, 2015.

[5] F. Rassaei, W.S. Soh, and K.C. Chua. "A statistical modelling and analysis of residential electric vehicles' charging demand in smart grids." In Innovative Smart Grid Technologies Conference (ISGT), Feb. 2015 IEEE Power & Energy Society, pp. 1-5.

[6] M.C. Falvo, G. Graditi, and P. Siano. "Electric vehicles integration in demand response programs." In Power Electronics, Electrical Drives, Automation and Motion (SPEEDAM), Jun. 2014 International Symposium on, pp. 548-553.

[7] G. Graditi, M. Di Silvestre, R. Gallea and E. Riva Sanseverino, "Heuristic-Based Shiftable Loads Optimal Management in Smart Micro-Grids", *IEEE Transactions on Industrial Informatics*, vol. 11, no. 1, pp. 271-280, 2015.

[8] D. Dallinger, D. Krampe and M. Wietschel, "Vehicle-to-Grid Regulation Reserves Based on a Dynamic Simulation of Mobility Behavior", *IEEE Transactions on Smart Grid*, vol. 2, no. 2, pp. 302-313, 2011.

[9] M. Honarmand, A. Zakariazadeh and S. Jadid, "Self-scheduling of electric vehicles in an intelligent parking lot using stochastic optimization", *Journal of the Franklin Institute*, vol. 352, no. 2, pp. 449-467, 2015.

[10] H. Nguyen, C. Zhang and J. Zhang, "Dynamic Demand Control of Electric Vehicles to Support Power Grid With High Penetration Level of Renewable Energy", *IEEE Transactions on Transportation Electrification*, vol. 2, no. 1, pp. 66-75, 2016.

[11] Y. Mou, H. Xing, Z. Lin and M. Fu, "Decentralized Optimal Demand-Side Management for PHEV Charging in a Smart Grid", *IEEE Transactions on Smart Grid*, vol. 6, no. 2, pp. 726-736, 2015.

[12] N. Nezamoddini and Y. Wang, "Risk management and participation planning of electric vehicles in smart grids for demand response", *Energy*, vol. 116, pp. 836-850, 2016.

[13] R. Yu, J. Ding, W. Zhong, Y. Liu and S. Xie, "PHEV Charging and Discharging Cooperation in V2G Networks: A Coalition Game Approach", *IEEE Internet of Things Journal*, vol. 1, no. 6, pp. 578-589, 2014.

[14] A.LA. Syrri and P. Mancarella. "Reliability evaluation of demand response to increase distribution network utilisation." In Probabilistic Methods Applied to Power Systems (PMAPS), Jul. 2014, pp. 1-6.

[15] D. Božič and M. Pantoš, "Impact of electric-drive vehicles on power system reliability", *Energy*, vol. 83, pp. 511-520, 2015.

[16] R. Billinton, "Power system reliability evaluation". Taylor & Francis, 1970.

[17] H. Kwag and J. Kim, "Reliability modeling of demand response considering uncertainty of customer behavior", *Applied Energy*, vol. 122, pp. 24-33, 2014.

[18] M. Behrangrad, "A review of demand side management business models in the electricity market", *Renewable and Sustainable Energy Reviews*, vol. 47, pp. 270-283, 2015.

[19] R. Dharani, M. Balasubramonian, T. Babu and B. Nastasi, "Load Shifting and Peak Clipping for Reducing Energy Consumption in an Indian University Campus", *Energies*, vol. 14, no. 3, p. 558, 2021.

[20] J. Endrenyi, et al. "Bulk Power System Reliability Assessment-Why and How? Part II: How?", *IEEE Transactions on Power Apparatus and Systems*, vol. -101, no. 9, pp. 3446-3456, 1982.

[21] R. Billinton and R. Allan, "Reliability Evaluation of Power Systems". New York (U.A.): Plenum Pr, 1984.

[22] C. Eid, E. Koliou, M. Valles, J. Reneses and R. Hakvoort, "Time-based pricing and electricity demand response: Existing barriers and next steps", *Utilities Policy*, vol. 40, pp. 15-25, 2016.

[23] M. Hassanzadeh and A. Badakhsh, "Evaluation of Well-Being Criteria in Presence of Electric Vehicles Consumption Increase and Load Shifting on Different Load Sectors", *International Journal of Renewable Energy Research*, no. 73, 2017.

[24] R. Billinton and R. Karki, "Application of Monte Carlo simulation to generating system well-being analysis", *IEEE Transactions on Power Systems*, vol. 14, no. 3, pp. 1172-1177, 1999.

[25] R. Billinton and M. Fotuhi-Firuzabad, "A basic framework for generating system operating health analysis", *IEEE Transactions on Power Systems*, vol. 9, no. 3, pp. 1610-1617, 1994.

[26] R. Allan. and R. Billinton., *Reliability Evaluation of Power Systems*. New York, NY: Springer, 2013.

[27] J. Endrenyi, *Reliability modeling in electric power systems*. Chichester: Wiley, 1978.

[28] P. Ziemba, "Monte Carlo simulated data for multi-criteria selection of city and compact electric vehicles in Poland", *Data in Brief*, vol. 36, p. 107118, 2021.

[29] R. Billinton, "Reliability Determination Methods", Presented at the panel on Required Reserve Margins, IEEE Power Engineering Society Winter Meeting, Feb. 1990, Atlanta, Georgia.

[30] J. Teng and C. Hsieh, "Modeling and Investigation of Demand Response Uncertainty on Reliability Assessment", *Energies*, vol. 14, no. 4, p. 1104, 2021.

[31] E. Zio, "The Monte Carlo Simulation Method for System Reliability and Risk Analysis". *Springer*, 2013.

[32] N. Nezamoddini and Y. Wang, "Risk management and participation planning of electric vehicles in smart grids for demand response", *Energy*, vol. 116, pp. 836-850, 2016.

[33] R. Billinton et al., "A reliability test system for educational purposes-basic data", *IEEE Transactions on Power Systems*, vol. 4, no. 3, pp. 1238-1244, 1989.

[34] P. Bangalore, "Development of test system for distribution system reliability analysis, integration of electric vehicles into the distribution system.", MS thesis, Chalmers University of Technology, 2011.

International Journal of Research and Technology in Electrical Industry

journal homepage: ijrtei.sbu.ac.ir

Shahid Beheshti University

Optimal Dispatchable DG Location and Sizing with an Analytical Method, based on a New Voltage Stability Index

Mohammad Aryanfar[1,*]

[1] *Tehran Electerical Distribution Company, Tehran, Iran*

ARTICLEINFO

Article history:
Received 18 January 2022
Received in revised form 30 April 2022
Accepted 08 May 2022

Keywords:
Distributed generation
Voltage stability index
Distribution network
Analytical methods
Optimal placement
Power losses
Voltage profile improvement

ABSTRACT

With the high penetration of DGS in the distribution network and its impact on the power loss and voltage profile of the network, the choice of location and the optimal size of the DG has become a challenge for utility companies. In this paper, a method for determining the optimal location and size of dispatchable DG at different load levels for optimal utilization of the distribution network is presented. The goal is to reduce active power losses and improve voltage profiles for stable system performance. The average daily load demand is considered as the load demand profile. The optimal location of DG is determined by sensitivity analysis based on a new voltage stability index. The voltage stability index is based on the voltage breakdown feature and provides an overview of the network voltage stability so that it can show the effect of DG installation location on network voltage stability. DG provides loads at different levels, then by selecting the appropriate bus from the most important buses in terms of index, the optimal size of DG is determined using a search algorithm and based on the lowest active power losses for different load levels. The proposed method on IEEE 33 bus network has been tested using MATLAB software, and its results have been compared with other available methods. The results show the effectiveness of the proposed method in reducing active power losses and improving the voltage profile compared to other available methods.

1. Introduction

With the expansion of Renewable energy resources, the issue of investment in the Distributed Production Resources (DG) sector has attracted the attention of many distribution companies. Considering renewable sources such as solar wind energy and micro-turbines, the use of DG can be an excellent solution for reducing greenhouse gas emissions, including CO2. Therefore, the development of DGs has been on the agenda of many countries, including the UK, [1], and examining the barriers, challenges, and opportunities of these resources is one of the most pressing topics in electrical engineering.

However, the use of DG, despite its advantages such as clean energy production, has requirements that must be considered when designing the networks containing DGs. By placing DGs in distribution networks, the network changes from inactive to an active network, and therefore issues related to voltage stability and system reliability in the network must be reconsidered. If the implementation of DGs is not considered carefully, not only does it not help network indices, but it may also weaken indices such as voltage stability and system reliability index. So

* Corresponding author
E-mail address: mohamad.aryanfar324@gmail.com
http://dx.doi.org/ 10.52547/ijrtei.1.1.95

weneed ways to take advantage of DG while preventing new problems.

The issue of DG sizing and allocation has been discussed in numerous papers. These studies are generally divided into two types. The first type is papers that use optimization methods to calculate an objective function and try to maximize or minimize variables. These variables can be the cost of energy production, lost power, or other indicators. The second category is methods that analyze the sensitivity of the buses to one or more indicators and then decide whether or not to place the DG on a bus. DG sizing is also achieved in these methods by considering various indices.

Methods that use the optimization algorithms include genetic optimization (GA) and particle rhythm (PSO) ant colonies (AC) Bee Colonies (BC) and various other heuristic and none heuristic methods. For example, in [2], an ant colony algorithm (AC) is used to find the optimal location of DGs, considering the reliability of the system .In [3], the genetic algorithm and PSO are used together to find the optimal location and size of DGs in the distribution network.

In [4], the method using craziness-based particle swarm optimization (CRPSO) algorithm based on the game-theoretical formulation strategy is used for optimal placement of DG units. In this method, the authors' goal is to reduce the cost of power supply, and the objective function is composed of the cost of buying power, power loss, communication, and load shedding. A two-step coordinate method has been used in [5] to locate heterogeneous DG in a micro-energy microgrid. In this method, uncertainties related to renewable resources are considered, and in addition to optimizing the location and capacity of DG units, to maximize the Net Present Value index, investment costs and type of DGs are also considered.

In [6], a new method called Harris Hawks optimization has been used to optimally locate and determine the capacity of distributed generation units in the radial distribution network. In this method, the authors aim to minimize lost power, and they compare the performance of this method with similar methods of heuristic optimization. There are many papers in the literature that use indices to locate and determine the size of DG units. For example, [7] suggests an analytical method that locates DG units. In this method, the goal is to minimize power loss, which has been investigated in two types of networks: the distribution network and transmission network.

In [8], an indicator was used for power loss sensitivity based on two matrices, the Bus-Injection to Branch-Current (BIBC) and Branch-Current to Bus-Voltage (BCBV) matrix to Calculates the power of the injected average .Using this index, the size and the location of DGs are determined. In [9], the authors used the loss sensitivity index to optimize capacity and extract power loss equations. The DG's optimal location is also calculated based on power loss. They also used an analytical approach based on sensitivity to the lost real power to obtain the optimal location and capacity of the DGs in the distribution network and minimize the wasted power.

A method for allocating distributed generation has been proposed in [10]. The authors use an index called Power Stability Index (PSI), which analyses the voltage of a stable node. The algorithm is used to visualize the impact of DG placement on system loss. Three deferent indices have been proposed in [11], which are used to determine the optimal location and size of DGs in the radial distribution network. These methods are then compared, and their pros and cons have been demonstrated. Authors in [12] use a proposed index to determine the system reliability and to minimize power loss. Also, an optimization method named the Imperialistic Competitive Algorithm (ICA) has been used to compare and evaluate the results. In[13], optimal multi-objective allocation of DG units to achieve more power loss reduction and reliability betterment is carried out by co-evolutionary multi-swarm particle swarm optimization (CMPSO) algorithm. In[14], a novel analytical algorithm is proposed to distinguish the optimal location and size of DGs in radial distribution networks based on a new combined index (CI) to reduce active power losses and improve system voltage profiles. [

A new probabilistic index is defined in [16] that measures the controllability of voltages and currents in the buses and lines of distribution systems. This index is then used to determine the location of Different types of DG in the distribution network. Authors in [17] use the protection coordination index (PCI) to determine the optimal location of DGs in the distribution network. The impact of fault current limiters on this index is also discussed in this paper.

In [18], a stability index-based technique is proposed for determining the optimal location and size of different types of DG units in the distribution systems to reduce line losses, improve voltage profile, and decrease pollution level. Authors in [19] used a planning approach based on Voltage stability index (VSI) with improved loss minimization (LM) formulation. They employed these methods to determine DG location and size in a loop test distribution network (LDN). There are a variety of analytical methods available to solve the DG sizing and placement problem, one of which is shown in [20], where authors have proposed an iterative analytical method to find the optimal size and location of distributed generation units in radial distribution networks with the objective of minimizing network loss.

This paper presents a method for optimal utilization of the distribution network by determining the optimal location and size of DG, to reduce annual energy losses and improve voltage profiles. The optimal DG location is determined by a new voltage stability index. This indicator is based on the characteristic of voltage collapse in power systems, which can show the positive effect of DG on network voltage stability. The characteristic of voltage collapse is not used in other papers in this field. The optimal DG size is also determined by a search algorithm based on minimizing active power losses.

The structure of the paper is as follows. In Section 2, the modeling load is presented.In Section 3, the formulation of the problem is presented.In Section 4, the proposed methods is presented. In Section 5, the discussion and

simulation results are reviewed, and, finally, in Section 4, the paper's overall conclusion is discussed.

2. Modeling Load

In this section, the network load is modeled for 1 year (8760 hours). The network load is first modeled for 1 day and then generalized to 365 days of the year [21]. The amount of load per hour varies from 0.4 to 1 per unit. The daily load model is shown in Fig.1, which varies from 0.4 to 1 per unit. Then, this pattern is considered for 1 year. Table 1 shows the average daily and annual load demand.

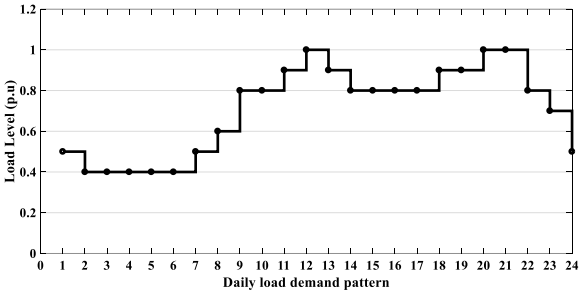

Fig.1. Daily load model pattern

Table I. Average hourly daily load model

Time	Load Level (p.u)	hours	T_{Time}(Hours/year)
1	0.5	1	365
2-6	0.4	5	1825
7	0.5	1	365
8	0.6	1	365
9-10	0.8	2	730
11	0.9	1	365
12	1	1	365
13	0.9	1	365
14-17	0.8	4	1460
18-19	0.9	2	730
20-21	1	2	730
22	0.8	1	365
23	0.7	1	365
24	0.5	1	365

3. Problem Formulation

3.1. Voltage stability index for optimal DG location

In this section, the proposed voltage stability index is modeled to determine the optimal DG location. This index is obtained using the active power bus equation for the receiver bus. Thus, the derivative of the voltage to the power of the receiver bass at the point of voltage instability is zero. According to Fig2, the power of the receiver bus is obtained by the following equation:

$$P_R = P_L - P_{DG} = \frac{V_S V_R \cos(\theta-\delta)}{Z} - \frac{V_R^2 \cos(\theta)}{Z} \quad (1)$$

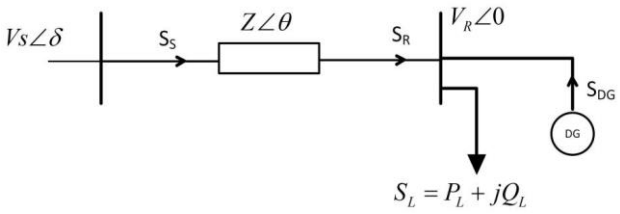

Fig.2. Study network

By rewriting the equation (1) based on the voltage of the receiver, the equation (2) is obtained as follows:

$$V_R^2 - \frac{V_S V_R \cos(\theta-\delta)}{\cos(\theta)} + \frac{P_R Z}{\cos(\theta)} = 0 \quad (2)$$

By deriving the equation (2) we have:

$$\frac{dV}{dP_R} = \frac{Z}{V_S \cos(\theta-\delta) - 2V_R \cos(\theta)} \quad (3)$$

The $\frac{dV}{dP_R} < \circ$ must always be true voltage stability, therefore:

$$V_S \cos(\theta-\delta) - 2V_R \cos(\theta) < \circ \quad (4)$$

According to equation (4), the following relation must always be true for voltage stability:

$$\frac{2V_R \cos(\theta)}{V_S \cos(\theta-\delta)} > 1 \quad (5)$$

According to equation (5), the voltage stability evaluation index for a network with l transmission lines, it is defined as follows:

$$VSI_l = 2 - \frac{2V_R \cos(\theta)}{V_S \cos(\theta-\delta)} \quad (6)$$

Equation (6) shows the stability of network lines. The following is a general main equation for the OVSI (Overall voltage stability index):

$$OVSI = \sum_{l=1}^{n-1} VSI_l \quad (7)$$

Where n is the number of network studied buses and l is the number of lines.

3.2. DG size optimization

In this section, the optimal DG measurement for active power loss is determined. After determining the appropriate location for the DG installation, by changing the DG size, from 0 to 100% of the total network active load, the ratio of active loss changes to the DG size is obtained. Then, by holding the permitted constraints of voltage, the DG size is selected so that the active network losses are minimized. It is important to note that, given that the DG power loss diagram is as large as the DG size,

the step size of the DG changes is very important in choosing the optimal DG size. In this paper, the step size at each stage is considered to be 1% of the total active load.

For determining the optimal DG size, the following constraints must be held:

- Voltage constraints:

$$V_i^{min} \le V_i \le V_i^{max} \quad (8)$$

- Power Balance Constraint:

$$P + P_{DG} = P_{load} + \sum RI^2 \quad (9)$$

$$Q + Q_{DG} = Q_{load} + \sum XI^2 \quad (10)$$

- DG Size constraint:

$$\begin{cases} P_{DG} \le P_{load} \\ Q_{DG} \le Q_{load} \end{cases} \quad (11)$$

4. Proposed Methods

In this section, a general algorithm for selecting the optimal location, and the optimal size of dispatchable DG is provided. To determine the right place to install DG, first, calculate the different OVSI load levels. The receiving bus of a line, which has the highest OVSI value for different load levels, is selected as the candidate bus for DG installation. By selecting a candidate bus, the optimal DG size for different load levels over 24 hours is obtained by holding the operating constraints following Section 2.3 to reduce losses. The flowchart of the proposed method for determining the optimal location and size of DG is shown in Fig.3.

By determining the optimal location and size of DG by the proposed method, the annual cost of energy losses and operating costs of DG are calculated as follows:

- Cost of energy losses:

By determining the optimal location and size of DG, the cost of energy losses is reduced. The cost of annual energy losses is as follows [11]:

$$C_{Losses} = (\text{Total Real Power Loss})_{Time} * K_P * T_{Time} \quad (12)$$

Where $K_P = 0.06(\frac{\$}{kwh})$.

- Operating costs of DG:

The DG cost function is according to Equation (13) [22]:

$$C(P_{DG}) = a * P_{DG}^2 + b * P_{DG} + c \quad (13)$$

Where $a = 0$, $b = 15$ and $c = 0.002$.

The reactive power cost function is obtained based on the trigonometric relations between active and reactive power as follows [23]:

$$C(Q_{DG}) = a'' * Q_{DG}^2 + b'' * Q_{DG} + c'' \quad (14)$$

Where the coefficients of the cost function are calculated as follows:

$$a'' = a * \sin^2(\theta)$$

$$b'' = b * \sin(\theta)$$

$$c'' = c$$

$$\theta = \cos(PF)^{-1}$$

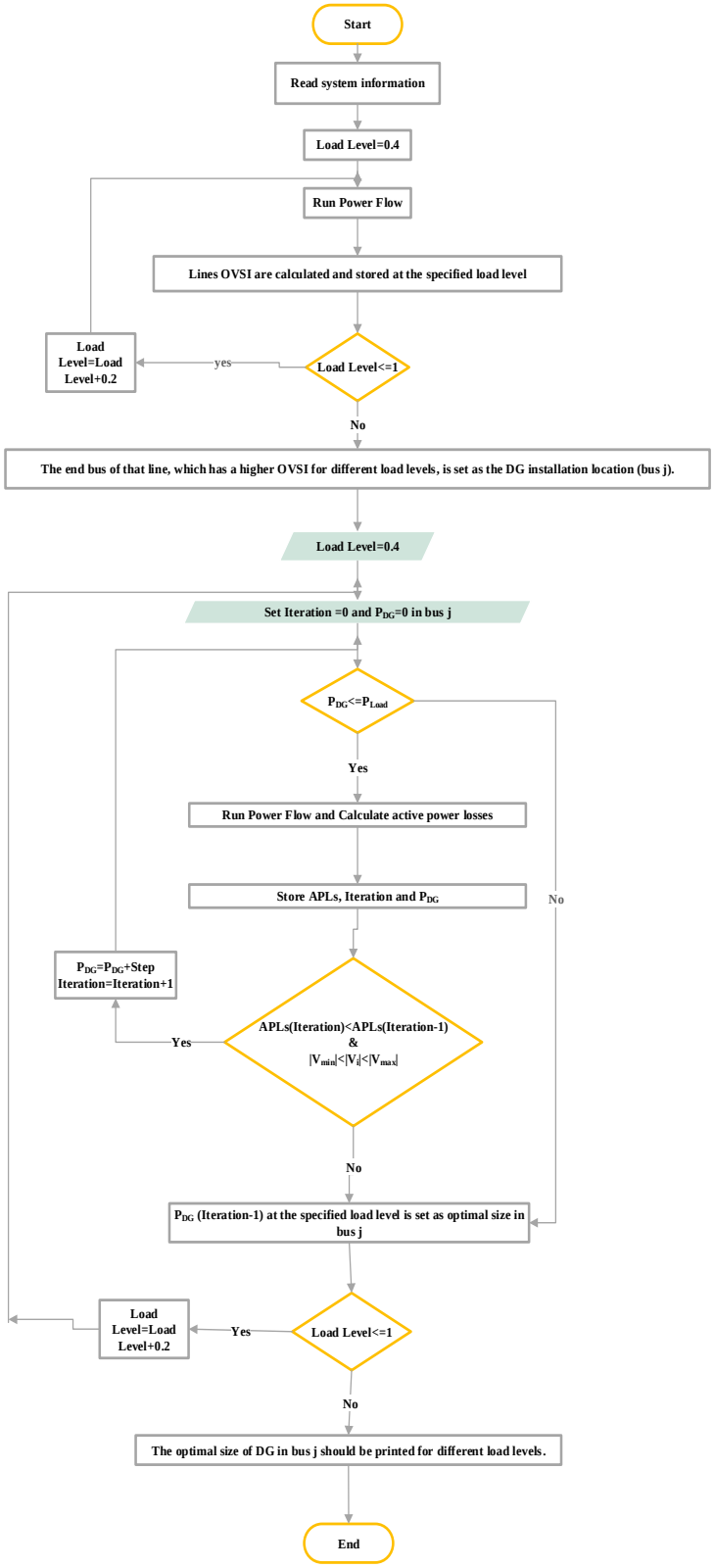

Fig.3. Flowchart of the proposed method algorithm

5. Results of simulation and discussion

To implement and examine the proposed method for optimal and sustainable utilization of the distribution network, the 33-bus IEEE [24] bus, has been selected as the study network. The 33-bus network has 3715 kW of active load and 2300 kW of the reactive load. In this simulation, the base voltage and the base apparent power are considered to be 12.66 kV and 100 MVA, respectively. The 33-bus network studied is shown in Fig3. The proposed model is implemented in MATLAB software.The model has been executed in a PC with Intel Core i7 CPU @3.20 CPU and 4 GBs of RAM.
In this section, according to the proposed algorithm, first, the optimal location of the dispatchable DG is determined, then the optimal DG size for different load levels is calculated in 24 hours with a unit power factor, 0.9 lag, and the optimal power factor. Then, the results obtained for the different power factors and load level 1 are compared with the Index vector (IV) method [25], voltage stability index (VSI) methods [11] and Voltage sensitivity index (VSI) methods [26].

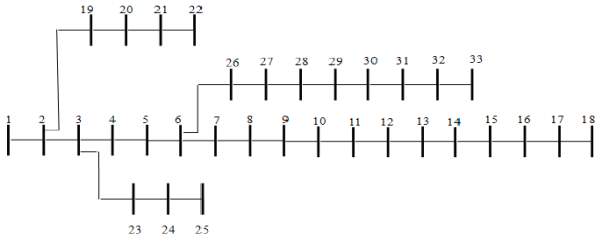

Fig.4 33-bus network

5.1. Dispatch able DG with unit power factor

In this section, the optimal location and size of the DG are selected for the unit power factor. According to the algorithm, the optimal place of DG is obtained first. Fig.5 shows the value of the VSI index for different load levels. The examination of Fig.4 shows that line 7 has the largest VSI value for different load levels. Therefore, Bus 8 at the end of Line 7 is the most suitable bus for installing DG.

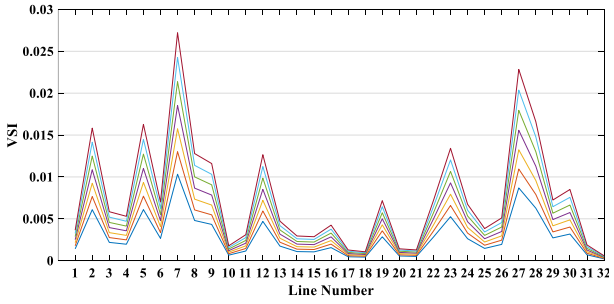

Fig.5. VSI index value for IEEE 33 bus network lines

By installing a dispatchable DG on Bus 8, the optimal DG size for different load levels over 24 hours is obtained according to the flowchart in Fig.3. Table 2 shows the dispatchable DG optimal size, total active and reactive losses without DG installation and with DG, minimum voltage, the annual cost of active power losses for DG installation mode without DG installation, and the annual cost of DG operation for different load levels. Give. The results of **Table.II** show that with the dispatchable DG installation, the Bus 33 voltage has the lowest voltage level in 24 hours. The minimum voltage measurement for the average daily load is shown in **Fig.6**. **Fig.7** shows a 33-volt mains voltage for a 0.8 per unit load level, without DG installation and with DG installation. Optimal DG installation increases the stability margin and network load. The P-V graph of bus 30 at the load level of 0.8 per unit is presented in **Fig.8** that confirms the results. With the presence of DG, the load and voltage stability margin of the network has increased.
As mentioned, choosing the optimal DG size for different levels of the load over a year reduces the resulting losses and costs. The cost of annual energy losses for 0.8 per unit load is higher than other load levels. Also, the installation of DG has reduced the cost of annual energy losses by $ 8678 for 0.8 per unit level load, which is the highest decrease compared to other load levels. The total cost of annual energy losses for different levels of the load before installing DG is $ 55,134, which has been reduced to $ 31,164 with DG installation.

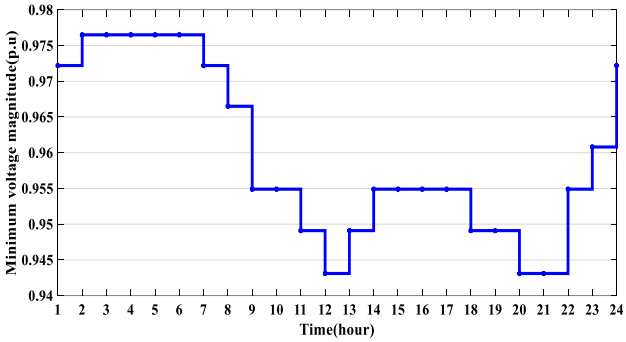

Fig.6. Minimum voltage measurement for average daily load by installing DG with unit power factor

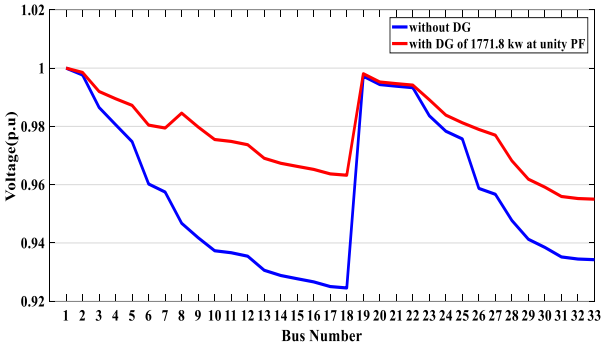

Fig. 7. 33 bus network voltage at 0.8 per unit load level without DG installation and with DG installation

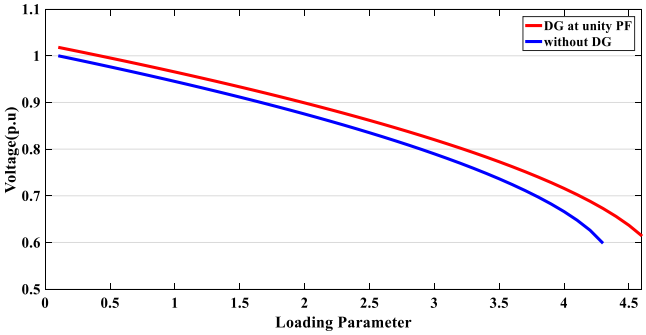

Fig.8. The effect of DG installation with unit power factor on increasing load and network voltage stability

Table II. Results for DG operating at the unit power factor

		Load Level						
Items		0.4	0.5	0.6	0.7	0.8	0.9	1
DG location bus		8	8	8	8	8	8	8
DG size in kVA		1486	1744.8	1756.6	1765.1	1771.8	1780.2	1788.18
Active power losses(kw)	Without DG	30.7186	48.6947	71.1646	98.3433	130.4654	167.7864	210.5861
	With DG	18.0680	28.0499	40.7663	56.0104	73.8571	94.3852	117.6781
Reactive power losses(kVAr)	Without DG	20.8229	33.0170	48.2656	66.7177	88.5355	113.8963	142.9942
	With DG	12.4102	19.6662	28.6045	39.320	51.867	66.313	82.817
Minimum voltage (Bus)		0.9765 (33)	0.9722 (33)	0.9665 (33)	0.9608 (33)	0.9549 (33)	0.9491 (33)	0.9431 (33)
Cost of energy losses ($/h)	Without DG	3363.7	3199.2	1558.5	2153.7	20000	11023	13836
	With DG	1974.4	1842.9	892.78	1226.6	11322	6201.1	7731.5
Net savings ($)		1385.3	1356.3	665.72	927.1	8678	4821.9	6104.5
Cost of P_{DG}($)		40686	28663	9618.8	9665.4	67914	38992	29375

5.2. Dispatchable DG with a power factor of 0.9 lag

According to the previous section, the optimal location for the dispatchable DG installation with a power factor of 0.9 lag at different load levels was bus 8, obtained according to the proposed algorithm. Therefore, the dispatchable DG is installed in Bus 8, and according to the search algorithm and by reducing the active power losses, the optimal DG size for different load levels during 24 hours period is obtained. **Table.III** shows the optimal DG measurement for 24 hours, active and reactive power losses for with and without DG modes, minimum voltage for different load levels, and the annual cost of active power losses for both DG-free and DG-mode modes, and annual DG utilization costs. The results of **Table.III** show similar to the DG installation mode with a unit power factor, in this case, for different load levels, and within 24 hours, bus 33 voltage has a minimum value. Bus 33 voltage levels are shown in **Fig.9** for 24 hours. **Fig.10** shows the network voltage profile of 33 buses for 0.8 per unit loads in two modes without DG installation and with DG installation. In mode without DG installation, bus 18 has the lowest voltage, and with the installation of DG in bus 8 causes bus 33 to have the lowest voltage, and therefore the network voltage level is optimal. A comparison of minimal voltage in DG installation mode with a unit power factor and a 0.9 lag shows the effect of reactive power on improving voltage profile. Also, the P-V diagram of bus 30 for the 0.8 per unit load level in **Fig.11** shows that the installation of DG with a power factor of 0.9 lag has a greater effect on increasing the voltage stability margin and increasing the network stability level. Therefore, in using DG, the optimum power factor should be considered. An examination of **Table.III** shows a good reduction in the cost of annual active power losses with DG installation. The cost of annual active power losses for the 0.8 per unit load level is higher than other load levels, which is reduced by $ 11863.9 with the installation of DG. The cost of annual active power loss for all load levels before installation is $ 55134, which is reduced to $24010 by installing DG. Their results show that the installation of DG with a power factor of 0.9 lag of 56.52% reduction in the cost of annual active power loss has been created.

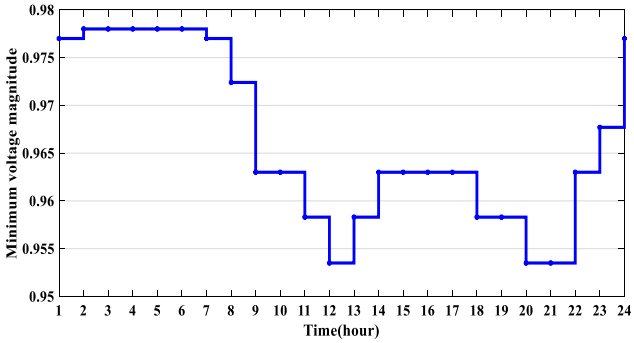

Fig.9. Minimum voltage for average daily load with the installation of DG with 0.9 lag

Table.III. Results for DG operating at 0.9 power factor lag

		Load Level						
Items		0.4	0.5	0.6	0.7	0.8	0.9	1
DG location bus		8	8	8	8	8	8	8
DG size in kVA		1651.1	2063.9	2077.4	2086.1	2100	2109.6	2120.2
Active power losses(kw)	**Without DG**	30.7186	48.6947	71.1646	98.3433	130.4654	167.7864	210.5861
	With DG	14.2483	20.3299	29.6444	40.3667	53.0729	67.6178	84.0419
Reactive power losses(kVAr)	**Without DG**	20.8229	33.0170	48.2656	66.7177	88.5355	113.8963	142.9942
	With DG	9.7753	14.9545	21.7020	29.7495	39.1643	49.9321	62.1113
Minimum voltage (Bus)		0.9780 (33)	0.9770 (33)	0.9724 (33)	0.9677 (33)	0.9630 (33)	0.9583 (33)	0.9535 (33)
Cost of energy losses ($)	**Without DG**	3363.7	3199.2	1558.5	2153.7	20000	11023	13836
	With DG	1559.8	1335.7	649.2	884.0	8136.1	5923.3	5521.6
Net savings ($)		1083.9	1863.5	909.3	1269.7	11863.9	5099.7	8314.4
Cost of P_{DG}($)		40686	30512	10238	10281.1	72444	41583	31346
Cost of Q_{DG} ($)		8591.8	6444.3	2161.8	2017.5	15297	8781.4	6618.5

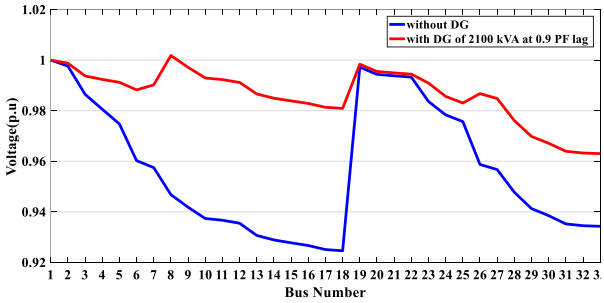

Fig.10. 33 bus network voltage at 0.8 per unit load level without DG installation and with

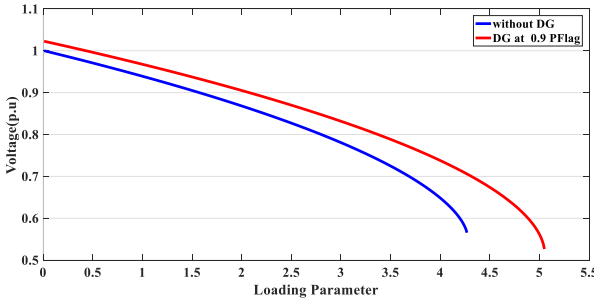

Fig.11. The effect of DG installation with 0.9 lag power factor on increasing the loading and network voltage stability

5.3. Dispatchable DG with optimal power factor

Given the importance of reactive power in minimizing losses and improving voltage profiles, the optimal DG power factor is very important. To minimize losses, $P_{DG} = P_{Load}$ must be true [27]. The optimum power factor for the 33-bus network is 0.85 lag. **Table.IV** shows results with the installation of DG with an optimal power factor. Examination of the results shows that, like installing DG with a unit power factor and 0.9 lag, in this case, bus 33 has a minimum voltage for different load levels. **Fig.12** shows the minimum network voltage profile for 24 hours. **Table.IV** shows that for the load level of 0.8 per unit, the optimal DG size is 2114.4 kVA, and **Fig.13** shows its effect on the voltage profile compared to the without DG mode. In the following, to investigate the effect of DG installation with optimal power factor on increasing voltage stability margin, the P-V diagram for Bus 30 at 0.8 load level in **Fig.14** is shown. The maximum load factor, in this case, is 5.06, and it is 5.05 in the case of results with a power factor of 0.9 lag, which are close to each other.

The results in **Table.IV** show the annual reduction in the cost of active power losses with the installation of DG. Before the installation of DG, the annual cost of active power losses was $ 55,134, and with the installation of DG, it reached $ 23,455 and decreased by $ 31,679. Active power losses for DG mode with unit power factor, DG with 0.9 lag power factor, and also DG with optimal power factor are shown in **Fig.15**. Examining **Fig.15** shows the effect of reactive power on reducing active power losses and highlights the importance of optimal power factor.

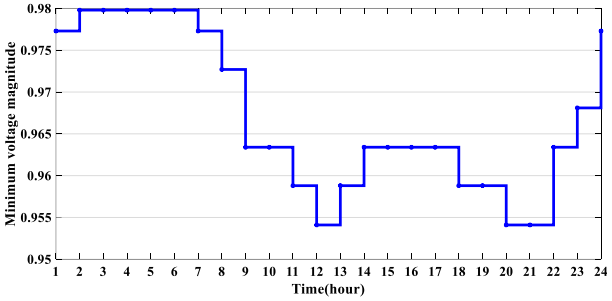

Fig.12. Minimum voltage measurement for average daily load by installing DG with optimal power factor

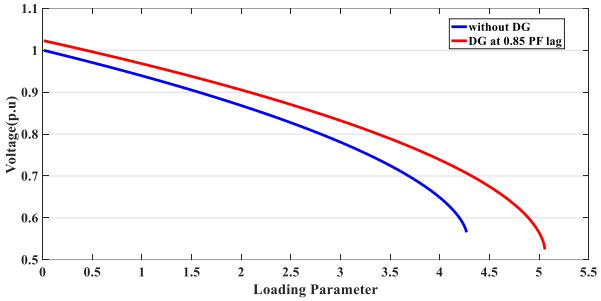

Fig. 14. The effect of DG installation with 0.85 lag power factor on increasing the loading and network voltage stability

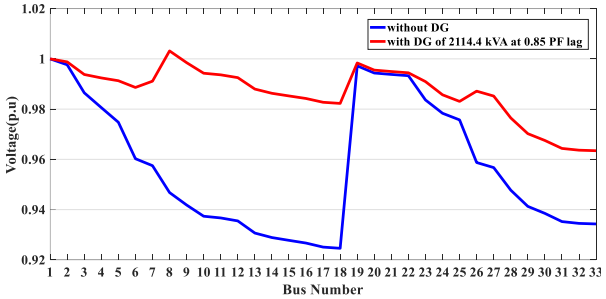

Fig.13. 33 bus voltage at 0.8 per unit load level without DG installation and with DG installation

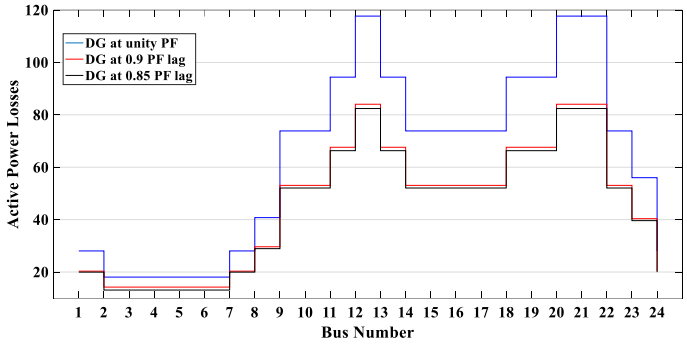

Fig.15. Active power losses for different power coefficients

Table.IV. Results for DG operating at 0.85 power factor lag

		Load Level						
Items		0.4	0.5	0.6	0.7	0.8	0.9	1
DG location bus		8	8	8	8	8	8	8
DG size in kVA		1748.2	2081.3	2091.1	2104.2	2114.4	2125.3	2137.8
Active power losses(kw)	**Without DG**	30.7186	48.6947	71.1646	98.3433	130.4654	167.7864	210.5861
	With DG	13.118	19.9619	28.9237	39.6151	52.0697	66.3219	82.4072
Reactive power losses(kVAr)	**Without DG**	20.8229	33.0170	48.2656	66.7177	88.5355	113.8963	142.9942
	With DG	9.2789	14.7799	21.4317	29.3902	38.6618	49.2859	61.3060
Minimum voltage (Bus)		0.9798 (33)	0.9773 (33)	0.9727 (33)	0.9681 (33)	0.9634 (33)	0.9588 (33)	0.9541 (33)
Cost of energy losses ($)	**Without DG**	3363.7	3199.2	1558.5	2153.7	20000	11023	13836
	With DG	1436.4	1311.5	633.4	867.5	7982.3	5809.8	5414.2
Net savings ($)		1927.3	1887.7	925.1	1286.2	12017.7	52013.2	8421.8
Cost of P_{DG} ($)		40686	29062	9732.9	9793.9	68889	29676	29851
Cost of Q_{DG} ($)		13285	6326.2	3178	3197.9	22494	12920	9746.8

5.4. Comparison of results with other available methods

In this section, for validation of the proposed method, its results are compared with IV, VSI, and VSI methods. A comparison of the results for the 33-bus network at level 1 and the installation of DG with a power factor of 0.9 lag is shown in **Table.V**. Examining the results of the proper performance of the proposed method in selecting the location and optimal size of DG and therefore shows the reduction of losses and improvement of the voltage profile.

Table.V. Comparison of results with DG at 0.9 PF lag for 33 bus system

Items	IV method[24]	VSI method[26]	VSI method[11]	Proposed method
DG location bus	30	16	33	8
DG size in kVA	1950	1200	1570.8	2120.2
Active power losses(k)	78.4	112.8	96.6	84.04
Reactive power losses(kVAr)	58.9	77.4	77.26	62.11
Minimum voltage(p.u)	0.9391	0.9378	0.9322	0.9535

6. Conclusion

In this paper, a new method is proposed to locate and determine the optimal dispatchable DG size. The average hourly load demand during the day is considered as the load profile. A new voltage stability index is provided to determine the optimal location for DG installation. The voltage stability index, obtained using the voltage collapse feature of power systems, has determined the appropriate location of the DG installation based on the analysis of the impact of DG installation on improving the voltage stability of the distribution network. Then, the optimal DG size for 24 hours a day, and different load levels are determined by the search algorithm to reduce active power losses. Optimal DG placement and dispatch has been performed for different load levels and three types of DG with a single "power" coefficient, 0.9 lag power factor, and optimal power factor.

In this paper, the proposed method is tested on the IEEE 33 bus network, and its results are analyzed. The use of the proposed method for optimal DG placement and dispatch for different hours of the day and different load levels on the IEEE 33 bus network has improved voltage profiles and voltage stability margins, as well as minimizing active power losses and costs. The proposed method for load levels of 1 per unit and DG with a power factor of 0.9 lag has been compared and validated with IV, VSI, and CPLS methods. A comparison of the obtained results shows the effectiveness of the proposed method in locating and determining the optimal DG size to reduce active power losses and improve voltage profiles. In general, it can be concluded that the proposed method is suitable for the deployment of dispatchable DG for optimal operation of distribution networks with stable performance.

In future work, in addition to power losses and voltage profile improvements, the reliability of the distribution system can also be considered.

7. References

[1]www.energynetworks.org/electricity/engineering/distributed generation/ requirements-for-generators.

[2] Wang, L., & Singh, C. (2008). Reliability-constrained optimum placement of reclosers and distributed generators in distribution networks using an ant colony system algorithm. *IEEE Transactions on Systems, Man, and Cybernetics, Part C (Applications and Reviews)*, *38*(6), 757-764.

[3] Moradi, M. H., & Abedini, M. (2012). A combination of genetic algorithm and particle swarm optimization for optimal DG location and sizing in distribution systems. *International Journal of Electrical Power & Energy Systems*, *34*(1), 66-74.

[4] Karimizadeh, K., Soleymani, S., & Faghihi, F. (2019). Optimal placement of DG units for the enhancement of MG networks performance using coalition game theory. *IET Generation, Transmission & Distribution*, *14*(5), 853-862.

[5] Li, Z., Xu, Y., Fang, S., & Mazzoni, S. (2019). Optimal placement of heterogeneous distributed generators in a grid-connected multi-energy microgrid under uncertainties. *IET Renewable Power Generation*, *13*(14), 2623-2633.

[6] Selim, A., Kamel, S., Alghamdi, A. S., & Jurado, F. (2020). Optimal Placement of DGs in Distribution System Using an Improved Harris Hawks Optimizer Based on Single-and Multi-Objective Approaches. *IEEE Access*, *8*, 52815-52829.

[7] Wang, C., & Nehrir, M. H. (2004). Analytical approaches for optimal placement of distributed generation sources in power systems. *IEEE Transactions on Power systems*, *19*(4), 2068-2076.

[8] Gözel, T., & Hocaoglu, M. H. (2009). An analytical method for the sizing and siting of distributed generators in radial systems. *Electric power systems research*, *79*(6), 912-918.

[9] Acharya, N., Mahat, P., & Mithulananthan, N. (2006). An analytical approach for DG allocation in primary distribution network. *International Journal of Electrical Power & Energy Systems*, *28*(10), 669-678.

[10] Aman, M. M., Jasmon, G. B., Mokhlis, H., & Bakar, A. H. A. (2012). Optimal placement and sizing of a DG based on a new power stability index and line losses. *International Journal of Electrical Power & Energy Systems*, *43*(1), 1296-1304.

[11] Murty, V. V., & Kumar, A. (2015). Optimal placement of DG in radial distribution systems based on new voltage stability index under load growth. *International Journal of Electrical Power & Energy Systems*, *69*, 246-256.

[12] Poornazaryan, B., Karimyan, P., Gharehpetian, G. B., & Abedi, M. (2016). Optimal allocation and sizing of DG units considering voltage stability, losses and load variations. *International Journal of Electrical Power & Energy Systems*, *79*, 42-52.

[13] Derakhshan, G., H. Shahsavari, and A. Safari. "Co-Evolutionary Multi-Swarm PSO Based Optimal Placement of Miscellaneous DGs in a Real Electricity Grids Regarding Uncertainties." Journal of Operation and Automation in Power Engineering 10.1 (2022): 71-79.

[14] Azad, Sasan, et al. "A Novel Analytical Approach for Optimal Placement and Sizing of Distributed Generations in Radial Electrical Energy Distribution Systems." Sustainability 13.18 (2021): 10224.

[15] Azad, Sasan, Mohammad Mehdi Amiri, and Mohammad Taghi Ameli. "Optimal Placement of Combined Heat and Power (CHP) Systems Considering the Cost of Environmental Pollutants." Whole Energy Systems. Springer, Cham, 2022. 153-168.

[16] Arefifar, S. A., Ordonez, M., & Mohamed, Y. A. R. I. (2015). VI controllability-based optimal allocation of resources in smart distribution systems. *IEEE Transactions on Smart Grid*, *7*(3), 1378-1388.

[17] Zeineldin, H. H., & El-Saadany, E. F. (2016). Protection coordination index enhancement considering multiple DG locations using FCL. *IEEE Transactions on Power Delivery*, *32*(1), 344-350.

[18] Sannigrahi, S., & Acharjee, P. (2017, December). A Stability Index Based Analytical Technique for Optimal Placement of Various DG Types in Distribution Networks. In *2017 14th IEEE India Council International Conference (INDICON)* (pp. 1-6). IEEE.

[19] Abbas Kazmi, S. A., & Shin, D. R. (2017). DG Placement in Loop Distribution Network with New Voltage Stability Index and Loss Minimization Condition Based Planning Approach under Load Growth. *Energies (19961073)*, *10*(8).

[20] Forooghi Nematollahi, A., Dadkhah, A., Asgari Gashteroodkhani, O., & Vahidi, B. (2016). Optimal sizing and siting of DGs for loss reduction

using an iterative-analytical method. *Journal of Renewable and Sustainable Energy*, *8*(5), 055301.
[21] Das, S., Das, D., & Patra, A. (2019). Operation of distribution network with optimal placement and sizing of dispatchable DGs and shunt capacitors. Renewable and Sustainable Energy Reviews, 113, 109219.
[22] Gautam, D., & Mithulananthan, N. (2007). Optimal DG placement in deregulated electricity market. Electric Power Systems Research, 77(12), 1627-1636.
[23] Hasanpour, S., Ghazi, R., & Javidi, M. H. (2009). A new approach for cost allocation and reactive power pricing in a deregulated environment. Electrical Engineering, 91(1), 27.
[24] Baran, M., & Wu, F. F. (1989). Optimal sizing of capacitors placed on a radial distribution system. IEEE Transactions on power Delivery, 4(1), 735-743.
[25] Murthy, V. V. S. N., & Kumar, A. (2013). Comparison of optimal DG allocation methods in radial distribution systems based on sensitivity approaches. International Journal of Electrical Power & Energy Systems, 53, 450-467.
[26] Qian, K., Zhou, C., Allan, M., & Yuan, Y. (2011). Effect of load models on assessment of energy losses in distributed generation planning. International Journal of Electrical Power & Energy Systems, 33(6), 1243-1250.
[27] Hung, D. Q., & Mithulananthan, N. (2011). Multiple distributed generator placement in primary distribution networks for loss reduction. IEEE Transactions on industrial electronics, 60(4), 1700-1708.

International Journal of Research and Technology in Electrical Industry

journal homepage: ijrtei.sbu.ac.ir

Shahid Beheshti University

Stator Fault Detection and Faulty Phase Identification in Network/Inverter-fed Induction Machines using Negative Sequence Current Component

Mohammad Hossein Nazemi[1], Farhad Haghjoo[1,*], Sérgio Cruz[2], Monia Bouzid[3]

[1] Faculty of Electrical Engineering, Shahid Abbaspour School of Engineering, Shahid Beheshti University, Tehran, Iran
[2] Department of Electrical and Computer Eng., University of Coimbra, 3030-290 Coimbra, Portugal, and Instituto de Telecomunicações, 3030-290 Coimbra, Portugal
[3] Laboratory of Electrical Systems, National School of Engineers of Tunis, University of Tunis EL Manar, and the National School of Engineers of Carthage, University of Carthage, Tunis, Tunisia

ARTICLEINFO

Article history:
Received 18 January 2022
Received in revised form 16 May 2022
Accepted 17 May 2022

Keywords:
Induction motors
Stator turn-to-turn faults
Fault detection
Faulty phase identification,
Negative sequence current component

ABSTRACT

This paper proposes a non-invasive negative sequence impedance-based technique to detect stator turn-to-turn faults (STTFs) and dentify the related faulty phase at early stages based on the tracking the magnitude and angle variations of the negative sequence current component generated due to STTFs. To extract these indicators, a simplified steady-state negative sequence equivalent circuit of the induction motor is used. To neutralize the effect of various produced disturbances by the inherent non-ideal construction of the machine and also unbalanced feed voltage to the STTF diagnosis, they will be estimated and removed from the main obtained component. It is shown experimentally that the introduced technique is independent of mechanical loading level (load variations) and is applicable for network or inverter-fed motors as well. Online fault detection and faulty phase identification, as the most important goals of the protection plan, are accessible by defining an appropriate threshold for the magnitude and allowable range of angle variation of the introduced criterion, respectively.

The performance of the method is evaluated by simulation as well as multiple experimental tests. The experimental results have shown that from the sensitivity point of view, even weak faults are detectable by such a technique. Also, the obtained tests showed that such technique is robust, reliable and secure in the face of unbalanced voltage sources and load level variations. In addition, the performance of this method for the inverter-fed mode showed that the related sensitivity will be increased in such a condition.

1. Introduction

More than 70% of the electricity required by industry is used to operate electric drives. Among them, around 67% are based on induction machines (IM) [1, 2]. IMs are exposed to several thermal, electrical, ambient, and mechanical (TEAM) stresses, depending on the industry's type of operation, driven load, and environment. Statistics have shown that despite their ruggedness and simplicity in construction, the motor annual failure rate is conservatively estimated at 3-5% per year. There are up to 12% in extreme cases, as in cement, mining, pulp, and paper industries [3]. Motor

* Corresponding author
E-mail address: f_haghjoo@sbu.ac.ir
http://dx.doi.org/ 10.52547/ijrtei.1.1.105

failures cause unexpected outages and possibly disrupt production and impose unforeseen costs such as repairs, replacements, and installation on the plant. Thus, proper protection is required to minimize the motor failure rate, prevent further damage to the equipment and ensure minimum outage time and productivity targets [4, 5].

Based on the results of IEEE and EPRI surveys on motor reliability and significant causes of motor failures, on average, about 33% of faults are related to the stator and rotor windings [6]. In the case of STTFs, the induced voltage in the shorted turns may lead to a circulating current up to twice the locked-rotor current [7]. If the protection system does not clear the fault, it can propagate and lead to more severe faults, such as phase to ground or phase-to-phase faults. In medium voltage motors, due to the high short-circuit power of the network, an uncleared earth fault can cause irreparable damage to the machine stator core [8].

The existing methods to detect STTFs can be classified into two main categories: invasive and non-invasive. Invasive techniques mainly use pre-fabricated sensors to monitor variations in the magnetic flux density, stray flux, temperature, and frame vibrations [9, 10]. Non-invasive or sensorless fault detection methods, which monitor the motor condition using only the terminal current and voltage signals, are preferred due to their reasonable cost and independence from the use of special sensors that may be difficult to fit into the motor. Although the invasive techniques have some advantages from the security, sensitivity, and reliability viewpoints, they generally require changes to the machine's construction, which sometimes has its own complexities in the field.

Some of the most common non-invasive techniques are:

- the motor current signature analysis (MCSA), based on the spectrum analysis of the motor supply current [11-13];
- the Park's vector approach [14, 15];
- the instantaneous active and reactive power analysis [16, 17];
- artificial intelligence-based (AI) techniques [18, 19], using raw data obtained from the speed, torque or negative sequence current signals;
- other techniques that use more sophisticated current signal processing techniques, such as the Discrete Wavelet Transform or the Hilbert Transform [20-22].

However, since this work proposes a model-based approach using the IM negative sequence equivalent circuit and the related current components to detect STTFs, previous methods closely associated with the proposed one are analyzed in more detail.

As stated in several papers, some of the primary causes of the negative sequence current component ($\bar{I}_2$) flowing in the stator windings of the IM are the imbalance of the supply voltages and the machine's inherent asymmetries caused by its non-ideal construction. The degree of imbalance of the supply voltages, measured as a percentage by the unbalance voltage factor $UVF = (V_2/V_1) \times 100\%$ has a significant impact on the motor performance, and even if relatively low, it can impose a lot of thermal stresses on the machine [23-25]. On the other hand, one of the primary effects of an STTF is the disruption of the symmetry of the stator currents by introducing an additional negative sequence current component. The separation of the effects of an STTF of the impact of unbalanced supply voltages and inherent motor asymmetries in the negative sequence current component is thus a major challenge for a correct decision in the fault detection process.

It was shown in [26] that as the negative sequence current (I_2) is not significantly affected by load level variations, it can be used as a more accurate and reliable indicator of STTFs. In [27], by using a reduced negative sequence model of the IM, the effective negative sequence impedance is assumed unaffected by the load level for a small number of shorted turns. Accordingly, the residual negative sequence current was used to introduce a fault criterion. Also, a self-tuning technique measured the intrinsic motor asymmetries to obtain a lookup table (as a function of I_1 and V_1) due to their sensitivity against voltage and slip variations in the mentioned paper. Although this method exhibits a high accuracy in detecting STTFs, the effect of the unbalanced voltage source (UVS) has not been investigated on the related performance. In addition, an acceptable protection threshold which is covering all non-ideal conditions was not provided. Another drawback is the technique for compensating the intrinsic IM asymmetries, which requires the inspection of each IM individually and using a learning stage to create a lookup table.

In [7], modified steady-state equivalent circuits were proposed for the negative sequence current component and short-circuit current when an IM has an STTF with a fault severity factor μ (defined as the ratio between the number of shorted turns and the number of turns per phase), as shown in Fig. 1.

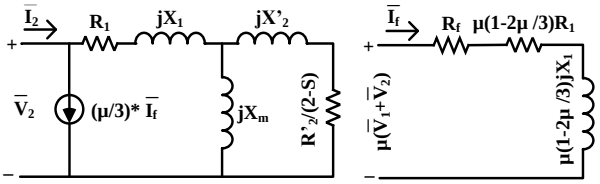

Fig.1. Steady-state equivalent circuits in [7] for an IM with STTFs: the negative sequence equivalent circuit (left) and the fault current (right).

Since $\bar{I}_2$ depends on the fault current ($\bar{I}_f$) as well as the negative sequence voltage ($\bar{V}_2$), it is given by:

$$\bar{I}_2 = \frac{1}{3}\mu\bar{I}_f + \bar{Y}_2\bar{V}_2 \qquad (1)$$

where $\bar{Y}_2$ is the negative-sequence admittance of an ideal symmetrical IM. According to those equivalent circuits, the fault current $\bar{I}_f$ is given by:

$$\bar{I}_f = \frac{\mu(\bar{V}_1 + \bar{V}_2)}{\mu\left(1 - {}^{2\mu}/_{3}\right)[R_1 + jX_1] + R_f} \qquad (2)$$

where R_1, X_1, and R_f are respectively the stator winding resistance, leakage reactance, and STTF contact resistance. By applying some minor simplifications due to the negligible value of μ and V_2 in comparison with V_1 (maximum 1.5% according to the grid codes of some

countries [28]), it can be concluded that the fault current depends approximately on the positive sequence voltage and stator winding impedance. Moreover, the fault current should always lag the reference voltage by an angle equal to the stator impedance angle (for a dead short-circuit). Although this relation provides a sense of perspective about the magnitude of the fault current, a detailed analysis of machine behavior in the nonlinear zone is very complicated due to the saturation of the stator core during the fault, which will definitely have a direct impact on the fault current angle or direction [29]. Moreover, the leakage reactance depends on the physical location of the faulted turns along the stator winding. In [7], and according to (1) and (2), $\bar{I}_2$ is a function of $\bar{V}_1$ and $\bar{V}_2$ and load-dependent coefficients $\bar{K}_1$ and $\bar{K}_2$ as $\bar{I}_2 = \bar{K}_1\bar{V}_1 + \bar{K}_2\bar{V}_2$. Using some datasets obtained at different loads, these coefficients can be estimated and a lookup table built in order to neutralize the effects of the inherent motor asymmetries and UVS, while such lookup table cannot be generalized to other IMs. In addition, the evaluation was done in perfectly linear conditions and only considering one value of the UVF. Lastly, a reliable method to determine the faulty phase was not provided.

Following a slightly different approach, in [30, 31], the variations of the off-diagonal elements of the admittance matrix for the IM's positive and negative sequence components are used to detect STTFs. This technique was applied to line-fed machines and inverter-fed ones [32-35]. Some of the undeniable advantages of such a diagnostic method are high accuracy, the study of the loading effects, modifying the non-ideal machine construction, and the limited unbalance voltage consideration in estimating the initial conditions. In contrast, complexity, the high computational burden, the need to repeat the learning stage for each particular IM, the lack of providing a reliable threshold value, and the absence of an algorithm to identify the faulty phase are the main drawbacks of this approach.

In [36-38], a semi-empirical formula based on theoretical and experimental data is recommended to compensate the inherent asymmetry of IMs, voltage variations, and other non-ideal dependencies. Despite extensive research and acceptable conclusions to provide a unique threshold to detect STTFs, there is a need for further improvements. In particular, other types of IMs, such as wound-rotor induction machines (WRIMs), have to be considered, and the variation of the effective negative sequence impedance angle due to the contribution of STTF current definitely has a great impact on the security and reliability of the pre-formed database.

In [39-42], the negative sequence current tracking is also used as the STTF detection criterion. In [39], it is theoretically proved that the negative sequence current angle ($\sphericalangle\bar{I}_2$) as the result of STTF location is as follows:

$$\sphericalangle\bar{I}_2|_{STTF@A} = 0°, \sphericalangle\bar{I}_2|_{STTF@B} = 120°, \sphericalangle\bar{I}_2|_{STTF@C} = 240° \quad (3)$$

Along with the innovations made and a specific glance at the $\sphericalangle\bar{I}_2$ behavior, it is explicitly concluded that $\sphericalangle\bar{I}_2$ is ineffective against slip and voltage variations, which is not compatible with simulation and experimental results in the same reference and [42]. This incompatibility stems from inherent asymmetry and the combination of loading and UVS effects that were not addressed in that paper. However, limited voltage variation in terms of magnitude and angle and non-calibrated measuring sensors effects are studied to some extent. Moreover, in [39, 40], any acceptable and secure threshold for STTF detection was not proposed.

There are other techniques based on neural networks [43-45], zero sequence voltage monitoring [46], and effective negative sequence impedance [47, 48]. A general comparison of all relevant techniques is summarized in Table I.

In this paper, a more comprehensive strategy is proposed to detect the STTFs in IMs based on the relative magnitude and angle of $\bar{I}_2$ for STTF detection and faulty phase identification in an online condition by the neutralization of the UVS related current component. Indeed, this paper uses a model-based approach to detect and locate STTFs in IMs. The method is based on monitoring the magnitude, and angle of the negative sequence current component caused by the circulation of the short-circuit current in the shorted turns, thus providing a reliable fault signature of STTFs.

The originality of this work can be explained by the following items:

- Extraction of the negative sequence faulty current component caused by the short-circuit current flowing in the branch containing the shorted turns by using the simplified model, which results from a modification introduced in the model (Fig. 2).
- Presentation of an efficient and generalized methodology to set the fault threshold level, leading to accurate STTF detection without false alarms. This threshold setting can be used with all types of IMs and takes into account all non-ideal conditions of the machine to diagnose STTFs with high reliability, accuracy, and sensitivity.
- Identification of the faulty phase by using the angle of the purified negative sequence current, while whole the trigonometric circle is devided to three symmetric regions for three phases to determine the faulty phase, as well.

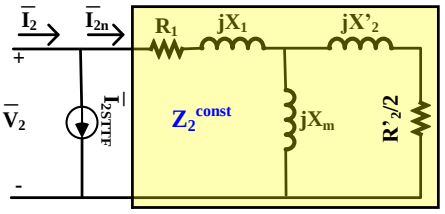

Fig.2. The proposed simplified negative sequence equivalent circuit of IMs.

In continue, the proposed method is described in the Sec. 2. The simulation and experimental results are presented in Sec. 3 and Sec. 4, respectively, anf finally, the paper is concluded in Sec. 5.

2. Proposed method to diagnose STTFs

According to the negative sequence equivalent circuit of Fig. 2, the equivalent rotor resistance referred to the stator side is approximately equal to half the rotor resistance ($R'_2/2$) since the slip "s" is very small ($s \leq 5\%$). Thus, it can be considered that in the proposed

simplified model of the healthy negative sequence impedance is a constant impedance $\bar{Z}_2^{const}$, insensitive to the motor load conditions. It should be noted that $\bar{Z}_2^{const}$ can be easily calculated from the rated values in the machine nameplate or from the general no-load and lock-rotor tests specified in IEEE Std 112 [49].

2.1. STTF Detection Procedure

As illustrated in Fig. 2, the simplified negative sequence equivalent circuit, supplied by the negative sequence voltage $\overline{V_2}$, is composed of two branches in parallel: the negative sequence impedance $\bar{Z}_2^{const}$ branch and the negative sequence faulty current ($\bar{I}_{2STTF}$) one, which represents the branch containing the effects of the STTF.

Table I. Summary of negative and zero sequence oriented techniques

Reference No.	Fault Index	Fault Type	Inherent Asymmetry Compensation Technique	Considering the Effect of Unbalance Voltage Source	Considering the Loading Level	Threshold	Faulty Phase Identification	Security Investigation Against Rotor Faults
[7]	$\|I_2\|$	STTF	Complex constant K estimation ($I_2 = K_1V_1 + K_2V_2$) & Look-up table	Complex constant K estimation ($I_2 = K_1V_1 + K_2V_2$) & Look-up table	✓	×	×	×
[27]	$\|I_2\|$	STTF	Look-up table	×	✓	×	×	×
[32-35]	Z_{np} (off-diagonal element of admittance matrix)	STTF	Estimation of Z_{np} in two different stages of V_2 & slip	Estimation of Z_{np} in two different stages of V_2 & slip	✓	×	×	×
[36-38]	$\|I_2\|$	STTF	Z_2 effective & thermal effect minimization ($I_2 = \frac{V_2 \sin\theta_2}{X_{h2}}$)	The semi-empirical quadratic function of healthy reactance (X_{h2}^1)	✓	✓	×	×
[39]	$\sphericalangle I_2$	STTF	×	Considering limited test points of injected unbalance voltage	×	×	✓	×
[40]	$\|I_f\|$ & $\sphericalangle I_2$	STTF	×	×	×	×	✓	×
[41]	$\|I_2\|$ & $\sphericalangle I_2$	STTF	×	×	✓	×	✓	×
[42]	$\|I_2\|$	STTF	Look-up table	Look-up table	×	×	×	×
[43-45]	$\|I_2\|$	STTF	Neural network	Neural network	✓	×	×	×
[46]	$\|V_0\|$	STTF	Using summation of the fundamental component of voltages	×	×	×	×	×
[47, 48]	Z_2^{eff}	STTF	×	×	×	×	×	×
This Paper	$\|I_{2STTF}\|$ & $\sphericalangle I_{2STTF}$	**STTF**	✓	✓	✓	✓	✓	✓

Hence, the total negative sequence current $\bar{I}_2$ generated in a faulty motor is the sum of the negative sequence current $\bar{I}_{2n}$ flowing in the negative sequence impedance $\bar{Z}_2^{const}$ (healthy part) and the negative sequence current $\bar{I}_{2STTF}$ flowing in the faulty branch as given by:

$$\bar{I}_2 = \bar{I}_{2STTF} + \bar{I}_{2n} \quad (4)$$

Using the three measured stator currents and voltages of the motor, the total negative sequence current $\bar{I}_2$ and the negative sequence voltage $\overline{V_2}$ are calculated at any moment by applying the Fortescue transformation or any other technique [50].

In healthy operating conditions, the current in the constant negative sequence impedance branch $\bar{I}_{2n}$ can be calculated by:

$$\bar{I}_{2n} = \bar{V}_2 / \bar{Z}_2^{const} \quad (5)$$

This current is not expected to be null even when $\bar{V}_2 = 0$ because of the different non-idealities of the machine mentioned in the introduction.

When the machine operates with an STTF, the STTF contribution branch's current $\bar{I}_{2STTF}$ will be assessed simultaneously by subtracting $\bar{I}_{2n}$ from the total negative sequence current $\bar{I}_2$ circulating in the machine as follows:

$$\bar{I}_{2STTF} = \bar{I}_2 - \bar{I}_{2n} \quad (6)$$

Hence, the variations in the amplitude and angle of $\bar{I}_{2STTF}$ will be considered as the main criteria for STTF detection and faulty phase identification.

On the other hand, it is worth noting that industrial protection relays commonly protect the motor using a fault detection criterion (FDC) based on the ratio between I_{2STTF} of and positive sequence current components magnitude (I_1). By analogy, in this work, the FDC used is defined as:

$$FDC = (I_{2STTF} / I_1) \times 100\% \quad (7)$$

It should be noted that due to the maximum permissible UVF of the grid (which can reach 1.5% in some countries [28]), due to the inherent machine asymmetries and even the minor effects of the load level variation on the actual value of the negative sequence impedance of the machine, in practical conditions $\bar{I}_{2STTF}$ will never be zero. As such, it is mandatory to choose an adequate and secure threshold (Th_{STTF}) to ensure accurate fault detection. The proposed threshold is defined based on several tests performed under different load conditions and for different negative sequence voltage component levels. The choice of the threshold value is addressed in the simulation and experimental sections.

Evaluating these experimental test results for adjusting the threshold value has the advantages of (i) practically eliminating any training process algorithm, (ii) the need to build a look-up table to compensate for non-idealities, (iii) the effects of unbalanced voltage sources, and (iv) the minimization of thermal effect aspects that were used and discussed in detail in previous references [36-38]. With the selected fault threshold value (Th_{STTF}), the STTF detection procedure is based on the monitoring and comparison of the

FDC with Th_{STTF}. If the FDC is smaller than Th_{STTF}, the machine is considered in healthy condition. Otherwise, an STTF has occurred and the fault location must be teraced for the second step of the diagnosis process.

2.2. *Faulty Phase Identification*

Once an STTF is detected, the identification of the faulty phase will be based on the monitoring of the angle $\measuredangle\bar{I}_{2STTF}$ of the negative sequence faulty current.

In the case of an STTF, a major portion of $\bar{I}_2$ flows in the parallel STTF branch of the proposed simplified equivalent circuit of Fig. 2. Thus, $\measuredangle\bar{I}_{2STTF}$ is close to $\measuredangle\bar{I}_2$ As mentioned in [41], for an STTF occurring in phases A, B or C, $\measuredangle\bar{I}_2$ is predicted to be 0, 120°, and -120°, respectively, and an identical behavior could be anticipated for $\measuredangle\bar{I}_{2STTF}$. However, in real conditions, $\measuredangle\bar{I}_{2STTF}$ is located around (not exactly on) the corresponding phase axes (0°, 120°, and -120°). This happens because the assumptions based on which the results in [41] were obtained are only an approximation of reality and do not reflect the exact electromagnetic behavior of the machine under the presence of an STTF. The neutral point of the stator windings, in a star-connected machine, will be shifted from its normal position when an STTF appears, and the magnetic axis of the shorted turns also does not coincide in many cases with the magnetic axis of the healthy phase windings. In addition, there is a reduction in the phase voltage of the winding affected by the fault as a consequence of the decrease in the effective number of turns of that winding. The circulation of a reverse current in the shorted turns reduces the linkage flux in a wide portion of the faulty winding, thus moving the operating point downwards in the B-H curve. Such variations in this region will also change the operating points of the other phase windings (healthy ones) in the common coil areas, as the coils of different phases overlap partially and share some core sections.

Accordingly, the negative sequence equivalent circuit can only be considered approximately under the presence of STTFs. It has an acceptable accuracy when the machine is in healthy conditions, i.e., when $\bar{I}_{2STTF} = 0$. In this work, this circuit is used only to calculate $\bar{I}_{2n}$ and obtain $\bar{I}_{2STTF} = \bar{I}_2 - \bar{I}_{2n}$. If $\bar{I}_{2STTF}$ is higher than the threshold value, an STTF has been confirmed. Afterward, when an STTF is detected, the faulty phase can be identified according to the sector in which $\measuredangle\bar{I}_{2STTF}$ is located:

$-60° < \measuredangle\bar{I}_{2STTF} < 60°$ → STTF is in phase A
$60° < \measuredangle\bar{I}_{2STTF} < 180°$ → STTF is in phase B
$180° < \measuredangle\bar{I}_{2STTF} < 300°$ → STTF is in phase C

2.3. *Flowchart of the Proposed Method*

According to the descriptions mentioned above, the entire procedure for the diagnosis of STTF can be illustrated with the aid of a logical flowchart depicted in Fig. 3. Based on this flowchart, using an appropriate threshold (Th_{STTF}) and an empirical range of angular changes around the central axis of each phase (0°, 120°, and -120°), an effective STTF detection is guaranteed, and the faulty phase can be identified without any overlap.

The fault detection process and faulty phase identification are summarized in the following steps:

- Data acquisition and calculation of $\bar{I}_2$ and $\bar{I}_{2n}$;
- Extraction of $\bar{I}_{2STTF}$ by using (6);
- Calculation of FDC and comparing it with Th_{STTF};
- If FDC exceeds Th_{STTF}, an STTF is confirmed;
- In a faulty case, the identification of the defective phase depends on the value of $\measuredangle\bar{I}_{2STTF}$ as mentioned in the previous subsection.

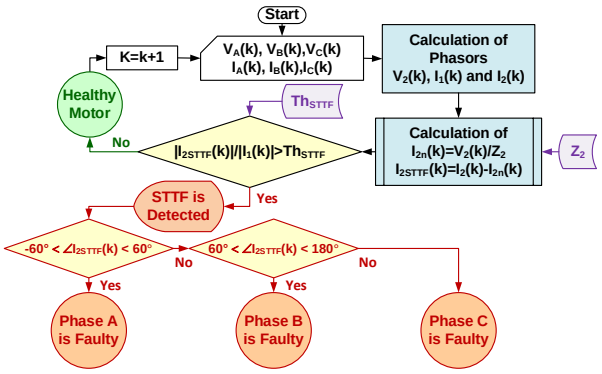

Fig.3. Flowchart of the proposed diagnostic method.

3. Simulation results

To validate the proposed diagnostic method, a WRIM was simulated in a finite element software package (Ansys Maxwell ver.16). The simulated WRIM is similar, although not precisely equal at the fundamental frequency of 50 Hz. The negative sequence impedance of the simulated WRIM is $\bar{Z}_{2,no\text{-}load}^{const} = 9.705\measuredangle 82.30° \, \Omega$ and $\bar{Z}_{2,full\text{-}load}^{const} = 8.534\measuredangle 81.10° \, \Omega$ and for no-load and full-load conditions, respectively.

To evaluate the weak points of previous studies and also highlight the advantages of the proposed diagnostic approach, the fault indices are studied with the machine under $STTF_5$ in each phase separately ($STTF_{5A}$, $STTF_{5B}$, and $STTF_{5C}$), both in balanced and unbalanced voltage supply conditions (with a permissible UVF=1%). The FDC is calculated considering a constant value for $\bar{Z}_2^{const} = \bar{Z}_{2,full\text{-}load}^{const}$.

In Fig. 4, the FDC calculated by (7) (which represents the modulus) and the angle $\measuredangle\bar{I}_{2STTF}$ are plotted in polar coordinates for three different faulty cases (encompassing faults in the three stator phases), for a balanced (blue crosses) and an unbalanced (red circles) voltage supply system, when the machine runs at no-load (left) and full-load (right). The results show that the FDC values are higher for the no-load condition in comparison with the full-load case, which is easily justifiable by the higher positive sequence current component for higher motor load levels, while $\bar{I}_{2STTF}$ is barely independent of the motor load condition. It is also visible the dispersion of the obtained points around the three colored areas being this dispersion more when there is an unbalanced supply voltage in addition to the STTF. In addition, it can be concluded by looking at Fig. 4 that FDCs for all cases is greater than 3.7%, while such a value can be chosen as an appropriate threshold (Th_{STTF}). Moreover, as can be seen, the related fault index angles ($\measuredangle\bar{I}_{2STTF}$) in both conditions are fully compatible with the recommended faulty phase detection algorithm in the flowchart and go through all non-ideal conditions. Although the results for the full load are focused on the specific regions on the angles zero, 120° and -120° for STTF occurrence on phases A, B, and C

respectively (Fig. 4, right), such results for the no-load condition are more distributed due to the lower I_1 in comparison to the I_{2STTF} in the FDC relation. However, the expected geometric location of these points for each specific STTF did not interfere with the adjacent areas for the healthy phases. Also, it can result that faulty phase identification may be made with more reliability in the full load than in the no-load conditions.

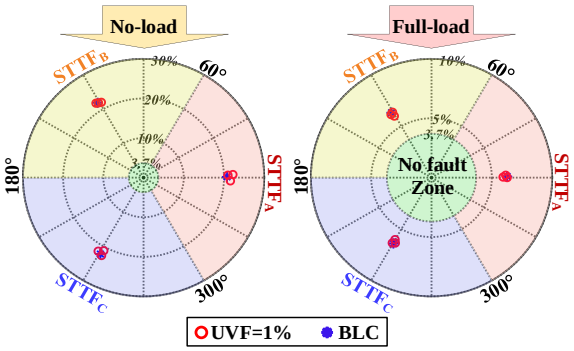

Fig.4. FDC and $\measuredangle\bar{I}_{2STTF}$ in the face of balanced and unbalanced (with UVF=1%) voltage sources in no-load (left) and full-load conditions for three faulty cases in the three phases ($STTF_{5A}$, $STTF_{5B}$, and $STTF_{5C}$).

4. Experimental results

4.1. Experimental Setup

In the experimental validation of the proposed diagnostic methodology, a three-phase WRIM with the specifications in Table II is used. For higher flexibility, three single-phase variacs (autotransformers) were used in order to control the degree and type of the unbalanced supply voltages applied to the machine in some experiments. The applied voltages and machine supply currents are sensed with three current transformers and three potential transformers and measured using synchronized analog to digital converters with a sampling frequency of 5 kHz. A low voltage synchronous generator that supplies a three-phase resistor bank is coupled to the WRIM shaft in order to control its mechanical load by adjusting its field current. Several taps are connected to different points along the three stator windings of the WRIM to allow the introduction of STTFs in an online condition. A schematic diagram and a picture of the experimental setup are shown in Fig. 5.

Table II. WRIM characteristics

Par.	Value	Par.	Value	Rat.	Value	Rat.	Value
R_1	2.606 Ω	X'_2	2.833 Ω	P_r	2.2 kW	Poles	4
R'_2	4.098 Ω	X_m	40.889 Ω	V_r	380 V (L-L)	n_r	1360 rpm
X_1	2.833 Ω	Z_2^{cosnt}	7.15∢51.21° Ω	P.F.	0.75	Turns	216

4.2. Unbalanced Voltage Source in a Healthy Machine

First, the effects of UVS applied to a healthy machine are evaluated, namely the variations of $\measuredangle\bar{I}_2$ w.r.t the imbalance voltage deviation direction, as shown in Fig. 6 using polar coordinates. The voltage imbalance was created by decreasing the voltage amplitude in each phase separately. For an imbalance in phase A, $\measuredangle\bar{I}_2$ varies somewhere along the axis of 180°. Similarly, if the voltage asymmetry is created in phases B and C, $\measuredangle\bar{I}_2$ will be located near or along the axes of -60° and 60°, respectively. These central axes values are opposite (phase-shifted by 180º) to the axes associated with the faults in the corresponding phases, as shown before in Fig. 4. In fact, the axes of each UVS coincide with the phase of the voltage vector of the negative sequence component of the motor supply voltages.

To cover all non-ideal situations and inevitably inaccuracies of the model used for STTF detection, the healthy operation of the machine is characterized by a negative sequence current vector. This vector lies in regions symmetrically built around each of the previously mentioned axes, with an opening of 120º so that they do not overlap, as highlighted by the three colored areas in Fig. 6. The motor's unbalanced supply voltage is arbitrary in actual operating conditions. In these circumstances, the healthy motor operation can be characterized by a negative sequence current vector that lies in an area of 120º built around the axis defined by the negative sequence component of the supply voltages.

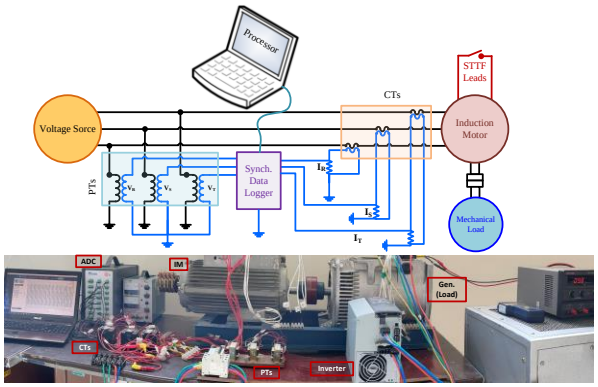

Fig.5. Schematic diagram and picture of the experimental setup.

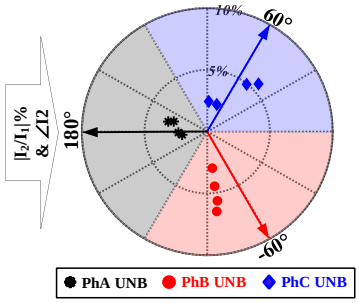

Fig.6. The variation of $\measuredangle\bar{I}_2$ respect to the imbalance voltage deviation direction (UVF variations are in the range of 0.5~1.7%).

4.3. Negative Sequence Current Components for STTFs

The impact of different STTFs (different numbers of shorted turns) in the negative sequence current components I_2 and I_{2STTF} for two values of the UVF are illustrated in Fig. 7 for different time windows of 100 ms. All current components were normalized w.r.t I_1 and expressed as a percentage.

As shown, the percent values of I_2 depend on the STTF severity and the degree of imbalance of the supply voltages. However, the calculated I_{2STTF} depends only on the STTF severity, and a linear relationship can approximate such dependency. As seen, by removing the unbalanced voltage

source effect on the I_{2STTF}, an approximately linear relationship will be appeared between the FDC value and the fault severity.

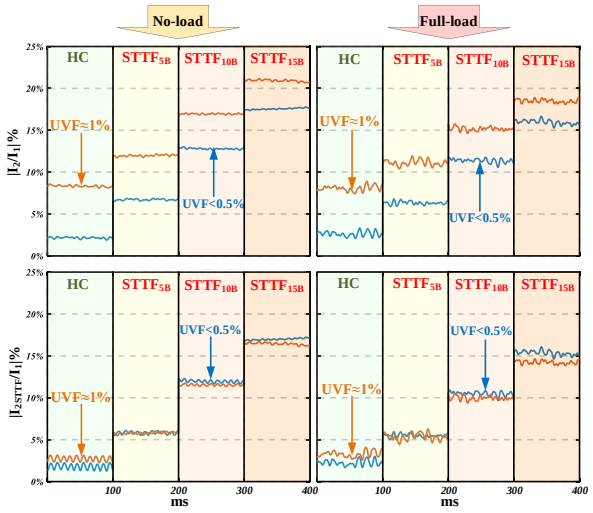

Fig.7. The percentage of I_2 (top) and I_{2STTF} (down) respect to I_1 at no-load (left) and full-load (right) conditions for different categories of HC and STTFs in almost balanced (UVF<0.5%, blue) and unbalanced voltage sources (UVF about 1%, red).

4.4. Fault Threshold Level Definition

Similar to other current-based diagnostic techniques, there is the need to define a reliable and secure threshold level to distinguish faulty cases from healthy ones. To determine such threshold level for STTF detection (Th_{STTF}), the motor FDC was evaluated for different voltage unbalances, ranging from the most severe cases (UVF>1%, up to 1.7%) to the lower ones (UVF<0.5%), with the motor in healthy conditions. In these tests, the inherent motor constructional asymmetries are taken into consideration. Fig. 8 shows that for the tested motor, both at no-load and full-load conditions, the FDC slightly exceeds 3% for a UVF≅1.7%. Accordingly, in order to provide a secure and reliable level for STTF detection, Th_{STTF} is selected 20% more than the maximum value in the healthy condition and is set as 3.7%. Choosing a lower Th_{STTF} (3.2~3.7%) would increase the sensitivity, decrease security, and vice-versa.

4.5. Detection and Location of STTFs in Real Conditions

To evaluate the performance of the introduced method, three faulty conditions, including $STTF_{5B}$, $STTF_{10B}$, and $STTF_{15B}$ have been applied to the machine running at no-load and rated load conditions. An UVF is also considered and applied as weak (UVF<0.5%), medium (0.5% < UVF < 1.1%), and severe (UVF>1.1~1.7%). In practice, it is illogical to investigate the effects of unbalanced voltage sources with a UVF>1.7%. In such cases, the motor protection would be the responsibility of adequate relays defined by the ANSI standard device numbers [51], namely the 47 (phase balance voltage relay) and 27/59 (under and over-voltage relay). Fig. 9 shows the experimental test results for such conditions. As can be seen, the FDC values for $STTF_{5B}$ are slightly higher than 5%, and the related $\measuredangle \bar{I}_{2STTF}$ are located between 120° and 180°. FDCs for $STTF_{10B}$ is around 10%, and the related $\measuredangle \bar{I}_{2STTF}$ are located in the vicinity of the 120° axis. For $STTF_{15B}$, FDCs are about 15% and the related $\measuredangle \bar{I}_{2STTF}$ is in the range 110~120°. Thus, all test points are concentrated in the predicted areas. Moreover, it can be concluded that the FDC values for the faulty cases depend on the STTF severity factor (μ).

To evaluate the methodology's performance for identifying the faulty phase, $STTF_{10A}$ was also applied to the machine, and the results are shown in the 4th column of Fig. 9. As can be seen, similar to the $STTF_{10B}$ case, the obtained FDCs for all test cases are around 10%, and the angle $\measuredangle I_{2STTF}$ now varies around the 0° axis, which is the axis of the faulty phase A. For the cases of faulty phase B, the angle was around 120º, thus validating the phase location procedure.

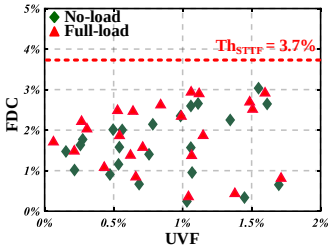

Fig.8. FDC values with the healthy motor at no-load and full-load conditions for different permissible UVF values.

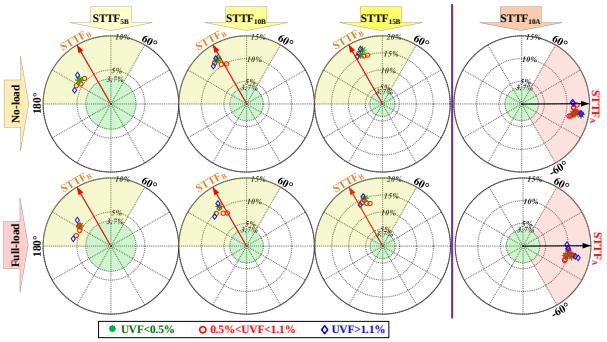

Fig.9. FDC and $\measuredangle \bar{I}_{2STTF}$ for no-load (top) and full-load (down) conditions, corresponding to $STTF_{5B}$, $STTF_{10B}$ and $STTF_{15B}$ (1st ~ 3rd col.), and $STTF_{10A}$ (4th col.), with different UVFs up to 1.7%.

4.6. STTF Detection for Inverter-Fed Machines

To evaluate the proposed diagnostic methodology in inverter-fed machines, the same WRIM was supplied by an inverter and the obtained drive system was operated in scalar control mode. In these conditions, the motor supply voltages are roughly symmetrical, consequently, there is no need to calculate the component $\bar{I}_{2n}$ due to unbalanced voltage sources. However, the measured current $\bar{I}_2$ is not null even when the machine is in healthy conditions, due to its intrinsic constructional asymmetries. The obtained results for different STTFs in phases A and B, at different supply frequencies ranging from 20 up to 60 Hz, are shown in Fig. 10 and Table III. The results show that with the machine in healthy conditions, the FDC value is lower than 1.2%, then increasing with the number of shorted turns. The STTFs are detectable with higher resolution at higher frequencies, as expected, due to the higher short-circuit current for higher frequencies (which leads to higher induced voltages).

In comparison with the line-fed case, for the same number of shorted turns, the method seems to have a higher sensitivity for the inverter-fed machine. In terms of fault location, as shown in Table III, the angle $\measuredangle \bar{I}_{2STTF}$ allows a

correct identification of the faulty phase, as demonstrated before for the line-fed situation.

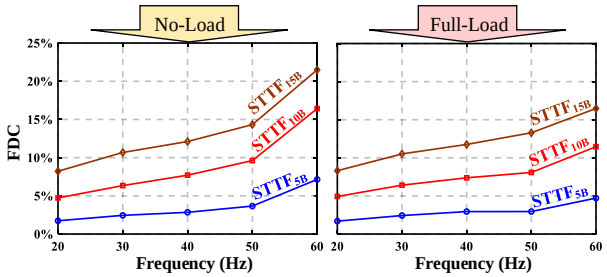

Fig.10. FDC versus the applied frequency for several numbers of shorted turns at no-load (left) and full-load (right) conditions.

Table III. Identification of the faulty phase through $\measuredangle\bar{I}_{2STTF}$

Load Condition	f (Hz)	$\measuredangle\bar{I}_{2STTF}$ (Deg.)			
		$STTF_{5A}$	$STTF_{10A}$	$STTF_{5B}$	$STTF_{10B}$
No-load	20	9.7	3.0	106.7	112.9
	30	7.7	-1.6	114.0	114.3
	40	6.6	-2.5	117.6	115.9
	50	7.3	1.7	128.8	122.0
	60	6.3	-8.7	130.7	114.0
Full-load	20	8.5	2.2	110.5	113.3
	30	6.0	-2.4	117.6	115.2
	40	5.0	-3.5	121.7	116.7
	50	3.2	-2.8	139.7	116.8
	60	8.4	-13.5	133.8	114.7

5. Conclusion

A comprehensive stator turn-to-turn fault diagnostic algorithm based on the negative sequence equivalent model is presented in this paper, which has the capability of fault detection and faulty phase identification in online conditions. With this reliable method, the effect of the negative sequence voltage component is eliminated. Moreover, the threshold level to detect STTF is obtained based on the actual construction of the machine (considering its inherent asymmetries), using a simple and straightforward procedure.

The experimental results have shown that from the sensitivity point of view, even weak faults with five shorted turns (2.3% of the total number of turns per phase) are detectable in the tested machine.

The robustness and security of this technique against unbalanced voltage sources with a permissible unbalance factor up to 1.7%, and load level variations from no-load up to full-load conditions were also demonstrated, making it a sensitive, reliable and secure non-invasive diagnostic method. Also, the performance of this method for the inverter-fed mode showed that the related sensitivity will be increased in such a condition.

6. References

[1] T. Javied, T. Rackow, R. Stankalla, C. Sterk, and J. Franke, "A study on electric energy consumption of manufacturing companies in the German industry with the focus on electric drives," Procedia CIRP, vol. 41, pp. 318-322, Jan. 2016.

[2] M. Kostic, M. Ivanovic, and S. Minic, "Reduction of electric energy consumption in induction motor drives by setting supply voltage," in 2012 2nd International Symposium On Environment Friendly Energies And Applications, June. 2012, Newcastle upon Tyne, UK, pp. 128-133: IEEE, **doi:** 10.1109/EFEA.2012.6294073.

[3] B. Venkataraman, B. Godsey, W. Premerlani, E. Shulman, M. Thaku, and R. Midence, "Fundamentals of a motor thermal model and its applications in motor protection," in 58th Annual Conference for Protective Relay Engineers, Apr. 2005, College Station, TX, USA, pp. 127-144: IEEE, **doi:** 10.1109/CPRE.2005.1430428.

[4] S. Cho, J. H. Shin, H. B. Jun, H. J. Hwang, C. Ha, and J. H. Wang, "A study on estimating the next failure time of compressor equipment in an offshore plant," Mathematical Problems in Engineering, vol. 2016, p. 14, Oct. 2016.

[5] J. Vico and R. Hunt, "Principles in motor protection," IEEE Industry Applications Magazine, vol. 17, no. 6, pp. 52-61, Dec. 2011.

[6] M. R. W. Group, "Report of large motor reliability survey of industrial and commercial installations, Part I," IEEE Trans. Industrial Applications, vol. IA-21, no. 4, pp. 853-864, Aug. 1985.

[7] R. M. Tallam, T. G. Habetler, and R. G. Harley, "Transient model for induction machines with stator winding turn faults," IEEE Transactions on Industry Applications, vol. 38, no. 3, pp. 632-637, June 2002.

[8] IEEE Recommended Practice for Conducting Short-Circuit Studies and Analysis of Industrial and Commercial Power Systems, IEEE Std 3002.3-2018, pp. 1-184, Mar. 2019.

[9] G. Mirzaeva and K. I. Saad, "Advanced diagnosis of stator turn-to-turn faults and static eccentricity in induction motors based on internal flux measurement," IEEE Transactions on Industry Applications, vol. 54, no. 4, pp. 3961-3970, Aug. 2018.

[10] F. Trutt, J. Sottile, and J. L. Kohler, "Condition monitoring of induction motor stator windings using electrically excited vibrations," in Conference Record of the 2002 IEEE Industry Applications Conference. 37th IAS Annual Meeting (Cat. No. 02CH37344), Oct. 2002, Pittsburgh, PA, USA, vol. 4, pp. 2301-2305: IEEE, **doi:** 10.1109/IAS.2002.1042767.

[11] G. Gentile, S. Meo, and A. Ometto, "Induction motor current signature analysis to diagnostics, of stator short circuits," in 4th IEEE International Symposium on Diagnostics for Electric Machines, Power Electronics and Drives (SDEMPED), Aug. 2003, Atlanta, GA,USA, pp. 47-51: IEEE, **doi:** 10.1109/DEMPED.2003.1234545.

[12] J. H. Jung, J. J. Lee, and B. H. Kwon, "Online diagnosis of induction motors using MCSA," IEEE Transactions on Industrial Electronics, vol. 53, no. 6, pp. 1842-1852, Dec. 2006.

[13] S. M. Cruz and A. M. Cardoso, "Diagnosis of stator inter-turn short circuits in DTC induction motor drives," IEEE Transactions on Industry Applications, vol. 40, no. 5, pp. 1349-1360, Oct. 2004.

[14] A. M. Cardoso, S. Cruz, and D. Fonseca, "Inter-turn stator winding fault diagnosis in three-phase induction motors, by Park's vector approach," IEEE Transactions on Energy Conversion, vol. 14, no. 3, pp. 595-598, Sep. 1999.

[15] S. M. Cruz and A. M. Cardoso, "Stator winding fault diagnosis in three-phase synchronous and asynchronous motors, by the extended Park's vector approach," IEEE Transactions on industry applications, vol. 37, no. 5, pp. 1227-1233, Oct. 2001.

[16] S. M. Cruz, "An active–reactive power method for the diagnosis of rotor faults in three-phase induction motors operating under time-varying load conditions," IEEE Transactions on Energy Conversion, vol. 27, no. 1, pp. 71-84, Mar. 2012.

[17] R. Maier, "Protection of squirrel-cage induction motor utilizing instantaneous power and phase information," IEEE Transactions on Industry Applications, vol. 28, no. 2, pp. 376-380, Apr. 1992.

[18] B. Wang, C. Shen, K. Xu, and T. Zheng, "Turn-to-turn short circuit of motor stator fault diagnosis in continuous state based on deep auto-encoder," IET Electric Power Applications, vol. 13, no. 10, pp. 1598-1606, Oct. 2019.

[19] R. M. Tallam, T. G. Habetler, and R. G. Harley, "Self-commissioning training algorithms for neural networks with applications to electric machine fault diagnostics," IEEE Transactions on Power Electronics, vol. 17, no. 6, pp. 1089-1095, Nov. 2002.

[20] I. P. T. Soumas, G. Georgoulas, E. D. Mitronikas, and A. N. Safacas, "Asynchronous machine rotor fault diagnosis technique using complex wavelets," IEEE Transactions on Energy Conversion, vol. 23, no. 2, pp. 444-459, June. 2008.

[21] G. A. Jimenez, A. O. Munoz, and M. A. Duarte-Mermoud, "Fault detection in induction motors using Hilbert and Wavelet transforms," Electrical Engineering, vol. 89, no. 3, pp. 205-220, Jan. 2007.

[22] B. A. Vinayak, K. A. Anand, and G. Jagadanand, "Wavelet-based real-time stator fault detection of inverter-fed induction motor," IET Electric Power Applications, vol. 14, no. 1, pp. 82-90, Jan. 2020.
[23] A. Siddique, G. Yadava, and B. Singh, "Effects of voltage unbalance on induction motors," in Conference Record of the 2004 IEEE International Symposium on Electrical Insulation, Sep. 2004, Indianapolis, IN, USA, pp. 26-29: IEEE, **doi:** 10.1109/ELINSL.2004.1380430.
[24] IEEE Guide for AC Motor Protection IEEE Std C37.96-2012 (Revision of IEEE Std C37.96-2000), pp. 1-160, Feb. 2013.
[25] A. Von Jouanne and B. Banerjee, "Assessment of voltage unbalance," IEEE transactions on power delivery, vol. 16, no. 4, pp. 782-790, Oct. 2001.
[26] S. Williamson and K. Mirzoian, "Analysis of cage induction motors with stator winding faults," IEEE transactions on power apparatus and systems, vol. PAS-104, no. 7, pp. 1838-1842, July 1985.
[27] G. Kliman, W. Premerlani, R. Koegl, and D. Hoeweler, "A new approach to on-line turn fault detection in AC motors," in IAS'96. Conference Record of the 1996 IEEE Industry Applications Conference 31st IAS Annual Meeting, Oct. 1996, San Diego, CA, USA, vol. 1, pp. 687-693: IEEE, **doi:** 10.1109/IAS.1996.557113.
[28] F. Ghassemi and M. Perry, "Review of voltage unbalance limit in the GB grid code CC. 6.1. 5 (b)," National Grid, Report, pp. 14-58, Oct. 2014.
[29] H. A. Toliyat and G. B. Kliman, Handbook of electric motors. CRC press, Oct. 2018.
[30] J. Sottile, F. C. Trutt, and J. L. Kohler, "Condition monitoring of stator windings in induction motors. II. Experimental investigation of voltage mismatch detectors," IEEE Transactions on Industry Applications, vol. 38, no. 5, pp. 1454-1459, Oct. 2002.
[31] F. C. Trutt, J. Sottile, and J. L. Kohler, "Online condition monitoring of induction motors," IEEE Transactions on Industry Applications, vol. 38, no. 6, pp. 1627-1632, Dec. 2002.
[32] S. B. Lee, R. M. Tallam, and T. G. Habetler, "A robust, online turn-fault detection technique for induction machines based on monitoring the sequence component impedance matrix," IEEE Transactions on Power Electronics, vol. 18, no. 3, pp. 865-872, May. 2003.
[33] S. Cheng, P. Zhang, and T. G. Habetler, "An impedance identification approach to sensitive detection and location of stator turn-to-turn faults in a closed-loop multiple-motor drive," IEEE Transactions on Industrial Electronics, vol. 58, no. 5, pp. 1545-1554, May 2011.
[34] A. Berzoy, A. A. Mohamed, and O. Mohammed, "Complex-vector model of interturn failure in induction machines for fault detection and identification," IEEE Transactions on Industry Applications, vol. 53, no. 3, pp. 2667-2678, May 2017.
[35] A. Berzoy, H. H. Eldeeb, and O. A. Mohammed, "Online detection of stator faults in DTC-driven IM using SC impedance matrix off-diagonal term," IEEE Transactions on Industry Applications, vol. 55, no. 6, pp. 5906-5915, Dec. 2019.
[36] M. Arkan, D. Perović, and P. Unsworth, "Online stator fault diagnosis in induction motors," IEE Proceedings-Electric Power Applications, vol. 148, no. 6, pp. 537-547, Nov. 2001.
[37] M. Arkan, D. Kostic-Perovic, and P. Unsworth, "Modelling and simulation of induction motors with inter-turn faults for diagnostics," Electric Power Systems Research, vol. 75, no. 1, pp. 57-66, July 2005.
[38] M. Arkan and P. Unsworth, "Stator fault diagnosis in induction motors using power decomposition," in Conference Record of the 1999 IEEE Industry Applications Conference. 34th IAS Annual Meeting (Cat. No. 99CH36370), Oct. 1999, Phoenix, AZ, USA, vol. 3, pp. 1908-1912: IEEE, **doi:** 10.1109/IAS.1999.805999.
[39] M. Bouzid and G. Champenois, "Accurate stator fault detection insensitive to the unbalanced voltage in induction motor," in 2012 XXth International Conference on Electrical Machines, Sep. 2012, Marseille, France, pp. 1545-1551: IEEE, **doi:** 10.1109/ICElMach.2012.6350084.
[40] M. Bouzid and G. Champenois, "A novel reliable indicator of stator windings fault in induction motor extracted from the symmetrical components," in 2011 IEEE International Symposium on Industrial Electronics, June 2011, Gdansk, Poland, pp. 489-495: IEEE, **doi:** 10.1109/ISIE.2011.5984074.
[41] M. B. K. Bouzid and G. Champenois, "New expressions of symmetrical components of the induction motor under stator faults," IEEE Transactions on Industrial Electronics, vol. 60, no. 9, pp. 4093-4102, Sep. 2013.
[42] S. Bakhri, N. Ertugrul, and W. L. Soong, "Negative sequence current compensation for stator shorted turn detection in induction motors," in IECON 2012 - 38th Annual Conference on IEEE Industrial Electronics Society, Oct. 2012, Montreal, QC, Canada, pp. 1921-1926: IEEE, **doi:** 10.1109/IECON.2012.6388908.
[43] R. M. Tallam, T. G. Habetler, R. G. Harley, D. J. Gritter, and B. H. Burton, "Neural network based online stator winding turn fault detection for induction motors," in Conference Record of the 2000 IEEE Industry Applications Conference. 35th IAS Annual Meeting and World Conference on Industrial Applications of Electrical Energy (Cat. No. 00CH37129), Oct. 2000, Rome, Italy, vol. 1, pp. 375-380: IEEE, **doi:** 10.1109/IAS.2000.881138.
[44] R. M. Tallam, T. G. Habetler, and R. G. Harley, "Continual online training of neural networks with applications to electric machine fault diagnostics," in 2001 IEEE 32nd Annual Power Electronics Specialists Conference (IEEE Cat. No. 01CH37230), June 2001, Vancouver, BC, Canada, vol. 4, pp. 2224-2228: IEEE, **doi:** 10.1109/PESC.2001.954450.
[45] R. M. Tallam, T. G. Habetler, and R. G. Harley, "Experimental testing of a neural-network-based turn-fault detection scheme for induction machines under accelerated insulation failure conditions," in 4th IEEE International Symposium on Diagnostics for Electric Machines, Power Electronics and Drives (SDEMPED), Aug. 2003, Atlanta, GA,USA, pp. 58-62: IEEE, **doi:** 10.1109/DEMPED.2003.1234547.
[46] M. A. Cash, T. G. Habetler, and G. B. Kliman, "Insulation failure prediction in AC machines using line-neutral voltages," IEEE Transactions on Industry Applications, vol. 34, no. 6, pp. 1234-1239, Dec. 1998.
[47] J. L. Kohler, J. Sottile, and F. C. Trutt, "Alternatives for assessing the electrical integrity of induction motors," IEEE Transactions on Industry Applications, vol. 28, no. 5, pp. 1109-1117, Oct. 1992.
[48] J. L. Kohler, J. Sottile, and F. C. Trutt, "Condition monitoring of stator windings in induction motors. I. Experimental investigation of the effective negative-sequence impedance detector," IEEE Transactions on Industry Applications, vol. 38, no. 5, pp. 1447-1453, Oct. 2002.
[49] IEEE Standard Test procedure for Polyphase Induction Motors and Generators, IEEE Std 112-2017 (Revision of IEEE Std 112-2004), pp. 1-115, Feb. 2018.
[50] D. Yazdani, M. Mojiri, A. Bakhshai, and G. Joos, "A fast and accurate synchronization technique for extraction of symmetrical components," IEEE Transactions on Power Electronics, vol. 24, no. 3, pp. 674-684, Mar. 2009.
[51] IEEE Standard Electrical Power System Device Function Numbers, Acronyms, and Contact Designations, IEEE Std C37.2-2008 (Revision of IEEE Std C37.2-1996), pp. 1-48, Oct. 2008.

International Journal of
Research and Technology in Electrical Industry

Next Issue

September 2022

Submit your papers in:

IJRTEI.sbu.ac.ir

Publisher:
Shahid Beheshti University
ISSN: 2821-0190
Frequency: Semiannual
Language: English

Website: IJRTEI.sbu.ac.ir
E-Mail: IJRTEI@sbu.ac.ir
Phone: (+98)21-73932321
Fax: (+98)21-73932321